UNIVERSITÀ
DEGLI STUDI
DI PADOVA

Sede Amministrativa: Università degli Studi di Padova

Dipartimento di Ingegneria Industriale

CORSO DI DOTTORATO DI RICERCA IN: INGEGNERIA INDUSTRIALE
CURRICOLO: INGEGNERIA DEI MATERIALI
CICLO XXX

ANALYSIS OF THE TRIBOLOGICAL EFFECTS OF MOLD SURFACE PROPERTIES ON THE MICRO INJECTION MOLDING PROCESS

Tesi redatta con il contributo finanziario della Fondazione Cariparo

Coordinatore: Ch.mo Prof. Paolo Colombo
Supervisore: Ch.mo Prof. Giovanni Lucchetta

Dottorando: Davide Masato

No amount of experimentation can ever prove me right; a single experiment can prove me wrong.

Alber Einstein

RINGRAZIAMENTI

Questo lavoro di tesi rappresenta per me la fine del Dottorato di Ricerca in Ingegneria Industriale, un percorso iniziato tre anni fa. Il raggiungimento ed il successo di questo traguardo non sarebbero stati possibili se non avessi incontrato le persone con le quali ho condiviso questo periodo.

Desidero innanzitutto dire grazie al prof. Lucchetta che è stato il supervisore del mio lavoro, che ha inspirato la mia passione per la ricerca e mi ha consentito di vivere delle esperienze incredibili. Grazie anche a Marco che mi ha supportato ed aiutato ogni giorno durante questi tre anni.

Ringrazio anche il Dr. Ben Whiteside e tutto il gruppo di ricerca dell'Università di Bradford per avermi accolto presso i loro laboratori. Un grazie a tutte le persone con cui ho collaborato, tra cui il Prof. Annoni e il Dr. Parenti del Politecnico di Milano e il Dr. Batal dell'Università di Birmingham.

Dico poi grazie a tutti gli amici e colleghi che ho incontrato durante le giornate trascorse al Laboratorio Te.Si., tra cui Luca, Riccardo, Filippo, Federico e Ruggero.

Un ringraziamento speciale ai miei genitori Silvia e Massimo e ai miei fratelli Gabriele e Giulio per il sostegno e l'affetto che non mi fanno mai mancare.

Infine, il ringraziamento più grande è per Federica perché la sua pazienza e il suo affetto mi hanno permesso di affrontare tutte le sfide che ho incontrato in questi anni.

D. M.

SOMMARIO

Lo stampaggio ad iniezione è una delle tecnologie più diffuse per la produzione di componenti in materiale plastico, per numerose applicazioni. Tuttavia, la crescente competitività del mercato spinge costantemente verso la progettazione di parti sempre più sottili e leggere, al fine di ridurre sia i costi che l'impatto ambientale. In questo contesto emergono notevoli problematiche, spesso legate alla progettazione degli stampi. In particolare, la progettazione della superficie dello stampo rappresenta una tematica strategica che può consentire di ottenere notevoli vantaggi in termini di miglior qualità delle parti stampate, ottimizzazione dei consumi energetici e di materiale.

In questo lavoro, le proprietà tribologiche della superficie dello stampo sono state analizzate focalizzando l'attenzione sulla caratterizzazione di trattamenti stampo convenzionali ed innovativi. Gli obiettivi principali di questo lavoro sono stati la riduzione della pressione di iniezione e delle forze di estrazione. Gli effetti delle proprietà dello stampo sulle fasi di riempimento ed estrazione sono stati studiati seguendo due strategie principali legate alla generazione della superficie dello stampo ed alla sua modifica mediante trattamenti superficiali. L'approccio adottato è stato basato su diverse campagne di stampaggio ad iniezione condotte utilizzando stampi appositamente progettati ed equipaggiati con strumentazione per il monitoraggio del processo.

L'analisi dell'effetto dei rivestimenti superficiali sulla fase di riempimento ha consentito di identificare i fenomeni che controllano la caduta di pressione in cavità (isolamento termico e scivolamento del fuso polimerico in corrispondenza della parete della cavità). La correlazione tra resistenza al flusso e velocità di scivolamento è stata studiata mediante visualizzazione del flusso. I risultati hanno indicato che la perdita di pressione in cavità è inversamente correlata alla velocità di scivolamento, indicando l'importanza nella scelta del rivestimento adeguato. Inoltre, è stato dimostrato che trattamenti al laser per la generazione di nano-strutture sulla superficie dello stampo possono essere utilizzati per controllare lo scivolamento del polimero a parete, a seconda dell'orientazione relativa delle strutture. Esperimenti condotti in condizioni standard di processo hanno evidenziato riduzioni della pressione d'iniezione superiori al 20%.

La caratterizzazione della fase di estrazione ha consentito di mettere in evidenza l'importanza per l'attrito durante l'estrazione delle interazioni all'interfaccia tra polimero e superficie dello stampo. I risultati hanno mostrato forti interazioni tra topografia dello stampo e parametri di processo che promuovono la replicazione, come la tem-

peratura stampo e la pressione di impaccamento. I rivestimenti superficiali sono stati dimostrati essere efficaci per la modifica dell'adesione tra polimero e superficie dello stampo.

La modellazione delle fasi di riempimento ed estrazione ha permesso di migliorare in modo significativo la comprensione dei fenomeni che controllano il processo di stampaggio ad iniezione. In generale, i risultati di questo lavoro costituiranno un'innovazione per la progettazione di componenti in materiale plastico più sottili e più piccoli, portando a risparmi economici e minor impatto ambientale, grazie alla riduzione dei volumi e dei consumi energetici.

ABSTRACT

Injection molding is one of the most widespread processes for the manufacturing of plastics products, for several applications. However, the increasing competitiveness of the current industrial environment constantly pushes the plastics industry towards the design of smaller, lighter and thinner parts, to reduce both product cost and environmental impact. This lead to significant manufacturing issues that are often related to the design of injection molding tools. In this contest, the design of mold surfaces represent a strategic point for the optimization of several key aspects of the process, especially those related to the filling and ejection phases.

In this work, the tribological effects of mold surface properties were investigated focusing on the characterization of conventional and unconventional mold surface treatments. The main objectives were the reduction of the injection pressure and the reduction of the demolding force. The effects of mold surface properties on both the filling and ejection phases were investigated following two main strategies, specifically 'Surface Generation' and 'Surface Modification'. The approach to the research was mainly based on injection molding experimentations, carried out with specifically designed molds equipped with state-of-the-art instrumentations for process monitoring.

The effects of mold surface coatings on the melt flow resistance allowed the identification of the phenomena that control the melt flow resistance (thermal insulation and wall-slip). The correlation between the melt flow resistance and the slip velocity was investigated using high-speed flow visualization. The results showed that the cavity pressure drop is inversely dependent on the slip velocity, thus indicating the importance of selecting a proper mold surface coating. Moreover, it was shown that different laser treatments can be exploited to drive the slipping of polymer melts depending on the relative orientation of the ripples. It was reported that nanostructures have the capability of reducing the injection pressure up to more than 20% under standard injection molding processing conditions.

The monitoring of the demolding force indicated that ejection friction is controlled by the mechanical interlocking created at the polymer/mold interface during the filling phase. The results of the experimental tests showed the strong interactions between the effect of mold surface topography and the ones of those injection molding process parameters that promote the replication, such as mold temperature and holding pressure. Mold surface coatings were demonstrated to be efficient solutions to modify the adhesion between the polymer and the tool surface.

Modeling of both the filling and ejection phases resulted in significant improvements for the understanding of the phenomena that control the injection molding process. In general, the findings of this work could be anticipated as an innovation for the design of thinner and smaller plastic parts, leading to manufacturing cost saving and reduced environmental impact, through the decrease of material and energy consumption.

CONTENTS

i LITERATURE REVIEW 1

1 OVERVIEW OF INJECTION MOLDING MANUFACTURING 3

1.1 The plastics market 3

1.1.1 Environmental impact 6

1.2 Injection molding 6

1.3 Thin-wall injection molding 7

1.3.1 Issues 7

1.3.2 Applications 8

1.4 Micro injection molding 9

1.4.1 Applications 10

1.4.2 Machines and process steps 12

1.5 State-of-the-art of thin-wall and micro injection molding 15

2 FILLING PHASE 17

2.1 Filling flow mechanisms 17

2.1.1 Fountain flow in conventional injection molding 17

2.1.2 Cavity pressure 18

2.1.3 Heat transfer coefficient 19

2.1.4 Filling in thin-wall and micro cavities 19

2.2 Reduction of the melt flow resistance 20

2.3 Wall slip phenomenon 21

2.3.1 Macromolecular chains adsorption 21

2.3.2 Parameters affecting wall slip 22

2.4 Wall slip in injection molding 25

3 EJECTION PHASE 27

3.1 The case of microfluidic devices 27

3.2 Ejection friction 28

3.2.1 Friction mechanisms during ejection 29

3.2.2 Friction description for rough surfaces 29

3.2.3 Interface adhesion in micro injection molding . 31

3.3 Parameters affecting the ejection force 31

3.3.1 Effects of injection molding process parameters 31

3.3.2 Effect of mold surface roughness 33

3.3.3 Effect of mold surface coatings 33

3.4 New demolding concepts for micro injection molding . 34

4 MOLD SURFACE DESIGN IN INJECTION MOLDING 37

4.1 Outlook on mold surface properties 37

4.2 Surface generation 38

4.2.1 Micro milling 38

4.2.2 Micro electro discharge machining 39

4.2.3 Laser Induced Periodic Surface Structures - LIPSS 40

4.3 Mold roughness description 42

4.4 Surface modification 43

ii MATERIALS AND METHODS 45
5 INJECTION MOLDING SETUP 47
5.1 Cavity design 47
5.1.1 Open-flow channel 47
5.1.2 Deep core geometry 48
5.2 Mold assembly design 50
5.2.1 Filling phase 50
5.2.2 Ejection phase 51
5.3 Process monitoring 52
5.3.1 Characterization of the melt flow resistance . . 53
5.3.2 Characterization of ejection friction 55
5.4 Injection molding machine 57
5.5 Ultrasound-assisted ejection 57
6 MOLD SURFACE MANUFACTURING 61
6.1 Surface generation 61
6.1.1 Laser treatments 61
6.1.2 Mold surface machining 62
6.2 Surface modification 67
6.2.1 Coatings selection 67
7 METROLOGY AND POLYMERS CHARACTERIZATION 71
7.1 Optical profilometry 71
7.1.1 Roughness measurements 71
7.2 Scanning Electron Microscopy 73
7.3 Geometrical characterization 73
7.4 Injection molding polymers 74
7.4.1 Rheological characterization 74
7.4.2 Polymer selection 75
8 OFFLINE CHARACTERIZATION 81
8.1 Wetting characterization 81
8.2 Friction testing 82

iii SURFACE GENERATION 85
9 EFFECT OF LASER-INDUCED PERIODIC STRUCTURES ON THE FILLING PHASE 87
9.1 Experimental approach 87
9.2 LIPSS characterization 88
9.2.1 SEM analysis 88
9.2.2 Topography characterization 88
9.3 Injection molding results 91
9.3.1 Effects of laser treatments 91
9.3.2 Effect of process parameters 93
9.4 Discussion 96
10 EFFECTS OF SURFACE GENERATION ON THE EJECTION FORCE 99

10.1 Impact of micro milling surface footprint 100
  10.1.1 Mold surface characterization 100
  10.1.2 Experimental approach 104
  10.1.3 Micro injection molding results 107
  10.1.4 Molded parts roughness evaluation 112
10.2 Effects of μEDM generated mold topography 115
  10.2.1 Mold surface characterization 115
  10.2.2 Experimental approach 117
  10.2.3 Injection molding results 118
10.3 Effects of machined cavity texture 124
  10.3.1 Texture characterization 124
  10.3.2 Experimental design 128
  10.3.3 Effect of the machining technology 128
  10.3.4 Effect of injection molding process parameters . 131
  10.3.5 Effect of first order interactions 131
10.4 Discussion 133

iv SURFACE MODIFICATION 137
11 EFFECT OF MOLD SURFACE COATINGS ON THE FILLING RESISTANCE 139
11.1 Effect of mold surface coatings on polymer filling flow 139
  11.1.1 Experimental design 139
  11.1.2 Coatings characterization 140
  11.1.3 Injection molding results 143
11.2 Characterization of wall slip of polystyrene 144
  11.2.1 Experimental design 144
  11.2.2 Injection molding results 145
  11.2.3 Flow visualization results 148
  11.2.4 Wetting behavior 152
11.3 Discussion 153
12 TRIBOLOGICAL EFFECTS OF MOLD SURFACE COATINGS ON EJECTION 155
12.1 Experimental approach 155
12.2 Coatings surface characterization 157
  12.2.1 Mold topography 157
  12.2.2 Roughness evaluation 157
  12.2.3 Wettability properties 158
12.3 Injection molding results 159
  12.3.1 Effects of polymer and coatings on the ejection force 161
  12.3.2 Effects on deformation contribution 161
  12.3.3 Effects on adhesion contribution 162
12.4 Coatings offline characterization 164
  12.4.1 Friction properties of coatings 164
  12.4.2 Evaluation of offline friction testing 165
12.5 Discussion 167

V MODELING 169
13 MODELING OF THE FILLING PHASE 171
13.1 Simulation of micro and thin-wall injection molding . 171
13.1.1 Scaling issues 172
13.2 Approach to modeling 173
13.2.1 Numerical model 173
13.2.2 Inverse analysis 175
13.3 HTC calibration and wall-slip hypothesis 176
13.3.1 Modeling of PET filling flow 176
13.3.2 Modeling of PS filling flow 177
13.4 Discussion 179
14 PREDICTION OF EJECTION FORCE IN MICRO INJECTION MOLDING 181
14.1 Ejection force model 181
14.2 Mathematical models for shrinkage prediction 182
14.2.1 Residual strain model 183
14.2.2 Residual stress model 184
14.2.3 Corrected residual in-mold stress model (CRIMS) 185
14.3 Shrinkage calibration 187
14.3.1 Part design and manufacturing 187
14.3.2 Shrinkage measurements 189
14.3.3 Inverse analysis 191
14.4 Calibrated shrinkage model 194
14.4.1 Shrinkage around deep cores 194
14.5 Ejection force prediction 196
14.5.1 Friction model calibration 197
14.5.2 Offline evaluation of friction coefficients 198
14.6 Discussion 200
14.7 Understanding ejection friction 200
14.7.1 Modeling of ejection friction 201
14.7.2 Model verification and discussion 202

VI CONCLUSIONS 205
15 CONCLUSIONS 207
BIBLIOGRAPHY 211

LIST OF FIGURES

Figure 0.1 Outline of the research activities presented and discussed in this work. xxiv
Figure 0.2 Weight reduction history for PET bottles. . . . xxv
Figure 0.3 Multi-layer microfluidic device considered in this work. xxvi
Figure 1.1 Global plastics production in million tons as reported by the Plastics Europe survey [1]. . . 4
Figure 2.1 Fountain flow of polymer melt in conventional injection molding [19]. 18
Figure 2.2 A schematic cavity pressure history. 18
Figure 2.3 Speed profile for a polymer melt flowing between parallel plates. 21
Figure 2.4 Entanglement of macromolecular chains. . . . 22
Figure 3.1 Example of multi-layer chip 28
Figure 3.2 Adhesion and deformation components of the friction force. 30
Figure 4.1 SEM micrographs of steel surfaces generated with NLL [120] 41
Figure 5.1 Design of the mold cavity and of the part [138]. 48
Figure 5.2 Design of the parts molded for the characterization of the ejection phase. 49
Figure 5.3 Part injection molded with *Mold B*. 50
Figure 5.4 Design and main components of the mold used to study the filling phase. 51
Figure 5.5 Design of mold insert and assembly - *MOLD A* [69]. 52
Figure 5.6 Design of mold insert and assembly - *MOLD B* [139]. 53
Figure 5.7 Pressure evolution measured in the cavity by the two piezoelectric transducers. 54
Figure 5.8 Setup used for the high-speed flow visualization of the polymer melt flow. 55
Figure 5.9 Consecutive acquired frames of the cavity. . . . 56
Figure 5.10 Stabilization behavior of the dry ejection force over cycles for *Mold B* [69]. 57
Figure 5.11 The MicroPower 15 Wittman Battenfeld. 58
Figure 5.12 Design of the ultrasound-assisted ejection system. 59
Figure 6.1 Micro milling of a lab-on-a-chip mold: 4 arrays of 28 pins - diameter 0.8 mm, height 2 mm. . . 62
Figure 6.2 Pin finishing strategies. 64

Figure 6.3 μEDM-milling of the mold cores. 65
Figure 6.4 Coated mold insert used for the characterization of the melt flow resistance. 68
Figure 6.5 Coated mold insert used for the characterization of the ejection force. 69
Figure 7.1 3D optical profiler used for the surface characterization. 72
Figure 7.2 Schematics of cores characterization [139]. . . . 72
Figure 7.3 Geometrical characterization performed on . . 73
Figure 7.4 Geometrical characterization performed on mold cores using x-ray Computed Tomography. . . . 74
Figure 7.5 Residual humidity and Newtonian viscosity for PET as a function of the drying time. 76
Figure 7.6 Rheological properties of the selected polymers at their specific melt temperature. 78
Figure 7.7 Storage modulus as a function of the mold temperature for the three polymers. 78
Figure 7.8 Different sensitivity of the selected polymers to temperature variations. 79
Figure 8.1 Example of a cylindrical polymer sample before melting (left) and of a melt drop of polymer melt during the wetting test (right). 81
Figure 8.2 Schematics of the experimental setup used for the characterization of the wetting properties of melt polymers [145]. 82
Figure 8.3 Schematics of the experimental setup designed to characterize the friction properties of the polymer/coating interface. 83
Figure 8.4 Design of the polymer sample used for the friction testing. 83
Figure 8.5 Friction testing setup - details of the coated and polymer surfaces. 84
Figure 9.1 SEM micrographs of the LIPSS treated mold surfaces. 89
Figure 9.2 3D topographies and profiles of the three differently treated LIPSS surfaces. 90
Figure 9.3 Main effect plots for the effect of LIPSS treatment and process parameters. 92
Figure 9.4 Analysis of the effects of mold temperature and injection speed for the LIPSS treated mold surfaces. 94
Figure 10.1 Breakage of multi-layer microfluidic device due to high ejection friction. 99
Figure 10.2 SEM micrographs of the micro-milled mold inserts at different magnifications. 100

Figure 10.3 3D and 2D views of the three mold insert topographies [69]. 101
Figure 10.4 Histograms of roughness parameters. 103
Figure 10.5 Response variables for the DoE plans. 106
Figure 10.6 Example of demolding force in-line acquisitions of DoE repetitions. 106
Figure 10.7 Main effect plots for the demolding peak force. 108
Figure 10.8 Main effect plots for the demolding force work. 108
Figure 10.9 Effect of the micro milling strategy on the demolding force curves. 108
Figure 10.10 Interaction plot for the optimization plan. . . . 111
Figure 10.11 Produced molded parts with: a) mold Insert 1 and b) mold Insert 2) [82]. 113
Figure 10.12 Roughness amplitude parameters evaluated on the plastic parts [69]. 113
Figure 10.13 SEM micrographs of the molded parts topographies. 114
Figure 10.14 SEM micrographs of the mold cores machined by μEDM 116
Figure 10.15 Effect of cores roughness on the mean value of the demolding force peak for the three polymers.119
Figure 10.16 Main effect plots for the effects of ultrasound vibration on the mean value of the demolding force for the three polymers. 119
Figure 10.17 Interaction plots for the three polymers. 121
Figure 10.18 Thermal imaging of the contact between the sonotrode and the mold cores. 122
Figure 10.19 Evolution of cores surface temperature during ultrasound vibration 122
Figure 10.20 SEM micrographs of the mold cores. 125
Figure 10.21 2D view, 3D view and profile of mold topographies. 126
Figure 10.22 Profile roughness parameters for the machined mold cores. 126
Figure 10.23 Evolution of the acquired ejection force signal [139]. 127
Figure 10.24 Main effect plots for the process parameters analyzed in the DoE experimental plan [139]. . 129
Figure 10.25 Isotropy of the cores textures. 130
Figure 10.26 Interaction plots between the machining technology and μIM process parameters [139]. . . 132
Figure 10.27 Ejection force results. 132
Figure 11.1 Topographies and SEM micrographs taken at 500X of mold surface coatings. 140
Figure 11.2 Cavity pressure measurements for PET. 141
Figure 11.3 Cavity pressure measurements for PS. 142

Figure 11.4 Flow curves obtained for PET at T_b = 300 °C [138]. 144
Figure 11.5 Experimental measurements of cavity pressure drop 146
Figure 11.6 Cavity pressure curves acquired close to the injection location and evidence of signal oscillation for increasing injection speed. 147
Figure 11.7 Effect of flow instabilities on injected polymer. 148
Figure 11.8 Coordinate tracking of silica carbide particles. 149
Figure 11.9 Velocity profiles for the injected polymer melt with the uncoated insert at different values of the injection speed. 150
Figure 11.10 Relation between slip velocity and cavity pressure drop for the different mold surface coatings.151
Figure 11.11 Correlation between cavity pressure drop and contact angle for the different coatings. 153
Figure 12.1 SEM characterization of the micro cores at 1000 X magnification. (a) uncoated insert, (b) DLC1, (c) DLC2, (d) CrTiNbN. 156
Figure 12.2 Values of *Sa* and *Sz* for the coated cores. 158
Figure 12.3 (a) Contact angle values for the different polymer/coatings combinations; (b) image of polymer drops on DLC1 coated surface. 159
Figure 12.4 Injection molded parts with the three different polymers. 160
Figure 12.5 Effects of polymer selection for the different mold inserts, (a) uncoated; (b) DLC2; (c) CrTiNbN; (d) DLC1. 160
Figure 12.6 Effects of the different surface coatings on the demolding force for (a) POM, (b) PS, (c) PA66. 160
Figure 12.7 Surface response for the ejection force peak as a function of polymers viscosity and mold surface roughness (*Sz*). 161
Figure 12.8 Correlation between the ejection force peak and the contact angle for the different polymers. . 163
Figure 12.9 Evaluation of the friction coefficient for PS with the different coatings. 164
Figure 12.10 Experimental values of the friction coefficient determined for the different polymers and coatings. 165
Figure 12.11 Correlation between the ejection force peak and the friction coefficient measured using the offline testing setup. 166
Figure 13.1 Modeling and Dual Domain discretization of the cavity geometry. 173

Figure 13.2 Injection molding simulation in Autodesk Moldflow and plot of cavity pressure in the monitoring position. 174
Figure 13.3 Schematics of the Artificial Neural Network use as meta-model for injection molding simulation. 174
Figure 13.4 ModeFrontier code for the inverse analysis. . . 175
Figure 13.5 Comparison between experimental and numerical results for PET at T_b = 300 °C [138]. 176
Figure 13.6 Simulated values of cavity pressure as a function of injection speed and HTC. 177
Figure 13.7 Comparison of experimental, simulated and ANN values of pressure as a function of the injection speed for the Uncoated insert. 178
Figure 14.1 Schematics of the model used for the analytical calculation acting on the mold cores [159]. . . 182
Figure 14.2 Test specimen used for CRIMS coefficients determination by Autodesk. 186
Figure 14.3 Design of the mold cavity and of the part. . . . 187
Figure 14.4 Parts molded with three polymers. 188
Figure 14.5 Measurements of the molded parts with the CMM machine. 189
Figure 14.6 Procedure followed for the dimensional measurements of the molded parts. 190
Figure 14.7 Modeling of parts used for shrinkage calibration - (a) mesh and (b) deflection results of the simulation. 191
Figure 14.8 Regression plot for the training of the ANN for PS. 193
Figure 14.9 Comparison of average shrinkage values for experimental, ANN, CRIMS and URSM - (a) PS, (b) POM and (c) COC. 195
Figure 14.10 Mesh of the case study part (a) and isotropic shrinkage result (b). 196
Figure 14.11 Steel surfaces machined by μEDM to reproduce the different topographies of the different mold surfaces. 199
Figure 14.12 Errors of the ejection force model. 203

LIST OF TABLES

Table 1.1 Micro Injection molding Applications 11

Table 5.1 Wittmann Battenfeld Micropower 15t technical data sheet. 58
Table 6.1 Micro milling strategies for the finishing operations of cores side. 63
Table 6.2 Combinations (A, B, C, D) of μEDM machining parameters adopted to generate different mold topographies. 65
Table 6.3 Process parameters adopted in μEDM machining. 66
Table 6.4 Main characteristics of the selected mold surface coatings. 67
Table 6.5 Main properties of the selected mold surface coatings. 68
Table 7.1 Main characteristics of the 3D optical profiler. 71
Table 7.2 Main properties of polymers injection molded over nano-structured tools. 75
Table 7.3 Main properties of the tested polymers. 76
Table 7.4 Main properties of the polymers selected for the molding experiments used to characterized the ejection phase. 77
Table 7.5 Main characteristics and properties of the polymers selected for the molding experiments. 79
Table 9.1 Process parameters considered for the characterization of the effects of LIPSS treatments. 87
Table 9.2 Experimental DoE plan designed for the molding experiments. 88
Table 9.3 AFM measurements of LIPSS mold surfaces. 89
Table 9.4 Analysis of variance for the DoE plans. 91
Table 9.5 Percentage reduction of the melt flow resistance compared to the untreated insert for PS. 95
Table 9.6 Percentage reduction of the melt flow resistance compared to the untreated insert for PP. 96
Table 9.7 Percentage reduction of the melt flow resistance compared to the untreated insert for LDPE. 96
Table 10.1 Average values and standard deviations of profile roughness parameters evaluated according to ISO 4287. 102
Table 10.2 Average values and standard deviations of profile roughness parameters evaluated according to ISO $13565-2$. 102
Table 10.3 Screening DoE plan. 105
Table 10.4 Optimization DoE plan. 105
Table 10.5 Anova table for the screening experiments designed in Table 10.3. 107
Table 10.6 Anova table for the optimization experiments designed in Table 10.4. 110

Table 10.7 Experimental results of the optimization plan. 111
Table 10.8 Molded parts roughness. 112
Table 10.9 Means and standard deviations of surface roughness parameters for the mold cores machined with different μEDM process parameters . . . 116
Table 10.10 Experimental DoE plan designed for the molding experiments. 117
Table 10.11 Process parameters selection for the three injection molding polymers. 117
Table 10.12 Anova table for the designed experiments. . . 118
Table 10.13 Effect of ultrasound vibration on the average value of the demolding force peak for the different combinations of polymer selection and mold roughness. 120
Table 10.14 Results of thermal measurements of mold cores during ultrasound vibration. 123
Table 10.15 Ejection force peak values with and without the application of the ultrasound vibration. . . 123
Table 10.16 Effect of the heating induced by the ultrasound vibration on the storage modulus for the three polymers. 123
Table 10.17 Means and standard deviations of profile roughness parameters for the machined cores. 125
Table 10.18 Experimental DoE plan designed for the μIM experiments. 127
Table 10.19 ANOVA table for the effects of the machining technology and μIM process parameters on the ejection force. 129
Table 11.1 Processing conditions for the experiments. . . 139
Table 11.2 Process parameters selected for the injection molding experiments. 145
Table 11.3 Slip velocity values for different coatings at an injection speed of 450 mm/s. 151
Table 11.4 Measurements of the contact angle of polystyrene for the different coatings. 152
Table 12.1 Process parameters for the injection molding of the three polymers. 155
Table 12.2 Average values and standard deviations of surface roughness parameters evaluated according to ISO 4287. 157
Table 12.3 Average values and standard deviations of surface roughness parameters evaluated according to ISO 13565. 157
Table 12.4 Coefficients of friction determined for the different coatings and polymers. 164

Table 12.5 Comparison of normal force during ejection and elastic modulus for the three polymers. . . 166
Table 13.1 Values of HTC determined for the mold surface coatings with PET. 176
Table 13.2 Results of HTC calibration for the coated inserts using PS. 178
Table 14.1 Process parameters used to mold the parts for shrinkage calibration. 188
Table 14.2 Selected ranges of variations for the CRIMS parameters for each polymer. 190
Table 14.3 Process parameters selection used for the three polymers for the training simulations. 192
Table 14.4 Selected ranges of variations for the CRIMS parameters for each polymer. 192
Table 14.5 Optimized CRIMS parameters for the three polymers. 194
Table 14.6 Calibrated predictions for shrinkage around a single mold core for the three polymers. 196
Table 14.7 Geometrical and material parameters used for the ejection force prediction. 197
Table 14.8 Mechanical properties of the three polymers. . 197
Table 14.9 Calibrated values of the normal force around mold cores during ejection. 198
Table 14.10 Calibrated values of the friction coefficients. . 198
Table 14.11 Values of the friction coefficients obtained from the offline characterization. 199
Table 14.12 General factorial plan designed to model the effects of polymer selection and mold surface roughness on the ejection force. 202
Table 14.13 Prediction of the ejection force peak for all the experimental combinations and prediction errors. 203

AIMS AND MOTIVATION

The design of the mold is one of the most critical issue when approaching the injection molding process. The failure of the injection molding process can often be related to wrong design solution in the mold. In the injection molding industry it is very common that a new mold has to go through several iterative modifications before production start up. This results in longer time required for the delivery of plastics products to the market and significantly higher costs.

Several strategies have been proposed in the scientific literature and are applied in the industry in order to optimize mold design and reduce time to production. The diffusion of Computer-Aided Engineering provided mold designers and plastics engineers with useful tools that allow the reduction of design errors. However, numerical simulations are just qualitatively reliable and they are strongly dependent on the calibration of the boundary conditions (e.g. thermal, rheological).

Moreover, the increasing demand for more complex and functionalized plastic products constantly pushes Plastics Engineering to the necessity for the development of new technologies and approaches to process design and control. In this sense, many efforts focused on the surface of both plastic products and molds. *'Surface functionalisation'* is a concept that has been gaining increasingly importance in injection molding considering the increasing interest for micro- and nano-structured polymer surfaces and the attention to mold surfaces design.

However, several limitations still exist when considering the relationship between mold surface and the injection molding process. The understanding of the tribological properties of mold surface and their interaction with the polymer is still limited and the lack of systematic approaches is evident. For instance, mold surface coatings have been widely implemented in the injection molding aiming at increasing wear resistance, while their effects on other key aspects of the process are neglected.

In this research, the tribological effects of mold surface properties on the injection molding process were investigated. Different products and applications were considered, being all characterized by the need for systematic approaches to mold surface design. The general goals that were fixed approaching the design of mold surface were:

- reduction of the injection pressure;
- reduction of the demolding force.

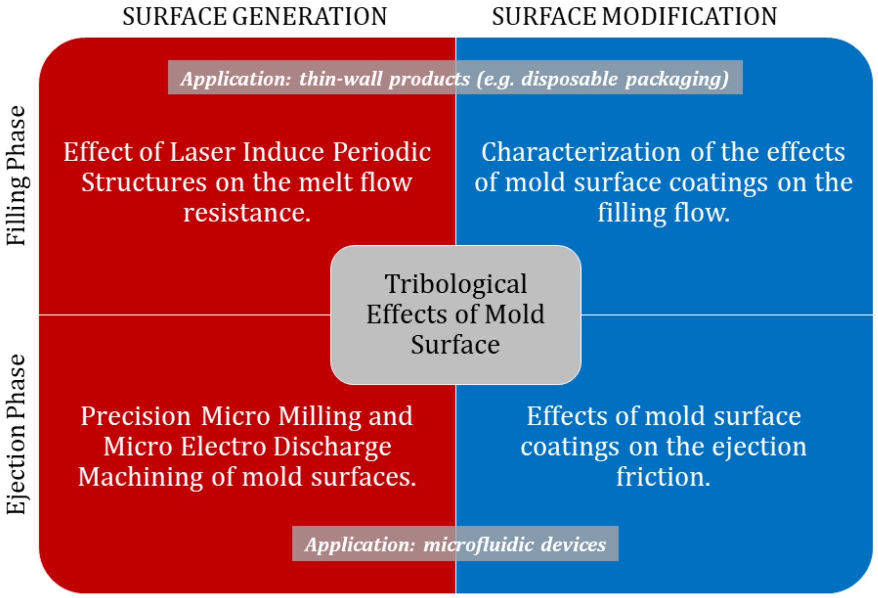
SURFACE GENERATION
SURFACE MODIFICATION
Filling Phase
Ejection Phase
Application: thin-wall products (e.g. disposable packaging)
Effect of Laser Induce Periodic Structures on the melt flow resistance.
Characterization of the effects of mold surface coatings on the filling flow.
Tribological Effects of Mold Surface
Precision Micro Milling and Micro Electro Discharge Machining of mold surfaces.
Effects of mold surface coatings on the ejection friction.
Application: microfluidic devices

Figure 0.1: Outline of the research activities presented and discussed in this work.

Figure 0.1 introduces the blueprint of this work showing the main approach adopted for the research. Specifically, the attention was focused on two categories of injection molding applications and products: thin-wall injection molding and micro injection molding. Indeed, due to the reduced dimensions, these applications of the conventional process can be significantly affected by mold design and specifically by the part-tool interface. The effects of mold surface on both the filling and ejection phases were investigated following two main strategies:

- Surface Generation
- Surface Modification

The research was mainly based on experimental injection molding investigations, which were designed aiming at maximizing accuracy in process control. Particular attention has been given to the design of injection molding molds that could allow the characterization of different mold treatments. Two different mold geometries were realized, one for the study of the filling phase and the other to study the ejection phase. Moreover, different monitoring instrumentations were implemented in the injection molding process allowing the accurate control of temperature, pressure and force during the different phases of the process.

Moreover, an ultrasound-assisted ejection system was designed and tested for different polymers and mold topographies. The proposed innovative solution aims at reducing the ejection friction by decreasing the adhesion component of the frictional force, which is con-

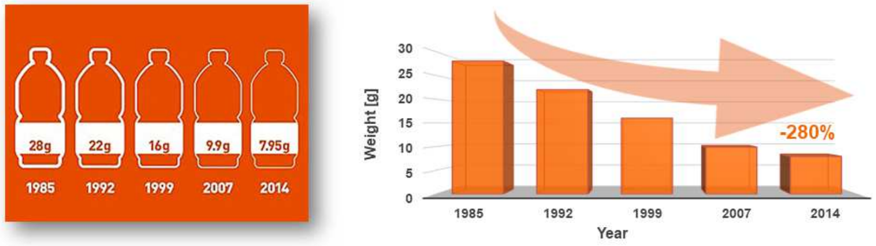

Figure 0.2: Weight reduction history for PET bottles.

trolled by the real contact area generated during the filling phase of the injection molding process. Furthermore, the combined effect on the ejection force of mold surface roughness, melt viscosity during filling and polymer elastic modulus at ejection was modeled to the experimental data.

The research activities were carried out considering different projects, all of which originated from industrial needs and strategic technological developments. In this section, the different projects are briefly presented showing their relevance for this work, the strategic objectives that they pose and how these brought up injection molding issues whose solving could be approached focusing on mold surface design.

THICKNESS REDUCTION

The current market for plastics products constantly pushes the plastics industry towards the design of lighter and thinner parts, to reduce both product cost and environmental impact. The main sector interested by this trend is the packaging industry and in particular the manufacturing of preforms for PET bottles. Figure 0.2 shows the history for weight reduction observed in these products indicating the trend towards a minimization of their wall thickness. However, this is limited by the capability of the injection molding machine to fill more and more thin cavities, by the design of the mold and by the thermo-rheological properties of the polymer.

In this work, an innovative approach to the reduction of the injection pressure was introduced by analyzing the tribological properties of different mold surface coatings that were characterized under standard injection molding conditions. Similarly, other commodity plastics and engineering plastics, were taken in consideration studying the effects of nano-structuring of the mold surface on the reduction of the melt flow resistance.

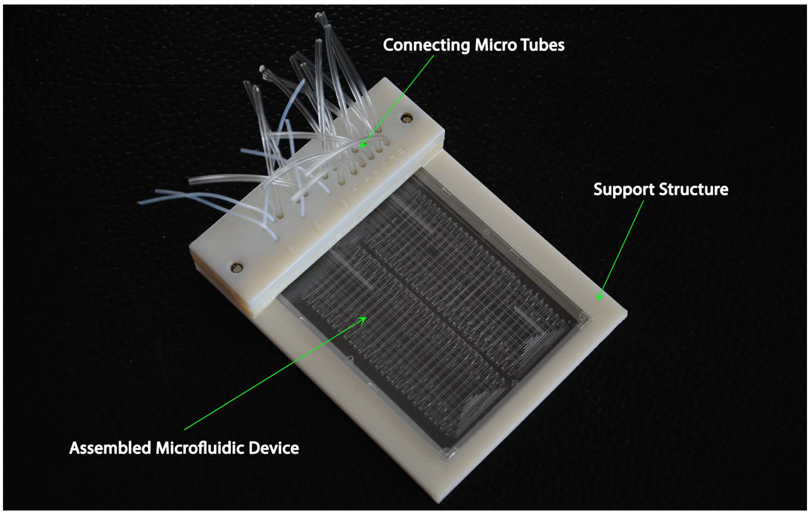

Figure 0.3: Multi-layer microfluidic device considered in this work.

PARTS MINIATURIZATION

Lab-on-a-chip are devices integrating several complex laboratory functions on a single chip to achieve automated and high-throughput analysis. These devices find their main application in the biomedical industry, e.g. drug testing and DNA analysis, and their functionalities are allowed by the presence of several micro features on their surfaces. The research in this field aims at developing new devices allowing more complex analysis in a simple and economic way. Consequently, developing effective manufacturing process chains supporting their mass production becomes an issue. However, the research in the field showed that the capabilities of the injection molding process in replicating micro- and nano-structured surface are hindered by inherent limitations of the process. In particular, the filling and the ejection phases are critical steps in determining the efficiency of the process.

In this work, the design of mold surfaces for a microfluidic application was studied aiming at optimizing their interaction with the polymer during the ejection phase, which causes the breakage of the molded parts. Figure 0.3 shows the design of the microfluidic product considered in this work. The device, which is characterized by two functional polymer layers and two PDMS sealing membranes, is at the moment manufactured by casting of silicon into a mold realized using soft lithography, thus being expensive and difficult to mass-produce. The main goal of the project is the development of the manufacturing process chain that could allow the mass-production of the product.

Part I

LITERATURE REVIEW

1

OVERVIEW OF INJECTION MOLDING MANUFACTURING

Plastics products and components are almost everywhere in our lives and their demand is constantly increasing. Nowadays, the contribution of plastics engineering and manufacturing to our society and economy is extremely significant and, in the future, it would be more and more important for their development.

Over the last decades, the request for plastic components has been subjected to a massive commercial growth, which has not been accompanied by an efficient development of the plastic manufacturing industry. This uncontrolled development led the plastics manufacturing industry to a poorly engineered industrial system characterized by low global competitiveness. In this contest, also the human impact on the environment has been constantly growing leading to unsustainability of the manufacturing industry. Energy savings and emissions reduction related to manufacturing are crucial issues, especially considering large-scale processes, as polymer processing technologies.

Research in the field of Plastics Engineering has the responsibility to lead manufacturing systems to improvements of technology, processes and products. This would result in a higher global competitiveness allowing both the technological and economic growth of the manufacturing industry. Moreover, the social implications following this would include the demand for new workforce and the availability of higher quality jobs, thus increasing the prosperity of the society we live in.

1.1 THE PLASTICS MARKET

The importance of the plastics market amongst the manufacturing industries has been rapidly growing since the 1950s and it is still getting more and more important (cf. Figure 1.1). The Plastics Engineering and Manufacturing economy has been pushed by the following market drivers:

- polymer processing technologies are usually characterized by low process costs, which can easily return the medium-high initial investments;

- high specific mechanical properties of polymers favored their employment as replacements of conventional materials (as metals);

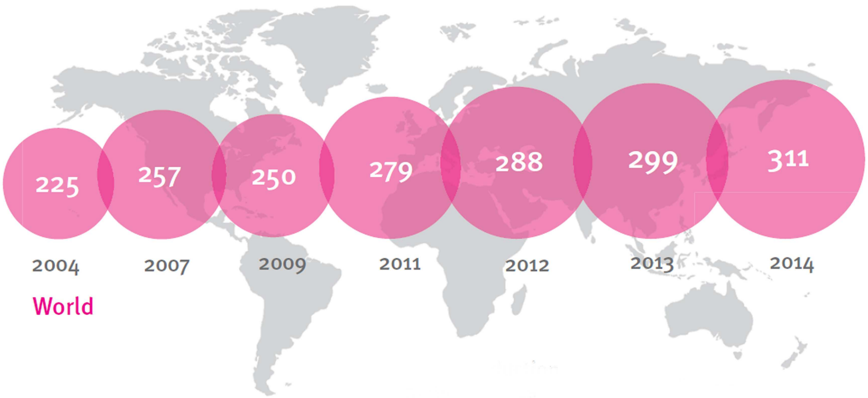

Figure 1.1: Global plastics production in million tons as reported by the Plastics Europe survey [1].

- ease of processability of polymers has facilitated the technological growth and development of polymer processing technologies;
- capability to obtain plastics products characterized by good geometrical, dimensional and aesthetic tolerances;
- the development and the diffusion of many types of polymers allowed the growth of several markets that needed to tailor the properties of the material to the very specific functionality of their products.

The main section of the plastics manufacturing industry is dominated by the so-called '*commodity plastics*', that are polyethylene, polypropylene, polyvinyl chloride and polystyrene (cf. Figure 1.2 (a)). Moreover, due to its large diffusion in the bottles industry, polyethylene terephthalate has also become very relevant.

Plastics could meet the needs of a wide variety of markets that ranges from low-added value product to sophisticated engineering applications (cf. Figure 1.2 (b)). Indeed, a large variety of polymers can be used to cover very different applications. In particular, the biggest quantity of plastics (i.e. 40%) is processed for packaging applications. In particular, the following polymers are mainly used in this market:

- *Polyethylene* - often used to produce very thin products (i.e. down to thicknesses of 0.25 mm);
- *Polypropylene* - very versatile and easily processable;
- *Polyvinyl Chloride* - largely employed for electrical housings, pipes and buildings due to its heat resistance and good mechanical properties;

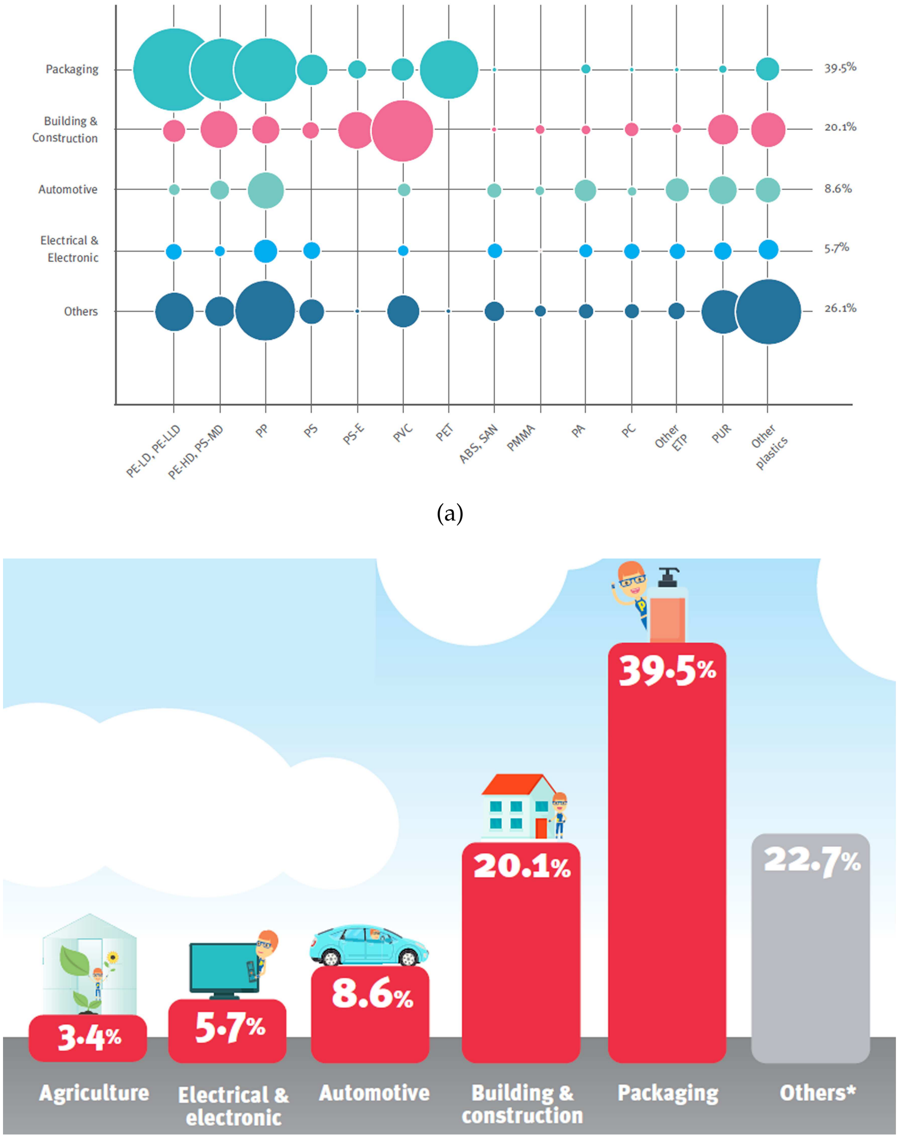

(a)

(b)

Figure 1.2: Distribution of European plastics demand by (a) polymer type and by (b) market segment [1].

- *Polystyrene* - transparent and low-cost material employed for food packaging, boxes and other packaging applications;
- *Polyethylene Terephthalate* - due to its transparency, high mechanical strength and ease of processability is the most used material for bottles.

1.1.1 *Environmental impact*

The continuous growth of the plastics industry and the increasing use of polymers for many applications made several environmental issues to emerge and to become more and more significant. The main problem related to plastics production is waste disposal. In fact, many plastic products are disposable and they are often not recycled. In 2016, the European market recycled just the 29% of plastics waste, while the 41% of those was burned to produce energy and the 30% was accumulated in dumping sites. Plastics recycling is low also in the USA where the percentage of recycled plastics is smaller than 9%; while in developing countries 50% of plastics waste is not even separated from other waste materials [2].

In this context, it is important to promote the development of more sustainable Plastics Manufacturing technologies, aiming at reducing their environmental impact. This could be achieved by developing the Plastics Engineering production technology, specifically new design and manufacturing solutions would be very significant.

1.2 INJECTION MOLDING

Injection molding is nowadays one of the most flexible, reliable and cost effective manufacturing technologies to produce complex plastic components [3]. The process is largely employed to produce very different products with very different materials. The process consists of the melting of polymer pellets by the mechanical action of a reciprocating screw, the injection of the material into a metallic mold, the cooling and the ejection of the final molded part.

The injection molding process requires a complex engineering design of all its components. In particular, a proper part design would allow the achievement of the following:

- facilitate the production process;
- optimize the volume of the material used for the part;
- achieve the desired shape and features of the part;
- guarantee process stability, control and repeatability.

In this work, the attention is focused on two categories of injection molding applications and products:

- Thin-wall injection molding;
- Micro injection molding.

1.3 THIN-WALL INJECTION MOLDING

Precision manufacturing of parts produced by injection molding has recently been driven down in size and weight, especially for packaging and electronic applications [4]. In this context, thin-wall injection molding is a specialized application of the conventional process that focuses on the production of plastic parts that are designed to be as thin and light as possible. This result in material cost savings and reduced cycle time, thus leading to higher productivity and overall lower cost for each molded unity.

The definition thin-wall refers to the flow length of the parts compared to their wall thickness. Specifically, injection molding is conventionally defined as thin-wall when the part has a nominal wall thickness of 1 mm or less and a surface area of at least 50 cm^2, with a flow length/thickness ratio above 100 or 150 [5].

In general, reducing the main thickness of injection molded parts leads to a smaller overall volume of the molded part, and corresponding material cost savings and smaller overall environmental impact (lower resources consumed, lighter products leading to improved efficiency). Moreover, the cycle time is shorter making the environmental and economical burdens related to the process less significant too. The main benefits of thin-wall injection molding are:

- faster cycle times compared to conventional thicker wall parts, hence reduce production time and costs;
- reduction of material consumption and reduced process costs, thus increased sustainability;
- reduce weight in automotive, electronics and packaging applications;

1.3.1 *Issues*

Despite the trend of miniaturization observed for injection molding applications, the molded parts remain relatively large, because of their complex design, which poses several manufacturing issues [6]. In particular, the thin wall that characterizes their typical geometry constitutes a major manufacturing constraint [7]. Hence, the commercial breakthrough of new and smaller products strongly depends on the necessity to develop low cost mass production technologies, which can provide dimensional accuracy and good part quality [8].

The main difficulty encountered when approaching the molding of thin-wall parts lies in the fact that, during filling, the thickness of the frozen layer is increasingly higher as the main cavity thickness is reduced. This leads to a difficult filling of the mold cavity and the possibility to achieve incomplete replication of the mold cavity. Moreover, it is also difficult to develop reliable process control strategies, as the selection of process variable is more complex than in conventional injection molding.

The main disadvantages of thin-wall injection molding can be summarized as follows:

- increased resistance to the melt flow, thus possible incomplete replication;
- injection molds need to be robust enough to withstand high stresses and pressures;
- the mold must also have a well-designed cooling system so that heat can be quickly extracted from the hot plastic part allowing fast cycle times;
- high capital investment cost for injection molders, because of the need for specialized molding machines and robots that can withstand the high stresses and fast cycle times;
- need for highly skilled molding technicians.

1.3.2 *Applications*

Computer, communication, consumer electronics and packaging industries are increasingly demanding lighter and thinner parts due to economical (i.e. lower process and material costs) and environmental reasons (i.e. reduced environmental burdens). Specifically, the following industrial sector are the ones that are mainly focusing on thin-wall injection molding:

- food packaging (e.g. food containers and lids);
- automotive (e.g. structural and aesthetic car parts);
- mobile telecommunications (e.g. mobile phone housings);
- medical (e.g. syringes and microfluidic devices);
- computing equipment (e.g. computer housings);
- electronics (e.g. connectors).

Considering the packaging industry, bottles made of polyethylene terephthalate (PET) are one of the most significant application of thin-wall injection molding, as they can be recycled to reuse the material out of which they are made and to reduce the amount of waste going into landfills. PET bottles are produced from injection molded preforms that are characterized by an high flow lenght and reduced wall thickness. However, this is limited by the capability of the injection molding machine to fill more and more thin cavities, by the design of the mold and by the thermo-rheological properties of the polymer. All these issues were considered in this work and they will be presented in the following sections.

Thin-wall designs are also common in micro-structured components for optical and biomedical applications, such as light guide plates and microfluidic devices. Lab-on-a-chip are devices integrating several complex laboratory functions on a single chip to achieve automated and high-throughput analysis. These devices find their main application in the biomedical industry, e.g. drug testing and DNA analysis, and their functionalities are allowed by the presence of several micro features on their surfaces [9]. The research in this field aims at developing new devices allowing more complex analysis in a simple and economic way. Consequently, developing effective manufacturing process chains supporting their mass production becomes an issue [10]. Indeed, Lucchetta et al. investigated the capabilities of the micro injection molding process in replication a micro-structured surface, highlighting the inherent limitations of the process [6]. Moreover, Masato et al. studied the manufacturing of plastic bio-mems for blood depletion characterized by a thin-wall substrate [11]. In these applications, it is important guarantee a proper filling of the mold cavity allowing a correct distribution of cavity pressure, which allows the achievement of complete replication of the micro features placed on the top surface of the substrate.

1.4 MICRO INJECTION MOLDING

Since the 1980s micro system technologies has grown in importance and they are expected to have a far reaching influence on device manufacture in the near future; this trend towards miniaturization needs to be sustained by a reliable and economical production. Micro products are nowadays required to enter the market at an increasing pace, in this sense polymer micro injection molding is a key enabling technology, with the potential to mass produce at a low cost. Consequently polymers will, in the near future, certainly play a fundamental role in the escalation of micro system applications, because their properties can be tailored to provide the desired processing and application-related properties. Polymers constitute the broadest and most diverse class of biomaterials, they are available in a wide variety of compositions, properties, form and they can be readily fabricated into complex shapes and structures. In this contest, micro injection molding is bounded to become one of the most important technology for the fabrication of micro products.

Injection molding is a manufacturing process for the production of polymeric parts by injecting the melted material into a mold. It is one of the most important technology for the mass production of complex plastic parts; among all the polymer-processing methods, it accounts for 32% by weight of all the polymeric material processed. Its peculiarities are standardized process sequences, high level of automation, short cycle times. Injection molded parts typically have good dimensional tolerance and require almost no finishing and assembly operations.

Micro injection molding technology was firstly introduced from conventional injection molding since late eighties, 1980s to satisfy the specific functional and technical requirements of new emerging micro products. At that time no appropriate technology was available and only modified commercial units of traditional injection molding machine could be used. Only in the middle nineties (March 1997 *Battenfeld* started the project for the *Microsystem* 50), subsequently new machines were developed to specifically address injection molding of micro parts.

Among the variety of micro manufacturing processes, micro injection molding possesses the advantage of having a vast know-how available from conventional plastics technology. The advantages that micro injection molding inherited from the conventional process, in addition to the considerable technological developments witnessed in the recent years, made it an ideal process for producing micro-molded plastic components for a wide range of applications.

1.4.1 *Applications*

Micro injection molding is one of the most promising technologies for high-volume fabrication of micro components; dimensional accuracy, replication fidelity and potential for automation are some of its characteristics. These capabilities, combined with the wide range of mechanical, thermal and optical properties of processable thermoplastic polymers, make it the main candidate for high-volume and low-cost production of micro products. Therefore micro injection molding of thermoplastic polymers have made an outstanding entry into the industrial market: a large variety of micro products is successfully manufactured with this process.

A broad variety of applications is already known for the micro molding of thermoplastic polymers (Table 1.1) and many more are expected to arise in the near future. Markets that need micro parts are the following:

- Automotive (e.g. micro-switch, sensors, ABS-Systems);
- Computer (e.g. head of an ink-jet printer);
- Telecommunication (e.g. mobile phone, SIM card connector);

APPLICATION FIELDS	EXAMPLES
Micromechanical parts	• Locking lever for micro mechanical industry or micro switch; • Latch for the watch industry; • Catch wheel for micro switch; • Operating pin; • Gear plate for motive power engineering.
Micro gear wheel	• Dented wheel for watch industry; • Rotor with gear wheel for watch industry; • Gear wheel for micro gear; • Spur wheel in the field of electrical technology; • Spiral gear in the field of electrical technology/metrology; • Spline in the field of electrical technology/metrology.
Medical industry	• Micro filter for acoustics, hearing aid; • Implantable clip; • Bearing shell/bearing cap; • Sensor housing implantable; • Aseptic expendable precision blade.
Optical and Electronic industries	• Coax plug/switch MID for mobile phone; • SIM card connector for mobile phone; • Pin connector for mobile phone; • Single mode and multi-mode ferrules.

Table 1.1: Application fields of the micro injection molding process [12].

- Connectors (e.g. plug connectors, couplers);
- Electronics micro parts on circuit boards;
- Micro-equipment (e.g. valve technology);
- Medical technology (e.g. micro-fluidic devices with micro-channels hearing aids, implants, devices for DNA analysis, bio-MEMS, tissue scaffolds, vascular clamp);
- Sensors (e.g. airbag sensors, sensor disk, bio-sensors);
- Micro-mechanics (e.g. micro-motor, rotor, micro-gears, micro-switch, locking lever, catch wheel, operating pins, sleeve);
- Optics (e.g. lenses, displays);
- Optical gratings (CD, DVD);
- Watches (e.g. gear wheels, latches, micro-transmissions)
- Glass fiber conductors (ferrules, connectors);
- Micro-structured micro-parts (lab on the chip, data carrier, self-cleaning surfaces, sensor disk structure);
- Patterned adhesives;
- Precise suppliers;
- Special materials (e.g. PIM (MIM/CIM), PTFE);
- Institutes, Universities (e.g. material, technology for research).

In general, miniaturized parts fabricated with micro injection molding, even from high-end materials, are suitable for applications requiring low cost, mass production, flexibility, geometrical quality, and disposable components.

1.4.2 *Machines and process steps*

Injection molding is the process of transferring a thermoplastic raw material in the form of granules (pellets) from a hopper into a heated barrel so that it becomes molten and soft. The material is then forced under pressure inside a mold cavity where it is subjected to holding pressure for a specific time to compensate material shrinkage. The material solidifies as the mold temperature is decreased below the glass-transition temperature of the polymer. After sufficient time, the material freezes into the mold shape and is ejected, then the cycle is repeated. A typical cycle lasts between few seconds to few minutes.

Conventional injection molding machines are comprised of the following parts:

THE PLASTICIZING AND INJECTION UNIT: their major tasks are to melt the polymer, fed it to the screw chamber, inject it into the mold cavity and maintain the holding pressure during the cooling phase;

THE CLAMPING UNIT: its role is to open and close the mold, and hold it tightly to avoid flash during the filling and the holding phases;

THE MOLD CAVITY: the mold is the central part of an injection molding machine, its function is to distribute the melt into the cavities, shape the part and cooling it.

Through these parts the injection molding process consists of the following phases:

1. Plasticizing: the rotating screw forces the pellets forward into the barrel that is heated to the desired melt temperature of the molten plastic. The melt is accumulated in front of the screw, ready to be injected;

2. Injection, Filling and Packing: the mold is close, the screw-plunger inject the molten polymer that fills the cavity. At the switchover point, the machine applies the packing pressure;

3. Cooling and Ejection: when the polymer in the cavity has solidified, the mold is opened and the ejectors demold the plastic part.

When downscaling to the micro injection molding process for the production of smaller parts two kind of problems arises:

TECHNOLOGICAL: reduced dimension of the product requires a smaller shot-size, but this would lead to a thinner and so weaker screw's core. Sometimes pellet's weight is even bigger than that of the micro-molded part. Thus it is impossible to reduce the screw-plunger size below a minimum value (12 mm) that ensures an adequate resistance and a minimum stroke to accelerate and apply adequate injection speeds;

PROCESSING: when molding micro components with a reciprocating screw is not possible to control the metering accuracy and the homogeneity of the melt. Moreover, due to channel configuration and high injection pressure, required to fill micro cavities, there is melt back-flow during injection.

For these reasons, when diminishing part volume and shot size, conventional injection molding machines are no longer technically and economically viable solution. Therefore, in micro injection molding machines the plasticizing and the injection units are decoupled: it is possible to obtain a precise injection (5-300 milligrams) with a small plunger, moved by an electric motor, supplied upstream by the rotating screw/extruder.

In other words, limitations of the conventional technology were overcome with the adoption of the plunger injection system, in which the plasticization and the injection phases are divided: the plasticization takes place in a dedicated functional part of the machine, which is separated from the injection unit. Injection plungers as small as 5 mm in diameter are used to produce polymer melt down to sub-gram levels; at the same time, a screw-extruder having sufficient channel depth to properly handle standard pellets and yet provide the required strength can be employed.

Consequently, the μIM process consist of the following phases:

1. Plasticizing: the polymer is melted by the action of the rotating screw and accumulated into the metering chamber;
2. Metering: after the set volume has been achieved, the plunger in the dosage barrel delivers the shot volume to the injection barrel;
3. Injection, Filling and Packing: the melt is injected into the mold, once the plunger injection movement is completed, a holding pressure is applied;
4. Cooling and Ejection: when the polymer in the cavity has solidified, the mold is opened and the ejectors demold the plastic part.

Summarizing, the main difference between conventional and micro injection molding machines lays in the decoupling of the plasticizing and injection units. The main benefits of having a dedicated injection module are the following [13]:

- all standard pellet sizes can be processed by the screw;
- stress free plasticization and dosing in a low pressure area are obtained;
- each shot is done with new raw material;
- shortest runners and gates and so control of process conditions near the cavity;
- injection of thermally homogeneous material;
- high processing security and excellent reproducibility results;
- minimum loss of pressure.

Moreover, in μIM applications, the need for micro scale tolerances, fine details, and desired surface finish surpass those encountered in tool manufacturing for conventional injection molding, where the cavity is usually machined directly on the mold plate. For micro injection molding applications the procedure has instead undergone substantial alterations, as to obtain tailored tool inserts.

1.5 STATE-OF-THE-ART OF THIN-WALL AND MICRO INJECTION MOLDING

Considering the context described in this chapter, micro injection molding and thin-wall injection molding can be regarded as key enabling technology with the potential to mass-produce complex parts at a low cost. However, as reported by Giboz et al., the demand for increasing complexity, and the trend toward miniaturization, poses several technological issues [14]. In particular, the filling and the ejection phases are critical steps in determining the efficiency of the process.

Injection molding of thin-wall and micro parts is a challenging task because of the higher raise of cavity pressure that can prevent the complete replication of the mold geometry [6]. On the other hand, Heckele and Schomburg suggested that part possessing dimensions or tolerances in the micrometric range make the ejection phase particularly critical [15]. Thus, the understanding of process constraints for the production route is essential at both the design and manufacturing stages.

2

FILLING PHASE

The increasing competitiveness of the current industrial environment constantly pushes the plastics industry towards the design of lighter and thinner parts, to reduce both product cost and environmental impact [16]. Computer, communication, consumer electronics and packaging industries are all interested in reducing the volume of injection-molded parts.

In general, reducing the main thickness of injection-molded parts leads to a smaller overall volume of the molded part, and corresponding material cost savings and smaller overall environmental impact (lower resources consumed, lighter products leading to improved efficiency). Moreover, as analyzed by Thiriez and Gutowski, the cycle time is shorter making the environmental and economical burdens related to the process less significant too [17].

The main feature of thin-wall injection molding is the high flow-length to thickness ratio, which requires a high cavity pressure at the gate during the filling phase, to drive the Poiseuille flow and achieve the flow length. The polymer viscosity combined with the small cross sectional area of the channel results in a very high-pressure gradient along the component, ultimately hindering the complete replication of mold geometry at the end of flow. Lucchetta et al. investigated technological limits of injection molding when injection molding a thin-wall cavity with micro features on its surface [6]. Masato et al. identified the pressure at the gate as the main factor determining the filling length of a thin-wall cavity [18].

The high filling resistance leads to the necessity to use more power from the injection molding machine in order to ensure the success of the process. However, this would result in higher energy consumption and environmental impact, indicating another important aspect regarding the reduction of the melt flow resistance for injection molding applications.

2.1 FILLING FLOW MECHANISMS

2.1.1 *Fountain flow in conventional injection molding*

In conventional injection molding, when the polymer melt enters the cavity, during the injection phase, the outer skin in contact with the wall freezes. The core remains in a fluid state and it moves forward towards the melt front area and out to the wall surface, cf. Figure 2.1. This is known as the *fountain flow*, and is characterized by a so called

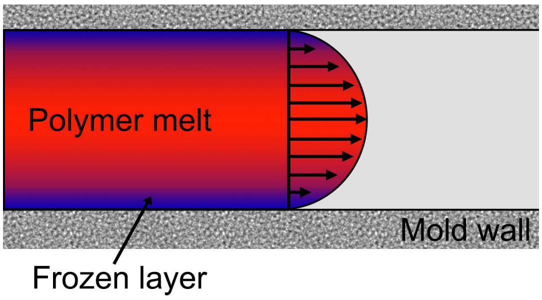

Figure 2.1: Fountain flow of polymer melt in conventional injection molding [19].

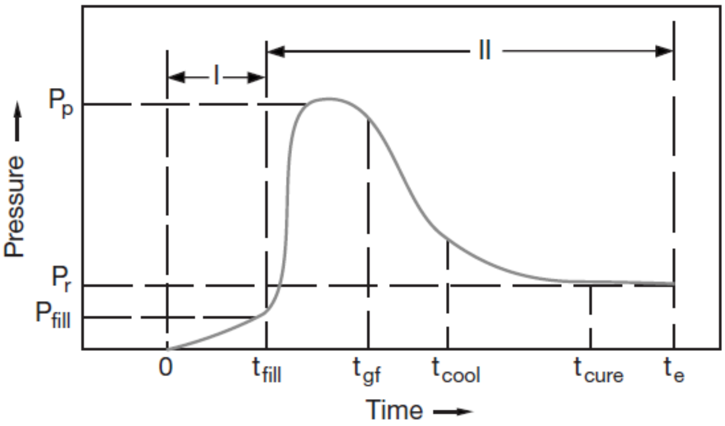

Figure 2.2: A schematic cavity pressure history.

skin-core morphology. The skin formed along the surface of the main cavity opposes to the filling of features placed on the surface, reducing the effect of the packing pressure [9]. This is commonly known as the *hesitation effect*.

2.1.2 *Cavity pressure*

One of the most important process function in injection molding is cavity pressure. Figure 2.2 shows a typical of cavity pressure during an injection molding cycle. Two different phases can be distinguished: (i) the filling phase governed by the thermo-rheological behavior of the polymer melt, (ii) the post-filling phase that is controlled by the heat transfer between the melt and the mold and by the compressibility of the solidifying polymer.

During the filling phase, the injection pressure grows rapidly until the polymer melt has reached the far end of the cavity. In fact, cavity pressure represents the head loss related to the polymer flowing ahead of the measuring point. If cavity pressure is too high, the polymer melt might not reach the end of the cavity, leading to incomplete replication of mold geometry.

In general, the characterization of cavity pressure can be very important to understand the filling of the cavity, providing indications about the final quality of the molded parts.

2.1.3 *Heat transfer coefficient*

The heat transfer coefficient (HTC) is generally used to describe the convection heat transfer between a fluid and a solid. It can be defined as the proportionality coefficient between the heat flux and the thermodynamic driving force of the heat flow (i.e. the temperature difference ΔT):

$$HTC = \frac{q}{\Delta T} \tag{2.1}$$

where:

- q is the heat flux (W/m^2);
- HTC is the heat transfer coefficient W/(m^2°C);
- ΔT is difference in temperature between the mold surface and the polymer melt.

It is known for macro-scale injection molding that the heat transfer coefficient at the interface between polymer and the mold changes with time during an injection cycle. During the packing and cooling stage, an air gap partial between the polymer melt and the mold wall might arise as a result of the thermal shrinkage, leading to a drop of the heat transfer coefficient. Typical values for the HTC range between 2000 and 5000 W/(m^2°C), however different values were observed for cavity characterized by reduced dimensions [20].

In thin-wall and micro injection molding, the cooling rates of the polymer melt in contact with the mold surfaces are much higher. Hence leading to the necessity for an accurate calibration of the HTC coefficient in simulation models.

2.1.4 *Filling in thin-wall and micro cavities*

When reducing the dimensions of the cavity and in particular its thickness, the filling mechanisms can be modified and their understanding is still not very clear in the literature. A smaller cavity thickness can cause shear rates to be order of magnitude higher than those experienced in conventional injection molding [21, 22]. Indeed, shear stress and shear rate are inversely proportional to cavity dimension:

$$\tau, \eta \propto \frac{1}{h} \tag{2.2}$$

Studies in the literature reported that the flow of polymer melts in cavities with reduced dimensions are characterized by different filling behavior compared to conventional cavities [23, 24]. For instance, viscosity was found to increase as cavity size decreases to micrometers [25].

The polymer melt was also found to slip over the wall surface as cavity thickness decreases, due to the increase of shear stresses at the wall above a critical value [26]. This phenomenon could be attributed to the excessive shear rate and disentanglement of polymer molecules at the melt/wall interface. Therefore the 'no-slip boundary condition', that is considered for the conventional injection molding process, is no longer valid. This lead also to inaccuracies in the definition of the rheological data used for the simulation of the process.

2.2 REDUCTION OF THE MELT FLOW RESISTANCE

For reduction of the melt flow resistance, several studies in the literature have been focusing on the optimization of the most significant process parameters [27]. In particular, this has been achieved by means of Rapid Heat Cycle Molding (RHCM), which sustains the mold cavity surface temperature at relatively high temperature during the filling phase, and then reduces the temperature during cooling so the correct ejection temperature can be achieved. De Santis and Pantani suggested that this counteracts the development of the solidified skin layer (which effectively reduces the cross sectional area of the channel) and sustains a lower viscosity of the polymer melt (by reducing cooling rates) [28]. Using RHCM, McFarland et al. molded polystyrene cantilever beams characterized by a thickness of 10 μm and aspect ratio higher than 170 [29]. Similarly, Chang and Hwang used infrared heating to increase the flow length [30], while Sorgato et al. pursued the same objective using electrical heating and they obtained improvements up to 50% [31].

As an alternative to RHCM, which requires high initial investments for the mold and complex optimization [32], high-speed injection molding can also be used to allow the polymer melt to completely fill the cavity before the thickening of the skin layer hinders the flow at the core. Masato et al. studied the morphology of a thin-wall cavity (i.e. with a thickness of 350 μm) observing that the extremely reduced thickness results in the absence of the core layer [33]. However, the non-uniform cavity pressure distribution and high shear stresses caused by the high injection speed leads to aesthetic defects, such as flow marks, evidence of polymer degradation and sink marks [34].

Besides process parameters optimization, Chen et al. proposed the use of cavity surface coatings made of low thermal conductivity materials for improving the quality of ABS parts [35]. The heat transfer delay and the associated interface temperature variations were inves-

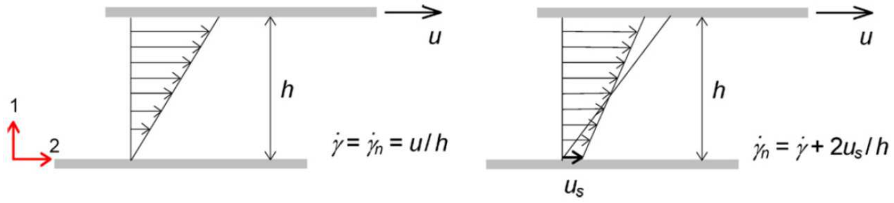
u
h
1
2
$\dot{\gamma} = \dot{\gamma}_n = u/h$
u
h
$\dot{\gamma}_n = \dot{\gamma} + 2u_s/h$
u_s

Figure 2.3: Speed profile for a polymer melt flowing between parallel plates with (a) no slip and (b) with wall slip [36].

tigated using TiN and PTFE coatings. Although this study gives some insight into the thermal effect of cavity surface coatings, it did not consider the reduction of flow resistance, separating the effects of heat conduction and potential wall slip related to the low-friction coatings. Hence, the potential reduction of melt flow resistance associated to the use of mold surface coatings is still to be properly characterized and understood. In particular, the relationship between mold surface properties and the rheology of the polymer melt during the injection phase is still not completely clear. Indeed, while several rheological studies were performed under isothermal conditions, very few investigations in the literature considered injection molding setups.

2.3 WALL SLIP PHENOMENON

Polymer melts, unlike Newtonian fluids, slip over solid surfaces when the shear stress at the wall exceeds a critical value [36]. The slip phenomenon plays a fundamental role in determining the rheology of polymers during their flow in manufacturing processes [37].

Brochard-Wyart and deGennes described the wall slip phenomenon proposing an interface rheological law in terms on an extrapolation length b [38]:

$$u_s = b\left[\frac{du}{dy}\right]_{y=0} = b\dot{\gamma}_w = \left[\frac{b}{\eta}\right]\sigma_w \qquad (2.3)$$

where u_s is the slip velocity, $\dot{\gamma}_w$ is the shear rate at the wall (i.e. the slope of the velocity profile at the interface, cf. Figure 2.3) and η is the viscosity of the melt at $\dot{\gamma}_w$.

2.3.1 *Macromolecular chains adsorption*

Polymer macromolecules of high enough molecular weight have the ability to entangle with each other forming a physical network. Considering a polymer melt flowing next to a solid wall, it can be assumed that exists a monolayer where macromolecular chains are attached (or adsorbed) to the wall through several sites along their backbone [39]. These molecules are connected with the bulk of the polymer through entanglements with other neighbor molecules. Un-

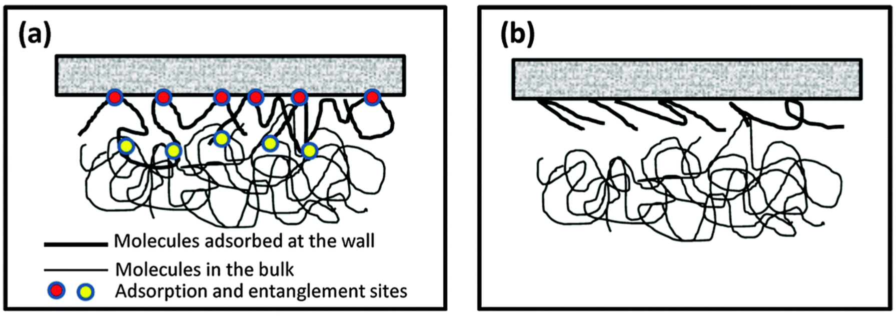
(a)
(b)
Molecules adsorbed at the wall
Molecules in the bulk
Adsorption and entanglement sites

Figure 2.4: Adsorption of macromolecular chains at the wall (a) and disentanglement of the adsorbed layer from the bulk material (b).

der flow conditions, the adsorbed macromolecules are pulled by the entanglements with the bulk molecules that are being stretched in the flow direction. When the applied forces increase above a critical value, the chains detach from the interface, leading to the onset of wall slip.

The slip model shown in Equation 2.3 is valid for passive polymer-wall interface, i.e. in the case that there is no adsorption of the macromolecular chains of the polymer at the interface. Conversely, for adsorbing surfaces a critical shear stress value exists, indicating the limit for the transition from a weak to a strong slip. Thus, depending on the flow conditions, different slip mechanism can occur:

i. *Adhesive slip* - detachment/desorption of the macromolecular chains from the wall that leads to weak slip, i.e. small deviations from a no-slip boundary condition;

ii. *Cohesive slip* - partial disentanglement of the bulk macromolecular chains from chains adsorbed at the wall that also leads to weak slip;

iii. *Strong slip* - under strong flow conditions the macromolecular chains adsorbed at the wall orientate towards the flow direction, and the mechanism of slip is a sudden disentanglement of the polymer chains in the bulk from those in a monolayer of polymer chains adsorbed at the wall [40]. In such conditions the velocity profiles of the polymer melt flow approaches that of a plug flow. The transition from weak to strong slip is mainly a characteristic of linear polymer (e.g. PS, PP), while it is not evident for polymer characterized by the presence of long chain branching (e.g. LDPE).

2.3.2 *Parameters affecting wall slip*

Wall slip of polymer melts is a complex phenomenon that depends on several parameters, including (*i*) the molecular weight of the polymer

[41], *(ii)* temperature [42], (*iii*) pressure [43], *(iv)* shear and normal stresses [37], *(v)* surface energy [44, 45] and *(vi)* roughness [46, 47].

2.3.2.1 *Effect of wall topography*

A simple phenomenological description of wall slip was at first introduced by de Gennes, which proposed that the slip velocity V_s can be related to the shear stress σ as follows [48]:

$$V_s = \sigma / \beta \tag{2.4}$$

where $\beta = \eta_i / a$ is an interfacial friction coefficient, η_i is a local viscosity at the interface and a is an interfacial thickness. This indicates a relationship between the wall slip effect and wall surface properties. Indeed, Boukany and Wang reported that solid surface can have different adsorbing properties [49]. In particular, they reported that shear deformation has different effects on the onset of wall slip for surfaces that adsorbs with different intensities.

Several researchers have reported that surface roughness, and in general surface topography, have a significant effect on the wall slip phenomenon [45, 50, 51]. In particular, the effect on an higher roughness is to decrease the slip effect and to shift to higher rates the transition from a weak to a strong slip regime. The roughness values for the wall surface considered in these studies are in the range of a few micrometers, thus being much larger than the coil size of a typical polymer macromolecular chain that is of the order of a few nanometers. Consequently, several chains of the polymer melt can be trapped in the space between the asperities that characterize the topography and the polymer-wall interface is replaced by a polymer-polymer interface.

Ebrahimi et al. investigated the slip of polymer melts over micropatterned metallic surfaces showing how surface characteristics can affect the slip velocity of polymer melts [52]. They used surface laser irradiation to produce different topographies in slit dies, which were then used in isothermal experiments performed on a capillary rheometer. Their results suggest that significant deviations from the linear viscoelastic behavior of the polymers are due to the occurrence of wall slip. Moreover, they observed that roughness reduces the slip velocity of the polymer to various degree depending on the type of topography. In fact, the polymer melt enters the micro cavities in the metallic substrate and many chains can be trapped in the space between asperities. Thus, the interactions between unbound chains and those trapped on the topography of the metallic die replace the chain/wall interactions. Therefore, the slip mechanism of polymer melt occurs within the first monolayer of macromolecular chains adsorbed at the wall and the polymer-wall interface is replaced by a polymer-polymer interface. The interactions at the polymer-polymer interface are much stronger than those with the cavity wall, hence leading to a decrease of the wall-slip phenomenon.

However, the effect of surface roughness on the filling flow was observed to be significant only below a critical cavity thickness value, which was identified at 150 μm [53, 54]. For thicker cavities the melt flow resistance is not significantly affected by the topography of the cavity.

2.3.2.2 *Dependence of slip on molecular parameters*

In general, the higher is the molecular weight of a polymer the higher is the probability for the macromolecular chains to entangle with each other forming a physical network [36]. Indeed, the slip velocity has been reported to be inversely proportional to the molecular weight of the polymer [42].

When wall slip occurs, the flow is controlled by the friction interactions between the polymer macromolecules adsorbed at the wall and those in the bulk thus being affected by polymer characteristics and in particular by their molecular weight. These interactions are affected by [41]:

- the adsorption density of polymer melts on high energy surface;
- the fact that adsorption on the metallic surface can occur in multiple sites, creating tails, loops and trains of different molecular weights;
- the stiffness of different polymer chains.

Moreover, the transition from weak to strong slip depends on the molecular characteristics of the polymer. Specifically, the higher the molecular weight the smaller the critical stress and the transition between the two regimes more abrupt.

2.3.2.3 *Effect of work of adhesion*

Hatzikiriakos et al. suggested that this effect can be further promoted using coatings that are generally characterized as 'low friction' [44]. Indeed, Lazzarabal et al. observed a linear relationship between the work of adhesion and the critical stress for slip [55]. Considering the definition by Israelachvili, the work of adhesion can be defined as [56]:

$$W_{adh} = \gamma_{LV}(1 + cos\vartheta) \qquad (2.5)$$

where γ_{LV} is the interfacial tension between the molten polymer and its vapor (air) and ϑ is the contact angle of the polymer in the melt state over the solid interface. Barrat proposed that, when a polymer melt slips over a solid surface, the coefficient of friction β defined in subsubsection 2.3.2.1 is proportional to the square of the attraction between the substrate and the liquid [57]. Hence, the slip velocity is inversely proportional to the work of adhesion:

$$u_s \approx W_{adh}^{-2} \tag{2.6}$$

In this sense, Ebrahimi et al. observed that slip velocity of HDPE is higher over silanized dies [52]. In fact, the higher the contact angle characterizing the coated surfaces promotes higher is the slip velocity.

2.4 WALL SLIP IN INJECTION MOLDING

Despite the great research efforts, most of the investigations on wall slip were performed under isothermal conditions, considering extrusion setups. Conversely, the knowledge on the onset of wall slip in the injection molding process is limited even though the phenomena is often mentioned in micro injection molding to explain the differences with the conventional process.

In injection molding, the wall shear stress generally increases with shear rate for a non-slip polymer-wall interface, as indicated by Zhang and Gilchrist [58]. However, Kelly et al. observed that when the shear rate exceeds 10^7 s^{-1}, the shear stresses can be greater than the critical values leading to deviation from linearity due to the onset of wall-slip [59].

According to Zhiltsova et al., the filling of thin-wall injection molding cavities is influenced by the occurrence of the wall-slip effect [60]. In fact, high values of shear rate increase the shear stress at the wall, leading to the disentanglement of the bulk polymer chains [36] and consequently to the unsuitability of the no-slip hydrodynamic boundary condition, which is normally assumed for the polymer flow in injection molding [61].

Chien et al. analyzed the cavity pressure drop of polymer melts flowing in injection molding cavities characterized by high shear stress distribution, observing that the wall-slip effect plays a dominant role [62]. Similarly, Chen et al. used a slit flow geometry to evaluate the reduction of the apparent viscosity that follows the onset of the wall-slip effect in thin-wall injection molding [63]. However, both experiments were carried out under isothermal molding conditions (i.e. mold temperature equals melt temperature), which do not apply in injection molding.

The intensity of the wall-slip phenomenon and of its effect on the melt flow resistance is connected with the properties of the polymer-mold interface [60]. Indeed, according to Yu et al., interface phenomena, such as wall slip, polymer surface tension, roughness and heat transfer, play a fundamental role in thin-wall injection molding that warrants further investigation [64].

3

EJECTION PHASE

In injection molding, the ejection phase (or demolding phase) is the process of removing the solidified polymer part from the tool. Demolding is a recognized reason for the failure of the injection molding process, often resulting in deformation or breakage of the molded parts [15]. The issues related to ejection are exacerbated in the case of micro parts, where the injection molding process is used to manufacture parts having either a mass in the range of few milligrams or features in the micrometer range. For these applications, dimensional tolerances are usually defined in the range of few micrometers, thus demanding high process accuracy.

In general, the demolding phase is carried out through the application of ejection forces in some designed locations of the part, as indicated by Araújo and Pouzada [65]. Griffiths et al. described that ejector pins should overcome the local friction at the part-tool interface without damaging the final parts [66]. However, Marson et al. observed that ejector pins can apply high local stresses to the part, causing possible distortion, stress marks and fractures [67].

Common approaches to molds for injection molding do not focus much attention on the design and optimization of the ejection phase. Experience-based solutions, which are the preferred solution in the industry, often results in the necessity for subsequent modification of the mold, leading to time and economic inefficiencies. Strategies for mold design that can solve demolding problems are currently not available in the literature [68]. Thus, the development of systematic approaches to tools design, as well as process monitoring and optimization are required to improve the quality of micro-molded parts and of the injection molding process.

3.1 THE CASE OF MICROFLUIDIC DEVICES

Demolding issues are particularly critical in the case of multi-layer microfluidic devices, where the mold cavity has several features that counteract the shrinkage of the polymer melt [67]. Indeed, the interconnections between the different layers are ensured by several arrays of through holes (Figure 3.1) that are realized by a series of deep cores tools in the mold. Typical multi-layer microfluidic devices involve critical design conditions, which lead to manufacturing issues. In particular, the presence of small through holes is a common design solution that allows the exchange of small volumes of fluids between the device layers through small pipes. In order to reduce the device

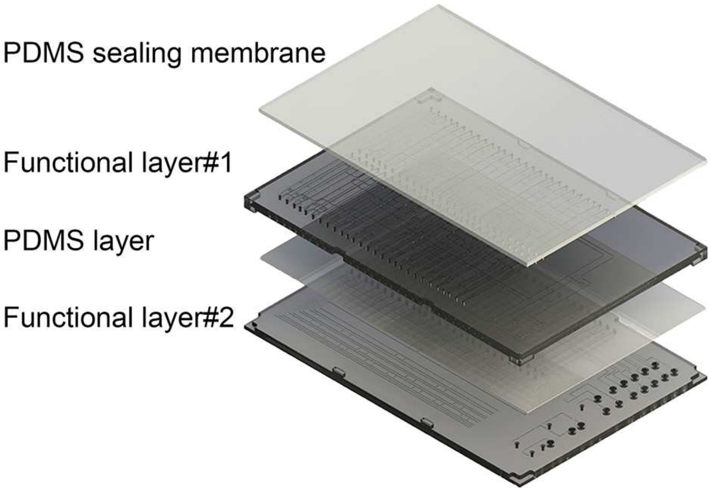

Figure 3.1: Example of multi-layer chip: 2 functional injection molded polymer layers - 2 PDMS sealing membranes [69].

dimension, whilst maintain high complexity/functionality, the holes are commonly arranged in tight arrays.

The combination of these design conditions makes μIM, and especially its ejection phase, particularly critical. In fact, Delaney and Kennedy described the development of demolding stresses during the μIM process, indicating how the normal force resulting from the polymer shrinkage affects the tangential force required during demolding and thus the efficiency of the demolding phase [70]. Hence, the successful separation of the replicated part from the mold requires to develop a reliable micro manufacturing process chain [15].

The shrinking of the polymer part, constrained by the tool during the μIM process, causes an increase of the thermally induced stress in the moldings, as described by Menges et al. [71]. The retaining forces that take place at the part-tool interface need to be overcome by a tangential force, generating a relative motion between the part and the tool. The successful manufacturing of plastic micro parts, characterized by high precision and good tolerances, requires to consider how the demolding force can be reduced [67]. Hence, the factors influencing the demolding phase have to be understood and analyzed to avoid any detrimental effects on molded parts [72].

3.2 EJECTION FRICTION

The interaction between the part and the tool at the beginning of the ejection phase determines the coefficient of friction between the two surfaces. In general, friction problems, as the ejection of molded parts, are interpreted according to the Amontons' laws, which indicates the constancy of the static friction coefficient and its independency to the nominal force:

$$\mu = F/L \tag{3.1}$$

where F is the tangential force and L the normal load. However, as reported by Blau, the friction coefficient is now recognized to be not constant, but dependent on the surface roughness, surface energy, mechanical properties, load and sliding velocity [73].

Persson indicated that for rough surfaces the mechanisms related to adhesion, deformation, contact, friction and wear are different from those observed for perfectly smooth surfaces [74].Thus, the polymer part friction during the ejection phase can be interpreted considering a two-term non-interacting model that combines both adhesion and deformation contributions [75].

3.2.1 *Friction mechanisms during ejection*

The understanding and the optimization of ejection friction must consider the history of the polymer material during the injection molding process. In particular, the following mechanisms contribute to the generation of the ejection force:

- during the injection phase, the polymer melt is capable of replicating the topography of the mold thus creating adhesion at the polymer-tool interface;
- upon cooling, the polymer shrinks onto mold cores being constrained by their presence, due to the differential shrinkage coefficients. This cause the generation of stresses in the cross section of the polymer part, resulting in forces normal to the mold surface.

During the ejection phase, a tangential force is required to overcome the combined effects of this two mechanisms and to generate relative motion between the part and the tool surface.

3.2.2 *Friction description for rough surfaces*

A more accurate description of the friction force F_e can be defined considering a two-term non-interacting model that combines both adhesion and deformation contributions [76]. Thus, the frictional work between the polymer and the mold surface is dissipated in two separate regions (Figure 3.2):

$$F_e = F_{adhesion} + F_{deformation} = F_0 + \mu L \tag{3.2}$$

where $F_0 > 0$ is a finite friction force measured at zero load L and μ is generally not constant. Specifically the two contribution are related to the following friction mechanisms:

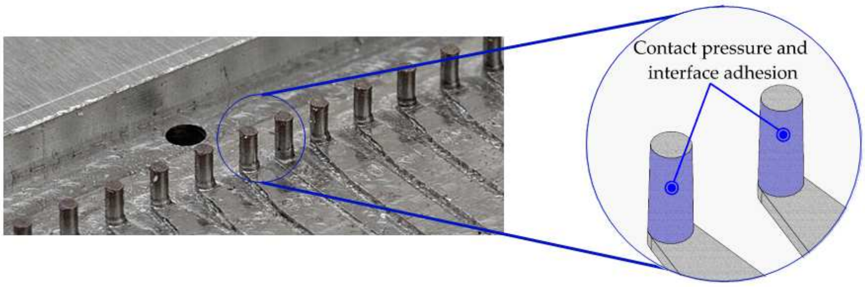

Figure 3.2: Adhesion and deformation components of the friction force.

- adhesion is a surface effect, which derives from the physical attraction forces between metal atoms and polymer molecules close to the interfacial area [77];

- deformation is a bulk effect governed by the mechanical interlocking intensity between the replicating tool and the part, which produces two different kinds of friction mechanisms: ploughing of solid metal surface asperities over the soft polymer surface [78] and elastic deformation of polymer surface asperities [76].

Israelachvili and Berman modified the conventional Amontons' law to the following [79]:

$$F_e = S_c A + \mu L \tag{3.3}$$

where A is the real contact area and S_c is the critical shear stress due to the adhesion force.

The friction during the ejection phase of the injection molding process is mainly dominated by the first term of equation Equation 3.3, thus being 'adhesion-controlled' [80]. In fact, the deformation mechanism is a combination of ploughing (i.e. plastic deformation of the sub-surface layer caused by hard asperities) and hysteresis (i.e. elastic or viscoelastic recovery of the polymer after indentation by mold surface asperities) acting together during the sliding of the two solid surface [81].

According to Parenti et al., the inherent footprint left on the mold surface by the machining process makes the deformation component the one controlling the frictional force developing at the polymer-tool interface [82]. In fact, during the filling phase, the polymer melt replicates mold topography creating 'mechanical interlocking' at their interface [18]. Then, upon ejection, the deformation of the polymer must be sufficient to allow the proper separation of the molded part from the tool.

3.2.3 *Interface adhesion in micro injection molding*

The interface adhesion is more marked in micro injection molding applications due to size effects and maximization of process settings. In fact, the reduced dimensions of the cavity make the phenomena occurring at the interface more relevant, indicating the importance of controlling mold surface properties. Indeed, the optimization of the demolding phase by controlling mold surface properties is a crucial aspect for the optimization of the injection molding process, especially at the micro scale where interfacial interactions are more relevant and for machining technologies that produce surface smearing.

Yao and Kim discussed the importance of size effects of in miniaturization of injection-molded parts indicating that interfacial interactions are more relevant when processing at the micro scale, making the micro injection molding process more sensitive to tool surface quality [83]. Zhang et al. evaluated the relationship between the mold surface and the melt flow behavior in micro injection molding, indicating that tool surface roughness affects the filling capabilities of the process by modifying the heat transfer at the part-tool interface [53]. Consequently, the interaction occurring during the pressurized filling of the cavity can increase the adhesion between the polymer and the mold thus affecting the friction during the demolding phase [84]. Even though surface roughness plays an important role during this phase [14], the micro scale effects of mold topography produced by conventional machining processes has not yet been properly investigated.

Moreover, in micro injection molding a proper filling of the cavity is achieved by adopting high values of the mold temperature, the melt temperature and of the injection speed [31]. A combination of high values of these process settings results in low viscosity of the injected polymer melt increasing its flow ability fill micro and nano cavities, but also its capability to replicate mold topography, generating higher interface adhesion.

3.3 PARAMETERS AFFECTING THE EJECTION FORCE

Studies reported in the literature have shown that in injection molding the friction at the part-mold interface depends on polymer type [81], mold materials or surface coatings [85], process parameters [72] and cavity surface finish [86].

3.3.1 *Effects of injection molding process parameters*

Considering injection molding process parameters, a distinction can be made considering parameters that affect the polymer shrinkage and those that affect the generation of mechanical interlocking at the part-tool interface.

3.3.1.1 *Effects on shrinkage*

The polymer shrinkage in the μIM process can be controlled by appropriately selecting the controllable process parameters [87]. In particular, a correlation exists between pressure during filling and packing phases and demolding parameters, as investigated by Griffiths et al. [88]. In their research, they showed that a proper combination of process parameters should be identified to achieve an optimal demolding behavior. Pontes and Pouzada noted that higher pressures reduce the differential shrinkage in the part, thus the diametric shrinkage and the consequent adhesion of the polymer to mold cores [89]. However, Pontes and Pouzada reported that when the applied packing pressure was lower a smaller ejection force was observed, because of the larger through-thickness shrinkage that can cause smaller contact pressure at the part-tool interface [90]. Moreover, the ejection forces are influenced by the process thermal boundary conditions. In particular, the temperature of the part in the demolding phase determines the polymer elastic modulus and affects the part-tool interface friction.

3.3.1.2 *Effects on topography replication*

Pouzada et al. described the friction mechanism at the polymer-tool interface, indicating that it is also controlled by the mold temperature, which determines the interlocking between the polymer melt and the mold that is formed during the filling phase [81]. In their work, they evaluated the coefficient of friction using a prototype apparatus showing that, due to replication, it can reach very large values (above 0.9).

Both the pressurized filling of the cavity and the shrinkage taking place during the part cooling, contribute to the surface interlocking, making the topography of the mold surface a fundamental parameter, as described by Ferreira et al. [91]. Masato et al. analyzed the filling of a micro-structured surface by μIM, indicating that during the injection phase the polymer melt is driven into the mold cavity, and replicates the mold surface texture [18]. Hence, the plastic part tends to stick over the cores surface after cooling, closely reproducing its surface finish. Therefore, the tribological conditions at the part-mold interface during the ejection phase are not only determined by the shrinkage-induced stresses, but also by the replication of the mold topography and the consequent mechanical interlocking. Moreover, Attia and Alcock studied the application of μIM processes to the replication of a micro-structured surface and they regarded the packing pressure as the main driving force that compels the polymer into micro cavities [10]. Consequently, this process parameter should be considered as a possible cause of higher part-tool surface interlocking.

3.3.2 *Effect of mold surface roughness*

Considering the effect of mold surface finish on the ejection forces in conventional injection molding several authors have performed different investigations. Schaller et al. compared the effects of different surface finish, obtained with different processes, reporting improvements up to 50% of the total force required to demold the part. In fact, the coefficient of friction increases with roughness, as the expected influence of the surface asperities and the burrs mechanical effect [92].

Sasaki et al. correlated the cavity surface roughness to the ejection force using different polymers and a deep core tool geometry [93]. Their results confirmed that ejection forces decrease with the mold roughness, but they found a limit beyond which the force increases. For PP, for example, the ejection force decreased by about 50% (from about 400 N to about 200 N) as Ra reduced from 0.689 μm to 0.212 μm. Then, after a minimum (i.e. 100 N for Ra of 0.212 μm), it started to increase rapidly at lower values of Ra (i.e. smaller than 0.026 μm), reaching a maximum value of about 1500 N. Similarly, an optimal value of surface roughness was determined for PET (ejection force range: 400 - 1100 N) and PMMA (ejection force range: 600 - 1100 N), for the corresponding minimum ejection force (i.e. 300 for PET and 400 for PMMA).

Correia et al. performed off-line tribological tests between steel tools, machined by EDM (0.039 μm < Ra < 1.952 μm), and PP plates [94]. Their results indicate that the minimum value of the friction was obtained for Ra values of about 0.5 μm. The same parameter was also used by Majewski et al., which compared the effect on the demolding force of the surface finish of differently polished and peened direct metal laser sintered tools (0.1 μm < Ra < 17.8 μm) with that obtainable with conventional machining processes, such as turning (0.5 μm < Ra < 4.2 μm) and EDM (1.7 μm < Ra < 5.2 μm).

3.3.3 *Effect of mold surface coatings*

Many studies in the literature focused on the optimization of mold surface properties, aiming at improving their interaction with the polymer during the demolding phase. Several strategies have been introduced in the literature aiming at the reduction of the adhesion between the tool and the polymer [95, 96].

Mold surface coatings have proven to be a viable solution to improve the tribological conditions at the part-tool interface during the ejection phase [66]. In fact, mold surface coatings can be exploited to modify the chemistry of the polymer – tool interaction [97].

During the filling phase of the injection molding process, a pressure-supported wetting of the cold mold surface by the hot polymer melt occurs. In contrast, the ejection phase can be regarded as the de-wetting of the adhering solidified polymer from the solid mold surface. Recent studies suggested that the interfacial tension (i.e. the external stress required to separate a liquid from a solid) could be used to predict the demolding resistance, being inversely proportional to the friction. Thus, the wetting parameters (i.e. the contact angle) can be used to describe the de-wetting of the solid polymer from the mold during the ejection phase [98]. In fact, the interfacial tension was reported to have high good qualitative inverse correlation to the measured friction at the solid/solid polymer-mold separating interface [84]. Thus, two materials showing high interfacial tension are easy to separate.

3.4 NEW DEMOLDING CONCEPTS FOR MICRO INJECTION MOLDING

Despite the miniaturized dimensions and the high-demanding tolerances, in micro injection molding the demolding of the parts is still carried out through the actions of conventional ejector pins that usually offer poor mechanical stability [65]. Further issues arises also from the necessity of applying the ejection force on the outer region of the parts, in order to avoid surface marking of the functional micro features [68]. This is critical in the case of mold cavities characterized by the presence of features that counteract the shrinkage of the polymer melt, as deep cores that creates tight arrays of micro holes in the molded parts (cf. section 3.1). The combination of these design conditions makes the ejection phase, and the overall processing, particularly critical.

In this context, in order to support the development of more reliable micro manufacturing process chains, new demolding concepts were proposed in the literature, such as the use of ultrasound vibrations [99]. The main idea behind this new demolding concept was the dissimilar propagation and dissipation of the ultrasonic waves through the different materials involved during the ejection phase (i.e. the mold steel and the polymer part). The application of the ultrasound vibration is supposed to decrease the demolding force due to the diverse oscillation behavior of the interface materials, which lead to reduced wall adherence and hence friction.

Michaeli and Gartner studied the effects of the application of ultrasound vibration to either the mold insert and the molded parts [99]. The results of their tests on POM, PMMA, PC showed no significant reduction of the demolding force in the former case and the damaging of the part in the latter due to melting.

Zwicker designed a mold setup in which the cavity is realized by the horn, which is assembled into the moving mold half [100]. During the demolding phase, the vibration of the cavity generates an air cushion at the interface with the mold cavity walls, which looses and sheds the molded part. The use of this injection molding setup with different polymers was reported to yield the absence of surface marking on the molded micro parts. However, the effects of the ultrasound vibration were not quantitatively compared to conventional ejection systems.

4

MOLD SURFACE DESIGN IN INJECTION MOLDING

The design of the mold is one of the most critical issue when approaching the injection molding process. The failure of the injection molding process can often be related to wrong design solution in the mold, which has to be modified thus increasing the time required to start up a production.

4.1 OUTLOOK ON MOLD SURFACE PROPERTIES

When approaching mold design, one of the most crucial aspect is the optimization of the properties of its surface. This is particularly important for the following applications:

- aesthetic parts - the higher the surface finish the higher is the surface gloss of the part [101];
- complex 3D parts - the friction at the mold surface can result in impairment of the molded parts or of its weak features (cf. chapter 3);
- difficult to fill parts - when the cavity is characterized by high resistance to the melt flow the surface properties can affect the filling [102];
- mold surface wear - certain injection molding polymers can cause the progressive wear of mold surface thus leading to molded parts characterized by geometrical defects and incorrect tolerances;
- mold surface fouling and clogging - during injection molding the polymer can accumulate in particular areas of the mold (e.g. vent slots), leading to the necessity for production stoppage and cleaning.

However, it is not an easy task for the mold designer to understand which are the characteristics of the mold surface to control. Indeed, several properties of the mold surface are involved during the process and they can affect the quality of the final parts. The main significant are:

- roughness;
- topography;
- chemical properties;

- wetting properties;
- friction properties.

The literature and the industry lack of systematic approaches to the design of mold surface properties, thus often working in unoptimized condition that results in production waste. Considering the literature, two different approaches can be distinguished:

- *Surface Generation* - i.e. design of the cutting and finishing processes for the tailoring of mold surface properties;
- *Surface Modification* - i.e. adoption of treatments after machining (e.g. coatings).

4.2 SURFACE GENERATION

Optimization of the surface finish is fundamental in determining the quality of the injection molding process, having significant effects on both the filling and ejection phases. In fact, machining processes adopted for mold manufacturing often produce intermittent smearing on cavity surface.

Tools for micro injection molding applications are commonly machined by means of micro milling and micro electro discharge machining, which both yield a characteristic mold topography [103, 104]. The formation of intermittent and directional burrs and smearing in micro milling and the isotropic craters resulting from micro EDM machining generate different cavity surface textures, which can diversely affect the ejection phase [105]. In fact, during mold production, the selected machining process leaves its technological signature or its 'surface footprint' on the generated mold surface.

The understanding of the effects of mold surface footprint on the ejection friction is crucial to improve the design of the process chain and the final quality of molded micro parts.

4.2.1 *Micro milling*

Micro milling (μM) is nowadays one of the most flexible and productive process to fabricate micro molds [106]. Compared to other micro manufacturing processes, such as micro electrical discharge machining (μEDM), μM gives higher productivity rates whilst maintaining similar geometrical accuracy, even on complex parts. Additionally, μM does not require part electrical conductivity and does not induce material substrate damages as μEDM does [103].

Compared to traditional milling, μM requires higher machine accuracy and finer parameter selections to cope with increased process complexity and constraints. At micro scale, additional phenomena affect the achievable performance in terms of ge-ometrical/dimensional, surface accuracy and also productivity [105]. Large ploughing action of milling tools and mini-mum chip thickness are some μM serious issues that cause burr formation, increased tool wear and high wear sensitivity with respect to cutting parameters. In addition, the small dimensions and low rigidity of the cutting system, driven by micro tool compliance, is a source of location errors and shape deviations of machined components, which can lead in worst cases also to tool failure [107].

Cutting large aspect ratio pins in multiple configuration worsen these limitations due to the additional flexibility coming from the workpiece features and also from the limited tool diameters, which are needed to machine close pins i.e. with small pin-to-pin center distances.

A good planning of μM involves the use of ultra-high precision milling machine and spindles, equipped with precise tool presetting systems [108]. On these machines, simple three-axis configurations are usually adopted for machining pins and other cylindrical features - as required by the molds for microfluidic devices - since they give more reliable accuracy performance in respect to five-axis configuration [109, 110]. μM accuracy is related with machine accuracy but also with process parameter selection and with the required dimensional and geometrical tolerances.

Moreover, the achievable surface roughness in μM is hard to predict in respect to standard macro milling process where indeed pure kinematic analysis of the cutting leads to good predictions. Despite the efforts in the literature to control footprint and texture generation in μM, this still is an issue, and there is not a sufficiently wide amount of reliable information to solve real industrial cases.

4.2.2 *Micro electro discharge machining*

Micro-electrical discharge machining (μEDM) is the application of conventional EDM technologies to the manufacturing of parts characterized by reduced dimensions. This means the necessity to adopt machine, tools and other process technologies that meet the requirements of micro manufacturing [111].

μEDM is a non-mechanical thermal machining process in which the material is removed by spatially and temporally separated electrical discharges between a workpiece electrode and a tool electrode [112]. The high frequency discharges cause the melting and the consectutive vaporization of the material on the surface of both electrodes. A dielectric fluid, which fills the working gap between the tool and the workpiece, is used to enhance the material removal rate.

The results of a single discharge is a crater-shaped pit on the surface of the workpiece. Depending of processing parameters, the diameter of the crater can vary from around 1 μm to around 100 μm.

Hence, the typical topography of a EDM machined surface is caused by the multitude of overlapping discharge craters. Surface roughness is affected by the discharge energy as reported by several researchers [113–115]. In fact, a higher discharging energy usually causes violent sparks and results in deeper erosion craters on the surface of the workpiece. Moreover, upon cooling the molten metal spilled around by the sparks solidifies increasing surface roughness [116].

Machining of micro-features using μEDM is becoming more and more significant in industrial micro manufacturing applications, due to its low set-up costs, elevated accuracy and large design freedom. Compared to other micro manufacturing technologies, μEDM yields many advantages when fabricating 3D complex shapes with high aspect ratio [117]. Moreover, all conductive materials regardless of hardness can be machined by EDM. Thus, μEDM is particularly useful to produce molds and dies for injection molding applications [103]. Specifically, the main advantages of μEDM include:

- no mechanical contact between the electrode and the workpiece;
- absence of burrs on the eroded component;
- no need for cost and time extensive cleaning procedures;
- negligible and only localized heating of the workpiece.

Moreover, despite being essentially a material removal process, efforts have been made to use EDM as a surface treatment method [118].

μEDM milling is a variation of the process where the material is eroded by a series of discrete sparks occurring between the workpiece and the rotating tool electrode [119]. The movement of the tool is controlled numerically to achieve the desired 3D shape with high accuracy, similar to what is usually done in micro milling operations. Indeed, the process is characterized by the feeding of the workpiece to the rotating tool electrode.

4.2.3 *Laser Induced Periodic Surface Structures - LIPSS*

Laser Induced Periodic Surface Structures (LIPSS), often referred as '*ripples*', are a universal phenomenon and can be generated on almost any solid material upon irradiation with linearly polarized radiation [121]. In general, LIPSS emerge as a surface nano-structure composed of quasi-periodic lines that exhibit correlation to the wavelength and polarization of the radiation.

Over the last decade, great interest has been given to their application due to their ease of generation. Indeed, surface nano-structuring with LIPSS can be generated in a single-step process, enabling surface

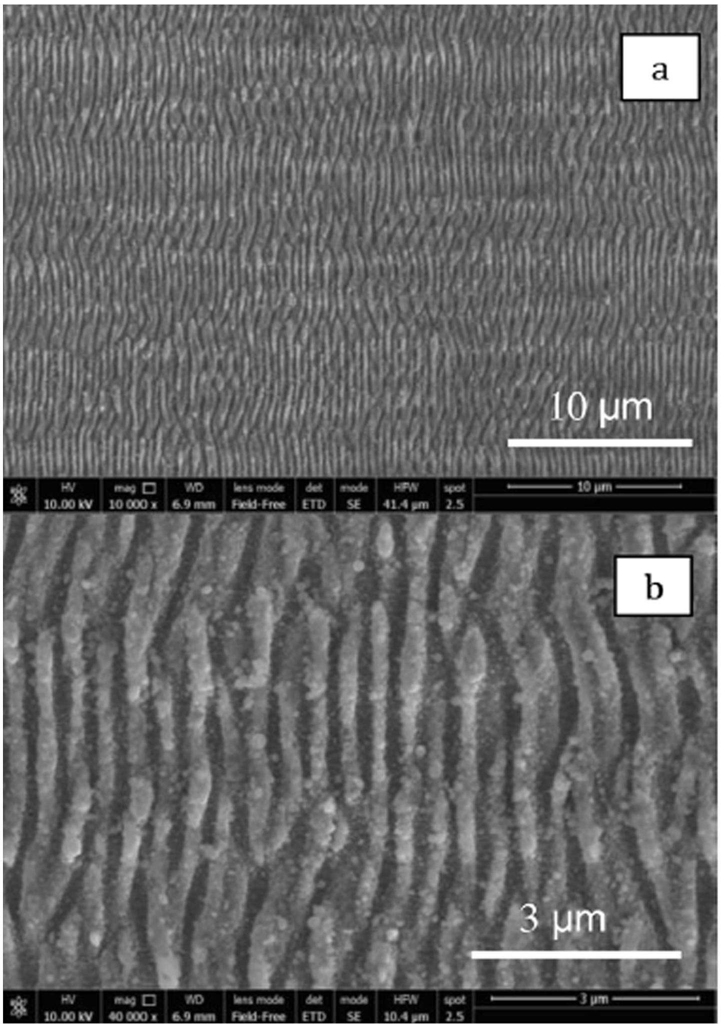
a
10 µm
HV 10.00 kV
mag 10 000 x
WD 6.9 mm
lens mode Field-Free
det ETD
mode SE
HFW 41.4 µm
spot 2.5
10 µm
b
3 µm
HV 10.00 kV
mag 40 000 x
WD 6.9 mm
lens mode Field-Free
det ETD
mode SE
HFW 10.4 µm
spot 2.5
3 µm

Figure 4.1: SEM micrographs of steel surfaces generated with NLL [120]

functionalization (e.g. for optical, mechanical or chemical surface applications). Among the different researches reported in the literature, the main applications of LIPSS are:

- controlled colorization through control of diffraction [122];
- hydrophobic/-philic behavior in wetting tests [123, 124];
- modification of cell and bacterial growth [125];
- friction and wear reduction in tribological applications [126].

Recently, a technique called *nonlinear laser lithography* (NLL) has been developed allowing the generation of uniform LIPSS-like nanostructures (cf. Figure 4.1) on large surface areas at an elevated production rate [127]. This technology is based on the use of a femtosecond laser with pulse energy in the order of nanojoules.

However, despite their increasingly higher diffusion, the use of these nano-structures in injection molding has not yet been investigated. Different tribology applications were taken in consideration [120, 128, 129].

4.3 MOLD ROUGHNESS DESCRIPTION

The employment of *Ra* to specify and control mold surface quality is supported by its wide use in the literature, and it is in accordance with the industrial practice where it is the main - and often the only - used roughness parameter [130]. Despite the breadth of available parameters, also the Society of Plastic Industry, which establishes polishing standards for plastic industry in the United States, specifies molds surface finish requirements based solely on the value of *Ra* [131].

However, when considering the different technologies available for micro molds manufacture, *Ra* might prove too general to be correlated with the complexity of the phenomena characterizing the ejection friction. Moreover, previous studies have investigated the effects on the ejection phase of mold topographies characterized by different roughness values, but they were machined using the same cutting technology and therefore they had the same 'process footprint'. Surface footprint is defined as the technological signature left by the machining process on the generated surface, and it can affect its functionality. In particular, in μIM the correlation between mold surface finish and the demoldability is complex and cannot be properly controlled by considering only *Ra*. Indeed, this parameter represents an average evaluation of the roughness amplitude on a profile. However, despite being representative for random surface roughness, this parameter do not provide any information about the shape, the irregularities and the spatial distribution of the considered profile.

4.4 SURFACE MODIFICATION

The use of low-friction and non-adhesive mold surface coatings is nowadays a widespread solution adopted in injection molding applications both in the literature and in manufacturing industries. Several researchers and coatings manufacturers have been claiming that their coatings can be used to either improve filling of mold cavities [97] or reduce the demolding stresses [93].

Several authors reported that the use of different coatings (e.g. titanium nitride, ceramic coatings, sol-gel coatings, teflon-like coatings) can preserve the integrity of the mold surface from the wear caused by the adhesion of the melt polymer [132–134]. Moreover, Dearlaney proposed the use of surface coatings to reduce the friction force and decrease the demolding energy [95].

In general, the adoption of anti-sticking and low-friction coatings have been demonstrated to play an important role in injection molding. However, the relationship between coatings and the phenomena that characterize the process is still to be further investigated. In particular, the reduction of the melt flow resistance needs to be thoroughly characterized, especially considering its relationship with the rheology of the polymer melt during the injection phase. Indeed, for thin-wall injection molding the rheological behavior is more complex, due to the effects of pressure [135] and viscoelasticity [136] on polymer viscosity.

Part II

MATERIALS AND METHODS

5

INJECTION MOLDING SETUP

The experimental investigations of the effects of mold surface treatments on the tribological conditions during the injection molding process were carried out using different experimental setups that could allow the process characterization of both the filling and ejection phases.

The basic approach followed for the design of the molds was the identification of strategies that allow the maximization of interactions between the polymer and the mold surface. Moreover, simple cavity geometries were taken into consideration pursuing the following objectives:

- design of mold geometries that represent typical features of real market products;
- accuracy of process control and monitoring;
- identification of geometries that could be easily model using analytical and numerical models.

In the following sections, the geometries and the features of the injection molding setups used for the experimentations are presented. A distinction between tools used for the filling and ejection phases is made.

5.1 CAVITY DESIGN

5.1.1 *Open-flow channel*

The analysis of the effects of mold surface treatments on the filling flow was carried out considering different experimentations. At first, a general characterization of the effects of mold surface coatings on the melt flow resistance was carried out in order to understand the phenomena that might influence the tribological interaction at the polymer/mold interface (*Investigation I*). Then, a different experimentation was carried out in order to further investigate the physical phenomena that control the filling resistance (*Investigation II*. The effects of surface generation were characterized using the setup of *Investigation II*.

In general, for all the experimentations, the cavity designed to study the effects of mold treatments on the filling phase is a thin-wall open-flow channel. The main advantages of this cavity design are the following:

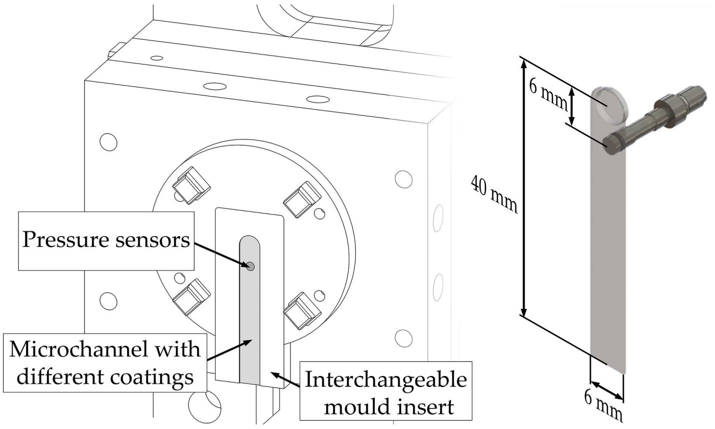
Pressure sensors
Microchannel with different coatings
Interchangeable mould insert
6 mm
40 mm
6 mm

Figure 5.1: Design of the mold cavity and of the part [138].

- the design allow the characterization of the melt flow resistance through the monitoring of cavity pressure;
- the injection of the polymer melt can be sustained until stationary flow conditions are reached within the cavity;
- the channel can be schematized using the '*Slit flow model*' [137].

The cavity design is characterized by a rectangular cross-section with a width (W) of 6 mm and a variable thickness (H) ranging from 400 μm to 800 μm (Figure 5.1).

5.1.2 *Deep core geometry*

The effect of mold surface treatments on the ejection force were experimentally investigated considering a *deep core* geometry. This geometry was selected for the following reasons:

- series of deep cores tools in the mold are common design solutions for microfluidic applications, where interconnections are ensured by the presence of arrays of through holes;
- allows the isolation of the effect of mold cores topography on the demolding force;
- the *deep core* geometry can be easily schematized and modeled.

The experiments comprised the design of two different parts in agreement with the use of different design solutions adopted for the realization of mold cores. Specifically the following parts were molded:

1. a disc with a diameter of 6.8 mm and a thickness of 1.5 mm; with four through holes, having a diameter of 800 μm and no draft angles (Figure 5.2 (a)). This will be identified as *MOLD A*;

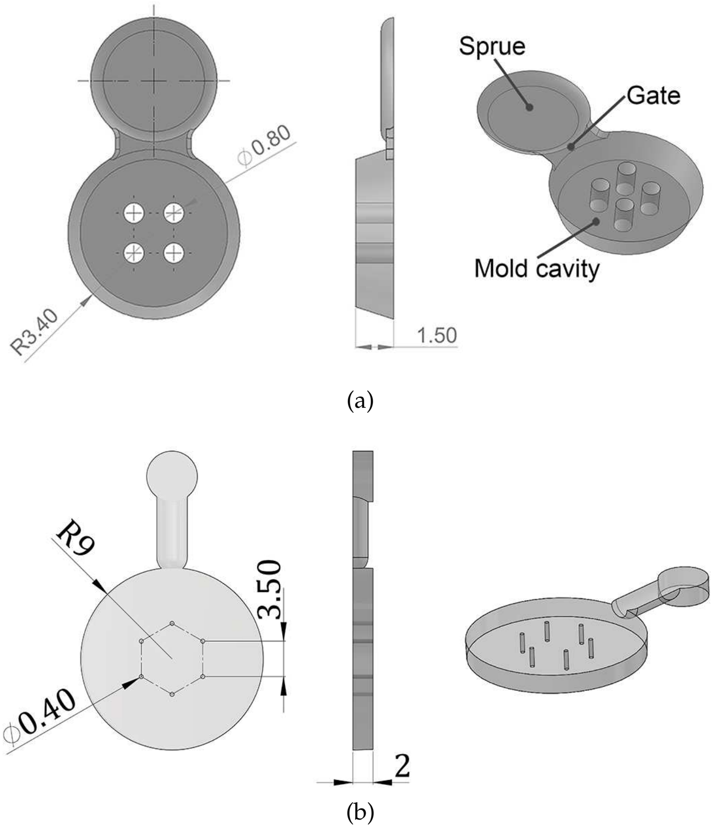
Sprue
Gate
⌀0.80
Mold cavity
R3.40
1.50
R9
3.50
⌀0.40
2

(a)

(b)

Figure 5.2: Design of the parts molded for the characterization of the ejection phase.

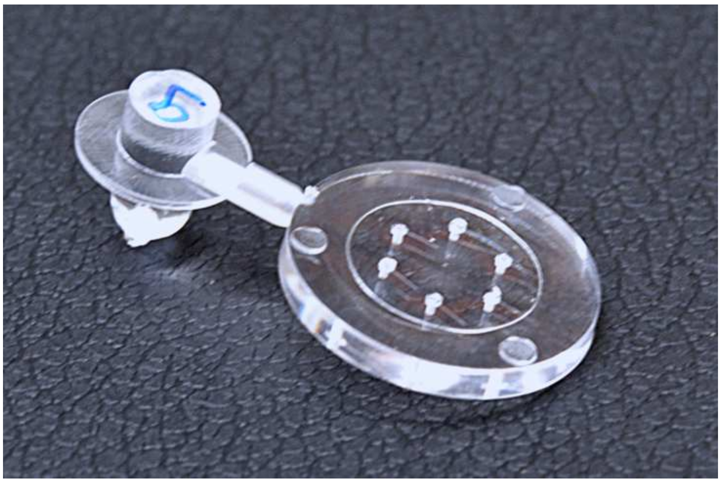

Figure 5.3: Part injection molded with *Mold B*.

2. a disc with a diameter of 18 mm and a thickness of 2 mm; with six through micro holes, with a diameter of 400 μm and no draft, located at the vertices of a centered regular hexagon having a side of 3.5 mm (Figure 5.2 (b)). This will be identified as *MOLD B*. Figure 5.3 shows a part molded with *Mold B*.

5.2 MOLD ASSEMBLY DESIGN

5.2.1 *Filling phase*

The mold used for *Investigation I* and *Investigation II* was designed to allow mounting of interchangeable inserts with different treatments, on both fixed and moving halves (Figure 5.4). The mold assembly was based on a Hasco K-standard modular system; several centering elements and coupling units were introduced to guarantee the accurate coupling of the two mold halves upon closing. The design of the moving half comprised two pressure transducers, which were flush mounted along the flow channel within each coated insert and allowed characterization of the pressure drop.

In order to characterize the velocity profiles of the melt flow across the channel thickness, the tool allowed the direct visualization of the cavity side during the molding cycle. Two sapphire windows (diameter: 12 mm, thickness: 7 mm) were mounted on the moving mold half allowing visualization and illumination using a transmission (rather than reflective) configuration.

For all the mold assembly, the temperature was set and controlled using two electrical cartridge heaters (diameter: 6.5 mm) and a single thermocouple in each of the mold fixed and moving halves.

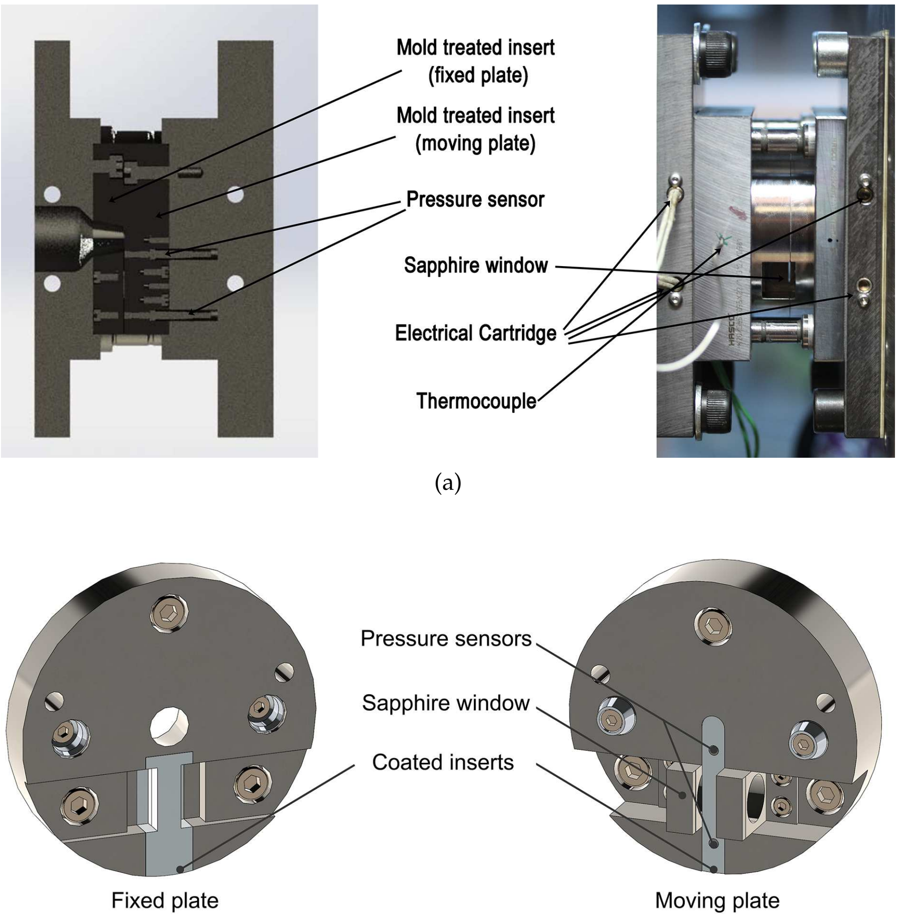
Mold treated insert (fixed plate)
Mold treated insert (moving plate)
Pressure sensor
Sapphire window
Electrical Cartridge
Thermocouple
Pressure sensors
Sapphire window
Coated inserts
Fixed plate
Moving plate

(a)

(b)

Figure 5.4: Design and main components of the mold used to study the filling phase.

5.2.2 *Ejection phase*

5.2.2.1 *Mold A*

The ejection system was realized by machining five cylindrical pins (diameter: 1 mm, aspect ratio: 3) on the top of a 6 mm diameter ejector rod, as displayed in Figure 5.5 (a). The pins served as small ejectors, which applied a distributed force around mold cores during the demolding phase.

The definition of the coupling tolerances between the ejector pins and their holes was critical, as it determined the final efficiency of the ejection system. Therefore, highly accurate micro milling strategies were implemented in the ejector rod and mold samples manufacture to satisfy the imposed micrometric tolerances.

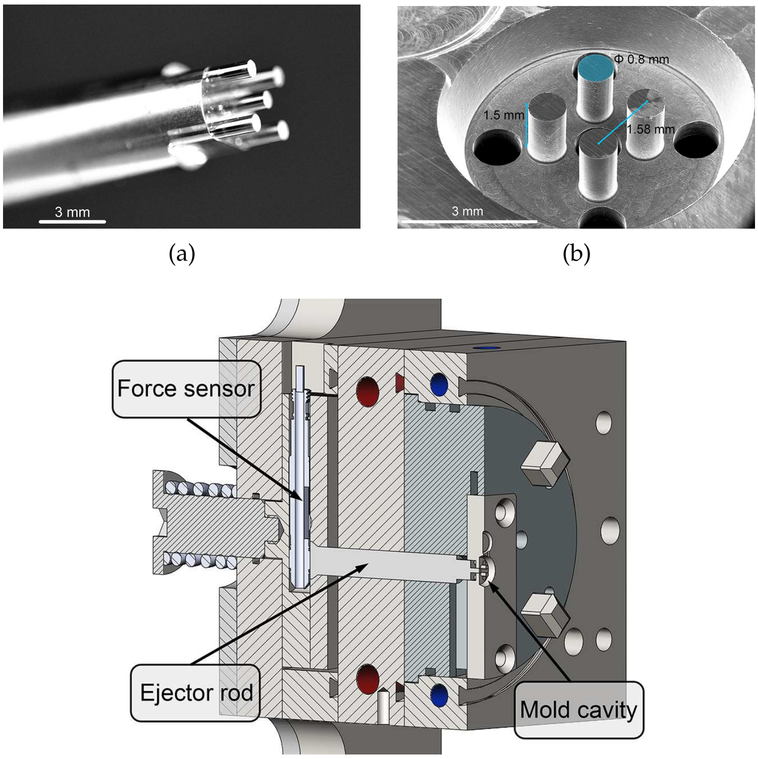

(a) (b)

(c)

Figure 5.5: Design of mold insert and assembly - *MOLD A* [69].

5.2.2.2 *Mold B*

The mold assembly was based on a Hasco K-standard modular system that was design to allow mounting of cavity cores as shown in Figure 5.6 (a). Ejection was carried through the action of three ejectors with a diameter of 2 mm.

5.3 PROCESS MONITORING

The online characterization of the injection molding process was performed using piezoelectric sensors placed within the mold assembly. The signals acquired from the sensors were the pressure of the polymer melt flowing in the cavity and the force applied to the solidified polymer by the action of ejectors.

During both cavity filling and part demolding, the transducers were subjected to mechanical loads producing piezoelectric charge signals. These signals were converted into outputs voltage using a Kistler Type 5039A charge amplifier and acquired by a National Instruments NI9205 16 bit analog input module. The sensor output signals were then downloaded onto a PC by a National Instrument NI cDAQ-9172 data acquisition unit and the measured values were analyzed using the National Instruments Labview 2013 software.

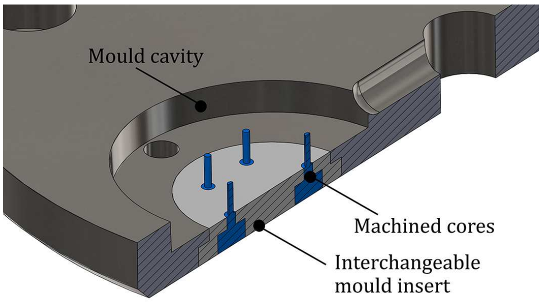

(a)

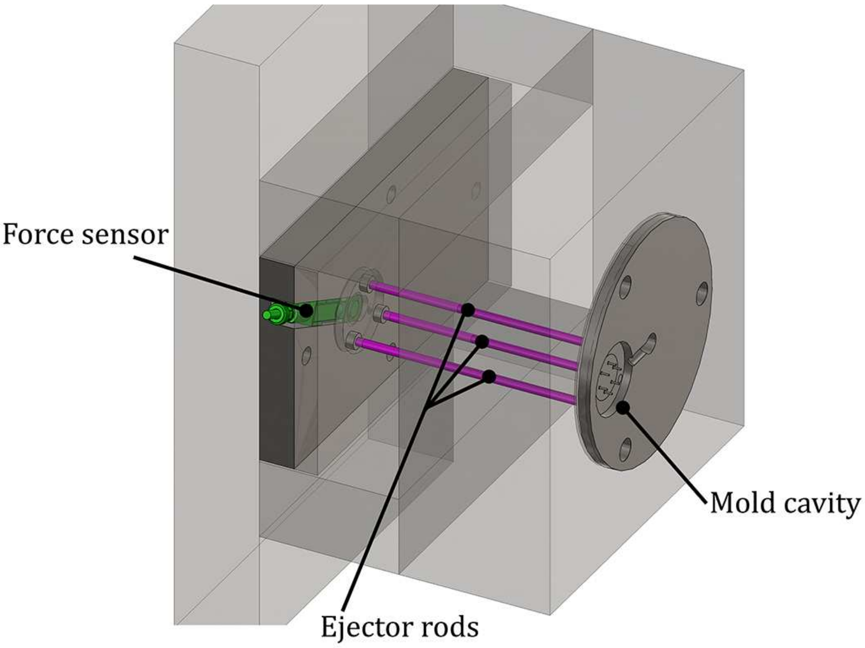

(b)

Figure 5.6: Design of mold insert and assembly - *MOLD B* [139].

5.3.1 *Characterization of the melt flow resistance*

5.3.1.1 *Cavity pressure measurement*

The effect of mold surface treatments on the flow resistance was investigated by monitoring the cavity pressure drop during the injection phase. The pressure was measured in two positions (at 6 mm and at 30 mm from the injection location) using Kistler 6182C piezoelectric pressure transducers, as shown in Figure 5.4.

The piezoelectric charge signal from the sensors was converted into output voltage signal using a Kistler Type 5039A charge amplifier, which was monitored with a National Instruments NI 9205 16-bit analog input module. The acquisitions were performed at a rate of 2500 s^{-1} (i.e. with a time step of 0.4 ms).

The acquired cavity pressure curves were aligned to the beginning of the injection phase, and the steady-state values of the cavity pres-

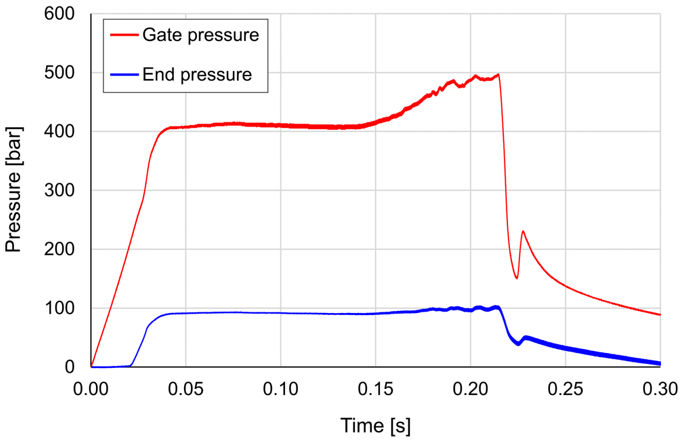

Figure 5.7: Pressure evolution measured in the cavity by the two piezoelectric transducers.

sure were collected (Figure 5.7). The melt flow resistance was then evaluated by calculating the difference between the average values of the steady–state zones of the two pressure signals (i.e. gate pressure, end pressure). In fact, the difference between the pressure values measured at the two extremities of the channel represents the pressure drop characterizing the mold cavity, which was selected as the response variable for the analysis.

5.3.1.2 *High-speed flow visualization*

In order to improve the understanding of the filling behavior of the polymer in coated thin-wall injection molding, the process was also characterized by direct high-speed flow visualization of the flowing polymer melt on the channel side.

The main components of the experimental setup and their position in the injection molding machine are shown in Figure 5.8 (a). A high-speed camera (NAC, Memrecam HX-3) was aligned to the mold allowing observation through the sapphire window. The online monitoring of the process was performed using a compact telecentric lens (5X Mitutoyo) with a 5x magnification and a working distance of 61 mm. The cavity was illuminated by a white light LED illuminator (SugarCUBETM, LED Illuminator) connected to a fiber optic light guide, which was positioned on the other side of the tool, aligned to the camera.

The recording was triggered using a digital signal output from the machine that was synchronous with the initial forward movement of the injection plunger during injection, after the mold closed to the viewing position (Figure 5.8 (b)). The image sequence was acquired with a frame rate of 12,000 fps, a field of view of 0.53 mm x 3.2 mm and a resolution of 320 x 1920 pixels.

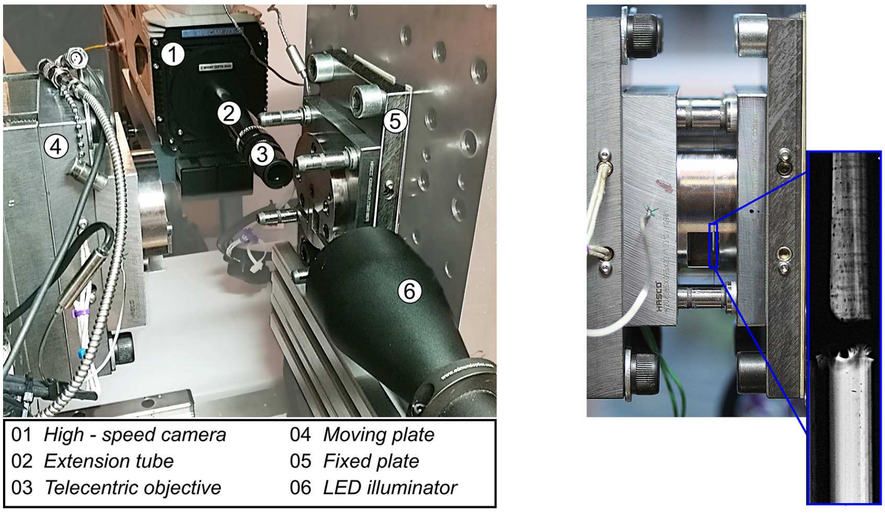

(a) (b)

Figure 5.8: Setup used for the high-speed flow visualization of the polymer melt flow, with (a) indication of its main components and (b) detail of the field of view in the closed mold.

5.3.1.3 *Particle image velocimetry*

The measurement of the velocity profile of the polymer melt was carried out using *Particle Image Velocimetry* (PIV), which is an optical method for flow visualization used to perform velocity measurements of flowing fluids [140]. In this work, the PIV analysis of the filling phase was carried out using silica carbide particles (particle size 17 μm), which were mixed with the polystyrene pellets (1% weight) in the hopper of the injection molding machine. The acquired image sequences (Figure 5.9) were processed using the java-based ImageJ software. For each image sequence, acquired for the different coatings at different injection speeds, the coordinates of selected particles were tracked and then plotted against the filling time. High-speed visualization of the filling flow was carried out in order to:

- track the velocity profiles of the polymer across the cavity thickness as a function of the set injection speed;
- evaluate the slip velocity of the polymer melt in the proximity of cavity walls and relate it to the different mold coatings.

5.3.2 *Characterization of ejection friction*

The monitoring of the demolding phase was carried out using a Kistler 9223A piezoelectric force transducer placed behind the ejector pins, as shown in Figure 5.5 and Figure 5.6. The design of the ejection mechanism and the location of the sensor allowed the acquisition of the overall force exerted by all the ejectors.

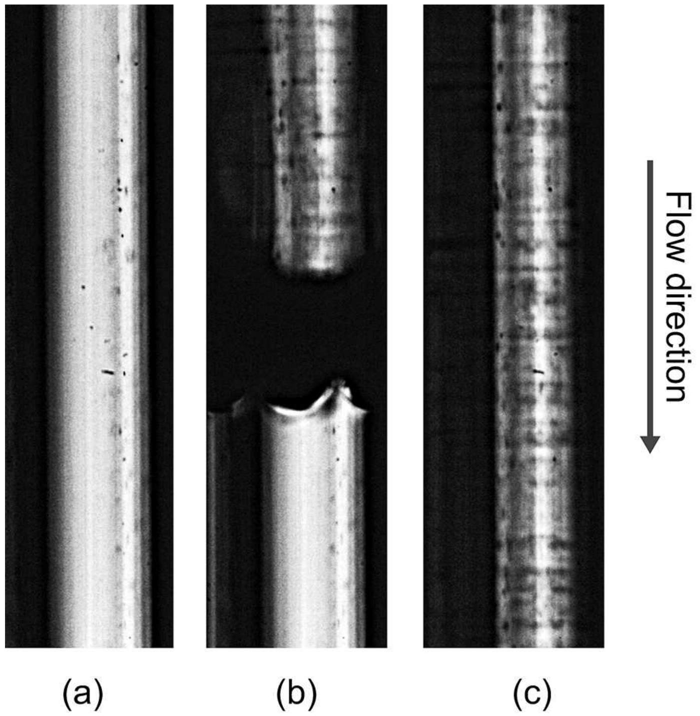

Figure 5.9: Frames of the cavity acquired (a) before the injection (empty cavity), (b) 1.2 ms after the injection (flow front) and (c) 4.7 ms after the injection (fully developed flow).

In order to avoid any data loss and properly monitor the force signal, ten samples were acquired at a sampling rate of 60 kHz, which corresponds to a sampling interval of about 0.2 ms.

Before all experiments, the stability of the different ejection systems (i.e. *Mold A* and *Mold B*) was initially verified by carrying out several dry cycles of the clamping and ejection units. The ejectors were cycled several times with ejector stroke and speed set us in the injection molding experiments. The mold temperature was set to the value designed for the following experiments. In general, the acquired dry cycle signals indicated that the demolding force reaches a stable value after about 50 cycles.

This was particularly important for *Mold A*, where the tight fit between the holes in the mold insert and the ejector pins, machined on the top of the ejector rod, needed to reach a stable behavior. The ejector was cycled 200 times (ejector stroke: 0.8 mm; ejection speed: 10 mm/s), allowing the evaluation of the functionality and robustness of the demolding force acquisition setup. The dry cycle trend analysis indicated how the ejection force reaches a stable value after 200 cycles, as shown in Figure 5.10. Moreover, the stabilized value of the dry demolding force was smaller than 1 N for all the produced mold inserts.

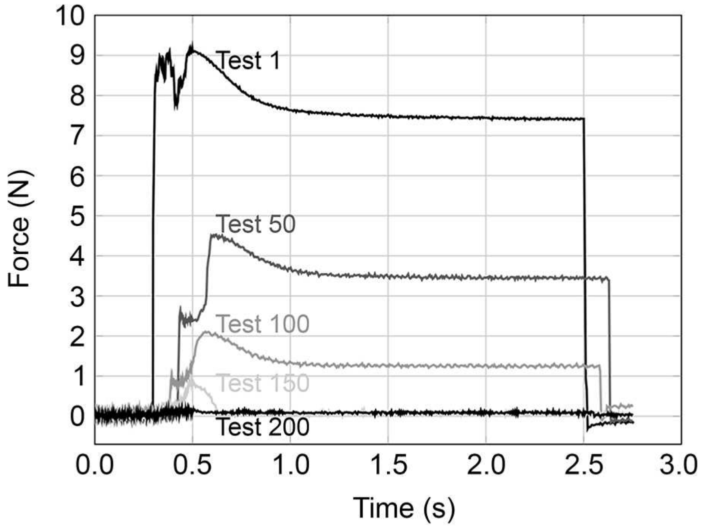

Figure 5.10: Stabilization behavior of the dry ejection force over cycles for *Mold B* [69].

In the case of *Mold B*, the stabilized value of the dry demolding force peak was reached after about 50 cycles and it was of about 10 N (with a standard deviation of 0.2 N).

In general, the dry force was neglected when comparing tests made with different mold inserts in the following analysis.

5.4 INJECTION MOLDING MACHINE

A state-of-the-art micro-injection molding machine (MicroPower 15 from Wittmann-Battenfeld) was used for the molding experiments (Figure 5.11). The machine is characterized by a maximum clamping force of 150 kN and a maximum injection speed of 750 mm/s. The plasticizing screw has a diameter of 14 mm and the injection plunger has a diameter of 5 mm. All the main characteristics of the machine are reported in technical data sheet in Table 5.1.

The *Unilog B6* control unit of the machine allowed the visualization of some process parameters on the actual value graphic and the evaluation of quality parts by checking the minimum cushion value.

5.5 ULTRASOUND-ASSISTED EJECTION

In this work, in order to reduce ejection friction, an innovative design for ultrasound-assisted demolding in μIM is proposed and analyzed. A commercial ultrasound horn, which movements were controlled using a robot arm installed in the injection molding, was used to vibrate the mold. The online monitoring of the demolding force allowed the evaluation of variations in the stiction at the interface between the part and the mold.

Properties	Unit	Value
Clamping unit		
Clamping force	kN	150
Opening stroke / Opening force	mm/kN	100/15
Ejector stroke / Ejector force	mm/kN	40/5
Injection unit		
Dosing screw diameter	mm	14
Dosing screw stroke	mm	26
Screw L/D ratio		20
Injection plunger diameter	mm	8
Injection plunger diameter	cm^3	4
Specific injection pressure	bar	2, 500
Max. screw speed	min^{-1}	200
Max.plasticizing rate	g/s	1.7
Max. screw torque	Nm	90
Nozzle stroke b / Contact force	mm/kN	230/40
Injection speed	mm/s	750
Injection rate into air	cm^3/s	38
Barrel heating power, nozzle inc.	kW	2.45
Drive		
Electrical power supply	kVA	9

Table 5.1: Wittmann Battenfeld Micropower 15t technical data sheet.

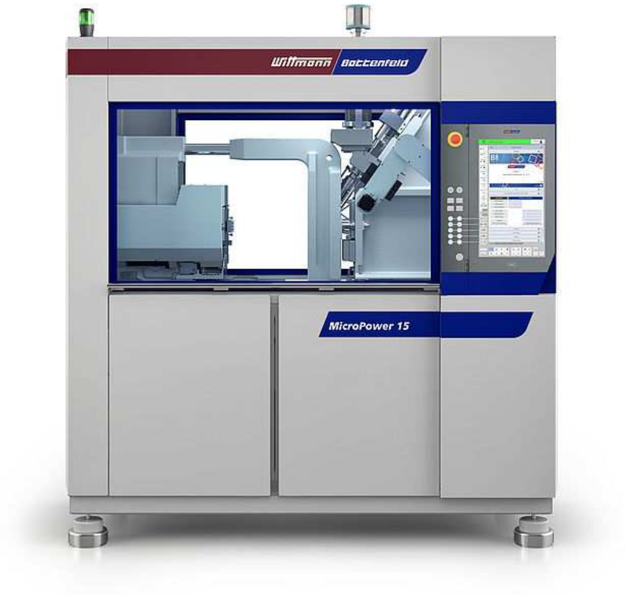

Figure 5.11: The MicroPower 15 Wittman Battenfeld.

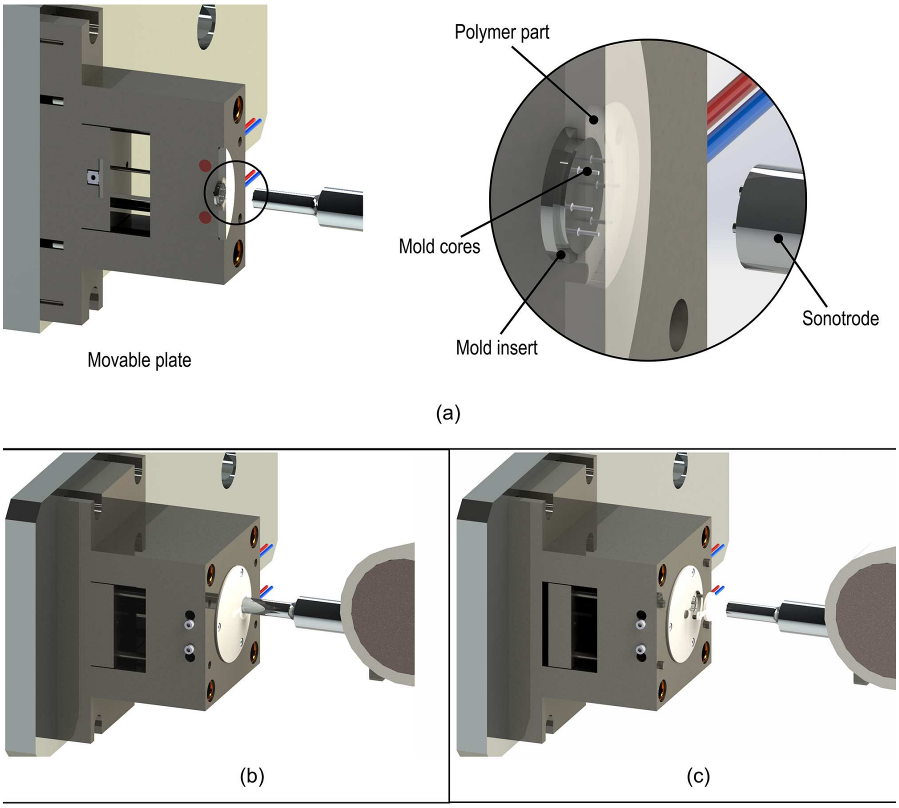
Polymer part
Mold cores
Sonotrode
Mold insert
Movable plate
(a)
(b)
(c)

Figure 5.12: Design of the ultrasound-assisted ejection system with its main components (a) and description of the ejection phase, (b) contact between the mold cores and the sonotrode, (c) retraction of the sonotrode and ejection of the part.

The new demolding technology proposed in this work exploits ultrasonic vibrations of the mold cavity to promote the decrease of the demolding force by inducing oscillations at the part/mold interface. In order to reduce wall adherence and stiction, an ultrasound horn vibrates the mold cavity cores after mold opening and before the beginning of the ejector stroke.

Ultrasound-assisted ejection of the part from the mold cavity was realized using a specifically designed vibrating system, realized from a conventional ultrasound welding setup and mounted in the injection molding machine. The system comprised a 35 kHz generator (Hermann Ultraschall, Ultrapack digital control 1000M PK) and an aluminum piezoelectric sonotrode, which converted the voltage output from the generator into mechanical oscillations (amplitude: 28 μm).

The vibration was transmitted by the contact between the cores in the mold cavity and matching pins (diameter: 1 mm) machined on the top surface of the sonotrode. In order to avoid the reflection of the ultrasound vibration, a thin damping polymeric layer was placed between the matching metal surfaces.

The sonotrode was fixed on a robotic arm installed inside the injection molding machine, allowing accurate positioning and proper transmission of the ultrasound vibration. The control unit of the machine (Wittmann-Battenfeld, Unilog B6) allowed the setup of sonotrode alignment and automatically ran the movements of the robot during the μIM cycle.

Figure 5.12 (a) describes all the steps of the innovative ultrasound-assisted demolding cycle. After mold opening, the sonotrode moves towards the mold reaching contact with mold cores, is switched on and kept in position for 3 seconds (Figure 5.12 (b)). Finally, the sonotrode is retracted from the mold and the ejector stroke begins ejecting the part from the cavity (Figure 5.12 (c)).

6

MOLD SURFACE MANUFACTURING

The tribological effects of mold surface on the injection molding process were investigated considering different strategies for both surface generation and modification. Particular attention has been given to the surfaces of the cavities presented in chapter 5. Considering the approach presented in chapter , this chapter presents the details of the processes adopted to treat the different mold surfaces.

6.1 SURFACE GENERATION

Mold surfaces are usually realized by means of different machining process, among which milling and electro discharge machining are the most common as discussed in section 4.2. However, when approaching miniaturization of the injection molding process, either in thin-wall injection molding or in micro injection molding, the effects of surface properties can gain significant importance and they cannot be neglected.

In this work, the effects of mold surface generation on the injection molding process were investigated considering the effects of conventional machining processes on the ejection phase and the effects of an innovative laser processing technique on the filling phase.

6.1.1 *Laser treatments*

Low surface energy fluoropolymer-based coatings have been reported to have the ability to suppress macromolecular adsorption at the polymer-wall interface and consequently to promote slip. However, they are not suitable for injection molding molds, as they are easily worn out by the injected polymers.

As an alternative, laser ablation has been recently used to affect the slip of polymer melts by varying the surface roughness (cf. subsubsection 2.3.2.1). However, all the proposed micro/nano-patterned surfaces resulted in a decrease of wall slip and a consequent raise of injection pressure. In this work, the adoption of Laser-Induced Periodic Surface Structures is proposed to reduce the pressure required to fill the cavity.

Using the geometry of the cavity and of the mold presented in subsection 5.1.1 and subsection 5.2.1, different laser treatment were used to generate different mold topographies. The laser treatments were realized by means of nonlinear laser lithography allowing the generation of ripples on the steel surface.

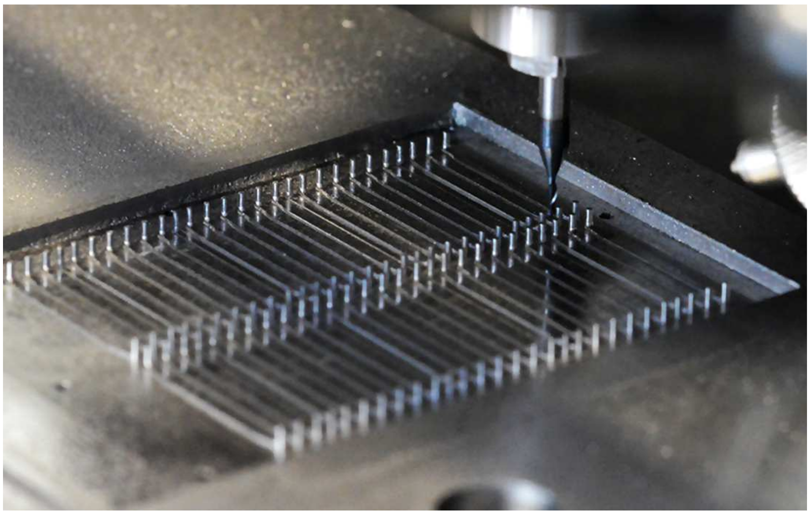

Figure 6.1: Micro milling of a lab-on-a-chip mold: 4 arrays of 28 pins - diameter 0.8 mm, height 2 mm.

Three different LIPSS topographies were generated by modifying the directionality of the laser treatment. Specifically,

- *Laser* 1 topography was realized by creating the ripples along the flow direction;
- *Laser* 2 topography was realized by generating the ripples opposed to the flow direction;
- *Laser* 3 topography was realized with two consecutive laser treatments, one in the flow direction and the other in the opposite direction. This laser treatment resulted in a crossed nanostructured topography.

All the laser treatments were carried out by adopting the same values for laser processing parameters.

6.1.2 *Mold surface machining*

The optimization of the ejection phase was carried out considering the case study of a microfluidic multi-layer device, which manufacturing issues were described in section 3.1. The peculiar deep cores geometry of the features in the cavity was simplified according the design of the mold inserts presented in subsection 5.1.2 and different machining technologies were considered.

6.1.2.1 *Micro milling*

Micro injection molding tools are mainly produced by machining processes, such as micro milling (cf. Figure 6.1. However, it is fundamental to investigate the generation of surface footprint in micro milling,

Parameter	Insert 1	Insert 2	Insert 3
Strategy (Z axis)	axial	axial	helicoidal
Cutting Speed [m/min]	37.7	50.3	37.7
Feed [mm/tooth]	0.012	0.006	0.006
Axial Depth of Cut [mm]	0.5	0.5	0.012
Radial Depth of Cut [mm]	0.02	0.01	0.015

Table 6.1: Micro milling strategies for the finishing operations of cores side.

analyzing the technological signature left by machining process on the generated mold surface. In this study, the surface topography of the cores surfaces was generated with different micro milling strategies, considering the effect of different cutting parameters. The obtained mold inserts were then used to investigate the effect of μIM process parameters on the demolding force.

Three mold inserts and one ejector rod (cf. Figure 5.5) were produced by micro milling using an ultra-high precision machining center (Kern Evo) in a 3-axis configuration. Coated tungsten carbide end-mills were used for the machining operation.

The three mold inserts were machined varying the milling strategies and the cutting parameters, based on state-of-the-art mold manufacturing strategies [141, 142]. The design of the roughing and semi-finishing operations for the three mold samples was performed by using the computer-aided manufacturing (CAM) software CimatronE.

Different micro milling cutting strategies (Figure 6.3) and parameters were selected for finishing of the cores lateral surface, which is the interface between the mold and the plastic part. Considering the mold surface topography importance for the ejection phase, different mold textures were produced with the aim of minimizing the interaction between the steel and the polymer sliding over it, as it is required in presence of features constraining the shrinkage of the polymer melt.

All finishing operations were performed with 0.5 mm diameter round-end milling tools with a corner radius of 50 μm (Union Tool, HLRS 2005-005-020). A new tool was used for each mold insert to avoid tool wear effects.

Table 6.1 reports the micro milling cutting parameters that were varied for finishing the three mold inserts [82]. Different strategies were adopted among the mold samples, moving from a "constant step-down" approach (i.e. multiple vertical shifting of the tool along the z-axis), used for *Insert* 1 and *Insert* 2, to a "top-down helicoidal approach" (i.e. an helicoidal downward movement along the side of the mold core) adopted for *Insert* 3. From the surface texture point of view, this latter strategy allows to reduce the formation of geometric localized defects generated by the bending of the tool and the pin. On the other side, the surface re-machining caused by tool overlapping

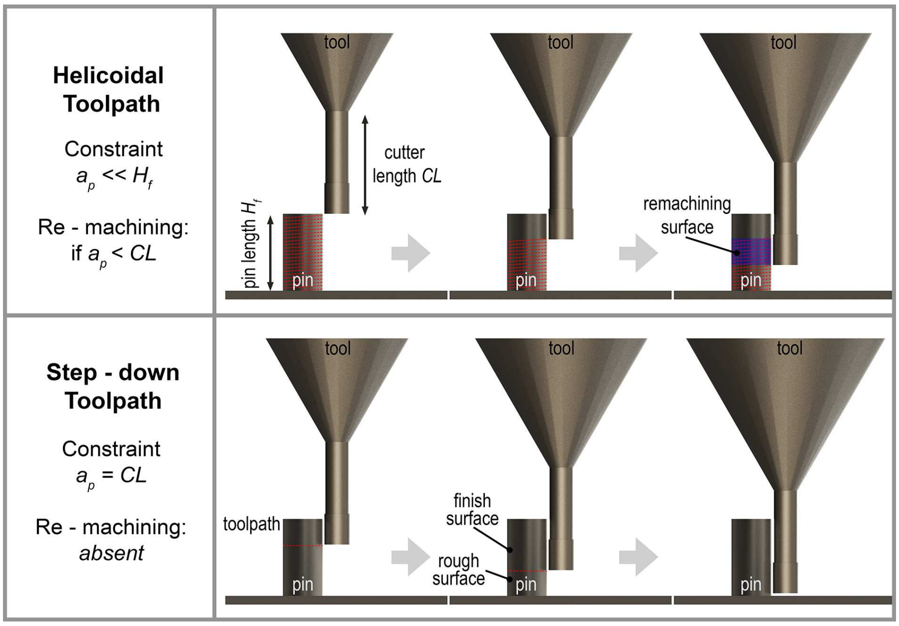
Helicoidal Toolpath
Constraint
$a_p << H_f$
Re - machining:
if $a_p < CL$
tool
cutter length CL
pin length H_f
pin
tool
pin
tool
remachining surface
pin
Step - down Toolpath
Constraint
$a_p = CL$
Re - machining:
absent
tool
toolpath
pin
tool
finish surface
rough surface
pin
tool
pin

Figure 6.2: Pin finishing strategies (three-axis cycle) [82].

(unavoidable with the adopted 3-axis cutting configuration) demonstrated to generate lower average height amplitude but characterized by a more irregular surface pattern. The optimization of cores finishing also involved the selection of cutting speed, tool feed and depth of cuts (both axial and radial). In particular, axial depth of cuts adopted in *Insert* 1 and *Insert* 2 were constrained by the adopted step-down strategy, which requires the use of the maximum axial engagement of the end-mills (to avoid surface re-machining and tool overlapping). *Insert* 1 and *Insert* 2 were differentiated in terms of more demanding cutting parameters used for the former sample, which generates bigger cutting forces and consequent higher tool-pin relative bending leading to bigger surface location errors. Indeed, feed per tooth used for *Insert* 2 and *Insert* 3 were fixed to a minimum value of 6 μm in order to reduce the impact of the uncut chip thickness effect. All of the samples were machined using a down milling cutting configuration since it is usually the most suitable approach for high aspect ratio features, as observed by Parenti et al. [106].

The tight coupling tolerances between the ejector pins and the mold inserts were met by machining and measuring the ejector pins before manufacturing the mold inserts. Drilling operations of the holes for the ejector pins were then performed by correcting their nominal diameter on the base of the actual ejector pin diameters (measured with a CMM machine). The operations were conducted with two-flute ball-end milling tools (0.5 mm diameter) and helicoidal tool paths, generated by the CAM software, were adopted. To ensure the required accuracy roughing operations were followed by semi-finishing and finishing operations, using for this latter fresh end mills.

Parameter	A	B	C	D
Incremental Depth [mm]	0.0008	0.001	0.0015	0.002
Frontal Gap [mm]	0.002	0.0025	0.003	0.005
Frequency [Hz]	180	140	130	90
Current [A]	100	100	50	80
Voltage [kV]	90	100	130	150
Gain	230	350	1500	1000

Table 6.2: Combinations (A, B, C, D) of μEDM machining parameters adopted to generate different mold topographies.

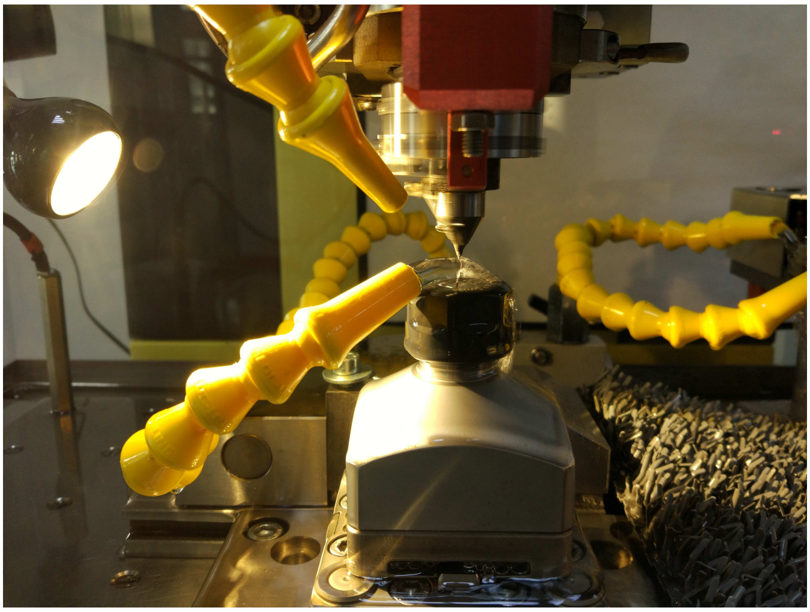

Figure 6.3: μEDM-milling of the mold cores.

6.1.2.2 *Micro electro discharge machining*

The study of ejection friction was then further investigated considering mold surfaces generated by means of μEDM. Different tribological conditions were investigated by considering different mold roughness values and by molding different polymers.

In order to study the effects of μEDM mold topography on ejection friction, four different sets of mold cores (each one comprising six units) were machined by means of micro electro discharge machining (μEDM – Sarix, SX-200) in order to obtain different surface roughness.

Mold cores were realized starting from commercial 0.8 mm diameter ejector, which were first cut to the proper length and then side-milled to reduce their diameter to a nominal value of 0.4 mm. The machining operations were carried out using a tungsten carbide electrode (diameter: 0.3 mm), which was moved around the workpiece with a constant step-down movement and with fixed incremental depth.

Width μs	Frequency kHz	Current index -	Voltage V	Gap index -	Energy index -
2	180	100	90	74	13

Table 6.3: Process parameters adopted in μEDM machining.

The side μEDM-milling operations were carried out by varying machining and discharge parameters, in order to obtain different mold topographies. Table 6.2 reports the different combinations (A, B, C, D) of μEDM machining parameters that were selected for the operations. The different combinations allowed the generation of different intensities of the discharge impulse, which then generates the spark between the electrode and the workpiece. Changing the parameters from combination to D, to C, to B, to A, the discharge impulse decreases its intensity leading to lower material removal rate and thus improved surface finish.

6.1.2.3 *Comparison*

In order to identify the parameters that most appropriately correlate differently generated mold topographies to the ejection force, two cavity surfaces having similar value of *Ra* were produced by micro milling and micro EDM, respectively.

Considering the design of the mold cavity presented in subsection 5.1.2 as *MOLD B*, two different sets of mold cores were realized by means of micro milling (μM – Kugler, Micromaster 5X) and micro electro discharge machining (μEDM – Sarix, SX-200), respectively. Each set comprised six mold cores machined with either μM or μEDM. The cutting strategies adopted for the two processes were optimized through preliminary tests to obtain similar value of *Ra* for both sets of mold cores.

Micro milling operations were performed using ball nose tools (Kyocera, 1625) with a 0.7 mm cutting diameter (D_{cap}). The cutting speed (v_c) was set at 60.5 m/min, with a feed per tooth (f_z) of 0.01 mm. A constant step-down approach with an axial depth of cut (a_p) of 0.07 mm was adopted to machine the cores.

The same machining strategy was adopted for the μEDM process, using a tungsten carbide electrode with 300 μm diameter and an incremental depth fixed at a constant value of 0.8 μm. Table 6.3 reports the process parameters used for the μEDM process. The electrode wear was compensated with the linear method, i.e. by feeding it into the work piece after it has travelled a certain distance along the tool path.

Insert	Coating	Coating Thickness [μm]
A	-	-
B	ALD	0.02÷0.05
C	DLC	0.5÷5
D	SiOx	0.5÷5

Table 6.4: Main characteristics of the selected mold surface coatings.

6.2 SURFACE MODIFICATION

Mold surface coatings are nowadays a common solution in the injection molding industry; specifically they are widely employed to improve the resistance of mold surface to wear. In fact, polymers characterized by marked adhesion properties can damage the surface of the mold leading to the necessity for periodic polishing of the worn surfaces. In this work, the use of mold surface coatings is proposed aiming at:

- reducing the drag of polymer melts in thin-wall cavities;
- reducing the ejection friction.

6.2.1 *Coatings selection*

The analysis of the effects of mold surface coatings on the filling flow was carried out considering three consecutive experimentations. At first, a general characterization of the effects of mold surface coatings on the melt flow resistance was carried out in order to understand the phenomena that might influence the tribological interaction at the polymer/mold interface (*Investigation I*). Then, another experimental campaign was carried out in order to further investigate the physical phenomena that control the filling resistance (*Investigation II*).

In this section, the different mold surface coatings that were selected for the injection molding investigations are presented. All the considered coatings are commercial products that are already available on the market, but their effects on the injection molding process are unknown or just speculated.

6.2.1.1 *Investigation I*

Three different mold surface coatings technologies were selected according to their tribological and thermal properties: (i) atomic layer deposition (ALD) of Al_2O_3, (ii) diamond like carbon (DLC) and (iii) plasma-enhanced chemical vapor deposition (PECVD) of SiO_x (Table 6.4).

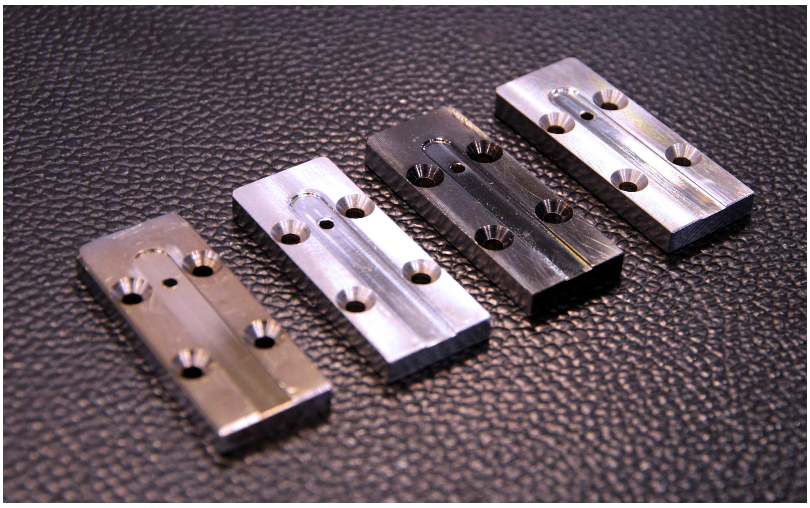

Figure 6.4: Coated mold insert used for the characterization of the melt flow resistance.

Property	Test Method	DLC v01	DLC v02	CrN	CrTiNbN
Coating thickness [μm]	UNI 1071 – 2	2.0 ± 0.5	2.0 ± 0.5	2.5 ± 0.5	3.0 ± 0.5
Adhesion [N]	UNI 1071 – 3	55 ± 4	55 ± 4	80 ± 5	80 ± 5
Hardness [HV]	IOS 14577 – 1	2200 ± 300	2200 ± 300	2050 ± 300	2973 ± 263
Friction coefficient	ASTM G99 – 04	0.15 ± 0.05	0.15 ± 0.02	0.60 ± 0.05	0.65 ± 0.05
Adhesion layer	-	Cr	CrN	Cr	Cr

Table 6.5: Main properties of the selected mold surface coatings.

6.2.1.2 *Investigation II*

Three different types of mold surface coatings were selected according to their tribology, hardness and thermal properties: (i) diamond like carbon (DLC), (ii) chromium nitride (CrN) and (iii) chromium titanium niobium nitride (CrTiNbN). All the coatings were deposited by means of Plasma Assisted – Chemical Vapor Deposition (PA-CVD). The use of two distinct adhesion layers allowed the deposition of two different DLC coatings. Table 6.5 reports the main properties of the selected coatings.

The surface coatings were deposited onto polished mold inserts (*Sa* < 0.2 μm before deposition) made of hardened and tempered H13 chromium-molybdenum steel, having a hardness of approximately 50 HRC.

In order to isolate the effects of surface coatings on the melt flow resistance, the surface roughness of the mold inserts was analyzed at five locations over the coated area by means of laser confocal mi-

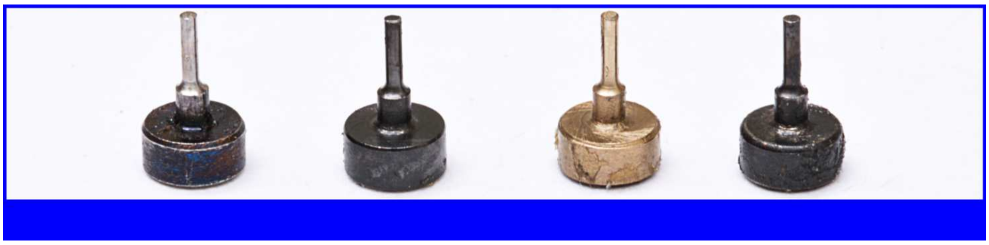

Figure 6.5: Coated mold insert used for the characterization of the ejection force.

croscopy (Olympus, LEXT OLS4100). The average values of the surface roughness (*Sa*) evaluated on the different mold inserts were in the range 30 to 50 nm. Thus, for the purpose of the current investigation, the topography of the mold inserts was considered comparable and possible effects of surface roughness on the melt flow resistance were neglected.

The geometry of the coated inserts, assembled into the fixed and moving mold halves, was characterized considering form errors and depth uniformity of the coated channel, in order to avoid any significant geometrical difference among the channels.

The effects of the same coatings were also considered to study the ejection phase. In particular, Figure 6.5 shows the coated mold cores that were used for the characterization of the effects of mold surface modification on the demolding phase.

7

METROLOGY AND POLYMERS CHARACTERIZATION

The surfaces of the mold cavities, which were either generated with different machining processes or modified using coatings, were thoroughly characterized using different inspection technologies and instrumentations that are presented in this chapter.

7.1 OPTICAL PROFILOMETRY

The surface texture of mold surfaces was characterized using a 3D optical profiler (Sensofar, Plu Neox) operating in confocal mode with a 20X objective. Table 7.1 reports the main characteristics of the profiler, which is shown in Figure 7.1.

7.1.1 *Roughness measurements*

For the cylindrical cores, in order to evaluate the texture of the machined surfaces, the topography of each core was acquired considering four projected areas of 1.5 mm x 85.5 μm, evenly distributed on the lateral surface in the circumferential direction (Figure 7.2). Three roughness profiles (1.2 mm long) were extracted along the ejection direction for each one of the acquired areas and the shape error was removed using a polynomial fitting. Then, for each profile, several roughness parameters were evaluated applying the appropriate Gaussian filter according to ISO 4287 and ISO 13565-2 standards [143, 144]. The selection of different Gaussian filters for different mold topographies was made following the different indications provided by the standards for periodic (e.g. μM) and aperiodic profiles (e.g. μEDM).

For flat surfaces, as those used for the study of the filling phase that are presented in subsection 5.1.1, roughness characterization consid-

	20X	100X
Numerical aperture	0.45	0.90
Maximum slope (deg.)	21	51
Field of view (μm)	636 x 477	127 x 95
Spatial sampling (μm)	0.83	0.17
Optical resolution (μm)	0.31	0.15
Vertical resolution (nm)	< 20	< 2

Table 7.1: Main characteristics of the 3D optical profiler.

Figure 7.1: 3D optical profiler used for the surface characterization.

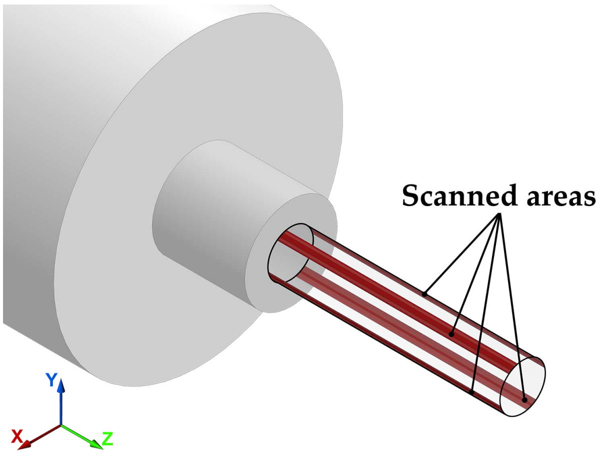

Figure 7.2: Schematics of cores characterization [139].

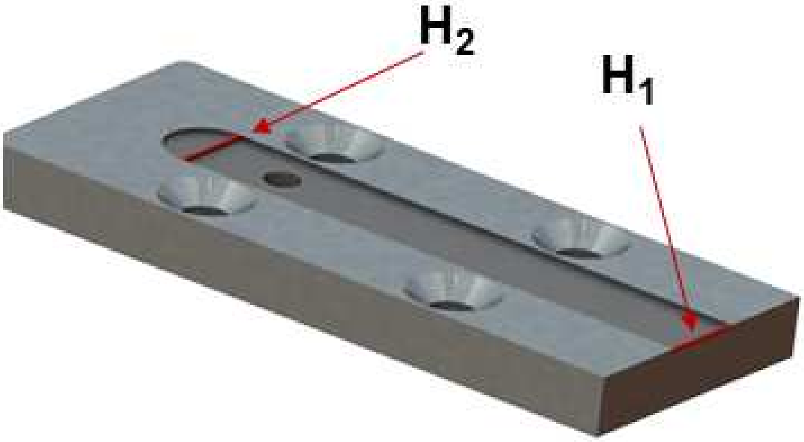

Figure 7.3: Geometrical characterization performed on

ered surface roughness parameters. Surface roughness of the mold inserts was analyzed at five locations over the treated area.

7.2 SCANNING ELECTRON MICROSCOPY

The qualitative inspection of the treated surfaces was carried out by means of scanning electron microscopy (SEM - FEI, Quanta 400). SEM analysis allowed the comparison of different mold topographies and the evaluation of treatments quality.

In general, before SEM characterization, the mold inserts were cleaned using ultrasound with a cleaning solvent for 5 minutes. Then, the SEM micrographs of the inserts surfaces were obtained with an acceleration voltage of 20 kV, a working distance of about 18 mm and a secondary and back-scattered electron detector (Everhart-Thornley detector - ETD).

7.3 GEOMETRICAL CHARACTERIZATION

The geometry of the inserts used to study the filling phase was characterized considering form errors and depth uniformity of the treated channel, in order to avoid any significant geometrical difference among the channels. The dimensions of the channels were measured in two different positions (i.e. H_1, H_2), as shown in Figure 7.3.

For the mold inserts used to study the demolding force, in order to isolate the effect of core treatments on the ejection force from other possible geometrical differences, the cores were analyzed using a metrological X-ray Computed Tomography (CT) system (Nikon Metrology, MCT 225). Both the diameters and the geometrical errors of the cores were evaluated by fitting least squares cylinders on the

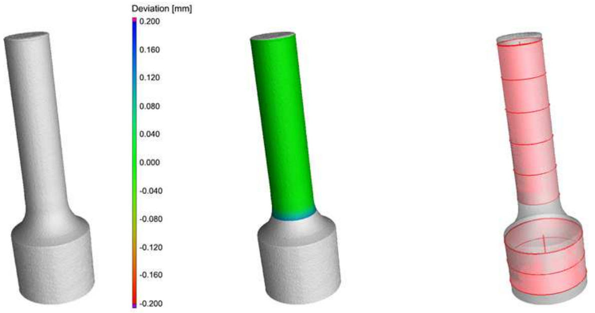

Figure 7.4: Geometrical characterization performed on mold cores using x-ray Computed Tomography.

3D volumetric dataset, as shown in Figure 7.4. The results of the measurements indicated that the average diameters of the cores had standard deviations of about 3 μm. Moreover, the average deviation from the cylindrical shape was about 10 μm, with a standard deviation of 2 μm.

7.4 INJECTION MOLDING POLYMERS

The experimental investigations carried out in this work involved different type of injection molding polymers. The different materials were used according to the specific objectives of the investigation and considering the final application of the related case study. This section describes the polymers that were selected for each application and the methodologies that were applied for their characterization.

7.4.1 *Rheological characterization*

In this work, the rheological properties of polymers considered for the injection molding experiments were characterized. A complete characterization was performed for the following reasons:

- the knowledge of the rheological properties allowed comparison of different polymers, which could be useful to understand the phenomena occurring during the injection molding process;
- the data from the rheological characterization were implemented in calibrated numerical simulation software.

The rheological properties of the selected polymer were characterized using a rotational rheometer (TA Instruments, ARES) and a capillary rheometer (Ceast, Rheo 2500). In order to determine the dependence of viscosity to temperature, the tests were conducted at different temperatures. With the rotational rheometer, measurements were performed for increasing values of the shear rate, in the 0.1 to 100 s^{-1} range. The pseudo plastic region of the flow curve was characterized

Polymer	LDPE	PP	PS
Structure	Crystalline	Crystalline	Amorphous
Density [g/cm^3]	0.918	0.905	1.05
Transition temperature [°C]	105	165	100
Melt Flow Index (g/10 min)	70	16	12
	190°C - 2.16 kg	230°C - 2.16 kg	200°C - 5 kg

Table 7.2: Main properties of polymers injection molded over nanostructured tools.

using a capillary rheometer (from 50 to 5,000 s^{-1}); two different dies were mounted to apply the Bagley correction. The Rabinowitch correction was also applied to substitute the hypothesis of Newtonian fluid with a Power-Law.

The Cross-WLF model was used to fit the rheological data. Specifically, the Cross model was used to describe the shear rate dependence of polymer melt viscosity on the whole range of variation of the shear rate:

$$\eta(\dot{\gamma}) = \frac{\eta_0}{1 + \left(\frac{\eta_0}{\tau^*}\dot{\gamma}\right)^{1-n}} \tag{7.1}$$

where $\eta(\dot{\gamma})$ is the the viscosity as a function of the shear rate, and η_0, τ^*, n are coefficients.

The effects of temperature on viscosity was accounted by means of the William-Landel-Ferry (WLF) model:

$$\eta_0 = D_1 \exp\left(\frac{-A_1(T - T^*)}{A_2 + (T - T^*)}\right) \tag{7.2}$$

$$T^* = D_2 + D_3 \cdot P \tag{7.3}$$

$$A_2 = \tilde{A}_2 + D_3 \cdot P \tag{7.4}$$

where D_1, D_2, D_3, A_1 and $\tilde{A}_2$ are constants to be determined, while T^* is a reference temperature.

7.4.2 *Polymer selection*

7.4.2.1 *Filling phase*

The characterization of the filling phase was carried out considering different polymers for different investigations. Specifically, the effects of surface generation (i.e. Laser Induced Periodic Surface Structures - LIPSS) were characterized considering three different commodity polymers. Conversely, the effects surface modification comprised the selection of different polymers in agreement with the approach to the three investigations introduced in subsection 6.2.1.

Property	Unit	Test Method	PS	PET
Density	g/cm^3	ISO 1183-2:2004	1.04	1.33
Melt Flow Index (200 °C – 5 kg)	g/10min	ISO 1133-1:2011	12	6
T_g (10 °C/min)	°C	ISO 11357-2:2013	100	80

Table 7.3: Main properties of the tested polymers.

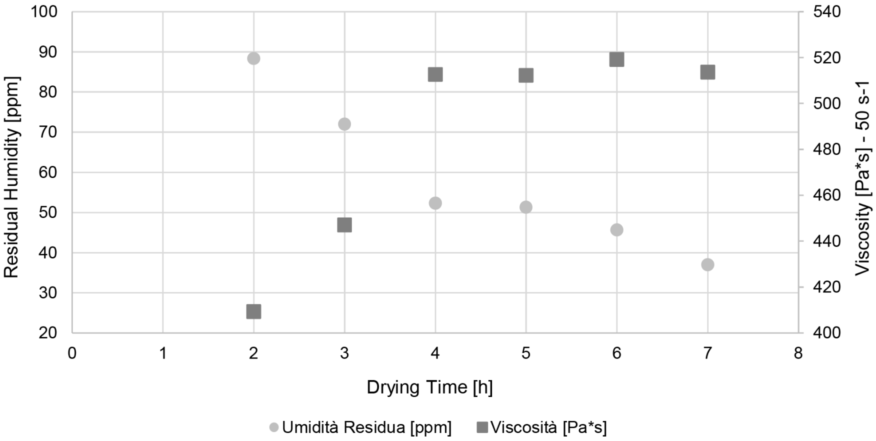

Figure 7.5: Residual humidity and Newtonian viscosity for PET as a function of the drying time.

SURFACE GENERATION The effects of nano-structures generated on the mold surface were investigated considering three different commodity polymers:

- low-density polyethylene (LDPE) - Total, LDPE 1700 MN18C;
- polypropylene (PP) - Total, PPC 7642;
- polystyrene (PS) - Total, PS Crystal 1540.

Table 7.2 reports the main properties of the selected polymers.

SURFACE MODIFICATION - *investigation i* **AND** *investigation ii* An amorphous polystyrene (PS, Total PS Crystal 1540) and a semi-crystalline polyethylene terephthalate (PET, Cepsa PET SR08) were considered for *Investigation I*. Indeed, PET is a polymer that is really widespread due to its use for the manufacturing of plastics bottles preforms, as discussed in subsection 1.3.2. On the other hand, PS is a commodity polymer that have been finding large diffusion in micro injection molding applications and for packaging products. Table 7.3 reports the main properties of the selected polymers.

The rheological characterization for both the materials was performed by means of rotational and capillary rheometers as described in subsection 7.4.1. However, for PET particular attention was given to the design of the drying process. The adsorbed moisture, and its influence on the Newtonian viscosity, was related to the drying time by

Material	Crystal 1540	Ultraform H2320	5013L-10
Structure	Amorphous	Crystalline	Amorphous
Density [g/cm^3]	1.04	1.4	1.02
Transition temperature [°C]	100	145	134
Melt Volume Rate [cm^3/10 min]	11.5 (200 °C - 5 kg)	2.9 (190 °C - 2.16 kg)	48 (260 °C - 2.16 kg)

Table 7.4: Main properties of the polymers selected for the molding experiments used to characterized the ejection phase.

measuring the residual humidity using a moisture meter (Brabender, Aquatrac). The results of the characterization, shown in Figure 7.5, indicate that a drying cycle of 8 hours at 180 °C produced a residual humidity smaller than 40 ppm. Thus, drying cycles were performed for the PET at 180 °C for 8 hours, with a dew point of - 45 °C. Drying was performed using a Moretto X Dry Air X White dehumidifying drier.

7.4.2.2 *Ejection phase*

SURFACE GENERATION Three commercial polymers were selected to experimentally characterize the effects of surface generation on the demolding phase: polystyrene (PS – Total, Crystal 1540), cyclic olefin copolymer (COC – Topas, 5013L-10) and polyoxymethylene (POM – Basf, Ultraform H2320). The materials were selected due to their wide use in micro injection molding (μIM) applications. In particular, PS and COC are commonly used for medical applications, because of their good biocompatibility and transparency, while POM is generally used for micro mechanical injection molded parts. Table 7.4 reports the main properties of the selected polymers.

For each polymer, the viscosity was measured at the value of the melt temperature set in the injection molding machine; i.e. 240 °C for PS, 305 °C for COC and 235 °C for POM. Figure 7.6 shows the Cross-WLF model for the three polymers, indicating that COC has a lower melt viscosity than PS and POM, which has the highest viscosity.

The mechanical properties of the selected polymer were characterized as a function of the mold temperature by means of dynamical mechanical analysis (DMA). The tests were carried out using a dynamical mechanical analyzer (TA Instruments, Q800) with a 3-point deformation mode. Rectangular injection-molded samples (10 mm wide, 47 mm long and 1.5 mm thick) of the three selected polymers were used to characterized the storage modulus from room temperature up to 100 °C. The results of the characterization are reported in Figure 7.7. It can be observed that the storage modulus (E') of PS is characterized by the steep decrease of its mechanical properties around its glass transition temperature (i.e. 100 °C). Conversely, COC

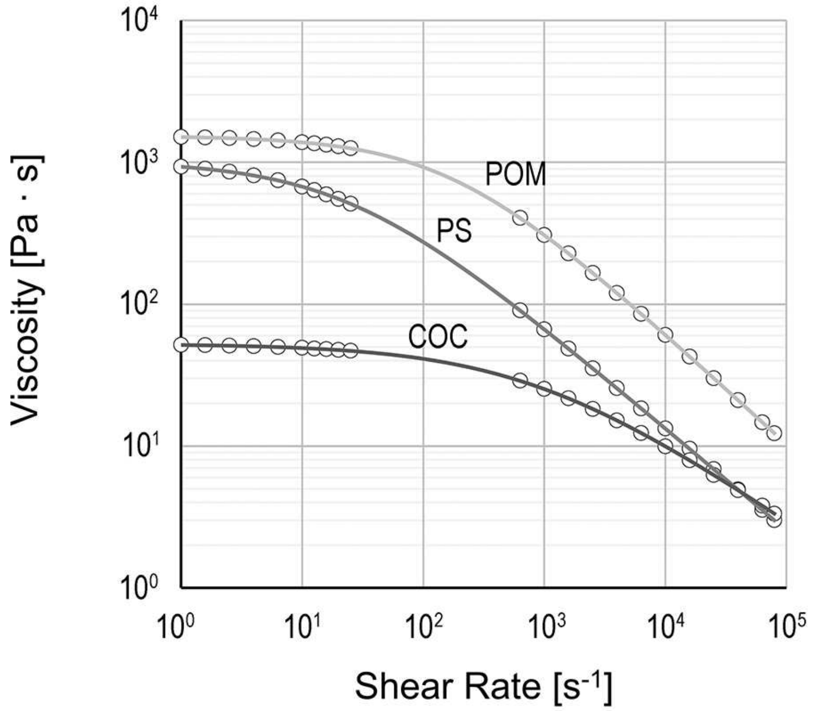

Figure 7.6: Rheological properties of the selected polymers (PS, COC, POM) at their specific melt temperature.

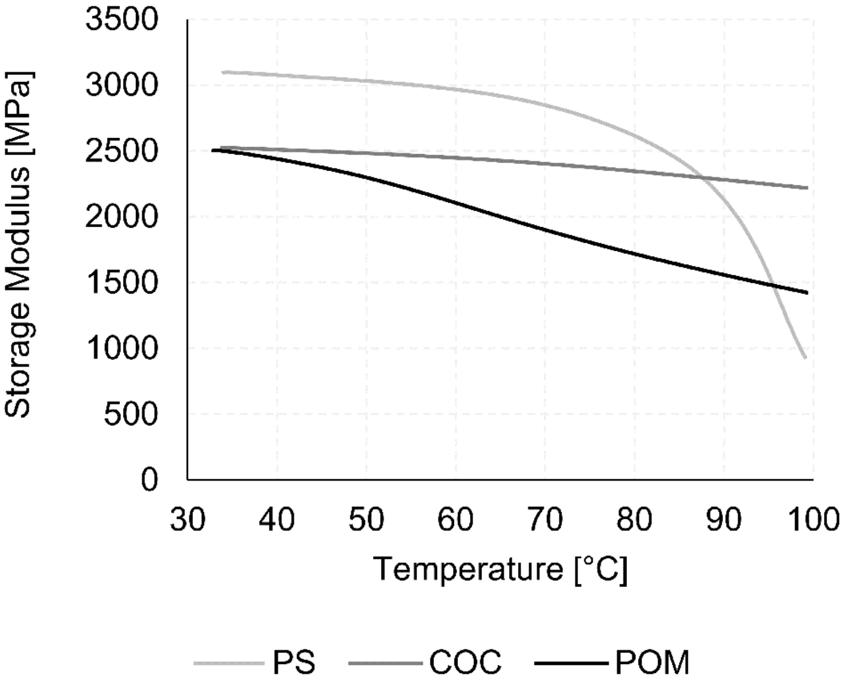

Figure 7.7: Storage modulus as a function of the mold temperature for the three polymers.

Material	Crystal 1540	Ultraform H2320	Ultramid A4H
Structure	Amorphous	Crystalline	Crystalline
Density [g/cm^3]	1.04	1.4	1.13
Transition temperature [°C]	100	145	230
Melt Volume Rate [cm^3/10 min]	11.5 (200 °C - 5 kg)	2.9 (190 °C - 2.16 kg)	35 (275 °C - 5 kg)

Table 7.5: Main characteristics and properties of the polymers selected for the molding experiments.

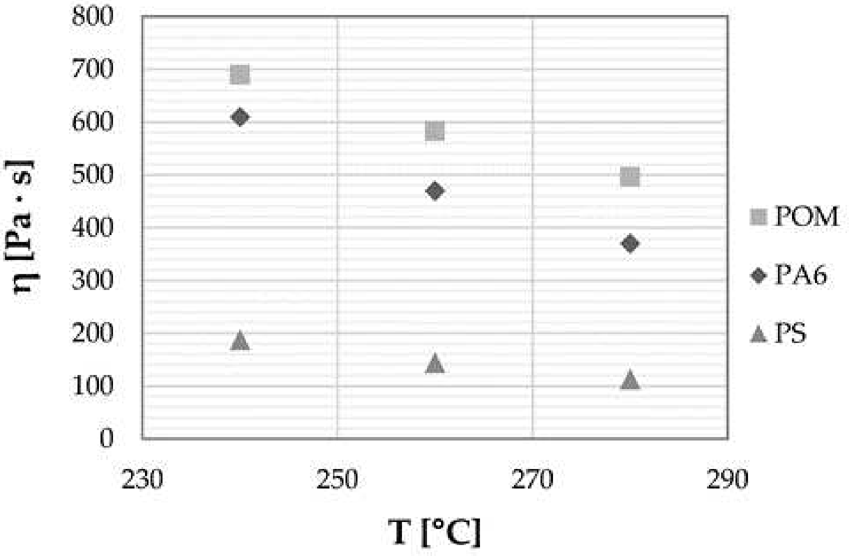

Figure 7.8: Different sensitivity of the selected polymers to temperature variations.

and POM exhibited a constant decrease of the storage modulus for increasing temperature.

SURFACE MODIFICATION Three commercial injection molding grade polymers were selected for the injection molding experiments: polystyrene (Total, PS Crystal 1540), polyoxymethylene (Basf, POM Ultraform H2320) and polyamide 66 (Basf, PA66 Ultramid A4H). Table 7.5 reports the main properties of the three polymers.

The viscosity of the three polymers was compared for a fixed shear rate value of 200 s^{-1}, for different temperatures. Figure 7.8 shows that PS has a markedly lower viscosity compared to POM and PA66. Hence, the capabilities of PS of replicating the topography of the mold surface are higher compared to that of the other polymers.

8

OFFLINE CHARACTERIZATION

The experimental procedures presented in the previous chapter for the characterization of the tribological properties of mold surface treatments were all based on injection molding experiments. However, despite their great accuracy with respect to the reality of industrial injection molding manufacturing environments, they are not easy and quick to setup for new treatments. In this chapter, a different approach is to the characterization of the effects of mold surface treatments. Specifically, offline characterization methods are proposed as they could offer an easy approximation of the injection molding tests, and they could constitute the instrument to be used for a quick screening of different treatments when at first approaching their selection. Indeed, very little knowledge is available in the industry and in the literature regarding the selection of mold surface treatment for a specific polymer.

8.1 WETTING CHARACTERIZATION

The wetting behavior of the surface coatings to the molten polymers was evaluated by measuring the contact angle of a melting cylindrical polymer sample Figure 8.1. According to Lee et al., the wetting properties of the coatings were evaluated at the melt temperature adopted for the injection molding experiments [146]. The experimental setup used for the wettability experiments included electrical heating of an insulated chamber, a light source and a high-speed camera Figure 8.2.

The tests were performed by (i) heating the chamber up to the test temperature, (ii) inserting the coated surface sample and (iii) recording the wetting behavior of the melting polymer for 10 minutes, as suggested by Sorgato et al. [31].

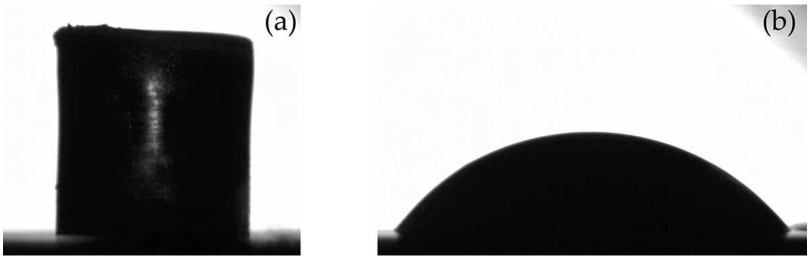

Figure 8.1: Example of a cylindrical polymer sample before melting (left) and of a melt drop of polymer melt during the wetting test (right).

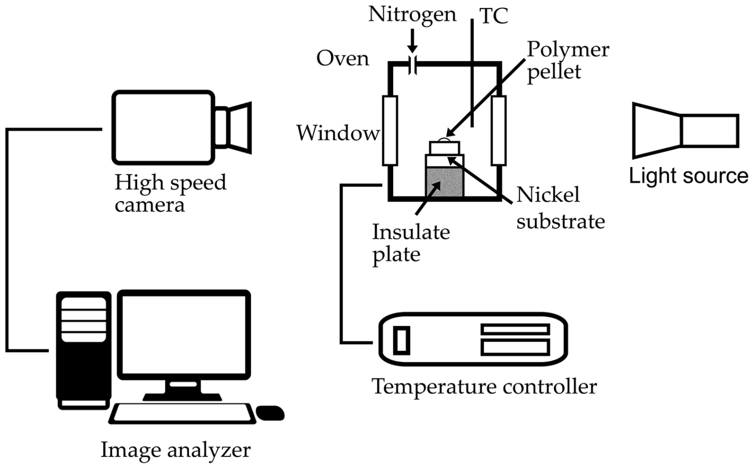

Figure 8.2: Schematics of the experimental setup used for the characterization of the wetting properties of melt polymers [145].

Images of the melting polymer sample were collected every 90 s using a 25X magnification lens. The contour of the melt polymer drop was defined by fitting the base line with a straight line and the curved profile with an ellipse. Then, the left and right contact angles were then calculated at the intersection points.

8.2 FRICTION TESTING

The tribological properties of the different coatings were evaluated, for all the selected molding polymers, using an offline friction test. The static friction coefficient (μ_s) was evaluated from the sliding of a coated flat sample over an injection molded polymer plate.

Figure 8.3 shows the schematics of the experimental setup that was designed for the characterization of the friction properties of a specific polymer/coating interface. The tests were realized using a tribometer (Cetr, UMT-3), a load cell (0-1000 N) mounted on its upper part and a supporting steel block mounted on its lower slider. In order to favor the adhesion between the coated surface and the polymer, an infrared light (IR light) was used to heat the polymer substrate before the application of the normal load. The coated samples were mounted on the upper part of the tribometer, connected to the load cell, using a 3D printed support. Conversely, the polymer sample was fixed on a slot machined on the lower steel block. Figure 8.5 displays the details of the friction testing apparatus, with indication of the coated surface and of the polymer sample.

The offline characterization of the friction properties of the three selected polymers with the different coatings was carried out with the following procedure:

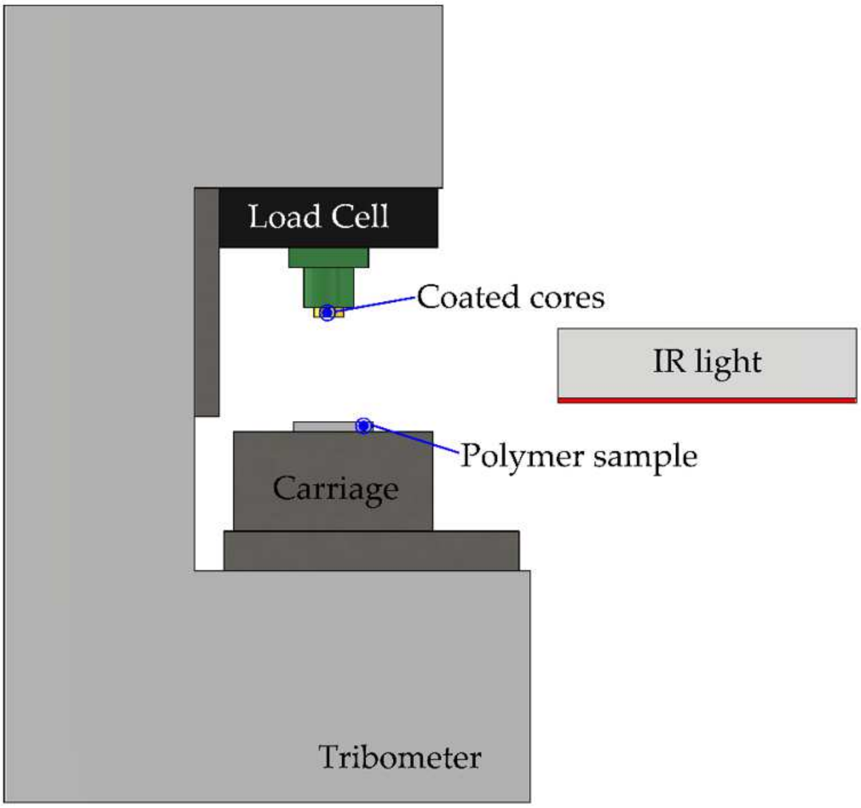
Load Cell
Coated cores
IR light
Polymer sample
Carriage
Tribometer

Figure 8.3: Schematics of the experimental setup designed to characterize the friction properties of the polymer/coating interface.

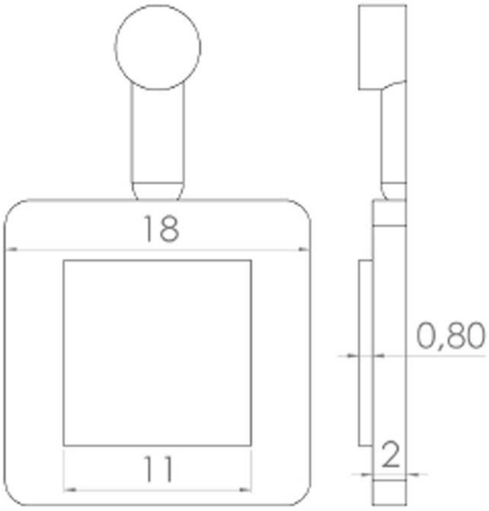

Figure 8.4: Design of the polymer sample used for the friction testing.

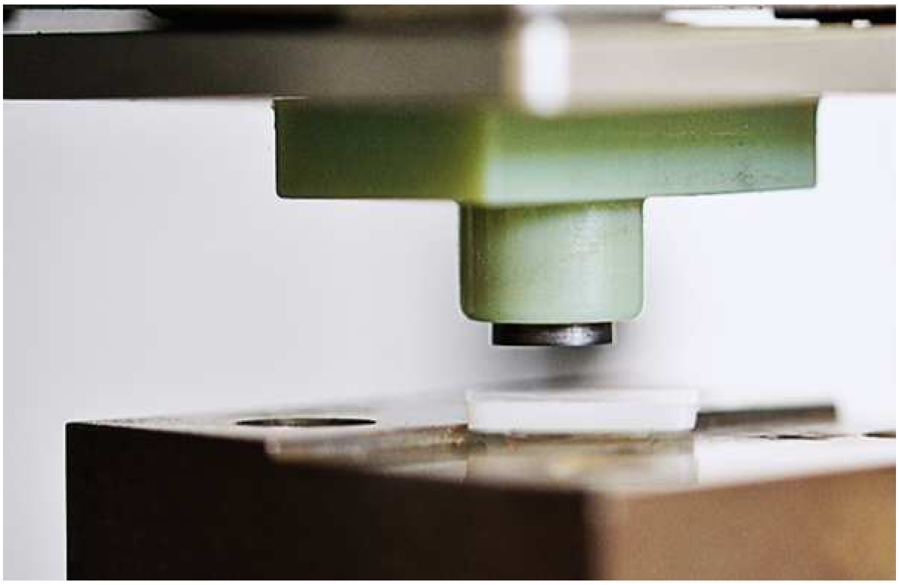

Figure 8.5: Friction testing setup - details of the coated and polymer surfaces.

i. Positioning of the polymer sample (cf. Figure 8.4) on the base steel block;

ii. Heating of the polymer sample with the IR light (the heating was calibrated to allow the polymer the time to reach a temperature of 10°C above the glass transition temperature of each polymer;

iii. Application of the normal load (F_N) for 20 seconds;

iv. Movement of the slider and acquisition of the tangential force (F_T) with the upper load cell;

v. Evaluation of the friction as the coefficient of linear regression in the plot of the tangential force against the normal force (i.e. Amontons law):

$$F_N = \mu \cdot F_T \tag{8.1}$$

Part III

SURFACE GENERATION

9

EFFECT OF LASER-INDUCED PERIODIC STRUCTURES ON THE FILLING PHASE

In injection molding, elevated pressures are required to fill the mold cavity, due to the high viscosity of thermoplastic polymers, the reduced thickness of the cavity and the low mold temperature. A significant pressure reduction can be achieved by inducing a slip of the polymer melt over the mold surface, which, as discussed in section 2.3, occurs within the first monolayer of macromolecules adsorbed at the wall.

As discussed in chapter 2, several researchers have reported the effects of surface roughness on the filling flow in injection molding. This effect was observed only for very thin injection molding cavities (i.e. below 150 μm). However, these studies (cf. [53, 54]) considered mold surfaces characterized by roughness values in the range of several micrometers (e.g. $40 \div 80$ μm). For these reasons, in this work the effect of conventional machining processes (i.e. micro milling and micro electro discharge machining) were not considered as they would produce micro-scale roughness values.

In this work, the effect of nano-scale roughness on the filling flow was studied. Indeed, Laser-Induced Periodic Surface Structures were generated on the mold surface by means of femto-laser treatment. The effects of the ripples on the filling flow were characterized by means of injection molding experiments carried out using a cavity thickness higher than the limit value observed in the literature.

9.1 EXPERIMENTAL APPROACH

The effects of the different LIPSS treatments were investigated by means of injection molding with different polymers (PS, PP, LDPE - cf. subsubsection 7.4.2.1) and by selecting different combinations of injection molding parameters. The injection molding parameters

	Polymer		
Parameter	PS	PP	LDPE
Melt Temperature [°C]	240	240	230
Mold Temperature [°C]	60,80,120		
Injection Speed [mm/s]	50,100,200,300,400,500,600,750		

Table 9.1: Process parameters considered for the characterization of the effects of LIPSS treatments.

	Level			
Parameter	1	2	3	4
Laser Treatment	untreated	*Laser 1*	*Laser 2*	*Laser 3*
Mold Temperature [°C]	60	80	120	
Injection Speed [mm/s]	100	300	750	

Table 9.2: Experimental DoE plan designed for the molding experiments.

that were varied during the experiments are the mold temperature (60÷120°C) and the injection speed (50÷750 mm/s). Table 9.1 reports the parameters that were varied during the experiments.

The injection molding experiments were carried out following the Design of the Experiment approach. For each one of the selected polymers, a general full factorial design was carried out considering variations of mold surface LIPSS treatment, mold temperature and injection speed. Table 9.2 reports the DoE plans carried out for each polymer.

In order to achieve an adequate stability of the injection phase, 20 molding cycles were performed before the acquisition of the cavity pressure. For each molding condition 10 acquisitions were collected, one every 5 cycles.

The melt flow resistance was then evaluated considering cavity pressure measured using a pressure sensors placed close to the injection location. In fact, the pressure measured in the cavity channel represents the pressure drop characterizing the mold cavity, which was selected as the response variable for the analysis.

9.2 LIPSS CHARACTERIZATION

9.2.1 *SEM analysis*

The mold surfaces generated with LIPSS were initially characterized by means of SEM, showing that the different inserts (i.e. *Laser*1, *Laser*2, *Laser*3) are characterized by diverse surface topographies. In particular, the ripples are oriented along the flow direction for *Laser* 1, while they are similar but opposed to the flow for *Laser*2. Nano structures are different for *Laser*3, where they are crossed and no significant directionality could be identified. The SEM analysis of the mold surfaces also indicated overall good homogeneity and the absence of defects for the whole laser treated surfaces.

9.2.2 *Topography characterization*

The topography of the LIPSS surfaces was further characterized by means of Atomic Force Microscope (AFM - Veeco Digital Instruments,

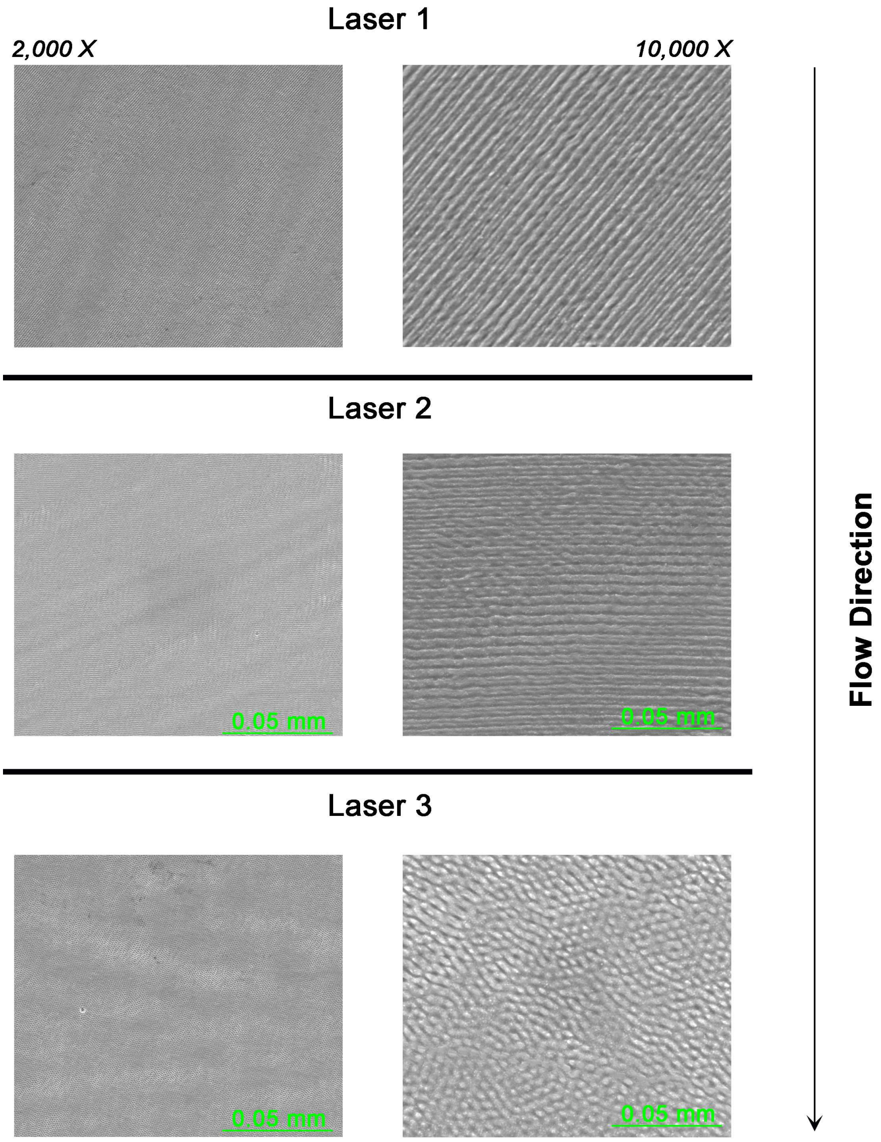
Laser 1
2,000 X
10,000 X
Laser 2
0.05 mm
0.05 mm
Laser 3
0.05 mm
0.05 mm
Flow Direction

Figure 9.1: SEM micrographs of the LIPSS treated mold surfaces.

	Pitch [nm]		Width [nm]		Depth [nm]	
Treatment	Avg. Val.	Std. Dev.	Avg. Val.	Std. Dev.	Avg. Val.	Std. Dev.
Laser 1	742	134	784	82	87	38
Laser 2	791	104	758	145	89	23
Laser 3	747	100	759	54	109	13

Table 9.3: AFM measurements of LIPSS mold surfaces.

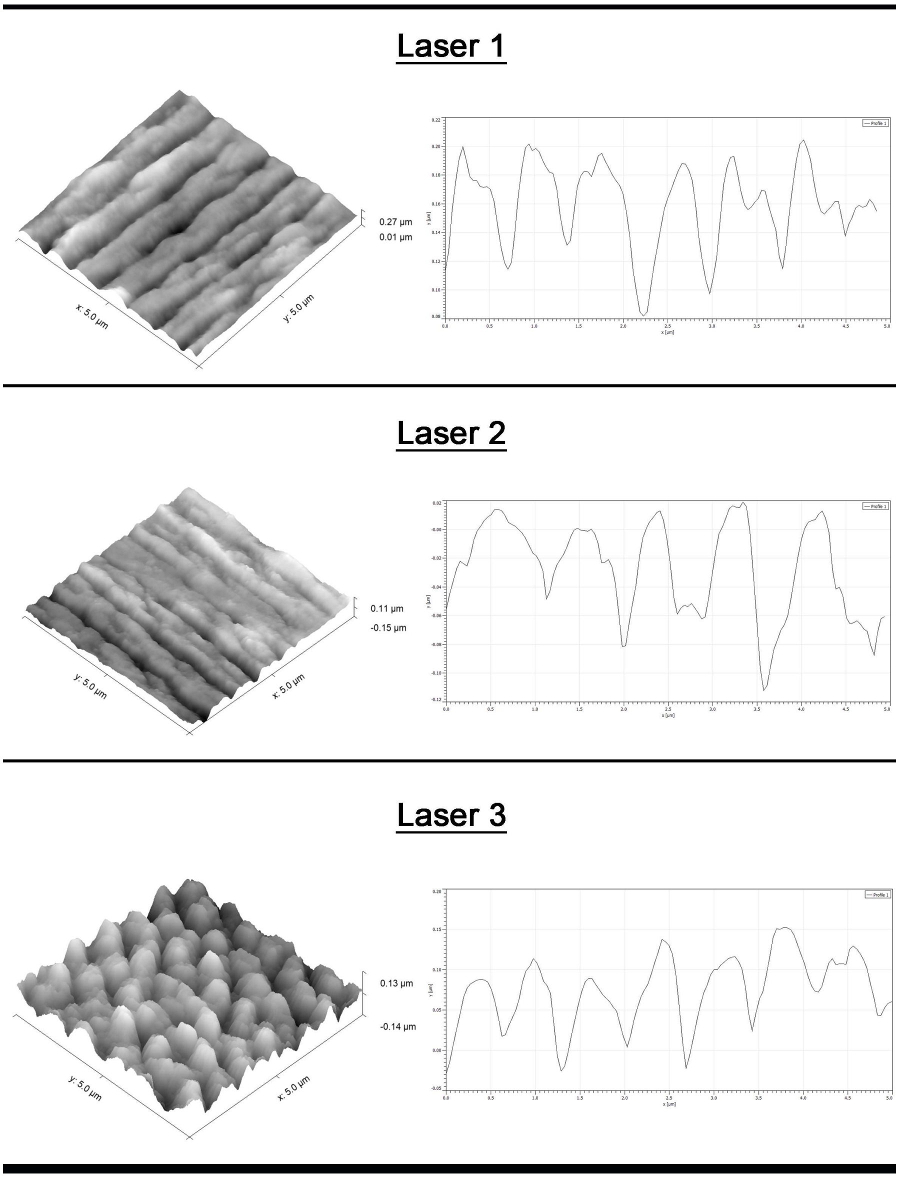

Figure 9.2: 3D topographies and profiles of the three differently treated LIPSS surfaces.

	P-Value		
Source	PS	PP	LDPE
Treatment	0.000	0.000	0.000
Injection Speed	0.000	0.000	0.000
Mold Temperature	0.002	0.000	0.000
Treatment · Injection Speed	0.000	0.000	0.000
Treatment · Mold Temperature	0.000	0.000	0.000
Injection Speed · Mold Temperature	0.000	0.000	0.000

Table 9.4: Analysis of variance for the DoE plans.

CP II), which was used to reconstruct the topography of the mold surface. The characterization was performed was performed using a sharp tip with a diameter of 4 μm. Figure 9.2 displays the3D topographies and the profiles acquired for the nano-structured surfaces.

Table 9.3 reports the results of the AFM characterization performed on the different LIPSS surfaces. The pitch, the width and the depth of the ripples generated on the steel surfaces were measured. The analysis showed no significant dimensional difference among the different mold surfaces. Indeed, the surfaces were realized using the same laser processing parameters, thus no difference was expected. The main difference between *Laser*1 and *Laser*2 mold inserts is the relative directionality to the melt flow, while *Laser*3 is characterized by the absence of directionality.

9.3 INJECTION MOLDING RESULTS

9.3.0.1 *Analysis of the factorial experiments*

Table 9.4 reports the results of the Analysis of Variance (ANOVA) performed, with a General Linear Model, on the factorial plans designed for each one of the polymers selected for the injection molding experiments. In order to determine the statistical significance of each factor and interaction, the P-value was used with a threshold value of 0.05. The results of the ANOVA indicate that, for all the polymers, all the factors included in the model resulted significant (P-value $<$ 0.05). The factors having P-value lower than 0.05 can be considered statistically significant on the response variable (i.e. cavity pressure).

9.3.1 *Effects of laser treatments*

The effects of changing the laser treatment resulted significant, regardless of polymer selection. However, the effects are not consistent among the different polymers. Thus, it can be supposed that the interaction between the polymer and the substrate is crucial for the

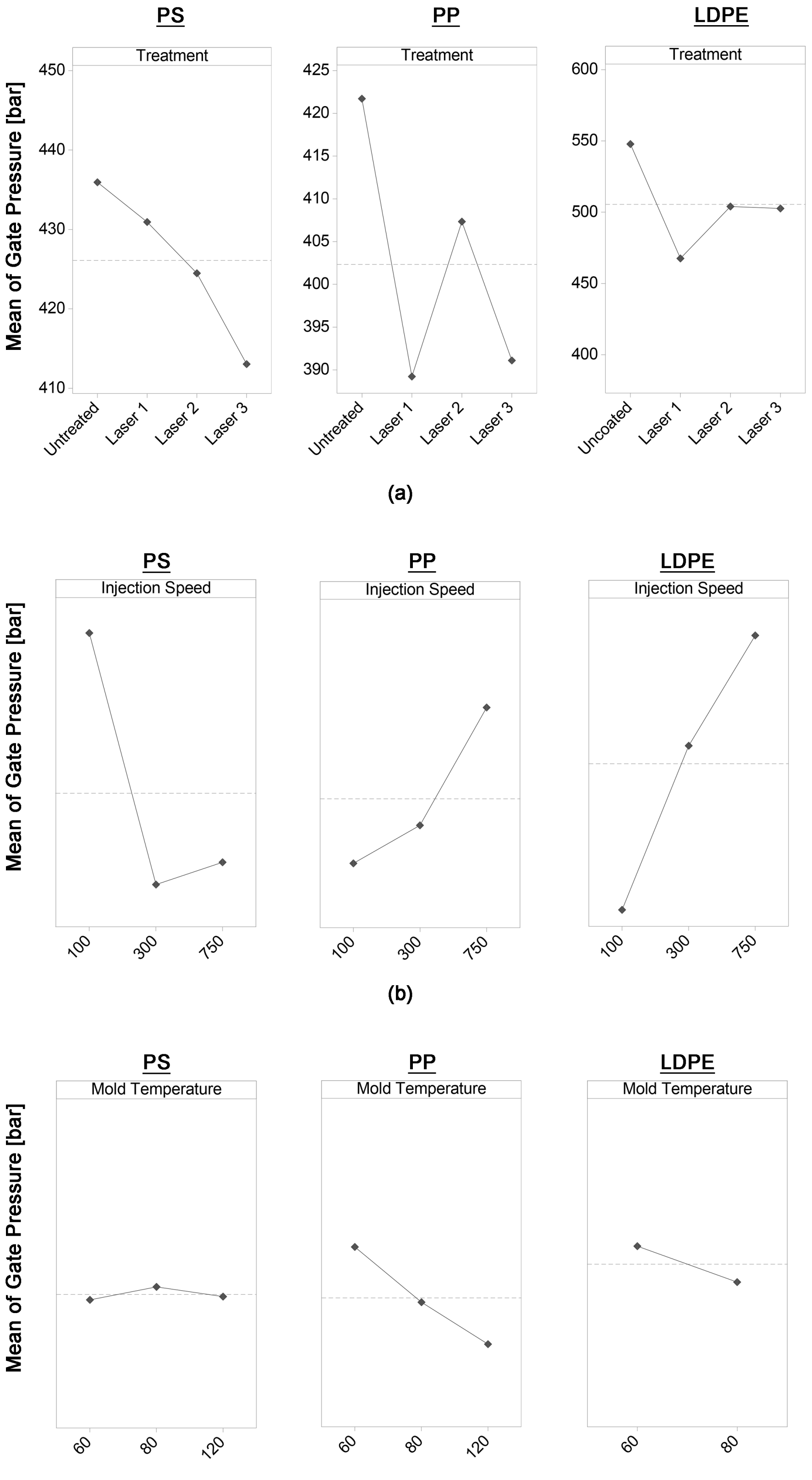

(a)

(b)

(c)

Figure 9.3: Main effect plots for the effect of LIPSS treatment and process parameters.

understanding of treatments effect and that polymers properties play a significant role.

For PS the highest reduction of the melt flow resistance was obtained when using *Laser*3 treatment (average reduction of -5%), while *Laser* 1 was the most effective mold treatment for PP (average reduction of -8%) and LDPE (average reduction of -15%). Figure 9.3 (a) shows the main effect plots for the effects of the different laser treatments for the three polymers.

Considering the results of the characterization of wall-slip discussed in section 11.2, it is known that the flow conditions for PS are affected by a speed of the polymer melt that is greater than zero in contact with cavity walls. Moreover, it is known from the literature (cf. subsubsection 2.3.2.1) that macromolecules get trapped between the asperities of the mold surface and the slip occurs at a polymer-polymer interface.

When molding with structures that are parallel to the polymer flow (i.e. *Laser* 1) the slip of polymer melts is promoted. Conversely, for structures that are perpendicular to the flow direction, the intensity of the slip phenomenon decreases with respect to the untreated surface. In fact, with this mold topography the ripples act as an obstacle to the melt flow. The entrapment of polymer chains in the space between the ripples is more likely to happen when they are perpendicular to the flow direction. When this occurs, the polymer-wall interface is replaced with corresponding much stronger polymer-polymer interface and the slipping of polymer melt decreases. And, as a consequence, the melt flow resistance is higher. Crossed structures drive a moderate slipping with an intermediate effect on injection pressure reduction.

Further understanding of the effects of the different laser treatments cannot be separated from the analysis of the effect of the injection molding parameters that were varied during the experiments.

9.3.2 *Effect of process parameters*

The main phenomena that control the melt flow resistance are the thermal insulation of the flow and the onset of wall slip. Different selections of mold temperature and injection speed affect those phenomena by:

- modifying the melt viscosity of the polymer;
- increasing or decreasing the replication of mold topography;
- changing the mobility of the macromolecules of the polymer melt;
- increasing or decreasing the adsorption of the polymer macromolecules at the mold surface.

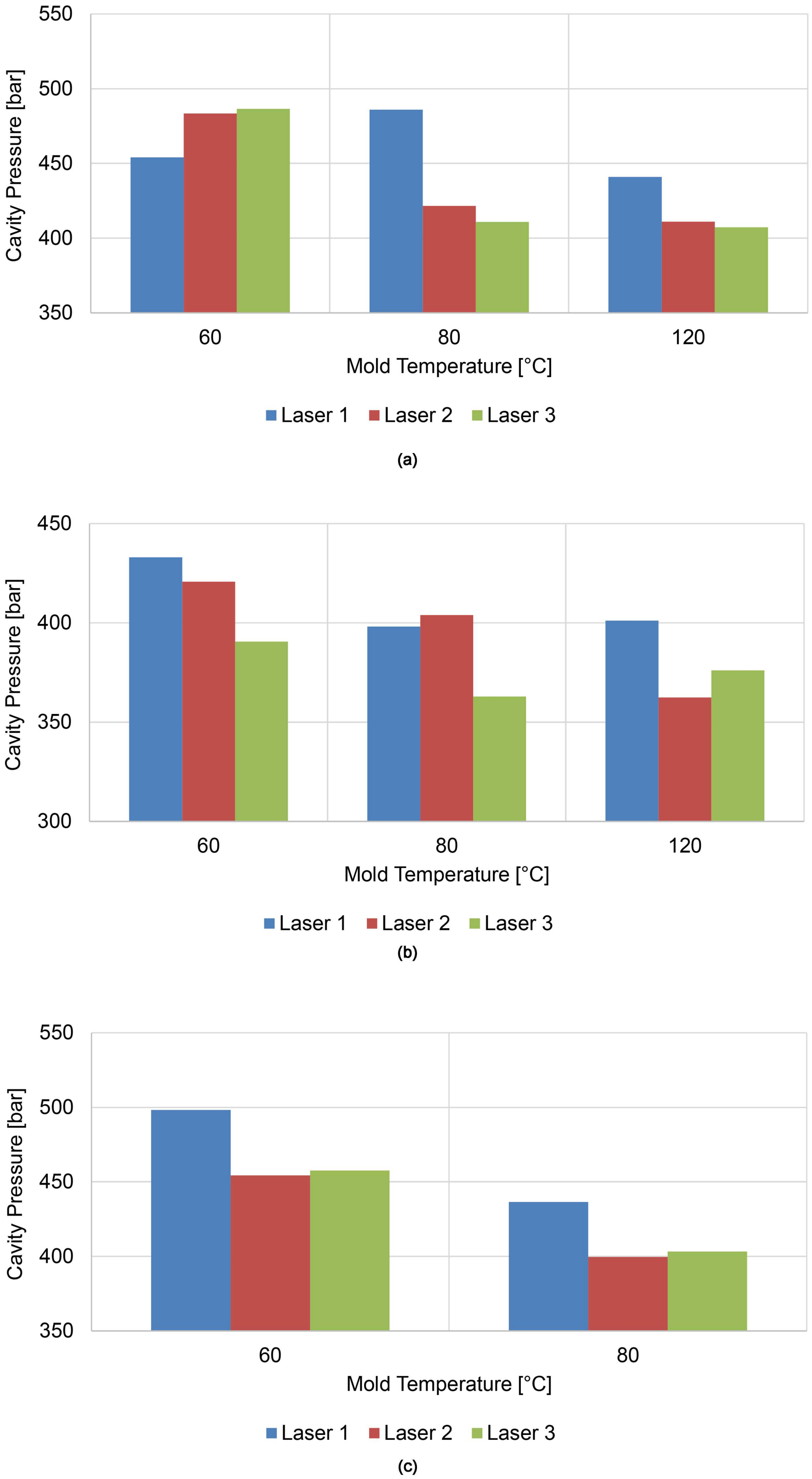

Figure 9.4: Analysis of the effects of mold temperature and injection speed for the LIPSS treated mold surfaces, (a) for PS, (b) for PP and (c) for LDPE.

		Reduction [%]		
Injection Speed [mm/s]	Mold Temperature [°C]	*Laser* 1	*Laser* 2	*Laser* 3
100	60	-4%	6%	7%
300		-8%	8%	7%
750		-8%	8%	9%
100	80	3%	-13%	-15%
300		4%	-7%	-16%
750		5%	-5%	-17%
100	120	-3%	-7%	-8%
300		0%	-5%	-6%
750		-1%	-5%	-4%

Table 9.5: Percentage reduction of the melt flow resistance compared to the untreated insert for PS, for different selection of mold surface treatments and injection molding process parameters.

However, these phenomena are diverse for the three polymers that were considered and they interact with the different laser treatment that were generated on mold surface.

9.3.2.1 *Polystyrene*

Considering the results of the injection molding experiments, at low value of the mold temperature the viscosity of the polymer is higher and hence its capability to replicated mold topography is mitigated (Figure 9.4 (a)). This results in weaker interaction with cavity walls and thus in higher slip velocity. Moreover, due to the favored orientation, the melt flow resistance is smaller with *Laser* 1 treatment; while, it is higher with *Laser* 2 and *Laser* 3. Table 9.5 reports the quantitative effects of the different laser treatments for PS.

At higher mold temperature (i.e. 80°C), the effect of mold surface replication is higher due to the lower viscosity of the polymer melt and the interaction with the mold surface is higher with *Laser* 1. Indeed, having the ripples oriented along the flow direction, the replication is favored and so is the adsorption of the macromolecules. Conversely, smaller interaction characterize the flow over *Laser* 2 and *Laser* 3, leading to higher slip velocities.

Increasing the mold temperature at 120°C above the glass transition temperature of the polymer (i.e. 100°C), results in higher replication, but this effect is mitigated by the higher mobility of the macromolecules which are easily disentangled from the bulk chains, thus yielding higher slip velocity.

9.3.2.2 *Polypropylene and low-density polyethylene*

The analysis of the results obtained with PP and LDPE (cf. Figure 9.3 (b)) suggest that the flow of this polymer is not affected by the onset of the wall slip phenomenon. Indeed, increasing the injection speed

		Reduction [%]		
Injection Speed [mm/s]	Mold Temperature [°C]	*Laser* 1	*Laser* 2	*Laser* 3
100	60	-5%	-3%	-10%
300		-8%	-3%	-14%
750		-8%	-2%	-12%
100	80	-1%	1%	-9%
300		-5%	0%	-4%
750		-6%	0%	-5%
100	120	-11%	-10%	-6%
300		-12%	-8%	-6%
750		-12%	-6%	-6%

Table 9.6: Percentage reduction of the melt flow resistance compared to the untreated insert for PP, for different selection of mold surface treatments and injection molding process parameters.

		Reduction [%]		
Injection Speed [mm/s]	Mold Temperature [°C]	*Laser* 1	*Laser* 2	*Laser* 3
100	60	-23%	-9%	-8%
300		-22%	-9%	-9%
750		-20%	-8%	-10%
100	80	-9%	-8%	-8%
300		-7%	-7%	-8%
750		-6%	-6%	-6%

Table 9.7: Percentage reduction of the melt flow resistance compared to the untreated insert for LDPE, for different selection of mold surface treatments and injection molding process parameters.

results in higher melt flow resistance, as it should be expected for shear flows due to the higher head loss.

From Figure 9.4 (b) and Figure 9.4 (c), it can be observed that for a low value of the mold temperature the melt flow resistance is higher with *Laser* 1 treatment. Indeed, this mold topography favors the replication of the ripples and the adsorption of the macromolecules. Thus, the fountain-flow of the polymer melt is slowed down in comparison with the cases of *Laser* 2 and *Laser* 3.

Increasing the mold temperature, results in higher mobility of the macromolecules for both polymers and thus in higher replication for unfavored mold topographies (i.e. *Laser* 2, *Laser* 3).

9.4 DISCUSSION

In this chapter, the effects of Laser-Induced Periodic Surface Structures (LIPSS) on the filling flow were characterized. It was shown that different LIPSS treatments can be exploited to drive the slipping of polymer melts depending on the relative orientation of the ripples. It was reported that LIPSS nanostructures have the capability of reducing the injection pressure up to more than 20% under standard injection molding processing conditions.

Ripples parallel to the polymer flow were observed to promote slip of polymer melts, due to reduced adsorption properties of the mold surface [147]. Conversely, perpendicular ripples hinder the orientation of adsorbed chain loops towards the flow direction, increasing the entanglement density between adsorbed and bulk chains [148]. Crossed structures drive a moderate slipping with an intermediate effect on injection pressure reduction.

Furthermore, we found that polymer chains can be trapped in the space between the ripples and this is more likely to happen when they are perpendicular to the flow direction. When this occurs the polymer/wall interface is replaced with corresponding much stronger polymer/polymer interface and the slipping of polymer melt decreases.

The results presented in this chapter have demonstrated how LIPSS can be used in injection molding to significantly promote filling. The treatment of the mold can also be used to control the filling flow pattern by selectively design parallel and perpendicular ripples as flow leaders and deflectors, respectively. These findings would be a starting point for the design of thinner plastic parts, leading to reduced environmental impact. Through the decrease of material and energy consumptions, significant manufacturing cost saving would be achieved.

10

EFFECTS OF SURFACE GENERATION ON THE EJECTION FORCE

In micro injection molding (μIM) the quality of 3D complex parts is influenced by the efficiency of the ejection phase. During demolding, the forces taking place at the component-tool interface, due to adhesion and friction, need to be overcome preserving the integrity of the part. This issue is severe in the case of molds characterized by the presence of several deep cores, which are used to manufacture interconnecting through holes in multi-layer microfluidic devices (cf. Figure 3.1). For these applications, the mold cavity has several features that counteract the shrinkage of the polymer melt [67]. Indeed, the interconnections between the different layers are ensured by several arrays of through holes that are realized by a series of deep cores tools in the mold. Typical multi-layer microfluidic devices involve critical design conditions, which lead to manufacturing issues. In particular, the presence of small through holes is a common design solution that allows the exchange of small volumes of fluids between the device layers through small pipes. In order to reduce the device dimension, whilst maintain high complexity/functionality, the holes are commonly arranged in tight arrays. The combination of these design conditions makes μIM, and especially its ejection phase, particularly critical. Figure 10.1 shows a molded microfluidic device for which the incorrect design of mold surface properties led to breakage during the ejection phase.

This chapter discusses the effects of mold topography on the ejection force considering the impact of different conventional machining processes. The surfaces characteristics were correlated to their influ-

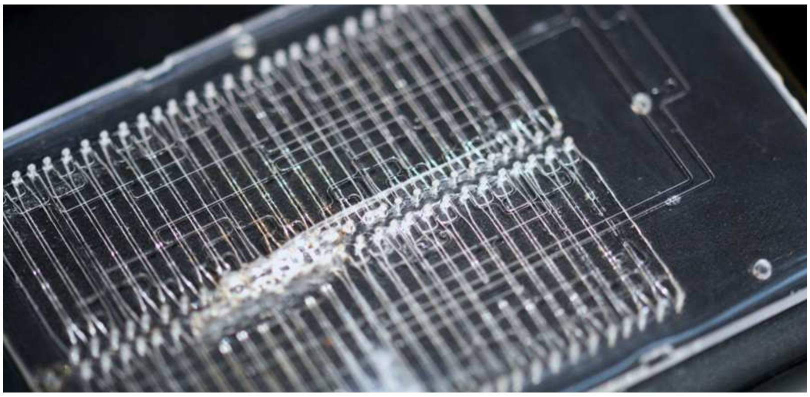

Figure 10.1: Breakage of multi-layer microfluidic device due to high ejection friction.

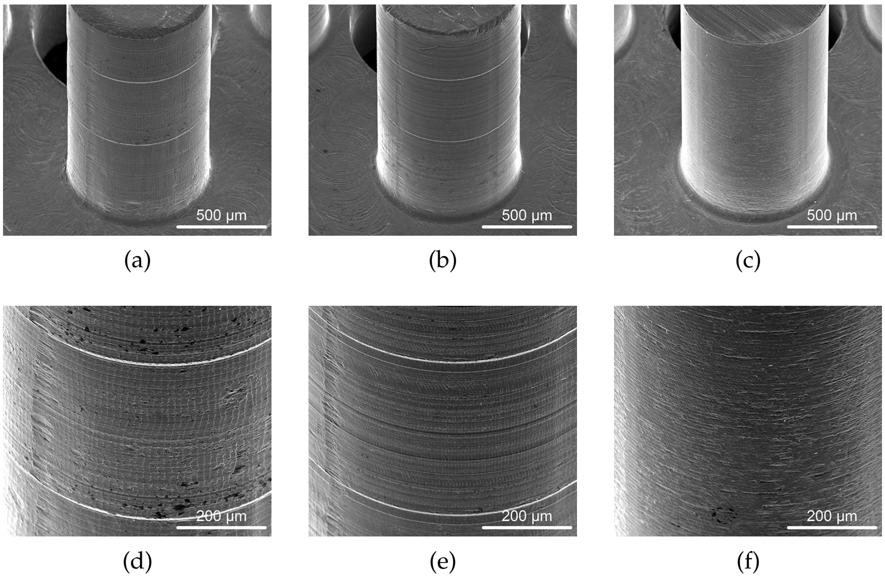

(a) (b) (c)

(d) (e) (f)

Figure 10.2: SEM micrographs of the micro-milled mold inserts at different magnifications. Insert 1 at (a) 200x and (d) 500x; Insert 2 at (b) 200x and (e) 500x; Insert 3 at (c) 200x and (f) 500x [69].

ence on ejection friction, evaluated as the experimental value of the demolding force. Experimental campaigns were conducted, by varying the main process parameters, to investigate possible interactions between the different cavity textures and μIM process conditions.

10.1 IMPACT OF MICRO MILLING SURFACE FOOTPRINT

10.1.1 *Mold surface characterization*

The mold cavity geometry limited the optical accessibility to mold cores sides, thus hindering the possibility to directly characterize their surfaces using non-destructive techniques, such as non-contact optical metrology. Therefore, the characterization of the micro-milled surfaces was performed according to a first qualitative SEM observation and a subsequent topography analysis on the cut cores.

10.1.1.1 *Mold topography characterization*

SEM (FEI, Quanta 400) analysis allowed the comparison of micro milling inherent machining marks and main topography defects of the different mold cores. The mold inserts surface topography characterization showed some differences in terms of surface finish moving from Insert 1 to Insert 2 and Insert 3, as visible in Figure 10.2 (a), (b), (c). This fact confirms the expected micro milling strategy and cutting parameters effect on the mold surface topography.

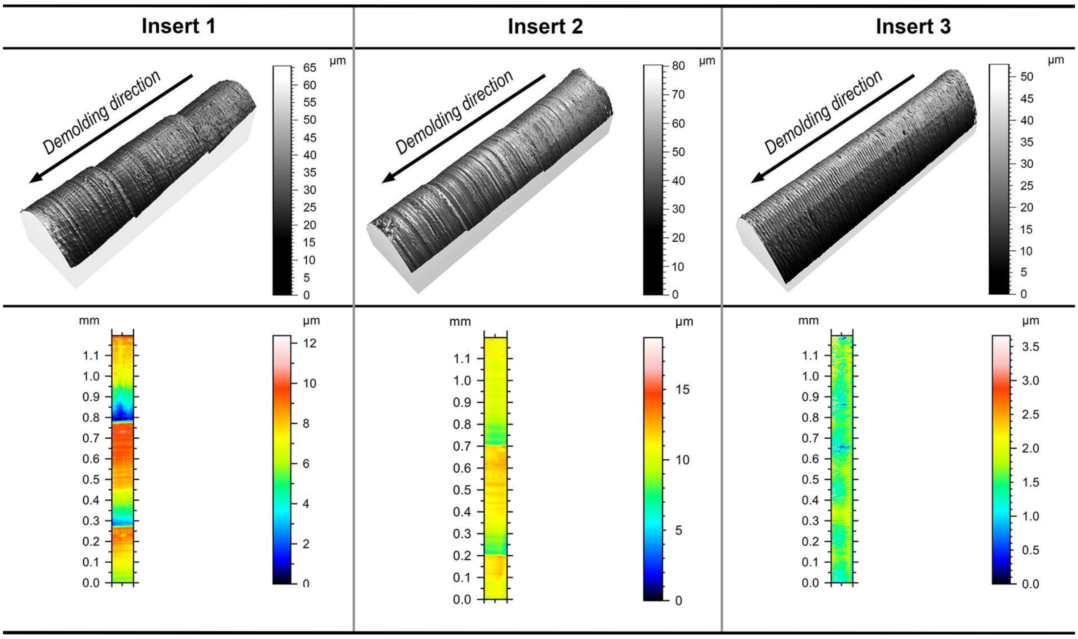

Figure 10.3: 3D and 2D views of the three mold insert topographies [69].

All the manufactured mold inserts are characterized by the presence of an inherent surface texture, typical of micro-milled surfaces. However, the topographies of Insert 1 and 2 are characterized by more evident feed marks with some minor smearing effects, due to the milling tool ploughing over the surface (Figure 10.3).

On the contrary, the ploughing and smearing action dominates Insert 3 due to its helicoidal tool path with small axial depth of cut. In this case, the tool repeatedly passes over the already machined surface producing a smooth and smeared finish.

The micro milling process generated on the mold inserts also localized geometrical defects, as clearly visible in Figure 10.2. On one side, the entire inserts showed four regularly spaced marks oriented in the vertical direction (with an angular shift of about 90 degrees). Their presence is compatibly related with machine axes inversion errors, caused by the circular tool trajectory on the X-Y plane. They showed relatively large height amplitude with respect to surface roughness. Despite that, their limited width (around 50 μm) and their vertical orientation make them assuming a minor role on the demolding forces generated by the molds.

Moreover, the strategy adopted for the movement of the tool in the vertical direction affected the formation of localized geometrical defects oriented in circumferential direction. Indeed, the presence of two micrometric circumferential steps, oriented oppositely to the demolding direction, was observed for mold Insert 1 and Insert 2 (Figure 10.2 (d), (e)). These vertical discontinuities constitutes micro milling-derived form error of the deep cores and represent possible undercuts for the ejection phase of the μIM process. The average

		ISO 4287			
Insert		*Rz* [μm]	*Ra* [μm]	*Rq* [μm]	*Rku*
1	Avg. Val.	4.09	0.34	0.57	6.97
	Std. Dev.	0.61	0.05	0.06	0.41
2	Avg. Val.	2.17	0.21	0.3	5.05
	Std. Dev.	0.37	0.02	0.03	0.78
3	Avg. Val.	1.3	0.13	0.18	5.81
	Std. Dev.	0.35	0.03	0.04	1.89

Table 10.1: Average values and standard deviations of profile roughness parameters evaluated according to ISO 4287.

		ISO 13565 − 2		
Insert		*Rk* [μm]	*Rpk* [μm]	*Rvk* [μm]
1	Avg. Val.	0.52	1.29	1.24
	Std. Dev.	0.12	0.13	0.11
2	Avg. Val.	0.53	0.46	0.66
	Std. Dev.	0.06	0.04	0.09
3	Avg. Val.	0.35	0.15	0.32
	Std. Dev.	0.06	0.04	0.11

Table 10.2: Average values and standard deviations of profile roughness parameters evaluated according to ISO 13565 − 2.

height of these defects, evaluated on the topographies acquired on the manufactured mold inserts, was 6.8 μm for Insert 1 and 3.3 μm for Insert 2. The presence of these steps was not observed in case of Insert 3, where a helicoidal tool path was applied (Figure 10.2 (f)).

10.1.1.2 *Roughness evaluation*

Table 10.1 reports the roughness characterization results, indicating an evident effect of the micro milling strategy on mold surface roughness (ISO 4287).

Micro milling cutting parameters affect both the presence of protruding peaks in the profile (*Rz*) and the overall roughness of the mold surface (*Ra*, *Rq*). In particular, the average value of *Ra* reduces by 39% by changing the cutting parameters from Insert 1 to Insert 2, and by 62% from Insert 1 to Insert 3.

The kurtosis parameter (*Rku*) was considered to measure the sharpness of the height distribution, which can potentially affect the friction between the mold surface and the polymer part during the ejection phase. As shown in Figure 10.4 (a), the *Rku* evaluated for the three mold samples is not significantly different, indicating that the micro milling process produced surfaces characterized by similar morphologies under this point of view.

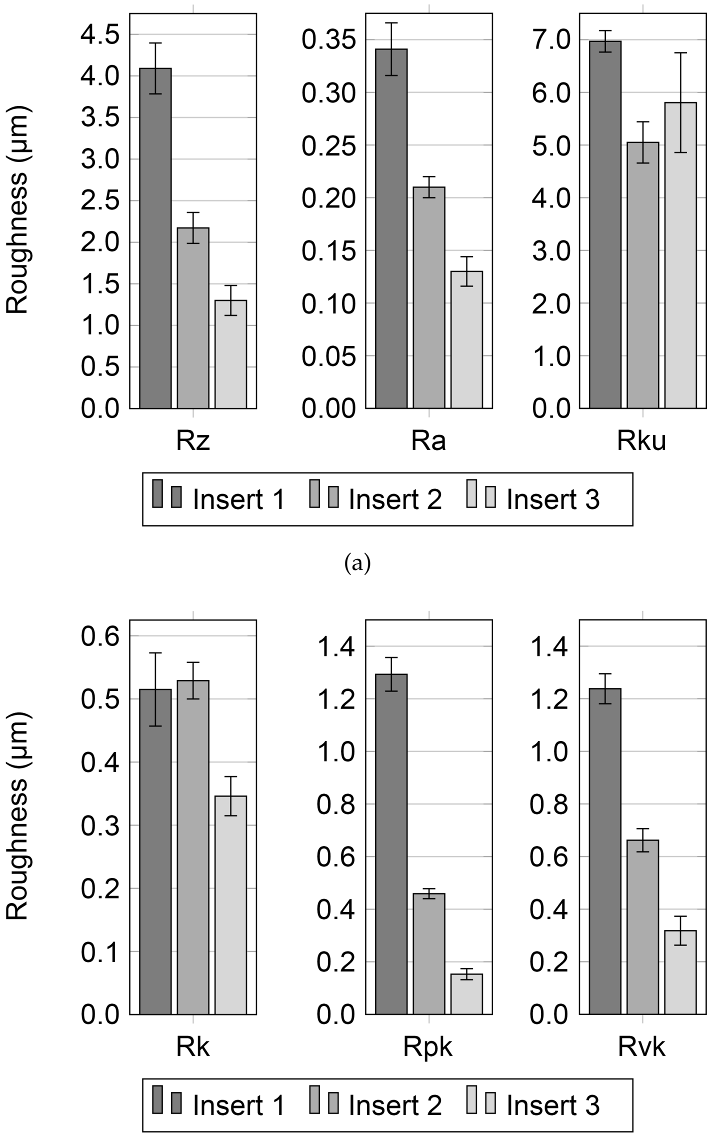

(a)

(b)

Figure 10.4: Histograms of roughness parameters for (a) ISO 4287 and (b) ISO 13565-2 [69].

However, amplitude parameters do not provide information about the shape, slope and size of the asperities or about the spatial frequencies of their occurrence [149], which can be important in determining the performance of the μIM ejection phase. Hence, in order to improve the understanding of the interface interaction between the mold surface and the replicating polymer, the Abbott-Firestone curves were evaluated [150]. According to ISO $13565-2$, this curve allows the determination of the *Rk* parameters from the linear representation of the material ratio curve that describes the increase of the material portion of the surface with increasing the roughness profile depth ISO $13565-2$. The curve provides information about the material and void volumes characterizing the surface topography, thus being important to study the potential replication behavior of different μIM mold surfaces [151].

Table 10.2 reports the *Rk* parameters values for the three micro-milled mold surfaces. The *Rk* values are about the same for Insert 1 and 2, while they are significantly different for Insert 3, as shown in Figure 10.4 (b). The values of *Rpk* and *Rvk* are significantly different for the three micro-milled inserts. In particular, they reduce from Insert 1 to Insert 2 to Insert 3.

High values of *Rvk* can negatively affect the ejection forces because of the higher void volumes in the mold surface, which can be replicated by the polymer that fills them causing higher interfacial interactions. Similarly, high values of *Rpk* can lead to increased friction between the mold and the part, because of the markedly higher presence of protruding peaks that causes higher demolding stresses.

10.1.2 *Experimental approach*

10.1.2.1 *Screening phase*

The combined effect on the ejection force of polymer shrinkage and surface finish was studied in relation with the main μIM process parameters by applying a design of experiments (DoE) approach. To characterize the effects of mold surface finish and μIM parameters on the demolding force variation (screening phase), a four-factor full factorial design was carried out, using PS as molding material. In addition to the micro milling strategy, the other process variables selected for the analysis were the packing pressure P_h, the cooling time t_c and the injection speed V_{inj}. The range values for each factor are reported in Table 10.3. During the μIM tests, the following parameters were fixed:

- mold temperature: 50 °C;
- melt temperature: 240 °C;
- metering size: 1.2 mm;

Factor	Low level	Medium level	High level
Insert	1	2	3
P_h [bar]	40	-	80
t_c [s]	2	-	10
V_{inj} [mm/s]	50	-	300

Table 10.3: Process parameters settings for the screening DoE plan.

Factor	Low level	Medium level	High level
Insert	1	2	3
Material	PS	-	COC

Table 10.4: Process parameters settings for the optimization plan.

- packing time: 2 s;
- clamping force: 120 kN.

The range values for the DoE screening plan and the fixed parameters values were defined considering the literature, recommendations of the material supplier (max. nozzle melt temperature 210-240 °C) and technological limitations of the available experimental setup.

10.1.2.2 *Optimization*

Considering the results of the screening phase, the ejection phase optimization was then carried forward by investigating the effect of a different polymer. In particular, the COC was introduced in the μIM experiments. To investigate the effect of the polymer, a two-factor full factorial plan was designed including the micro milling strategy as the only other parameter (Table 10.4). According to the results of the screening phase, the μIM process parameters were fixed to the following values:

- injection speed: 300 mm/s;
- packing pressure: 40 bar;
- cooling time: 10 s. The other fixed parameters were held to the screening phase values.

10.1.2.3 *Response variable*

The understanding of the ejection force reduction effects on process quality needs to consider all the mechanical loads applied to the plastic part during the demolding phase. For this reason, the response variables selected for both the DoE campaigns were the demolding force peak F_{peak} and the subtended area F_{area}, as shown in Figure 10.5.

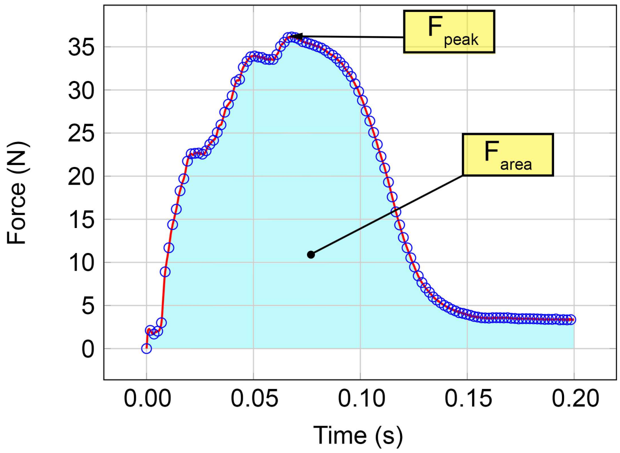

Figure 10.5: Response variables for the statistical analysis of the experimental data [69].

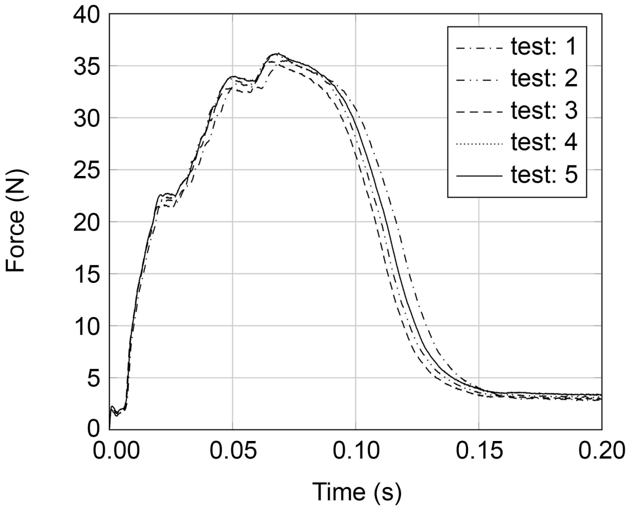

Figure 10.6: Example of demolding force in-line acquisitions of DoE repetitions - std. dev. F_{peak}: 0.38 N, F_{area}: 0.75 N·s [69].

	p-value	
	F_{peak}	F_{area}
Insert	0.000	0.000
P_h	0.000	0.000
t_c	0.000	0.001
V_{inj}	0.000	0.007
Insert$\cdot P_h$	0.000	0.000
Insert$\cdot t_c$	0.000	0.000
Insert$\cdot V_{inj}$	0.000	0.000
$P_h \cdot t_c$	0.004	0.317
$P_h \cdot V_{inj}$	0.000	0.000
$t_c \cdot V_{inj}$	0.046	0.000

Table 10.5: Anova table for the screening experiments designed in Table 10.3.

Indeed, the acquired force peak represents the maximum load stressing the molded part, while the curve subtended area stands for the demolding work, under the hypothesis of constant speed of the ejectors.

To guarantee the μIM process and the online force monitoring setup stability, 10 molding cycles were carried out before the first demolding force acquisition. Then, 5 acquisitions were collected, one every 5 cycles, for each molding condition. The acquired data were then aligned to the beginning of the ejection phase and overlapped to evaluate their repeatability (Figure 10.6). The response variables were then calculated and collected for each DoE combination using Matlab.

10.1.3 *Micro injection molding results*

The developed experimental plans were analyzed to identify the significant factors on the demolding force. In order to perform a univariate analysis of variance (ANOVA), a general linear model was fit to the experimental data. The statistical significance of the factors included in the model was evaluated comparing the p-values with a threshold value of 0.05. The factors having a p-value lower than 0.05 can be considered statistically significant on the selected response. The results reported in Table 10.5, indicate that all the main effects significantly affect both the demolding force peak F_{peak} and subtended area $_{F}area$. Moreover, some first-order interactions included in the model are statistically significant.

10.1.3.1 *Effect of the micro milling strategy*

The effect of the micro milling parameters on the ejection force is significant for both F_{peak} and F_{area} (p-value: 0.000). The effect of improv-

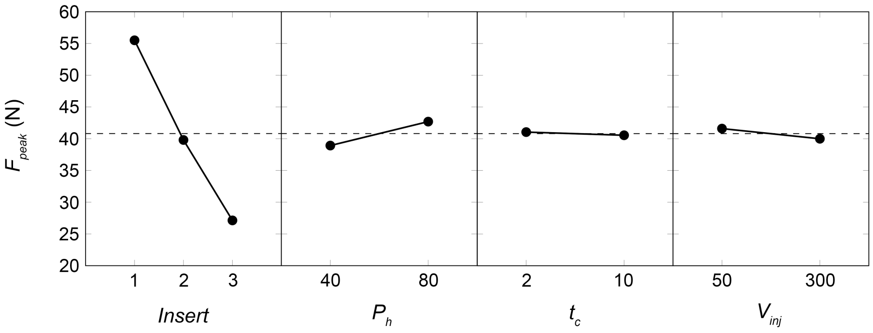

Figure 10.7: Main effect plots for the demolding peak force F_{peak} (screening plan) [69].

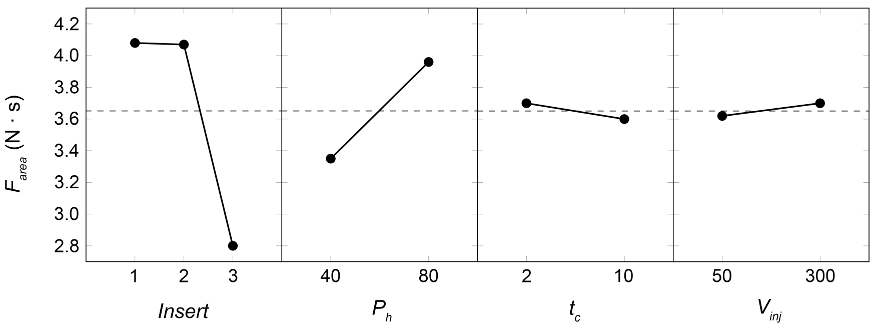

Figure 10.8: Main effect plots for the demolding work F_{area} (screening plan) [69].

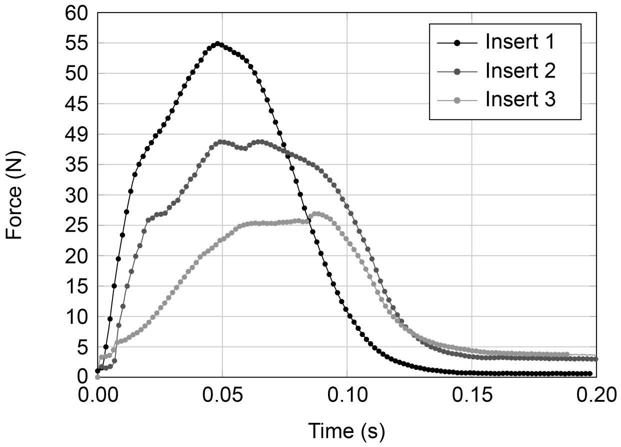

Figure 10.9: Effect of the micro milling strategy on the demolding force curves - max. standard deviation: 0.5 N [69].

ing the cores surface finish by changing the micro milling parameters from Insert 1 to Insert 2 and from Insert 1 to Insert 3 is to reduce F_{peak} by respectively 28.2% and 51.1% (Figure 10.7), and the F_{area} by respectively 0.3% and 31.5% (Figure 10.8).

Comparing the effect of the three mold inserts, it was observed that the shape of the curves is the same, as shown in Figure 10.9. However, it is clear that the mold surface topography markedly affects the values of the force applied to the molded parts during the demolding phase. The maximum overall ejection force was acquired when using mold Insert 1, indicating that the plastic was subjected to the highest stress during the ejection phase with this mold topography.

The higher demolding forces observed for Insert 1, which was produced with a combination of higher micro milling cutting parameters (i.e. feed and depths of cut), are explained by its worst surface finish. This fact is confirmed by the mold surface characterization (subsection 10.1.1), which showed that Insert 1 presents the larger asperities compared to other micro-milled mold inserts.

The higher the mold surface roughness, the higher the resistance at the part-tool interface. In fact, when filling the cavity, the polymer melt can replicate the surface topography of the mold and, as a consequence, produce interlocking between the two surfaces. Then, the force required to initiate the solidified polymer sliding over the mold steel surface is higher and so is the demolding force peak. By improving the mold surface roughness, F_{peak} gets lower as also the mechanical effect of surface asperities is smaller. During the ejection, the sliding of the two solid surfaces is characterized by localized ploughing and deformation mechanisms that increase in case of worst mold surface finish.

The demolding force reduction is consistent with the surface roughness reductions quantified on the mold cores. The amplitude parameters able to represent the micro milling strategy effect on F_{peak} are *Rz* (-47% from Insert 1 to Insert 2, -68% from Insert 1 to Insert 3), *Ra* (-39%, -62%) and *Rq* (-47%, -68%). Moreover, *Rpk* (-65%, -88%) and *Rvk* (-47%, -74%) decrease as F_{peak} when changing the micro milling parameters.

The main effect of the micro milling strategy on F_{area}, displayed in Figure 10.8, is more or less insignificant moving from Insert 1 to Insert 2. On the contrary, the reduction is markedly evident moving from Insert 2 to Insert 3. This fact is explained by the presence of two circumferential undercuts, responsible for higher F_{area} in mold Insert 1 and Insert 2. The absence of this geometrical defect in Insert 3, thanks to the micro manufacturing strategy improvement, led to a significantly lower demolding energy.

The F_{peak} values are more sensitive to mold surface finish improvements because of the large part-tool interlocking effect on the static friction, which directly influences the maximum value of the load ap-

	p-value	
	F_{peak}	F_{area}
Insert	0.000	0.000
Material	0.000	0.000
Insert·Material	0.000	0.000

Table 10.6: Anova table for the optimization experiments designed in Table 10.4.

plied to the part. Indeed, the energy absorbed during the ejection phase F_{area} depends on the dynamic friction between the two sliding surfaces, which is less affected by a topographical defects reduction (i.e. cores surface finish improvement).

10.1.3.2 *Effect of μIM process parameters*

Considering the ANOVA results, it is clear that the thermal shrinkage of the polymer around deep cores is an important factor affecting the stress generated during the demolding phase. The contact pressure generating during the μIM cycle and determining the ejection friction, is produced by the effect of process parameters on the polymer thermal shrinkage, such as the packing pressure.

The main effect of increasing the packing pressure from 40 to 80 bar is to increase F_{peak} by 10% and F_{area} by 18% (Figure 10.7, Figure 10.8). In fact, high values of P_h affect the replication of deep cores topography, determining a higher mechanical interlocking between the part and the mold. This is supported also by the significance of the first order interaction between the *Insert* and the P_h (p-value: 0.000), which showed larger effect of the packing pressure for worst surface finish. Thus, the higher adhesion at the interface, resulting from a higher replication, prevails over the expected reduction of the contact pressure at the part-mold interface that is caused by a lower diametric shrinkage. Moreover, as suggested by Pontes and Pouzada, at low values of the packing pressure the part and the mold surfaces are likely to separate, causing a reduction of the heat transfer and keeping the polymer at a higher temperature during the demolding phase [90].

As shown in Figure 10.7 and Figure 10.8, the main effects of the cooling time and injection speed are less important than the other factors considered in the analysis, indicating that their effect on both the topography replication and the contact pressure was not significantly improving the demolding phase.

10.1.3.3 *Effect of molding polymer*

Selecting a different molding polymer resulted statistically significant according to the optimization plan ANOVA (p-value: 0.000) reported

		F_{peak} [N]		F_{area} [N·s]	
Insert	Polymer	Avg. Val.	Std. Dev.	Avg. Val.	Std. Dev.
1	PS	49.9	0.3	3.6	0.1
2	PS	35.7	0.4	3.5	0.1
3	PS	25.8	0.1	2.6	0.1
1	COC	95.2	0.6	9.5	0.3
2	COC	60.3	0.5	6.4	0.1
3	COC	33.1	0.5	3.7	0.1

Table 10.7: Experimental results of the optimization plan.

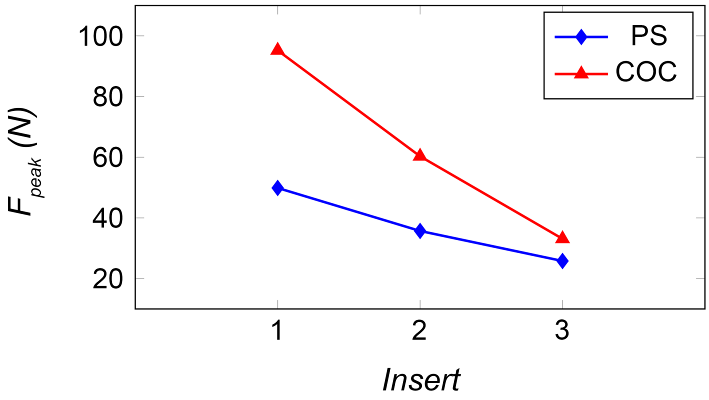

(a)

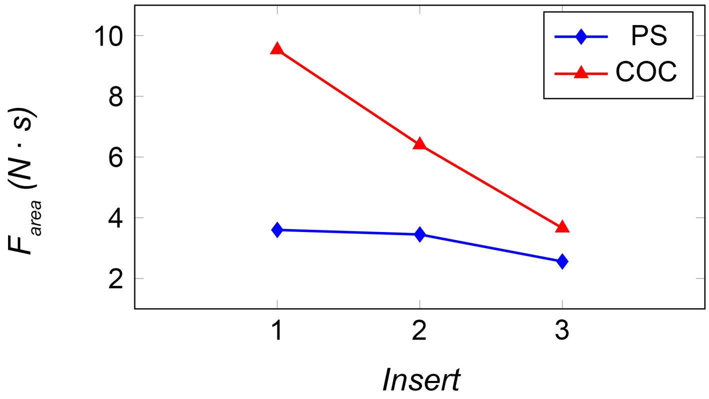

(b)

Figure 10.10: Interaction plot for the optimization plan. (a) demolding force peak; (b) demolding force area [69].

Insert	Material		*Rz* [μm]	*Ra* [μm]	*Rq* [μm]	*Rku*	*Rk* [μm]
1	PS	Avg. Val.	2.18	0.29	0.38	3.94	0.91
		Std. Dev.	0.28	0.03	0.04	1.07	0.13
2	PS	Avg. Val.	1.66	0.22	0.29	3.85	0.62
		Std. Dev.	0.27	0.03	0.04	0.43	0.17
3	PS	Avg. Val.	1.03	0.14	0.18	3.31	0.44
		Std. Dev.	0.13	0.02	0.02	0.45	0.08
1	COC	Avg. Val.	2.68	0.35	0.42	4.07	1.17
		Std. Dev.	0.12	0.03	0.05	0.55	0.06
2	COC	Avg. Val.	2.1	0.27	0.36	3.99	0.73
		Std. Dev.	0.38	0.04	0.06	0.67	0.13
3	COC	Avg. Val.	1.3	0.18	0.23	3.66	0.55
		Std. Dev.	0.21	0.02	0.03	0.94	0.1

Table 10.8: Molded parts roughness (optimization plan).

in Table 10.6. In particular, using COC instead of PS produced an average increase of the demolding force peak and work by 69% and 104% (Table 10.7).

The effect of the molding material on the ejection phase stress is related to a combination of higher shrinkage properties and lower viscosity, at the selected melt temperature. In particular, the COC was reported to be more prone to higher interactions at the part-tool interface during the μIM process [31].

The analysis of variance indicated that the influence of the first order interaction between the mold insert and the polymer is important for a complete understanding of the effect of the micro milling strategy on the ejection phase. In particular, the better the mold surface finish the smaller the difference between the force values acquired for the two polymers, as shown in Figure 10.10.

A combination of worst mold surface finish (i.e. Insert 1) and low viscosity of the polymer (i.e. COC) resulted in higher demolding friction, because of the markedly higher interlocking at the tool-part interface. In fact, COC gives a better replication of the mold surface topography, thus causing a higher interfacial interaction. On the contrary, improving the mold surface finish attenuated the interlocking and consequently the influence of the polymer.

10.1.4 *Molded parts roughness evaluation*

The through holes topographies of the molded parts, shown in Figure 10.11 were evaluated in order to improve the understanding of the relation between the mold surface topography and the micro manufacturing process. The μIM molded parts were micro-milled (Kugler,

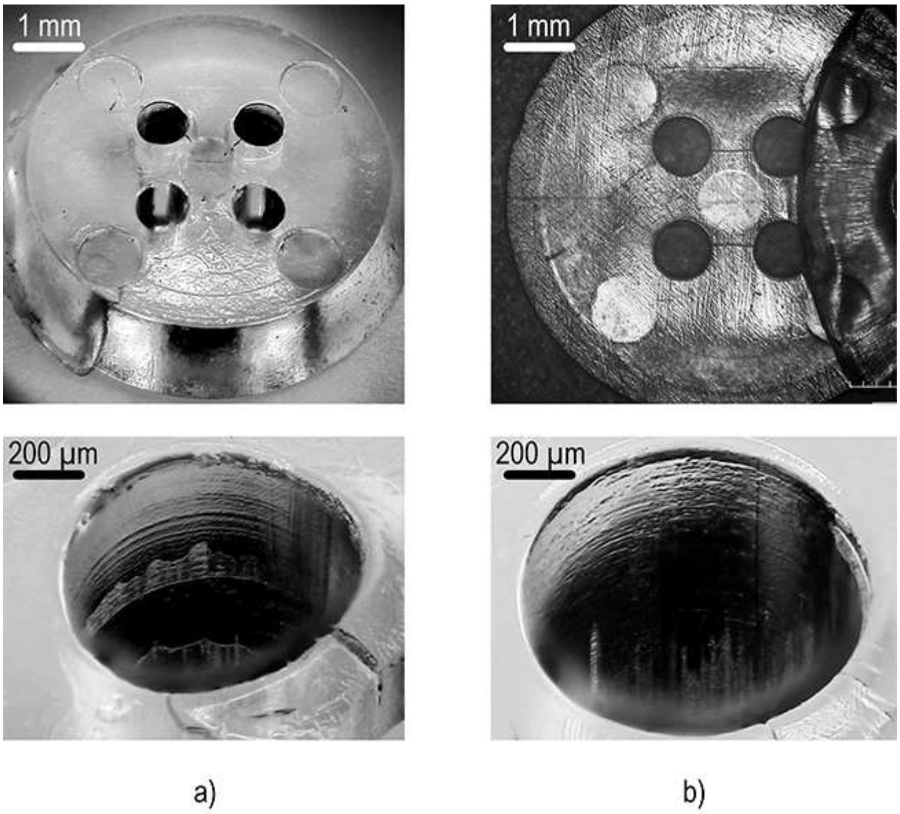

Figure 10.11: Produced molded parts with: a) mold Insert 1 and b) mold Insert 2) [82].

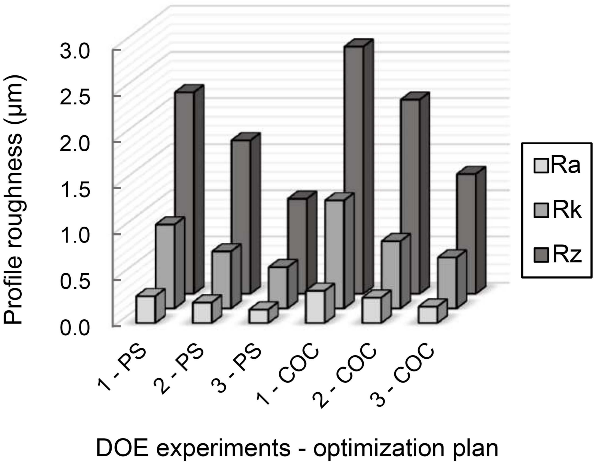

Figure 10.12: Roughness amplitude parameters evaluated on the plastic parts [69].

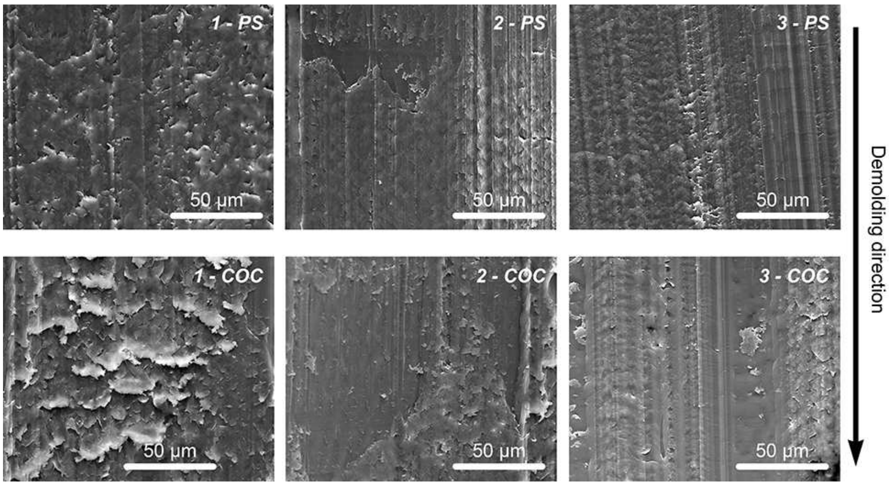

Figure 10.13: SEM micrographs of the molded parts topographies - magnification: 2000x [69].

Micromaster 5X) in order to make the 800 μm holes accessible and then inspected using a SEM (FEI, Quanta 400) and a 3D optical profiler (Sensofar, Plu Neox) operating in confocal mode with a 20x objective.

In order to evaluate the μIM molded parts roughness, the topography of two holes for each replication and each run of the optimization plan was acquired in a projected area of 0.4 x 1.5 mm. Topographies were analyzed using the MountainsMap software, to evaluate different profile roughness parameters. Three profiles where extracted for each measurement (length: 1.5 mm), the shape error was corrected and the selected roughness parameters were evaluated applying a 80 μm gaussian filter, according to ISO 4287 and ISO $13565 - 2$.

The effects of different polymers on the tribological conditions during the ejection phase are due to the different mold surface topography replication that they obtained. In particular, the worst the surface finish the larger the volume that can be filled by the polymer during the injection phase. Specifically, the average depth of the profile valleys projecting through the roughness core profile *Rvk* increased from Insert 1 to Insert 2 to Insert 3.

Table 10.8 reports the roughness parameters evaluated for each run of the optimization plan on the inner surface of the through holes in the molded parts. The values of *Rz*, *Ra*, *Rq* and *Rk* indicate that a clear effect of the mold surface topography exists on the molded parts roughness. Indeed, the higher the mold replication obtained during the injection phase, the rougher the part surface after the ejection phase. The *Ra* values observed in the molded parts decrease from Insert 1 to Insert 2 and from Insert 1 to Insert 3 by 23% and 50%, respectively. The same trend was observed for *Rz* (23%, 52%), *Rq* (18%, 48%) and *Rk* (35%, 52%), as shown in Figure 10.12.

Rku values, instead, do not show significant variations, indicating that all the parts are characterized by the same height distribution sharpness after demolding. It seems that, regardless of the mold surface topography and molding material, the mold surface asperities produced the same surface morphology.

Considering all the profile parameters evaluated on parts molded with different polymers, it was found that the roughness was smaller on PS than on COC, indicating that the replication of mold surface topography is markedly higher with COC. The effect of micro milling strategies and molding polymers on the demolding phase was confirmed by observing the inner surface of molded parts with SEM, as shown in the micrographs reported in Figure 10.13. In particular, it is clear that the part surface is characterized by a smoother topography with less asperities for inserts with improved surface finish. Moreover, the higher replication obtained with COC was observed by comparing parts made with the two different polymers. This fact confirms the higher interlocking and the consequent higher friction between part and tool in case of COC.

10.2 EFFECTS OF μEDM GENERATED MOLD TOPOGRAPHY

10.2.1 *Mold surface characterization*

The mold cores surface characterization, initially performed by means of SEM, clearly showed the different surface topographies obtained using different μEDM machining parameters (Figure 10.14). In general, the topographies of the mold surfaces are characterized by the presence of a multitude of overlapping discharge craters, typical of the μEDM process. The effect of changing the μEDM combinations of parameters from A to B, to C and to D is to decrease the size and the depth of the craters. In fact, the smaller is the intensity of the discharge impulse the lower is the material removal rate.

The topography of the mold cores machined with different selections of μEDM machining parameters was evaluated considering several surface roughness parameters, allowing the evaluation of the differences between the mold surfaces.

Table 10.9 reports the mean and standard deviations value of the selected surface parameters evaluated on the acquired topography. Comparing the different sets of mold cores, it is evident that they are all characterized by significantly different roughness. In particularly, the values of *Sa*, which represents the roughness amplitude of the topography, increases by +161%, +69%, 65% when changing μEDM combinations of parameters from A to B, to C and to D. Moreover, the values of the functional parameters *Svk* and *Spk* indicate that also the distribution of peaks and valleys changes significantly, modifying the possible interface interactions between polymer and mold surface.

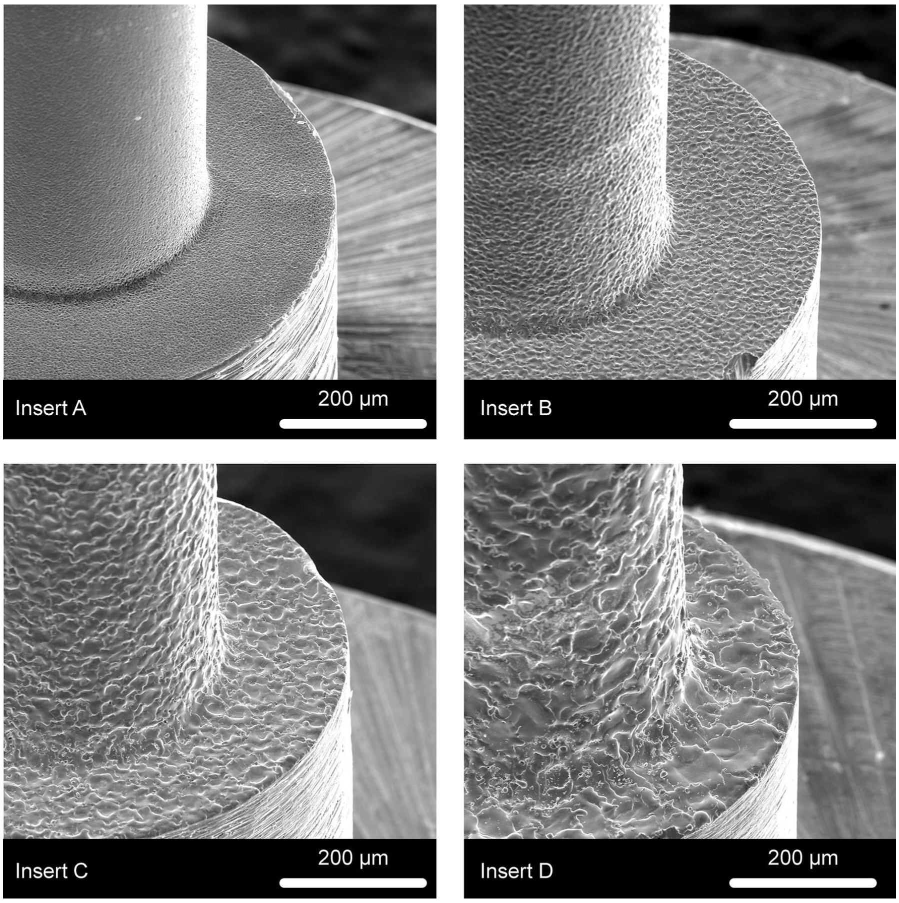

Figure 10.14: SEM micrographs of the mold cores obtained with different μEDM machining parameters (magnification: 500 X).

μEDM		Sa	Sq	Sp	Sv	Sz	Ssk	Spk	Svk
A	Mean	0.23	0.3	3.06	1.67	4.73	0.44	0.26	0.24
	Std. Dev.	0.02	0.03	1.35	0.19	1.41	0.38	0.02	0.02
B	Mean	0.6	0.77	4.93	3.83	8.96	-0.71	0.53	0.76
	Std. Dev.	0.05	0.07	0.87	0.24	1.63	0.87	0.05	0.14
C	Mean	1.01	1.31	11.93	30.17	44.53	-1.65	0.83	0.95
	Std. Dev.	0.03	0.02	4.37	4.54	9.8	1.37	0.04	0.06
D	Mean	1.67	2.39	28.38	64.98	96.75	-4.88	1.39	1.46
	Std. Dev.	0.02	0.03	11.83	2.49	13.63	0.55	0.16	0.2

Table 10.9: Means and standard deviations of surface roughness parameters for the mold cores machined with different μEDM process parameters, evaluated according to ISO 4287, ISO 13565 [143, 144]. These values were calculated on 24 topographies: 4 topographies per each core and 6 cores per cavity.

	Level Values			
Sa [μm]	0.23	0.6	1.01	1.67
US	Off	On	-	-

Table 10.10: Experimental DoE plan designed for the molding experiments.

Polymer	Crystal 1540	Ultraform H2320	5013L-10
Melt Temperature (°C)	240	235	305
Mold Temperature (°C)	80	80	50
Injection Speed (mm/s)	200	200	200
Packing pressure (bar)	150	150	150
Packing Time (s)	6	6	6
Switch-over v/p (bar)	600	640	670
Cooling Time (s)	10	10	10

Table 10.11: Process parameters selection for the three injection molding polymers.

10.2.2 *Experimental approach*

The effects of μEDM generated mold topographies on the demolding friction were investigated following the Design of Experiments (DoE) approach. Moreover, considering the high roughness value obtained with some of the combinations of μEDM process parameters, this mold surfaces were also used to characterize the ultrasound-assisted ejection setup, which was introduced in section 5.5. Different tribological conditions were investigated by using mold inserts characterized by different roughness values and by molding different polymers (PS, COC, POM).

For each one of the selected polymers, a general full factorial design was carried out considering variations of mold surface roughness (Sa - 4 levels) and of the ultrasound (US - 2 levels), as reported in Table 10.10.

The process parameters were fixed to the constant values (Table 10.11), with exception for the temperatures that were set to proper values for each polymer. The ejection of the part from the cavity was carried out with a stroke of the ejection system of 3 mm at a speed of 10 mm/s.

The peak of the demolding force signal (F_{peak}) was selected as the response variable for the analysis, as indicated in subsection 5.3.2.

Before the acquisitions, the ejection system was initially verified and stabilized by carrying out several dry cycles of the clamping and ejection units. The F_{peak} value acquired during the dry cycles was stable after about 50 cycles and smaller than 10 N. Thus, when analyzing the effect of the ultrasound vibration the dry force was neglected.

	P-Value		
Source	PS	COC	POM
Model	0.000	0.000	0.000
Sa	0.000	0.000	0.000
US	0.000	0.000	0.000
2-Way Interactions	0.000	0.000	0.000
Sa · US	0.000	0.000	0.000

Table 10.12: Anova table for the designed experiments.

In order to achieve stability of both the molding process and the online monitoring setup, ten cycles were carried out before the first ejection force acquisition. Then, for each run of the experimentation, 10 acquisitions were collected, one every 5 cycles.

10.2.3 *Injection molding results*

10.2.3.1 *Analysis of the factorial experiments*

Table 10.12 reports the results of the Analysis of Variance (ANOVA) performed, with a General Linear Model, on the factorial plans designed for each one of the polymers selected for the injection molding experiments. In order to determine the statistical significance of each factor and interaction, the P-value was used with a threshold value of 0.05. The results of the ANOVA indicate that, for all the polymers, all the factors included in the model resulted significant (P-value $<$ 0.05). The factors having P-value lower than 0.05 can be considered statistically significant on the response variable (i.e. F_{peak}).

10.2.3.2 *Effect of mold roughness*

The effect of changing the combination of μEDM parameters resulted significant, regardless of polymer selection. For all the polymers, the maximum overall ejection force was acquired when using mold *insert D*, indicating that with this mold topography the solidified polymer part was subjected to the highest stresses during the demolding phase. In particular, the average effect of improving the surface finish of the cores by changing the parameters from combination from *D* to *C*, from *C* to *B* and from *B* to *A*, is to reduce F_{peak} by 23%, 10% and 22%, respectively.

The higher roughness amplitude *Sa*, which is due to the adoption of higher intensity of the discharge impulse, explains the higher F_{peak} values observed for mold insert *D*. Moreover, as described in the roughness characterization, the topography of these cores is also characterized by higher average height of the protruding peaks (i.e. higher *Spk*) and higher depth of valleys (i.e. higher *Svk*). Indeed,

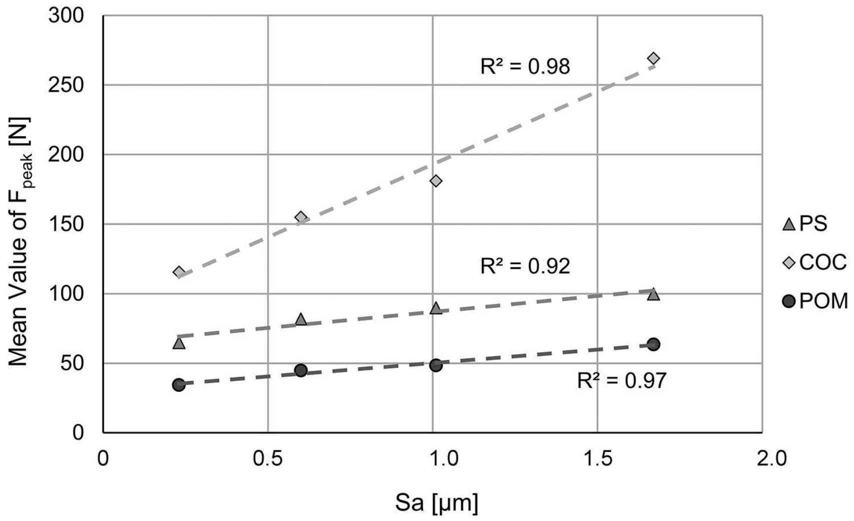

Figure 10.15: Effect of cores roughness on the mean value of the demolding force peak for the three polymers.

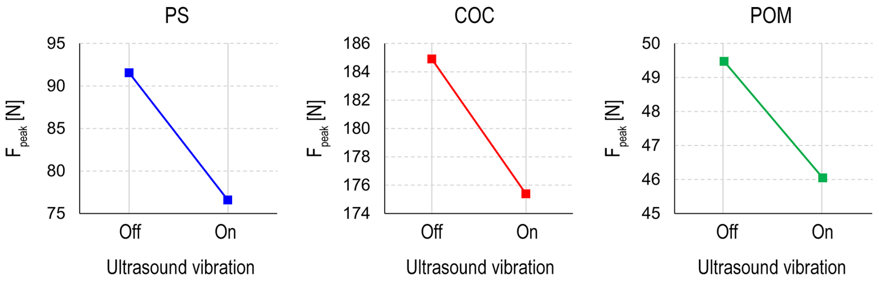

Figure 10.16: Main effect plots for the effects of ultrasound vibration on the mean value of the demolding force for the three polymers.

these functional parameters provide insight on both the friction and the mechanical interlocking generating at the part/mold interface and determining the demolding force, as previously discussed in section 10.1.

The demolding force peak was observed to be linearly correlated to the measured surface roughness, in particular to the value of *Sa*, as shown in Figure 10.15. This suggest that the effect of reducing the amplitude of surface roughness is to linearly reduce the demolding force peak. However, it can be observed that the demolding force is more sensitive to increase of *Sa* when molding COC, which characterized by lower melt viscosity and thus by higher replication capability.

10.2.3.3 *Effect of ultrasound vibration*

The main effect of vibrating the mold cavity before the ejection phase resulted in a reduction of the mean value of the demolding force peak for all the selected polymers, as reported in Table 10.13. However, the intensity of this reduction is not consistent among the dif-

		PS		COC		POM	
Insert	Sa [μm]	Off	On	Off	On	Off	On
A	0.23	66	63.9	115.3	115.7	34.6	34.1
B	0.62	88.3	75.4	158.9	151	45.3	44.3
C	1.01	98.7	80.9	187.1	175.1	49.7	47.1
B	1.74	113.5	86.1	278.4	259.9	68.2	58.8

Table 10.13: Effect of ultrasound vibration on the average value of the demolding force peak for the different combinations of polymer selection and mold roughness.

ferent polymers. Specifically, the improvements were more marked for PS (Figure 10.16 (a)), where the mean value of F_{peak} reduced by 16%. Conversely, the effect of the ultrasound vibration was smaller for COC (Figure 10.16 (b)) and POM (Figure 10.16 (c)), for which the response variable reduced by 3% and 7%, respectively.

The reduction of the demolding force that results from the use of an ultrasound vibration, applied to the mold cavity before the beginning of the ejectors stroke, can be reconducted to its effects on the part/mold interface interactions. Indeed, during the filling phase the polymer melt is able to replicate mold topography creating mechanical interlocking and thus affecting the stiction between the two surfaces. Vibrating mold cores can affect the demolding force by reducing these interactions, thus favoring the sliding of the two surfaces that occurs during the ejection phase.

10.2.3.4 *First order interactions*

The analysis of variance of the experimental plans indicated that the interaction between the mold surface roughness *Sa* and the use of ultrasound *US* is important for a complete understanding of the effects of vibrating the mold cavity on the ejection phase. Figure 10.17 reports the interaction plots for the three polymers, indicating that the DoE factors yield diverse interactions for the different polymers.

The effect of the ultrasound vibration is more marked when the mold is characterized by the highest surface roughness (i.e. *insert D*). With this mold topography, when using polystyrene, the use of ultrasound technology yields a reduction of the mean value of F_{peak} by 24%. Similarly, for POM the maximum reduction (-14%) was observed with mold *insert D*.

When molding COC the effect of ultrasounds is negligible (average reduction: -2%) for all the values of mold surface roughness (Figure 10.17 (b)). Conversely, for PS (Figure 10.17 (a)) and POM (Figure 10.17 (c)) the effects are increasingly evident for higher roughness. However, for these polymers below a certain level of *Sa* (0.23 μm for PS and 0.62 μm for POM) the effect is negligible.

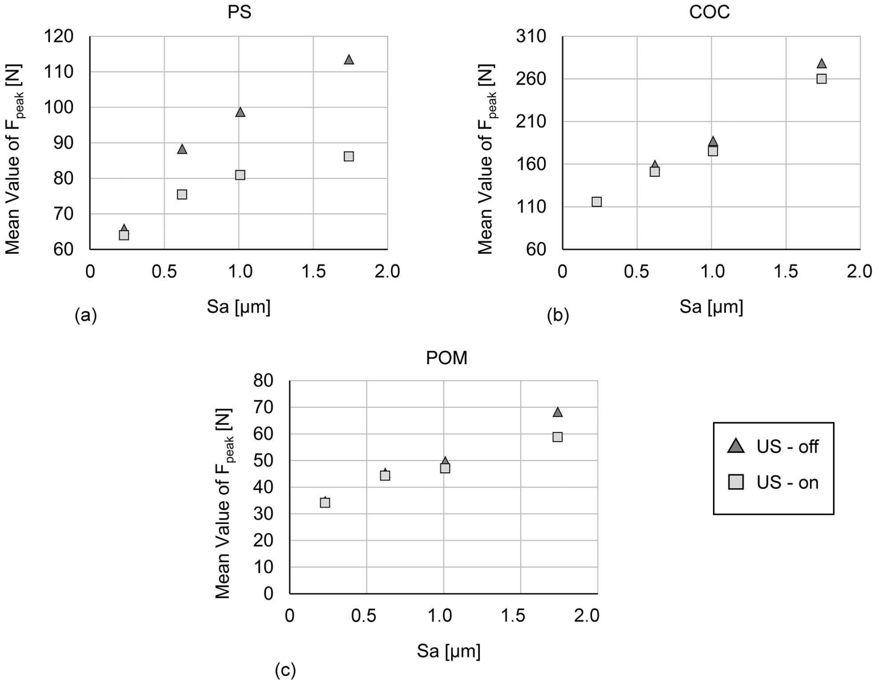

Figure 10.17: Interaction plots for the three polymers, (a) polystyrene, (b) cyclic olefin copolymer and (c) polyoxymethylene.

Considering the interactions between *US* and *Sa*, it is possible to observe that the effect of the ultrasound vibration is related to the replication of mold topography that occurs during the filling phase of the injection molding process. The oscillations induced in the mold cavity can reduce the mechanical interlocking at the part/mold interface and consequently the stiction that has to be overcome by the ejectors. In fact, vibrating the mold cores can result in heating of the mold surface, which results in localized softening of the polymer reducing its mechanical properties. Thus, both the ploughing of the solid metal surface asperities and the elastic deformation of the polymer surface asperities are favored.

However, the response to the application of ultrasounds is not consistent for all the polymers, suggesting that they yield different behavior when the mold cavity is vibrated. Indeed, the polymer used for the experiments have different mechanical properties and different dependence to temperature variations.

10.2.3.5 *Effect of ultrasound vibration on cores temperature*

The effects of the proposed demolding technology were further investigated analyzing the thermal conditions at the mold-part interface by means of thermal imaging. The thermal analysis of mold cores vibration was performed using an infrared camera (FLIR Systems, Thermovision A40), which was mounted as shown in Figure 10.18. The camera has a 24° x 18° field of view and operates in the spec-

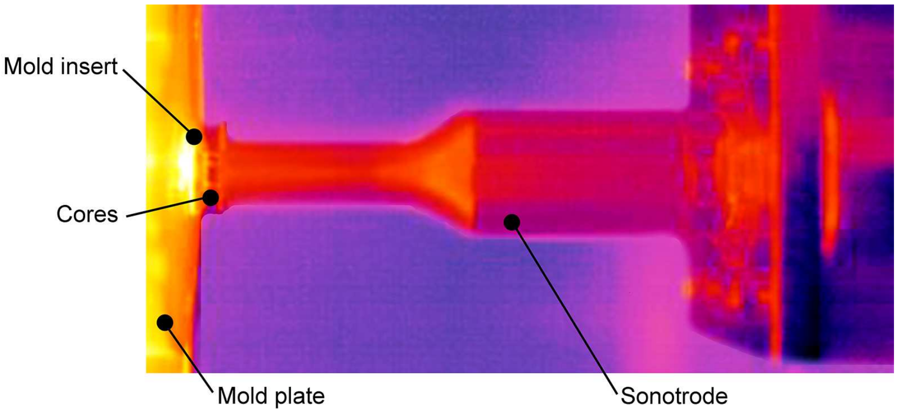

Figure 10.18: Thermal imaging of the contact between the sonotrode and the mold cores.

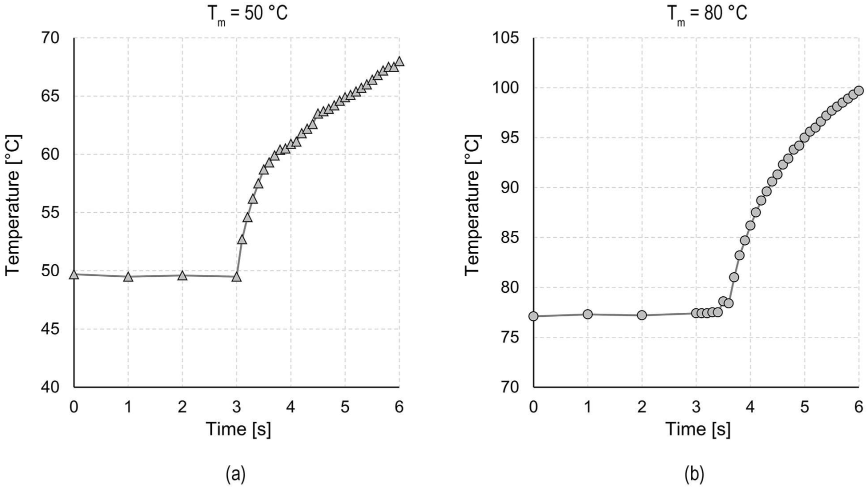

Figure 10.19: Evolution of cores surface temperature during ultrasound vibration, for mold temperatures of (a) 50 °C and (b) 80 °C.

tral range of 7.5 to 13 μm with a spatial resolution of 1.3 mrad. The detector has a thermal sensitivity of 0.08 °C at 30 °C.

The vibration of the cores in the mold was directly observed during the contact with the sonotrode for the 3 seconds of vibration time. The tests were carried with a mold temperature of 80 °C, used for PS and POM, and of 50 °C, used for COC. For each set mold temperature, the thermal analysis were repeated three times (Figure 10.19), averaging the temperature on the three mold cores that are in front of the camera. In order to guarantee a proper thermal measurement, the analysis were performed without injecting the polymer, which would block the direct viewing of the cores.

Table 10.14 reports the results of the thermal measurements of the cores surface during ultrasound vibration. It can be observed that the effect of vibrating the mold cores is that of increasing the mold surface temperature. Specifically, for a mold temperature of 50°C,

	Pin Temperature		
Mold Temperature [°C]	Avg.	Std. Dev.	ΔT
50	66.9	2.3	16.9
80	98.6	1.5	18.6

Table 10.14: Results of thermal measurements of mold cores during ultrasound vibration.

	Ejection force peak [N]		
Polymer	US Off	US On	Reduction [%]
PS	91.6	76.6	-16
COC	184.9	175.4	-5
POM	49.5	46	-7

Table 10.15: Ejection force peak values with and without the application of the ultrasound vibration.

which was adopted for COC, the average increase if of about 17°C (Figure 10.19 (a)). While for a mold temperature of 80°C, which was set for PS and POM, the increase was of about 19°C.

Table 10.15 and Table 10.16 compares the reduction of the demolding force peak and that of the storage modulus of the polymer when the mold cores are vibrated using the ultrasound. It can be observed that the effect of the ultrasound is maximized for PS which mechanical properties are more reduced when the ultrasound vibration is applied. The effect is similar, but mitigated, when molding POM that is characterized by a smaller reduction of the storage modulus. Conversely, the reduction of the mechanical properties is less significant for COC, for which also no significant reductions of the demolding force where observed.

Considering the results of the thermal measurements, the effect of the ultrasound-assisted ejection on the reduction of the demolding force is explained by the heating effect induced at the part/mold interface by the ultrasound vibration. Indeed, the higher surface temperature of the mold lead to a decrease in the mechanical properties

	Storage Modulus [Mpa]		
Polymer	Mold Temp. US On	Mold Temp. US On	Reduction [%]
PS	2614	1219	-53
COC	2483	2418	-3
POM	1718	1456	-15

Table 10.16: Effect of the heating induced by the ultrasound vibration on the storage modulus for the three polymers.

of the polymer side of the interface. Hence, during sliding the resistance to deformation of the polymer, which had replicated the mold topography during filling, is smaller and so is the friction force. Moreover, polymers whose mechanical properties are more reduced by a higher temperature (i.e. PS) are more sensitive to the application of the ultrasound vibration. In general, the ultrasound-assisted setup designed in this research has been proven to effectively reduce the ejection friction. Specifically, the ultrasound vibrations reduces the resistance to deformation of the polymer side of the interface. However, the interactions with the mold surface roughness and polymer selection were shown to significantly affect the ejection force reduction.

10.3 EFFECTS OF MACHINED CAVITY TEXTURE

section 10.1 and section 10.2 discussed the effects of mold surface generated by micro milling and micro electro discharge machining on ejection friction. In this section, in order to identify the parameters that most appropriately correlate ejection friction to the machining process, the two machining technologies are compared.

10.3.1 *Texture characterization*

10.3.1.1 *SEM analysis*

The characterization of mold cores surfaces machined according the description reported in subsubsection 6.1.2.3, initially performed by means of SEM, clearly showed the different surface textures typically obtained from the two micro machining technologies (Figure 10.20).

Due to the adopted μM strategy, the surface of the milled cores is characterized by visible marks oriented in the circumferential direction (i.e. perpendicularly to the ejection direction) with small axial depth of cut, as shown in Figure 10.20 (a). Moreover, some 25° oriented marks are present because of vibrations induced by machine axis inversion, which is caused by the circular tool trajectory on the X-Y plane. Conversely, the surface of the μEDM cores, shown in Figure 10.20 (b), is characterized by the presence of a multitude of overlapping discharge craters.

10.3.1.2 *Roughness analysis*

The impact of the different machining processes on the demolding force was experimentally investigated by evaluating the texture of the machined cores, as shown in Figure 10.21. Several profile roughness parameters were evaluated in order to identify those that most properly correlate the characteristics of cores texture to the ejection force.

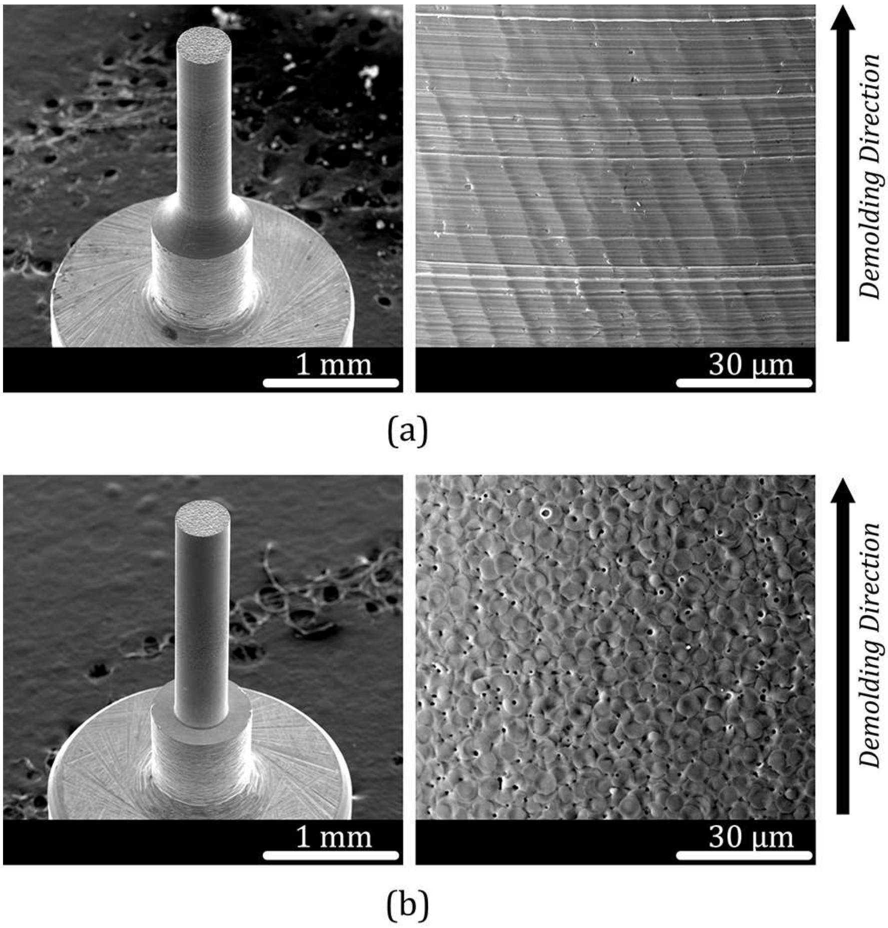

Figure 10.20: SEM micrographs of the mold cores for (a) μM and (b) μEDM at magnification of $100X$ (left) and of $2500X$ (right) [139].

	μEDM		μM		
Parameter	Mean	Std. Dev.	Mean	Std. Dev.	p-value
Rp/μm	1.166	0.063	0.52	0.092	0.000
Rv/μm	0.888	0.103	0.526	0.161	0.001
Rz/μm	2.053	0.153	1.000	0.171	0.000
Rk/μm	0.658	0.069	0.633	0.107	0.632
Rpk/μm	0.386	0.021	0.261	0.045	0.000
Rvk/μm	0.290	0.030	0.335	0.054	0.101
Ra/μm	0.219	0.019	0.211	0.013	0.415
RSm/mm	0.018	0.001	0.024	0.002	0.000

Table 10.17: Means and standard deviations of profile roughness parameters for the machined cores, evaluated according to [143, 144]. These values were calculated on 72 profiles: 3 profiles area, 4 areas per core and 6 cores per cavity.

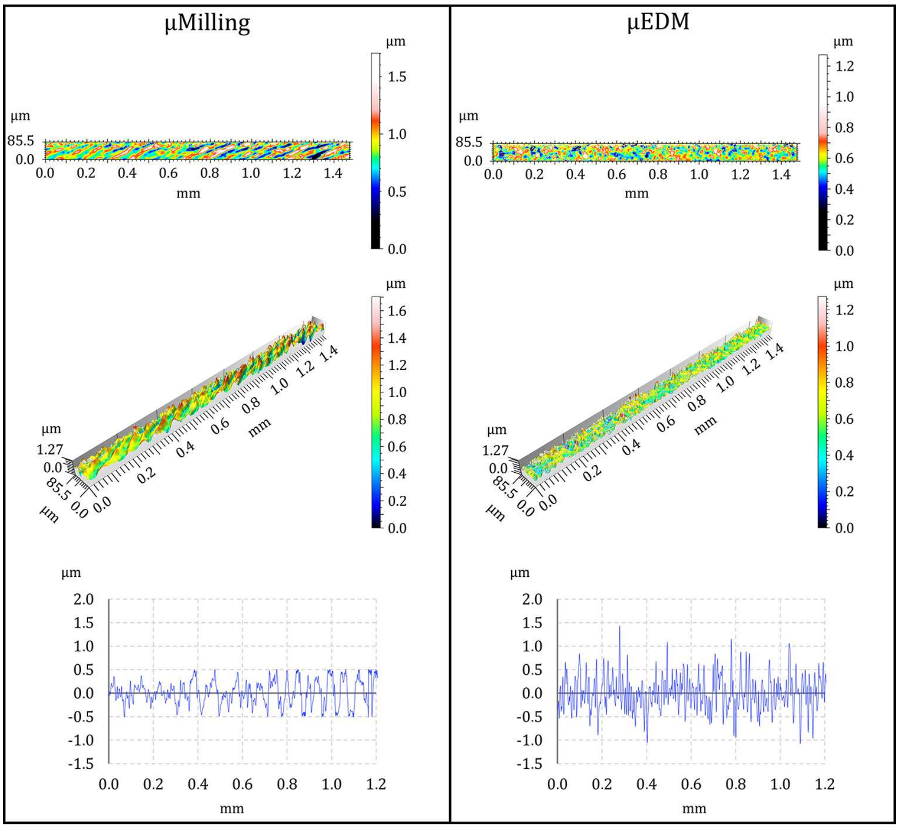

(a) (b)

Figure 10.21: 2D view, 3D view and profile of the (a) micro milling and (b) micro EDM mold topographies [139].

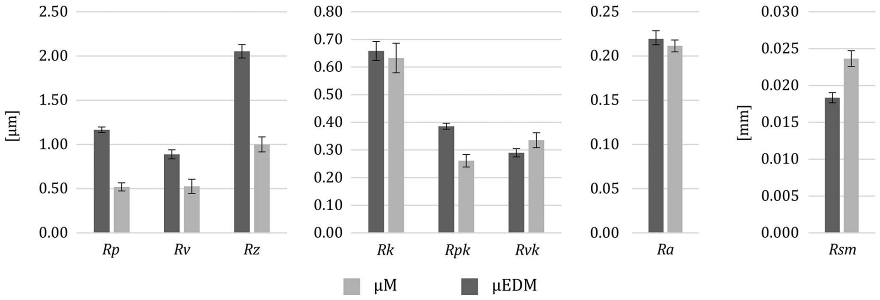

Figure 10.22: Profile roughness parameters for the machined mold cores. Error bars represent the standard deviation [139].

Level	T_m /°C	V_{inj} /mm/s	P_h /bar	Machining technology -
Low	95	100	160	μM
High	120	400	650	μEDM

Table 10.18: Experimental DoE plan designed for the μIM experiments.

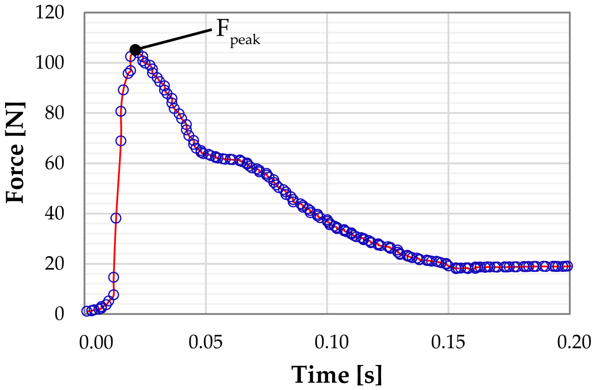

Figure 10.23: Evolution of the acquired ejection force signal [139].

Table 10.17 and Figure 10.22 report the roughness characterization results, which confirm that both μM and μEDM produced surfaces characterized by similar values of Ra. Specifically, the analysis of the extracted profiles returned average Ra values of 0.219 μm for μEDM and 0.211 μm for μM.

A univariate analysis of variance (ANOVA) was performed considering the effect of the machining technology on each parameter. The p-values reported in Table 10.17 indicate that the change in machining technology significantly influenced all the considered roughness parameters ($p\text{-value} < 0.05$), except Ra, Rk and Rvk.

The higher average height of the protruding peaks (i.e. higher values of Rpk) suggests that the μEDM surfaces should offer increased friction. However, they are characterized by craters having lower mean line peak spacing (RSm), if compared to μM. Indeed, a complete understanding of the tribological conditions at the interface during the ejection phase should consider both the mechanical effect of surface asperities and the adhesion effect due to the mechanical interlocking generated during the filling phase, as observed in section 10.1. Therefore, in order to understand which one of these aspects predominantly affects the demolding force and which roughness parameter is more correlated to the ejection friction, the ejection force results from the μIM experiments need to be analyzed.

10.3.2 *Experimental design*

The possible interactions between the different core textures and μIM processing conditions were investigated by varying the main process parameters according to a two-level, four-factor Design of Experiment (DoE) plan. Three μIM parameters were selected based on results reported in subsubsection 10.1.3.2: mold temperature (T_m), injection speed (V_{inj}) and holding pressure (P_h). In fact, these are the main factors determining the capability of the polymer to replicate mold texture. A full factorial plan was designed considering also the machining technology as a factor (Table 10.18). The introduction in the DoE of the '*Machining technology*' factor allows the statistical analysis of the effect of cores topography on the demolding force. Thus, allowing the understanding of the relation between the main effect of this DoE factor and the characterized roughness parameters.

The demolding signal (Figure 10.23) is characterized by a rapid growth of the force at the very beginning of the stroke until it reaches a peak, which represents the force required to overcome the initial stiction. The response variable for the DoE plan was the demolding peak force signal (F_{peak}), because it is the maximum load stressing the molded part during the ejection phase.

The stability of the ejection system was initially verified by carrying out several dry cycles of the clamping and ejection units. The ejectors were cycled 100 times (ejector stroke: 3 mm; ejection speed: 10 mm/s), allowing the evaluation of the functionality and robustness of the demolding force acquisition setup. The cycles were performed at a mold temperature of 120 °C that was the maximum value set in the following μIM experiments. The acquired dry cycle signals indicated that the demolding force reaches a stable value after about 50 cycles. Moreover, the stabilized value of the dry demolding force peak was about 10 N (with a standard deviation of 0.2 N) with both sets of cores machined by μM and μEDM. Consequently, the dry force was neglected when comparing tests made with the differently machined sets of cores.

10.3.3 *Effect of the machining technology*

The ANOVA performed on μIM experimental results indicates that all the main factors considered in the investigation significantly affect the demolding force peak (Table 10.19). In particular, the selection of different machining technologies for the generation of cores surface affect the tribological conditions at the part-tool interface during demolding. In particular, the main effect of changing the machining technology from μM to μEDM, whilst maintaining a similar value of *Ra*, was to reduce the mean value of the ejection force peak by 8%, as shown in Figure 10.24 (a). This indicates that the functionality of the

Source	Degree of freedom	Adj MS	F–value	p–value
Technology	1	2489.8	158.2	0.000
T_m /°C	1	23100.3	1468.0	0.000
V_{inj} /mm/s	1	18356.3	1166.5	0.000
P_h /bar	1	3681.8	234.0	0.000
Technology · T_m	1	12486.5	793.5	0.000
Technology · V_{inj}	1	290.9	18.5	0.000
Technology · P_h	1	2313.4	147.0	0.000
$T_m \cdot V_{inj}$	1	197.5	12.6	0.001
$T_m \cdot P_h$	1	3915.5	248.8	0.000
$V_{inj} \cdot P_h$	1	21.4	1.4	0.248
Total	79			

Table 10.19: ANOVA table for the effects of the machining technology and μIM process parameters on the ejection force.

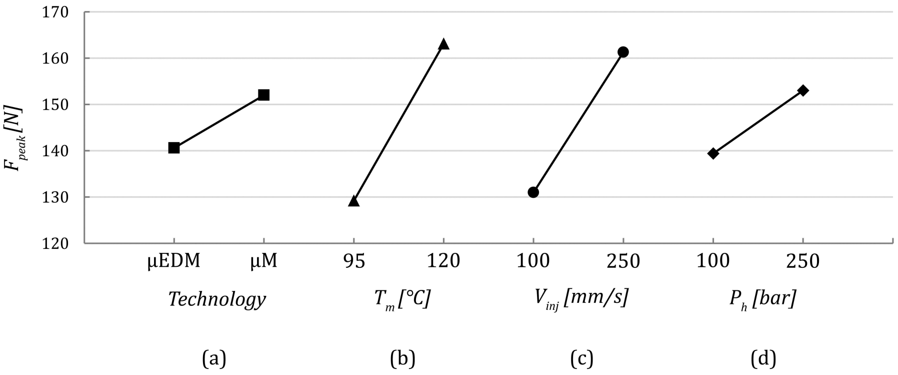

Figure 10.24: Main effect plots for the process parameters analyzed in the DoE experimental plan [139].

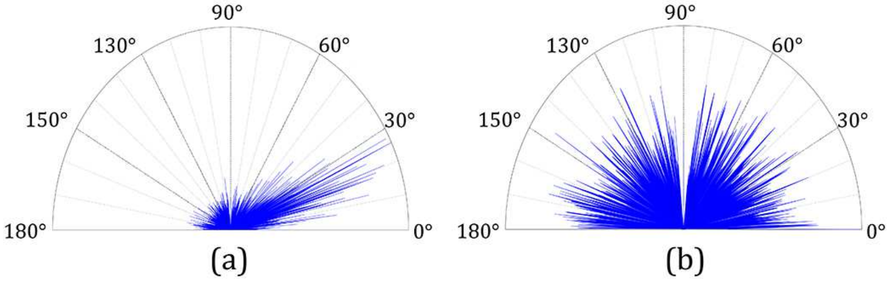

Figure 10.25: Isotropy of the cores textures generated by (a) μM and (b) μEDM [139].

surfaces was different, despite being characterized by similar value of *Ra* that is the parameter commonly used to specify mold roughness for molds. However, as reported inTable 10.17, other roughness parameters were significantly different for μM and μEDM, thus providing more evidence about the main effect of the '*Machining technology*' factor.

The main effect of the machining technology observed in the DoE result contrasts with the indications provided by the trend evaluated for the average distribution of protruding peaks. Specifically, compared to μM, the μEDM surface is characterized by higher values of *Rpk* (+48%) and of *Rp* (+124%). Hence, the frictional effect between the two sliding surfaces should increase due to the higher effect of the mechanical asperities characterizing the μEDM roughness profile. However, the understanding of the frictional effect at the interface should consider also the mechanical interlocking generated at the interface during the process. The polymer melt during the injection phase is able to replicate the larger valleys characterizing the μM topography (higher *Rvk* and *RSm*), thus increasing the stiction at the polymer-mold interface.

The different demolding behavior observed with the two core textures is also supported by their surface isotropy. Indeed, a surface texture can be characterized by a dominant direction or orientation bias, which can markedly affect its functionality (e.g. friction and adhesion in injection molding).

The surface isotropy of the differently generated mold topographies was determined and quantified using the MountainsMap software, which employs the Fourier transform and the autocorrelation function to determine the power spectrum and the isotropy parameter [152, 153].

The results of the analysis indicated that the μEDM surface (isotropy parameter: 60%) was characterized by higher isotropy compared to the one machined by μM (isotropy parameter: 23%). Moreover, the power spectrum integrated in polar coordinates (Figure 10.25) - in which the angle with the largest vector represents the principal direction of the texture - was taken in consideration. It was possible to determine that the μM texture is characterized by 25° oriented marks. Thus, compared to μEDM, the oriented μM texture should offer a higher interface interaction during the demolding phase.

In general, the results of the DoE analysis indicated that the functionality of the cores surface in terms of demoldability cannot be described simply using Ra. Indeed, this parameter was proven too general to represent the complexity of the friction phenomena occurring in the μIM process. Thus, the specification and control of mold surface quality should consider additional surface topography parameters, such as Rvk, RSm, Rvk, RSm and isotropy.

10.3.4 *Effect of injection molding process parameters*

The main effect of increasing the mold temperature from 95 to 120 °C is to increase the ejection force peak by 26%, as shown in Figure 10.24 (b). This effect is explained considering the replication of mold topography, and the consequent mechanical interlocking, that is generated when the melt polymer fills the cavity. This effect could be explained considering the replication of mold topography. Indeed, mold temperature has been identified in the literature as the main parameter controlling the replication of micro features in μIM [18]. Similarly, increasing the injection speed from 100 to 250 mm/s results in an ejection force peak increase of 23% (Figure 10.24 (c)), due to the higher replication and consequent higher adhesion at the interface. Interestingly, the main effect of increasing the packing pressure, which should result in lower diametric shrinkage and then in lower friction, is dominated by the markedly high interface stiction. Specifically, by varying it from 100 to 250 bar, the peak of the force signal increases by 10% (Figure 10.24 (d)). Hence, the identification of a proper description of mold roughness was confirmed to be crucial for the understanding of the phenomena that characterize the demolding tribology.

10.3.5 *Effect of first order interactions*

The plots reported in Figure 10.26 clearly indicate the strong interactions between the cores texture and the μIM process parameters that promote the replication, such as mold temperature and holding pressure.

The interaction between the selection of different machining technologies and the mold temperature is particularly significant, as shown in Figure 10.26 (a). In particular, at low value of T_m the ejection force is higher for μM than for μEDM texture, while the trend is the opposite when molding at T_m=120 °C, as shown in Figure 10.27. This behavior is related to the ability of the molten polymer to replicate the cores texture. In fact, at high value of mold temperature, the polymer

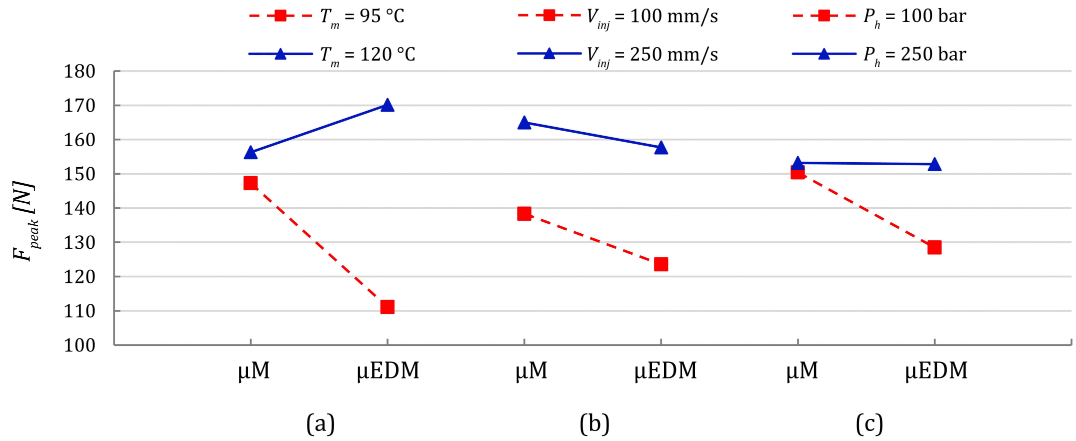

Figure 10.26: Interaction plots between the machining technology and μIM process parameters [139].

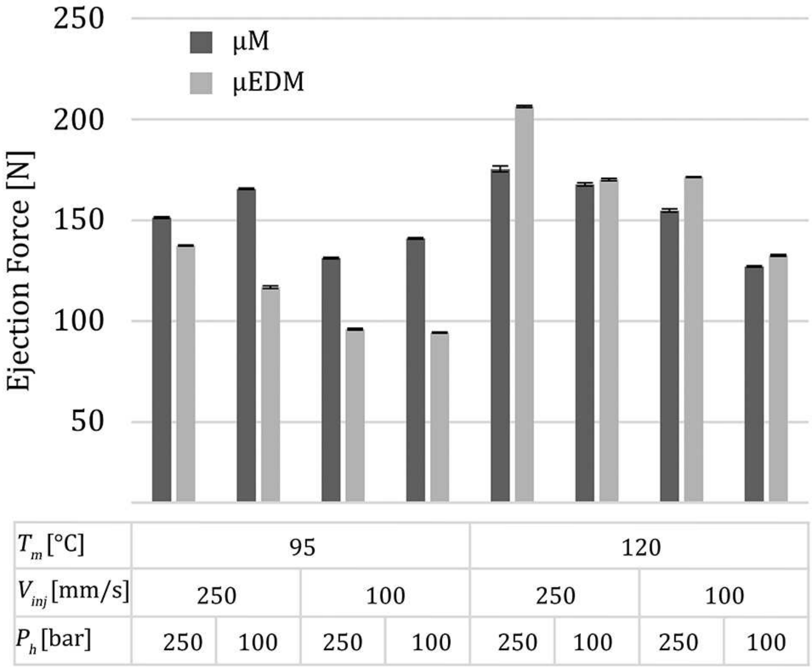

Figure 10.27: Ejection force results. Error bars represent the standard deviation (maximum ejection force peak variability: 1.5 N) [139].

melt better replicates the μEDM surface texture, which is characterized by smaller (*RSm* for μEDM is 25% smaller than for μM) but deepest valleys (*Rpk* for μEDM is 48% greater than for μM). Hence, with a mold temperature of 120 °C the effect of changing the machining technology from μM to μEDM is to increase F_{peak} by 9%. Conversely, at low values of T_m, the mechanical interlocking at the polymer-mold interface is smaller, and the effect of changing from μM to μEDM is to decrease F_{peak} by 25%.

The interaction between the machining technology and the injection speed resulted less significant, as shown in Figure 10.26 (b). However, it confirmed the effect of mold texture replication on F_{peak}, showing that with low value of the injection speed the effect of changing the machining technology from μM to μEDM is to reduce F_{peak} by 11%. Conversely, with higher injection speed the surface replication is higher and the effect of the machining process is smaller (-4% when using μEDM instead of μM).

Figure 10.26 (c) shows how the different cores textures and the packing pressure interact to affect the experimental value of the demolding force. Specifically, when molding with high value of P_h the effect of selecting different machining technology is negligible. Conversely, when adopting low value of P_h, the cores surface generated by μM yields a higher peak (+17%) of the ejection force.

10.4 DISCUSSION

In this chapter, the effects of different surface generation strategies on the ejection force were characterized considering the impact of different machining processes. The surfaces characteristics were correlated to their influence on ejection friction, evaluated as the experimental value of the demolding force. Experimental campaigns were conducted, by varying the main process parameters, to investigate possible interactions between the different cavity textures and injection molding process conditions.

All the experiments were characterized by the adoption of a *deep cores* geometry that was design specifically to study the tribological conditions at the interface between the polymer and the tool deep cores. Indeed, this design allowed the maximization of the interactions at the interface between the mold and the polymer, and thus of ejection friction. The demolding phase was optimized by means of design of experiments, considering the combined effect of polymer replication onto deep cores and surface finish, in relation with the main μIM process parameters.

The generated mold surfaces were thoroughly characterized by means of scanning electron microscopy and by reconstruction of the topography. Particular attention has been given to the evaluation of profile and surface roughness, which was carried out considering several parameters. The results of the injection molding experiments indicated that *Ra* is too general to be correlated with the complexity of ejection friction, especially considering the different technologies available for micro molds manufacture. In order to specify and control micro mold surface quality, average parameters need to be complemented by a better description of valleys width.

The results of the characterization of surfaces generated by either micro milling or micro electro discharge machining indicated that ejection friction is controlled by the *mechanical interlocking* created at the polymer/mold interface during the filling phase. The latter being strongly related to the replication capability of the polymer.

The results of the experimental tests showed the strong interactions between the effect of mold surface topography and the ones of those μIM process parameters that promote the replication, such as mold temperature and holding pressure. In particular, at low value of mold temperature, the ejection force is higher for the micro-milled topography, because the polymer melt during the injection phase is only able to replicate the larger valleys characterizing the μM topography (higher *Rvk* and *RSm*). Conversely, at high value of mold temperature, which is a common condition in micro injection molding, the ejection force is higher for the μEDM topography, since the polymer melt better replicates the μEDM surface topography, characterized by thinner valleys (lower *RSm*).

The molding polymer affected the ejection phase by modifying the interface interactions between the part and the mold. In particular, a combination of worst surface finishing and low viscosity resulted in higher replication of the cores surface topography and thus in higher demolding forces. This replication-related effect was investigated by evaluating the molded parts through holes inner surface roughness. Moreover, the molding polymer was observed to interact with the different micro milling strategy selection. In fact, the better the surface finish, the smaller the possibility for the melt polymer to replicate the mold topography, thus producing smaller interface interlocking and consequently less demolding stresses.

Finally, in this chapter, a novel ultrasound-assisted system was used to vibrated mold cores in order to reduce interface stiction during the ejection phase. The online monitoring of the demolding force allowed the evaluation of the different tribological conditions at the part/mold interface. The injection molding experiments were carried out by varying mold roughness and by selecting different polymers. The main effect of vibrating the mold cavity before the ejection phase resulted in a reduction of the mean value of the demolding force peak for all the selected polymers. However, the intensity of this reduction is not consistent among the different polymers. In fact, vibrating the mold cores resulted in heating of the mold surface, which results in localized softening of the polymer reducing its mechanical properties. Thus, both the ploughing of the solid metal surface asperities and the elastic deformation of the polymer surface asperities are favored. The effects of the proposed demolding technology were further investigated by means of thermal imaging analyzing the heating at the mold-part interface. The results showed that, when the ultrasound vibration is activated, the higher is the reduction of the mechanical properties that accompanies the heating of the mold surface the higher is the reduction of the demolding force.

Part IV

SURFACE MODIFICATION

11

EFFECT OF MOLD SURFACE COATINGS ON THE FILLING RESISTANCE

The filling phase of thin-wall injection molding cavities is critical due to the large cavity pressure gradient required during the filling phase, which can inhibit complete replication of the mold cavity surface, particularly at locations distant from the gate. Low-friction mold surface coatings can be used to improve outcomes in such scenarios, however the understaind of their effects on the melt flow resistance is still unclear in the literature. This chapter presents the results of the online characterization of different coatings for different applications and different molding materials.

As introduced in subsection 6.2.1, the analysis the effects of mold surface coatings on the filling flow comprised two consecutive investigations:

i. general investigation (*Investigation I*);

ii. effect of wall slip (*Investigation II*);

11.1 EFFECT OF MOLD SURFACE COATINGS ON POLYMER FILLING FLOW - INVESTIGATION I

11.1.1 *Experimental design*

The flow of the polymer melt was experimentally analyzed by varying the injection speed (V_{inj}) for both polymers, the mold temperature (T_m) only for PS and the melt temperature (T_b) only for PET. The range values for the selected controllable process variables were defined considering the literature, recommendations of the materials supplier and the technological limits of the available experimental setup (Table 11.1). The tests were performed using different depth of the coated channels for the two polymers. In particular, a channel depth of 800 μm was adopted for PET, a depth of 400 μm for PS, accordingly with their different rheological properties. To ensure

Parameter	PS	PET
T_m [°C]	80, 120	15
T_b [°C]	240	300,280
V_{inj} [mm/s]	100, 200, 300, 450, 600, 750	

Table 11.1: Processing conditions for the experiments.

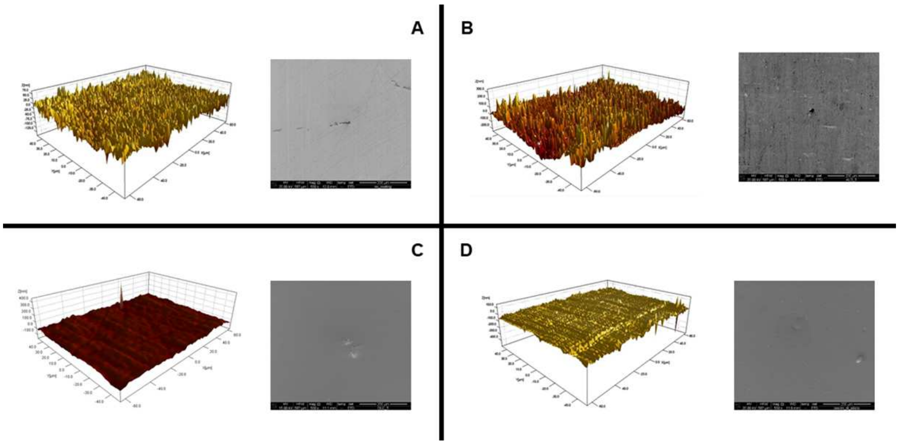

Figure 11.1: Topographies and SEM micrographs taken at 500X of mold surface coatings.

the stability of the injection phase, 20 injection cycles were performed before the acquisition of the cavity pressure. For each molding condition 5 acquisitions were collected, one every 5 cycles and each material was taken from a single batch.

11.1.2 *Coatings characterization*

The coated mold inserts (shown in Figure 6.4) were evaluated both in terms of surface quality and channel geometry. Morphology and continuity of the coated surface was observed using scanning electron microscopy (FEI, Quanta SEM 400). Figure 11.1 shows the topographies and the SEM micrographs for the coated surfaces.

The surface roughness of the coated inserts was characterized using a contact stylus roughness tester (Zeiss-TSK Surfcom 1400A), with a cut-off filter of 0.25 mm and a background noise below 7 nm *Ra*. Results were not showing significant differences in roughness parameters among coated surfaces, with average values of *Ra* in the range 25-45 nm. For the purposes of the current investigation, no significant differences were observed and therefore it was assumed that surface topography is not influencing the filling flow.

The mold cavity inserts were also characterized in terms of form errors and depth uniformity of the coated channel, using a coordinate measuring machine (ZEISS, Prismo VAST 7) with contact probing, to ensure that no significant geometrical differences among channels exist after coating.

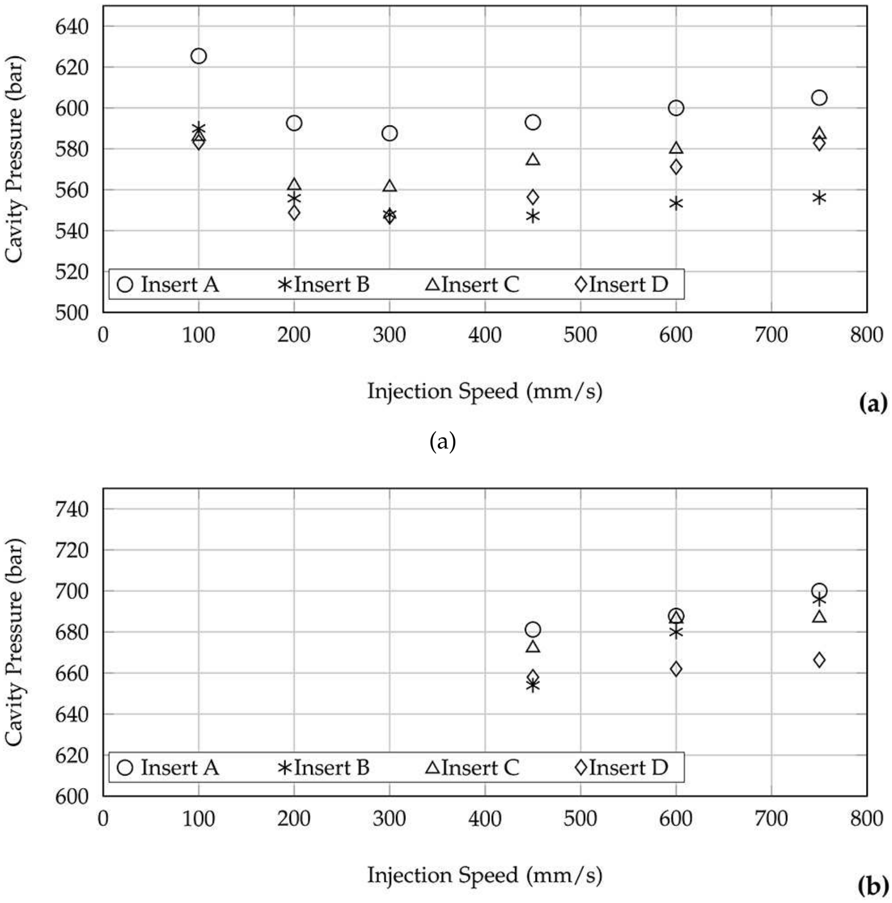

(a)

(b)

Figure 11.2: Cavity pressure measurements for PET at a) T_b = 300 °C and b) T_b = 280 °C [138].

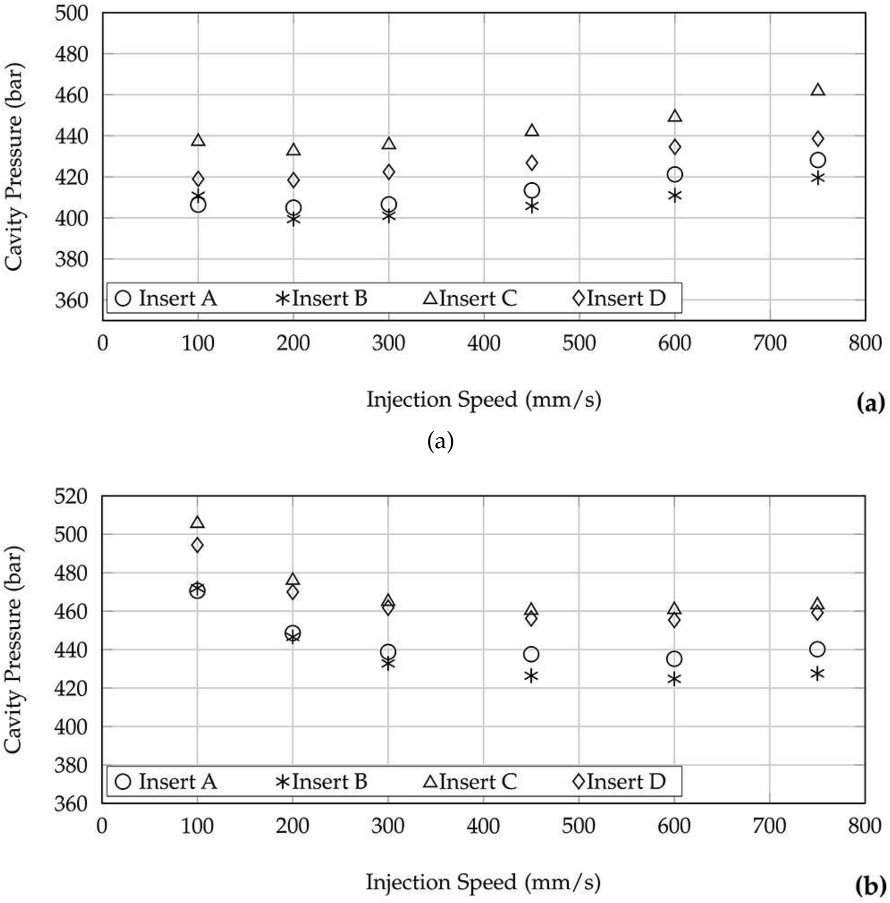

(a)

(b)

Figure 11.3: Cavity pressure measurements for PS at a) T_m = 120 °C and b) T_m = 80 °C [138].

11.1.3 *Injection molding results*

11.1.3.1 *Effects of mold surface coatings*

Figure 11.2 and Figure 11.3 show the relationship between the steady-state cavity pressure and the injection speed for PET and PS.

Comparing the coated inserts with the uncoated one it is clear that coatings reduce PET flow resistance up to 8% at T_b = 300 °C. This effect is still evident but less significant (-5%) at T_b = 280 °C. DLC has a lower influence on pressure reduction at both temperatures while Al_2O_3 and SiO_x have a larger effect but it is very sensitive to the melt temperature. The same coatings have different effects on PS flow resistance at T_m = 80 °C. While Al_2O_3 reduces the pressure up to 3% at high injection speeds, DLC and SiO_x increase it up to 6%. At Tm = 120 °C the coatings consistently show the same trend but with attenuated effect. Considering the minor pressure reduction obtained with PS further investigations were focused only on PET.

11.1.3.2 *Evaluation of flow conditions*

According to Dealy, for a straight, rectangular channel having length, L, width, w, and thickness, h, with the assumptions of a fully developed steady state laminar flow with no-slip on the wall, the apparent shear rate and real shear stress in the *slit model* are given by [137]:

$$\dot{\gamma} = \frac{6Q}{wh^2} \tag{11.1}$$

and

$$\tau_{w(real)} = \frac{wh}{2(w+h)} \cdot \left(\frac{-\Delta P}{L}\right) \tag{11.2}$$

where Q is the volumetric flow rate and ΔP the pressure drop. According to the Walter correction [154], the wall shear rate of a non-Newtonian fluid can be determined by:

$$\dot{\gamma}_{w(real)} = \dot{\gamma}_{w(app)} \cdot \left(\frac{2}{3} + \frac{1}{3}n\right) \tag{11.3}$$

where n is the power law index, which can be calculated using the Sch$\ddot{u}$mmer approximation:

$$x* = \left(\frac{3n+1}{4n}\right)^{\frac{n}{n-1}} \tag{11.4}$$

where x^* is a weak function of n, which is 0.79 for a slit geometry [154].

In injection molding the wall shear stress increases with shear rate for a non-slip wall-polymer interface. According to Mhetar and Archer, there are three slip regimes: (i) a weak slip regime at low shear stresses when slip exceeds a first critical stress (0.1–0.3 MPa); (ii) a stick-slip regime at intermediate shear stresses marked by periodic

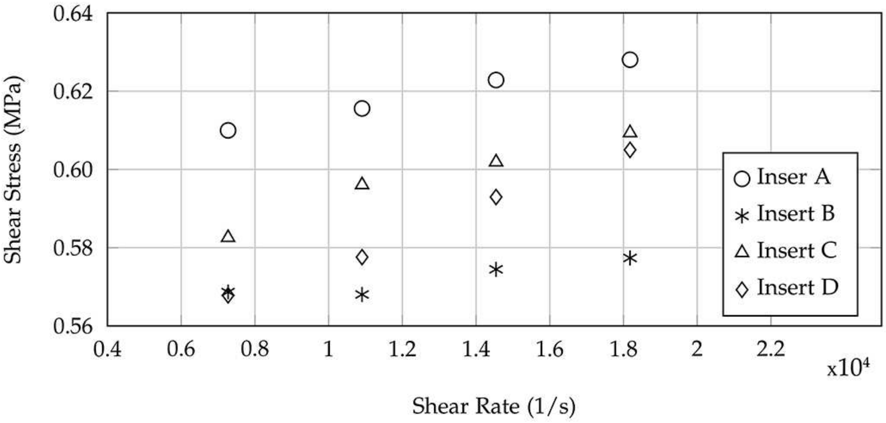

Figure 11.4: Flow curves obtained for PET at T_b = 300 °C [138].

oscillations in slip velocity and shear stress; (iii) a strong slip regime at high shear stresses [45].

Considering the cavity geometry selected for the characterization of the filling phase, which was presented in subsection 5.1.1, it is clear that the *slit flow model* can be applied as it is just a balance of the force applied to the flowing polymer melt. Indeed, the model was used to evaluate the shear rate and shear stress in the cavity using the values of the pressure drop acquired during the injection molding process.

Figure 11.4 depicts the flow curves of PET melts for the different inserts. It can be observed that for inserts A, C and D the shear stress gradually increases with shear rate with smaller slope and the polymer melt might be in the weak slip regime. For insert B the shear stress oscillates with an increasing shear rate. This indicates that polymer melt might be located in the stick-slip regime.

11.2 CHARACTERIZATION OF WALL SLIP OF POLYSTYRENE - INVESTIGATION II

The results of *Investigation I* showed that the melt flow resistance could be affected by the effects of thermal insulation and wall-slip at the polymer/wall interface. In this section, the experimental investigation of the effects of wall-slip on the melt flow resistance are presented. The experiments were characterized using only PS as due to its lower viscosity it is more likely to be affected by the wall-slip phenomenon.

11.2.1 *Experimental design*

The effects of mold coatings on wall slip and melt flow resistance were analyzed by varying the injection speed from 50 mm/s to 750 mm/s. The other main process parameters were fixed at the values

Parameter	Unit	Value
Injection Speed	mm/s	50,100,200,300,450,600,000
Mold Temperature	°C	80
Melt Temperature	°C	240

Table 11.2: Process parameters selected for the injection molding experiments.

reported in Table 11.2, which were defined considering the literature, recommendations of the materials supplier and the technological limits of the available experimental setup.

In order to achieve an adequate stability of the injection phase, 20 molding cycles were performed before the acquisition of the cavity pressure. For each molding condition 10 acquisitions were collected, one every 5 cycles.

The melt flow resistance was then evaluated by calculating the difference between the average values of the steady–state zones of the two pressure signals (i.e. gate pressure, end pressure). In fact, the difference between the pressure values measured at the two extremities of the channel represents the pressure drop characterizing the mold cavity, which was selected as the response variable for the analysis.

The measurement of the velocity profile of the polymer melt was carried out using Particle Image Velocimetry (PIV), as described in subsubsection 5.3.1.3. High-speed visualization of the filling flow was carried out in order to:

1. track the velocity profiles of the polymer across the cavity thickness as a function of the set injection speed;

2. evaluate the slip velocity of the polymer melt in the proximity of cavity walls and relate it to the different mold coatings.

11.2.2 *Injection molding results*

11.2.2.1 *Effect of coatings on flow resistance*

The effects of the selected mold coatings on the flow resistance was analyzed considering the pressure drop in the channel, which was evaluated as the difference between the steady-state values of the pressure signals acquired in the two locations.Figure 11.5 shows the dependence of cavity pressure drop on injection speed and mold coating.

Comparing the experiments performed with the different coatings and the uncoated insert, it is clear that DLC v01 is the coating that most significantly reduces the cavity pressure drop, with an average reduction of about -28%. The effects of CrN (-3%) and CrTiNbN (-2%) are still positive compared to the uncoated steel but less significant.

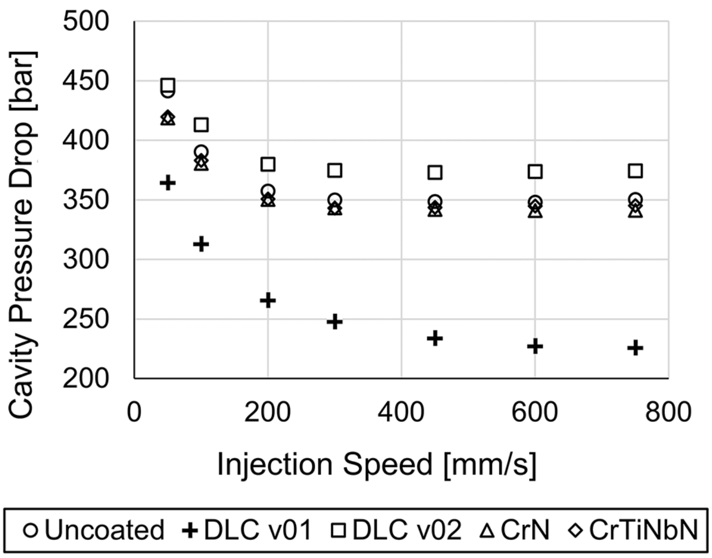

Figure 11.5: Experimental measurements of cavity pressure drop as a function of injection speed for the different coatings.

Conversely, the results obtained with DLC v02 indicated a negative effect on the cavity pressure drop (+6%).

For all the tested coatings, the observed effect of increasing the injection speed is to decrease the cavity pressure drop until the achievement of a stabilized value at about 300 mm/s. However, the plateau observed at high injection speed (i.e. from 300 to 750 mm/s) differs from the normal increase that occurs in conventional injection molding, which is due to the head loss increase at higher flow rates. This leads to the hypothesis that the flow conditions for high injection speed are affected by the presence of slipping occurring at the cavity walls (i.e. where the shear stress is maximum), which can be assessed by detecting evidence of flow instabilities on the molded parts.

11.2.2.2 *Flow instabilities evaluation*

In injection molding, when there is a non-slip condition at the mold-polymer interface, the shear stress at the wall increases for higher injection speed. However, in thin-wall injection molding the melt flow is characterized by an extremely high value of the wall shear stress, which can lead to the onset of phenomena that are normally neglected for conventional injection molding, such as wall-slip [3].

According to Mhetar and Archer [45], three slip regimes can be distinguished for molten polymers at increasing shear stress: (i) a weak-slip regime beyond a first critical stress (0.1-0.3 MPa); (ii) a stick-slip regime with periodic oscillations of the melt flow; (iii) a strong slip regime characterized by stable flow conditions.

The pressure curves acquired in the cavity, especially in the location closer to the gate, are characterized by the presence of periodic

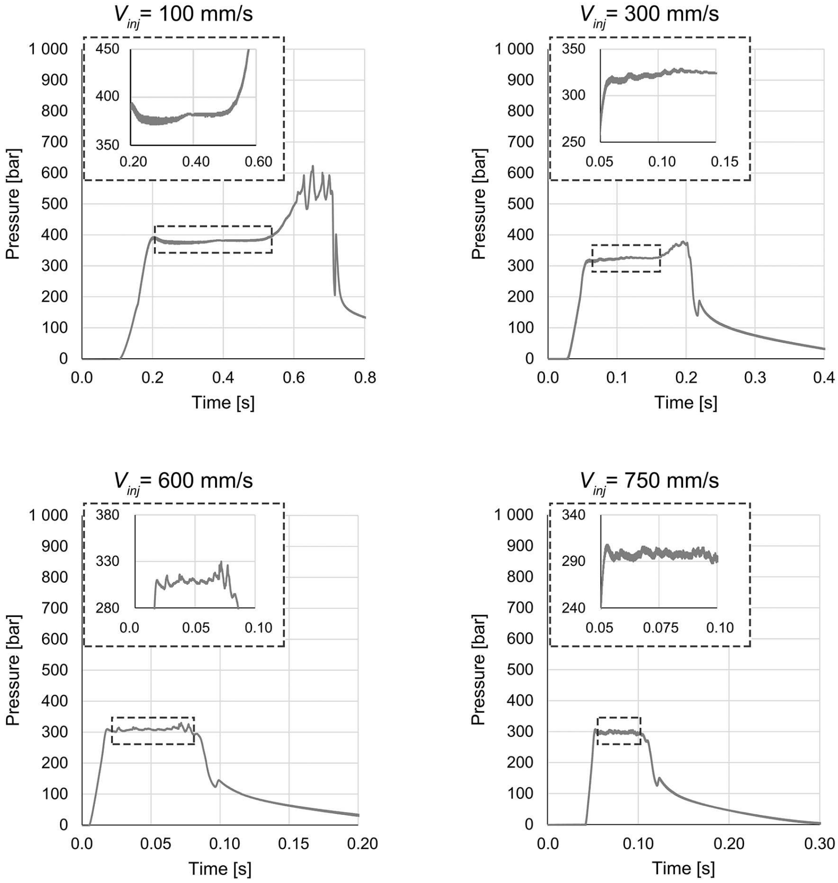

Figure 11.6: Cavity pressure curves acquired close to the injection location and evidence of signal oscillation for increasing injection speed.

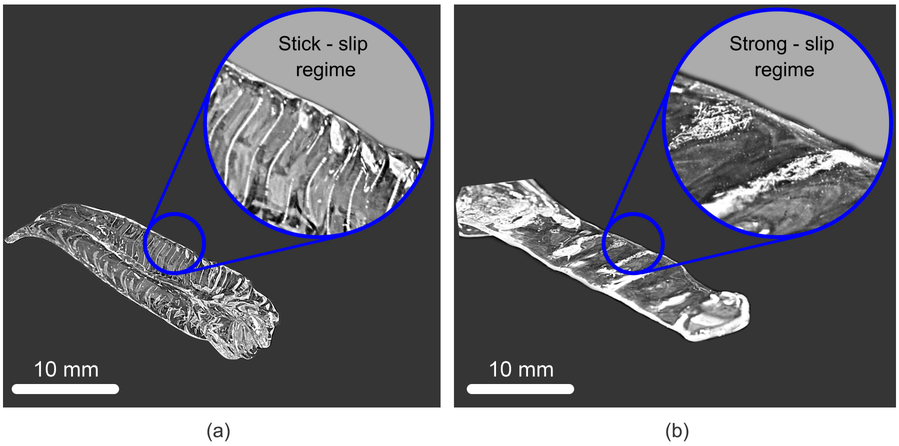

Figure 11.7: Effect of flow instabilities on polymer injected at (a) 450 mm/s and (b) 750 mm/s.

vibrations of the signal, as shown in Figure 11.6. These oscillations of the plateau-value of cavity pressure indicate that the flow conditions of the injected polymer melt are not stable, thus suggesting the presence of wall-slip. This unstable behavior was observed to become more evident for increasingly higher injection speed, indicating the effect of this process parameter on the instability of the flow conditions. Indeed, for higher injection speed, the shear stress increases and so does the intensity of the wall-slip effect.

Moreover, it was possible to observe that parts molded with injection speed up to 600 mm/s were characterized by the presence of small amplitude periodic distortions on their surface, which are related to wall slip [44]. Figure 11.7 (a) shows the presence of such defects, also known as sharkskin in polymer extrusion, on the surface of a part injected at 450 mm/s. For higher injection speed (i.e. 750 mm/s), the melt flow shifts to a strong slip regime characterized by stable conditions. In fact, the surface of the injected polymer is smoother and no sharkskin defects were observed, as shown in Figure 11.7 (b). This agrees with the observation from Münstedt et al. [155], which identified smooth flow conditions for the extrusion of polyethylene when increasing the shear rate above the stick-slip regime.

11.2.3 *Flow visualization results*

11.2.3.1 *Characterization of speed profiles*

The filling behavior of the polymer melt was characterized by means of high-speed direct imaging of the flow. The speed profiles of the polymer melt in the uncoated cavity were evaluated during the injection phase by tracking the coordinates of the dispersed silica carbide particles.

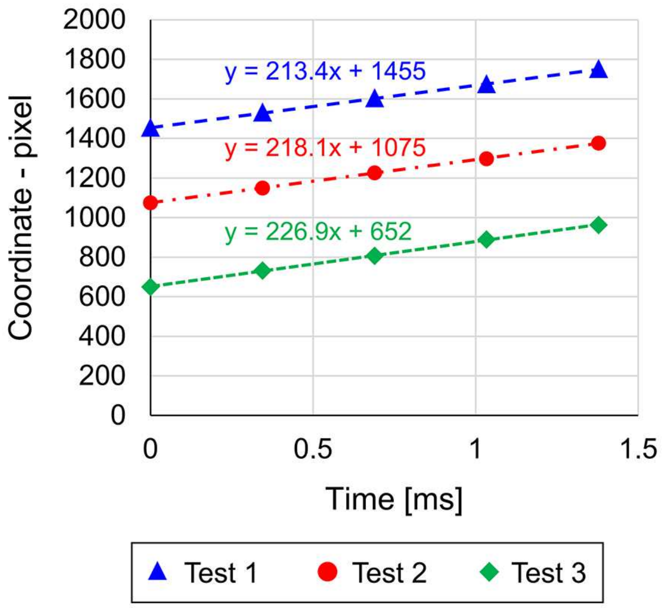

Figure 11.8: Coordinate tracking of silica carbide particles in consecutives frames along the cavity (for an injection speed of 50 mm/s).

For each value of the injection speed, three injection molding tests with flow visualization were carried out. The acquired image frames were analyzed with ImageJ to track the coordinates of selected particles in at least 5 consecutive images. The camera was triggered to the forward movement of the injection plunger and the velocity of the polymer melt was evaluated when the pressure signal had reached its plateau-value.

Figure 11.8 reports the results obtained for the coordinates tracking for three repeated injection molding tests executed at an injection speed of 50 mm/s. The position of the silica carbide particles advances linearly along the channel and the slope of the plot represents the actual polymer speed.

The characterization was performed by exploiting the symmetry of the cavity, and the particles were tracked in only one half of the channel. In order to thoroughly characterize the speed profiles, for each value of the injection speed 5 particles were selected across half of the thickness of the mold cavity. Thus, for each value of the injection speed 15 particles were tracked, for a total of 90.

The results of the characterization of the speed profiles for the uncoated cavity are reported in Figure 11.9, showing the actual polymer speed along the thickness of the cavity for injection speed ranging from 50 to 600 mm/s.

For all the considered injection speed values, the velocity profiles in the thin-wall cavity are quite flat, which shows that the injected polymer melt is characterized by a plug flow. This proves the presence of wall slip at the polymer-mold interface. Wall slip could be observed

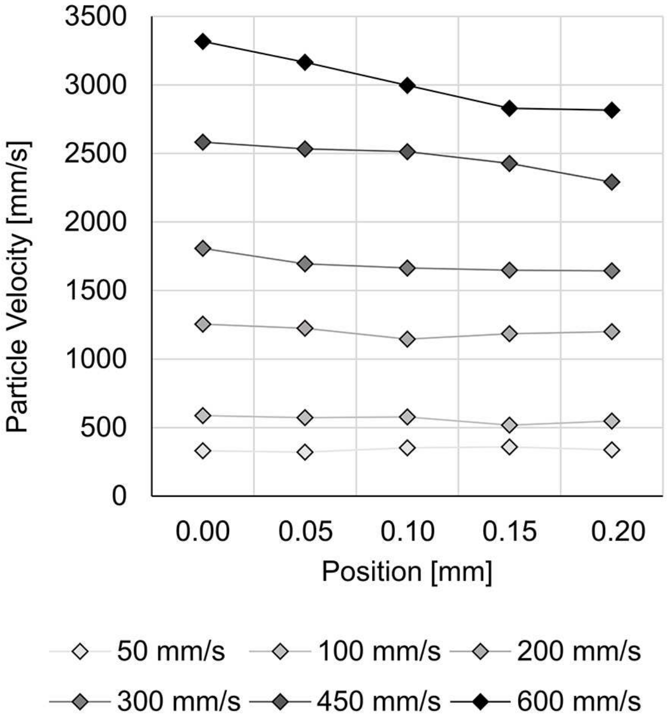

Figure 11.9: Velocity profiles for the injected polymer melt with the uncoated insert at different values of the injection speed (0.00 mm corresponds to cavity thickness midplane and 0.20 mm to cavity wall).

	Slip velocity [mm/s]	
Coating	Avg. Val.	Std. Dev.
Uncoated	2437	79
DLC v01	2652	52
DLC v02	2319	153
CrN	2019	209
CrTiNbN	2267	189

Table 11.3: Slip velocity values for different coatings at an injection speed of 450 mm/s.

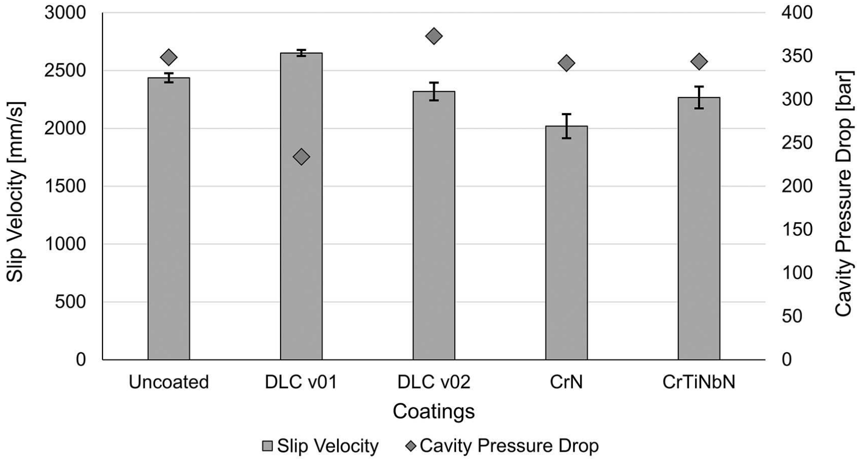

Figure 11.10: Relation between slip velocity and cavity pressure drop for the different mold surface coatings.

for all the values of the injection speed, indicating that the extremely reduced thickness of the cavity produced shear stress at wall above the threshold for the onset of wall slip.

11.2.3.2 *Slip velocities*

The slip velocity of the polymer melt in contact with mold walls was then characterized for the different mold surface coatings, by tracking the coordinates of the particles as close as possible to the cavity walls. Indeed, due to optical limitations the minimum distance of the particles from the cavity wall was limited to 25 μm. The analysis was performed for the injection molding experiments carried out with an injection speed of 450 mm/s.

Table 11.3 reports the average and standard deviation values of the slip velocity obtained from the PIV analysis of three injection molding replications. The results of the analysis show that the different coatings result in different slip velocities of the polymer melt. In particular, DLC v01 is the coating that resulted in the highest polymer slip velocity at the wall.

	Contact Angle [°]	
Coating	Avg. Val.	Std. Dev.
Uncoated	44.5	1.2
DLC v01	51.2	1.3
DLC v02	42.6	1.4
CrN	45.5	1.3
CrTiNbN	46.7	1.3

Table 11.4: Measurements of the contact angle of polystyrene for the different coatings.

The slip velocities were then related to the cavity pressure drop measured in the injection molding experiments carried out with the different coatings (Figure 11.10). The plot indicates that cavity pressure drop is inversely dependent on the slip velocity. In fact, coatings that yield low cavity pressure drop are characterized by higher slip velocity. This is particularly evident for DLC v01, which provides the lowest resistance to the flow and has the highest slip velocity.

11.2.4 *Wetting behavior*

During the filling phase of the injection molding process, a pressure-supported wetting of the cold mold surface by the molten polymer occurs. Thus, in order to improve the understanding of the effects of the coatings on the melt flow resistance, the wetting behavior of the different coatings to the polystyrene was analyzed, in agreement with the procedure described in section 8.1.

Table 11.4 reports the values of the contact angle, indicating that the coatings resulted in diverse wetting behavior due to the different interface interactions. Indeed, the affinity between each coatings-polymer couple is controlled by the different chemistry, as observed by Vera et al. [156].

The slip behavior of the injected polymer melt in contact with the coated mold surface is affected by the interface interactions at the polymer-mold interface. In general, Berger et al. reported that the higher the contact angle the smaller the interactions between the two materials [84]. Indeed, the interfacial tension (i.e. the external stress required to separate a liquid from a solid) is higher for polymer-coating couples characterized by low values of the contact angle. This was proven by correlating the cavity pressure drop, measured during the injection molding process, with the value of the contact angle for each one of the selected coatings.

The results, reported in Figure 11.11, show that the cavity pressure drop is linearly correlated (R^2 = 0.9121) to the wetting properties measured for each specific polymer-coating interface. Specifically, the

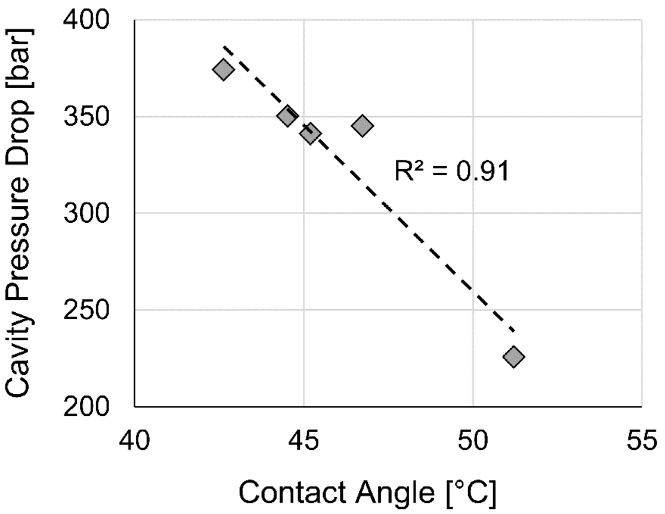

Figure 11.11: Correlation between cavity pressure drop and contact angle for the different coatings.

values acquired for cavity pressure drop are inversely proportional to the values of the contact angles. Thus, the wetting behavior of a melt polymer sample over a coated surface can be used to predict the melt flow resistance characterizing the filling phase in thin-wall injection molding.

11.3 DISCUSSION

In this chapter, the analysis of the effects of mold surface coatings on the filling flow was carried out considering three consecutive experimentations. At first, a general characterization of the effects of mold surface coatings on the melt flow resistance was carried out in order to understand the phenomena that might influence the tribological interaction at the polymer/mold interface (cf. *Investigation I*). Then, a different experimentation was carried out isolating the effects of wall slip (cf. *Investigation II*).

The experimental results of *Investigation I* indicated that all the coatings could be effectively exploited to reduce the cavity pressure (up to 8%) for PET, while they were less significant for PS, for which only Al_2O_3 caused a reduction of the filling pressure of (up to 3%). The experiments also gave some insight into the influence of the process parameters. In particular, for PET the lower value of melt temperature attenuated the coatings effect. With PS, an increase in mold temperature reduced the influence of the coatings on the filling pressure. High values of wall shear stress indicated the onset of a slip regime. As wall slip occurs at high shear rates, a numerical model was calibrated using the experimental results obtained at low values of injection speed. This way a HTC was identified for each coating, separating the effects of heat conduction from the wall slip. Experimental and numerical results clearly indicate that the investigated mold coatings can be effectively exploited to reduce the filling pressure of PET, aiding the complete replication of the mold geometry. In particular, SiOx is more effective in lowering the HTC at low shear rates while Al_2O_3 promotes the wall slip at the interface at high shear rates.

The main objective of *Investigation II* was the analysis of the filling flow of polystyrene in thin-wall injection molding with coated and uncoated cavities. The results showed that the DLC deposited on chrome substrate is the coating that most significantly reduces the cavity pressure drop (-28% compared to the uncoated insert). Limited effects were observed with CrN (-3%) and CrTiNbN (-2%) coatings, while an increase flow resistance (+6%) was observed with the DLC deposited on chromium nitride. Considering the effect of injection speed, it was observed that at high injection speed the cavity pressure drop reached a plateau, due to the presence of slipping occurring at the cavity walls. The hypothesis of wall slip was further proved by observing periodic oscillations of the pressure signal. Moreover, the surface of parts molded at injection speed up to 600 mm/s showed the presence of small amplitude periodic distortions (sharkskin defect), indicating a stick-slip regime with periodic oscillations of the melt flow. At higher injection speed (i.e. 750 mm/s) the flow shifts to a strong slip regime characterized by stable conditions, as supported also by the absence of sharkskin defects on the surface of the injected polymer. The filling behavior of the polymer melt was then characterized by means of high-speed visualization of the flow. The velocity profile of the injected polymer was characterized for different values of the injection speed, showing a fully developed plug flow with the presence of a significant wall-slip for both coated and uncoated cavities. In fact, the extremely reduced thickness of the cavity produced shear stress at wall above the threshold for the onset of wall slip. The measurement of the slip velocities allowed its comparison with the cavity pressure drop for each coating. In particular, it was observed that cavity pressure drop is inversely dependent on the slip velocity, thus indicating the importance of selecting a proper mold surface coating. In order to predict the melt flow resistance characterizing the filling phase in thin-wall injection molding, the interface interactions between the polymer and the coatings can be evaluated considering their wetting behavior. The contact angle of a hot polystyrene sample over each coated surface was measured, showing that the melt flow resistance is inversely correlated to the wetting properties.

12

TRIBOLOGICAL EFFECTS OF MOLD SURFACE COATINGS ON EJECTION

This chapter discusses the effects of different mold coatings on the ejection force in micro injection molding. The ejection force signal was monitored during injection molding experiments for different thermoplastic polymers. The results of the online characterization were then correlated with offline characterization tests.

12.1 EXPERIMENTAL APPROACH

The effects of mold coatings on the ejection friction were analyzed by monitoring the demolding force signal for the three polymers during injection molding processing. The process parameters were fixed at the values reported in Table 12.1, which were defined considering the literature, recommendations of the materials supplier and the technological limits of the available experimental setup. In particular, melt and mold temperature were specifically selected for each polymer.

The demolding force peak F_{peak}, which represents the maximum load stressing the molded part during the demolding phase, was selected as the response variable for the analysis (cf. subsection 5.3.2). To guarantee the stability of the μIM process and of the online force monitoring setup, 50 molding cycles were carried out before the first demolding force acquisition. Then, 30 acquisitions were collected, one every 5 cycles, for each polymer/coating combination.

Material	Crystal 1540	Ultraform H2320	Ultramid A4H
Melt temperature (°C)	240	235	280
Mold temperature (°C)	60	87	135
Injection speed (mm/s)	200	200	200
Packing pressure (bar)	150	150	150
Switch-over v/p (bar)	690	640	670
Cooling time (s)	6	6	6

Table 12.1: Process parameters for the injection molding of the three polymers.

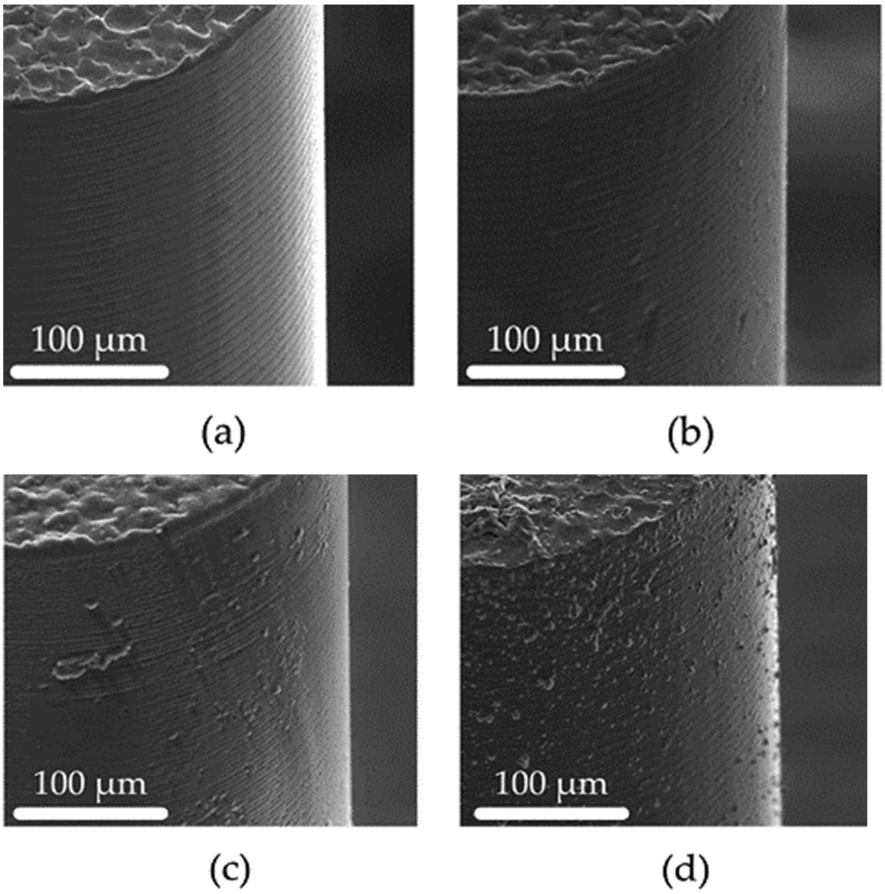
100 µm
100 µm
100 µm
100 µm
(a)
(b)
(c)
(d)

Figure 12.1: SEM characterization of the micro cores at 1000 X magnification. (a) uncoated insert, (b) DLC1, (c) DLC2, (d) CrTiNbN.

Coating		*Sa* [μm]	*Sp* [μm]	*Sv* [μm]	*Sz* [μm]
Uncoated	Avg. Val.	0.08	1.26	1.3	2.57
	Std. Dev	0.02	0.15	0.36	0.47
DLC1	Avg. Val.	0.13	1.97	1.92	3.24
	Std. Dev	0.03	0.35	0.37	0.39
DLC2	Avg. Val.	0.12	1.87	1.94	3.54
	Std. Dev	0.02	0.38	0.33	0.23
CrTiNbN	Avg. Val.	0.13	2.03	1.74	3.77
	Std. Dev	0.02	0.37	0.23	0.25

Table 12.2: Average values and standard deviations of surface roughness parameters evaluated according to ISO 4287.

Coating		*Sk* [μm]	*Spk* [μm]	*Svk* [μm]
Uncoated	Avg. Val.	0.19	0.11	0.16
	Std. Dev	0.04	0.04	0.05
DLC1	Avg. Val.	0.34	0.17	0.2
	Std. Dev	0.05	0.05	0.06
DLC2	Avg. Val.	0.3	0.16	0.19
	Std. Dev	0.04	0.04	0.05
CrTiNbN	Avg. Val.	0.31	0.19	0.21
	Std. Dev	0.06	0.05	0.06

Table 12.3: Average values and standard deviations of surface roughness parameters evaluated according to ISO 13565.

12.2 COATINGS SURFACE CHARACTERIZATION

12.2.1 *Mold topography*

The SEM analysis of the mold inserts showed that, compared to the uncoated surface, the deposition of the coatings on mold cores modified their topography. The uncoated cores (Figure 12.1 (a)) are characterized by the presence of an inherent surface texture, typical of micro–milled surfaces, and an overall good surface finish. Conversely, the coated inserts present some agglomerations that formed during the deposition of the coatings, due to the reduced curvature radius of cores lateral surface. These surface defects could affect the demolding force because particle agglomerations represent possible undercuts that increase the mechanical interlocking between the polymer and the mold cores surface.

12.2.2 *Roughness evaluation*

Table 12.2 and Table 12.3 reports the results of the surface roughness characterization performed on the mold cores, according to ISO

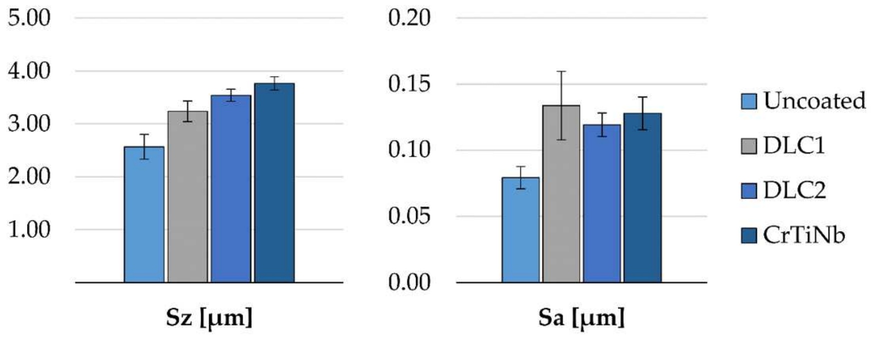

Figure 12.2: Values of *Sa* and *Sz* for the coated cores.

4287:1996 and ISO 13565-2:1996. The results of the analysis indicate that surface coatings affect both the presence of protruding peaks in the surface (*Sz*) and the overall roughness of the mold surface (*Sa*). In particular, the average value of *Sa* increases by 30% from the uncoated cores to the coated ones (Figure 12.2 (a)), due to the presence of agglomerates. Considering *Sz* (Figure 12.2 (b)), which is the sum of the height of the largest peak and the depth of the largest pit, its values increases by 21%, 27% and 32% percent in average from the uncoated insert to the DLC1, DLC2 and CrTiNbN, respectively.

The Abbott-Firestone curves were evaluated to allowing the determination of the functional parameters *Sk*, *Spk* and *Svk*. In fact, the curve provides information about the material protruding and the voids characterizing the surface, thus being important to study the potential replication behavior of the μIM process. The values of these parameters are comparable for all the coated inserts, while they are significantly different for the uncoated. High values of *Svk* can negatively affect the ejection forces because of the higher void volumes in the mold surface, which can be replicated by the melt polymer during the filling phase, thus causing higher interfacial interactions. High values of *Spk* can lead to increased friction between the mold and the part, because of the higher presence of protruding peaks.

12.2.3 *Wettability properties*

The results of the wettability analysis conducted for the selected polymers and the coatings are reported in Figure 12.3, indicating that among the selected polymer PA66 has a higher contact angle with all the coatings. Hence, PA66 is the polymer that has yields less chemical interactions with the differently coated substrates. Conversely, the wetting behavior is more marked (i.e. higher interaction with the coated surface) for POM and even more for PS, which had the smallest average contact angle.

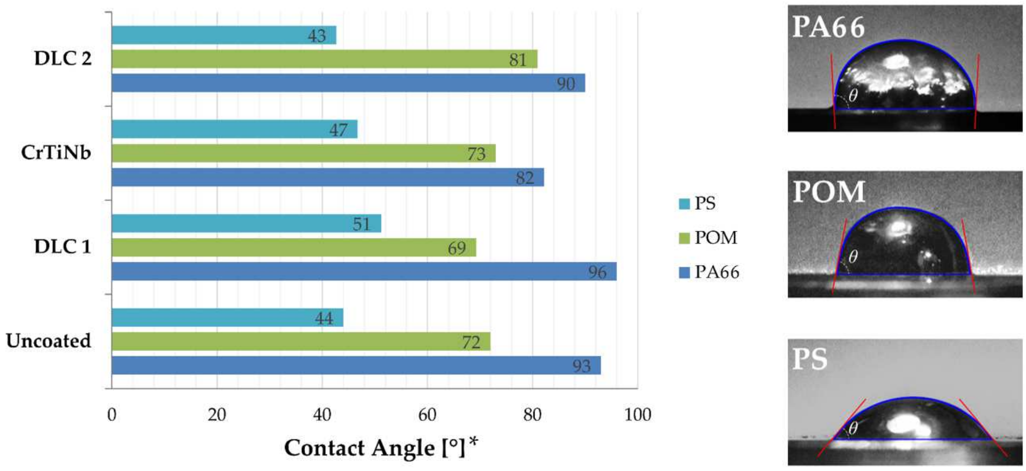

*Max std. dev. = 2.14 °

Figure 12.3: (a) Contact angle values for the different polymer/coatings combinations; (b) image of polymer drops on DLC1 coated surface.

The wetting behavior of the melt polymer over the coated surface is affected by both polymer and coating selection. However, it was observed that the value of the contact angle is mainly determined by polymer selection. In fact, by changing the polymer from PA66 to POM and PS the contact angle varied reduced by 17% and 47%, respectively, and the trend was consistent for all the coatings. Conversely, by changing the coatings the contact angles had different behaviors for each polymer and the variations were smaller (max reduction 16%, min reduction 8%).

The effects of the different coatings on the contact angle is different for each one of the tested polymers. The minimum contact angle was observed with DLC2 for PS, with DLC1 for POM and with CrTiNbN for PA66. In fact, the wetting behavior is controlled by the chemical affinity of the interface, which is different for each polymer/selection.

12.3 INJECTION MOLDING RESULTS

Following the experimental approached described in section 12.1, the effect of the different coatings was characterized by means of injection molding experiments and by online monitoring of the demolding friction. Considering Equation 3.2, the results of the injection molding experiments are discussed considering the contribution to the friction force of both adhesion and deformation, respectively.

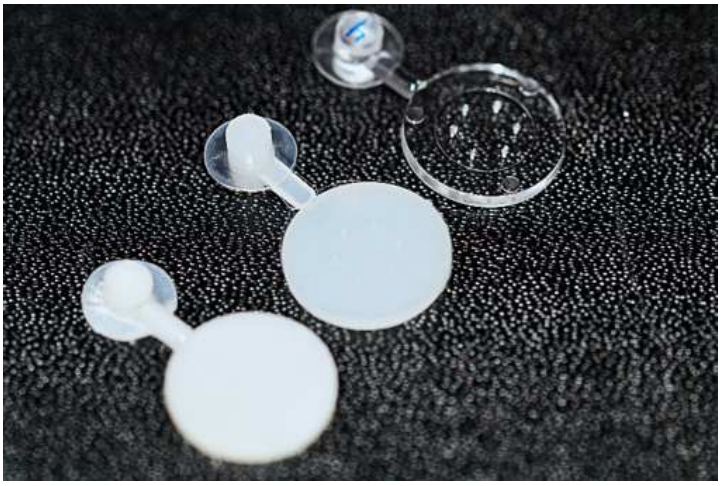

Figure 12.4: Injection molded parts with the three different polymers.

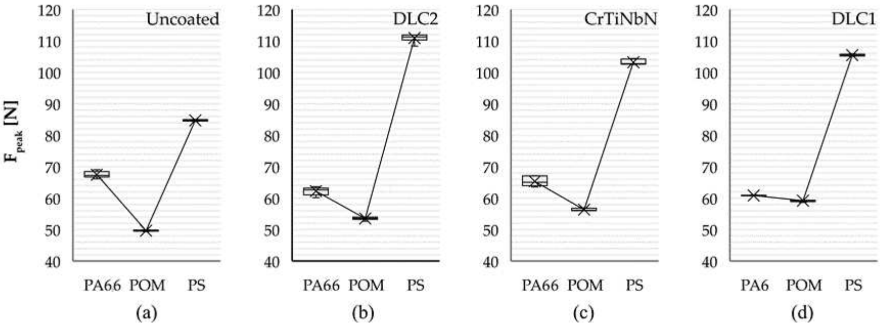

Figure 12.5: Effects of polymer selection for the different mold inserts, (a) uncoated; (b) DLC2; (c) CrTiNbN; (d) DLC1.

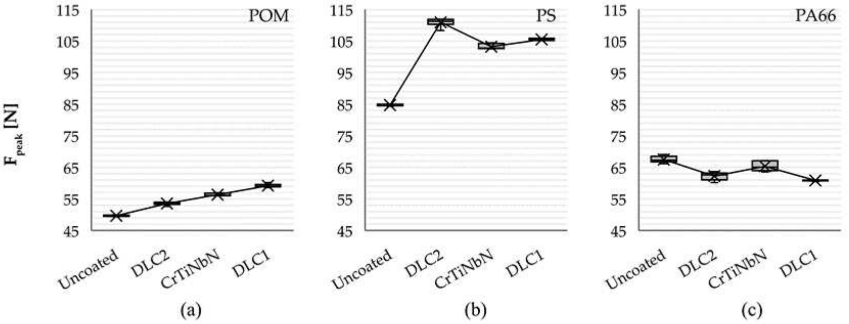

Figure 12.6: Effects of the different surface coatings on the demolding force for (a) POM, (b) PS, (c) PA66.

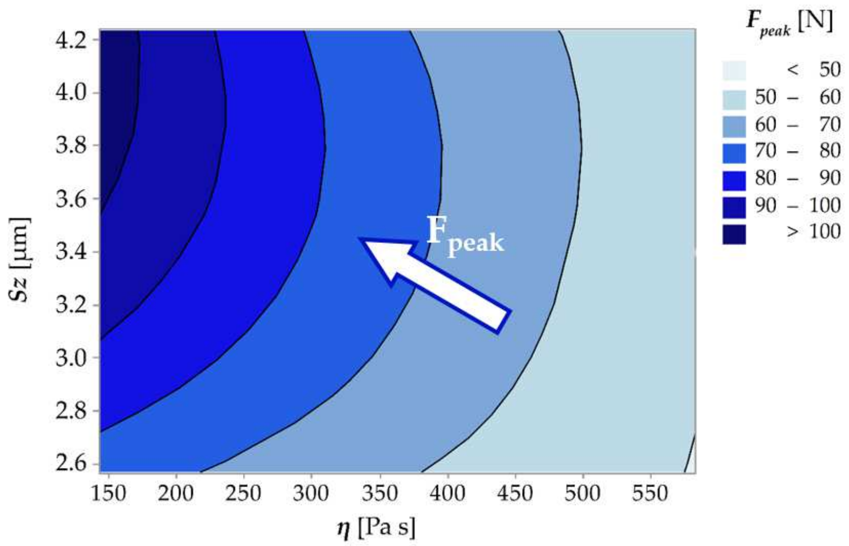

Figure 12.7: Surface response for the ejection force peak as a function of polymers viscosity and mold surface roughness (*Sz*).

12.3.1 *Effects of polymer and coatings on the ejection force*

The results of the online acquisitions for the demolding force are reported in Figure 12.5 as a function of the different coatings polymers.

Considering the effects on the ejection force peak of polymer selection it was observed that the demolding friction is minimized when molding POM. In particular, when molding it instead of PA66 and PS the demolding force decrease by 26% and 41%, respectively. Conversely, the maximum forces were observed when molding PS.

The analysis of the μIM experiments results indicated that, for each polymer selection, the demolding force peak is also affected by the different surface treatments (Figure 12.6). For each one of the selected polymers, the effect of the mold coating on the demolding force was different, thus providing further evidence about the importance of the chemical adhesion at the interface. However, the demolding force is minimum, with the exception for PA66, when using the uncoated inserts due to the worsening effect of coating on surface finish. The agglomerations that characterize the coated surfaces yielded higher interface interactions during the ejection phase, due to higher mechanical interference and higher friction.

12.3.2 *Effects on deformation contribution*

Considering the results of the injection molding experiments, the values of the ejection force peak were plotted in Figure 12.7 as a function of mold surface roughness (*Sz*) and polymers viscosity. From the surface plot it is clear that the maximum ejection friction is observed when molding PS, while the minimum friction is obtained when using the uncoated cores. This suggest that the higher mechanical interference and the higher ejection friction are caused by the agglomerations that were observed for the coated cores.

In general, a combination of low viscosity and high surface roughness (e.g. when molding PS with the CrTiNbN coating) leads to an increase of the demolding force due to the higher mechanical interlocking at the interface ($F_{deformation}$). Conversely, a marked reduction of the force is observed when the viscosity of the polymer melt is higher, as in the case of POM, and the surface is smoother (i.e. uncoated mold insert). In fact, when injection molding POM the replication of mold topography is lower, thus the mechanical interlocking at the part/mold interface is weaker.

The tribological conditions at the part-tool interface are affected by the chemical adhesion at the interface but also by the rheological properties of the polymer melt. In fact, the viscosity represents the ability of the polymer to replicate the mold surface topography during the pressurized filling phase. When filling the cavity, the polymer melt can replicate the texture of the mold and, therefore, produce interlocking between the two surfaces, causing an increase of the force required to initiate the sliding of the solidified polymer.

12.3.3 *Effects on adhesion contribution*

The wetting behavior of each polymer over the differently coated surfaces was observed to be different, as discussed in subsection 12.2.3, thus contributing to the understanding of the effects of polymer selection. When molding PS, the demolding force is maximized by the low value of the contact angle, which is responsible for the high interface interaction. However, considering the results for POM and PA66 the effect is different. In fact, PA66, which has higher contact angle compared to POM, is also characterized by higher demolding force.

Figure 12.8 shows the interaction between the measured contact angles (CA) and the ejection force for the different polymers and coatings. A good linear regression ($R^2 \sim 1$) between the value of the contact angle and the demolding force peak was reported. This indicates that higher values of the contact angle correspond to a lower demolding force. In fact, two materials showing high interfacial tension are easier to separate [84].

However, considering the ejection force results obtained with the uncoated cores it is clear that the model is strongly affected by surface roughness. The blue points in Figure 12.8 represent the uncoated cores, indicating their lack of fit with the linear model obtained for the coated cores. This further confirms the contribution of deformation to the demolding force, indicating that the adhesion contribution (i.e.

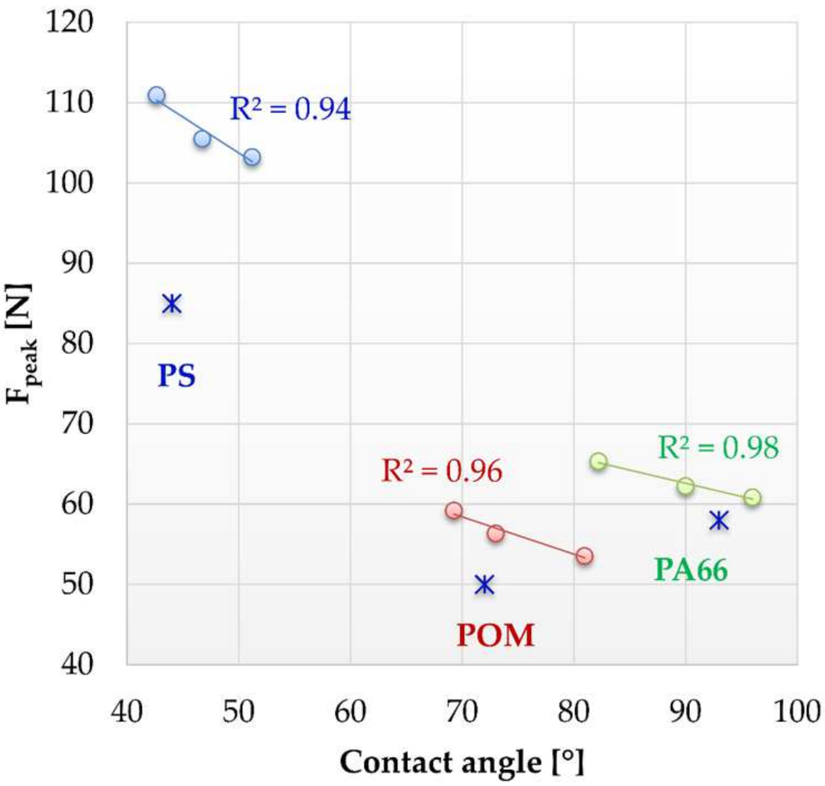

Figure 12.8: Correlation between the ejection force peak and the contact angle for the different polymers.

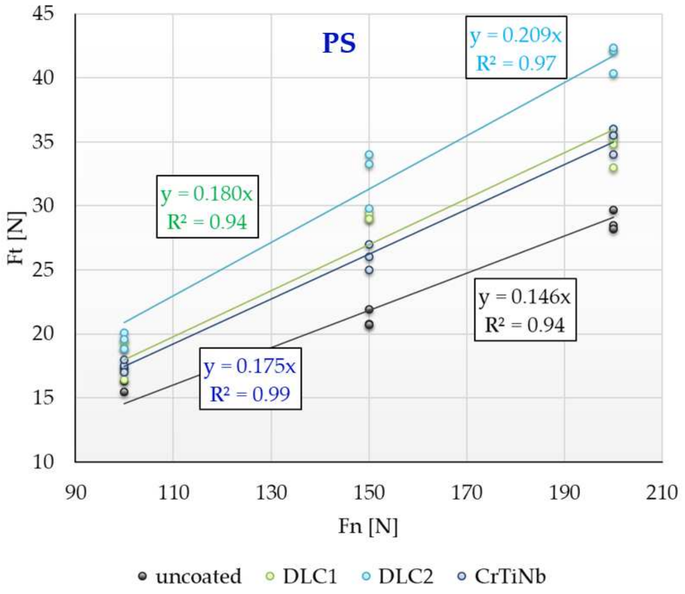

Figure 12.9: Evaluation of the friction coefficient for PS with the different coatings.

Coating	PS	POM	PA66
Uncoated	0.14	0.1	0.18
DLC1	0.18	0.13	0.2
DLC2	0.21	0.13	0.21
CrTiNbN	0.17	0.12	0.22

Table 12.4: Coefficients of friction determined for the different coatings and polymers.

wetting) is not capable of describing the whole friction phenomena occurring at the polymer/mold interface.

12.4 COATINGS OFFLINE CHARACTERIZATION

The tribological properties of the different coatings were also characterized offline, following the methodologies described in chapter 8.

12.4.1 *Friction properties of coatings*

The friction tests were conducted for each polymer and each coatings with different values of the normal load, i.e. 50, 100, 150 N. The values of the tangential force read by the load cell were then plotted for each one of the coatings, as shown in Figure 12.9 for PS. For each polymer, the experimental data were fitted using a linear regression model that represents the Amontons friction law (cf. Equation 3.1).

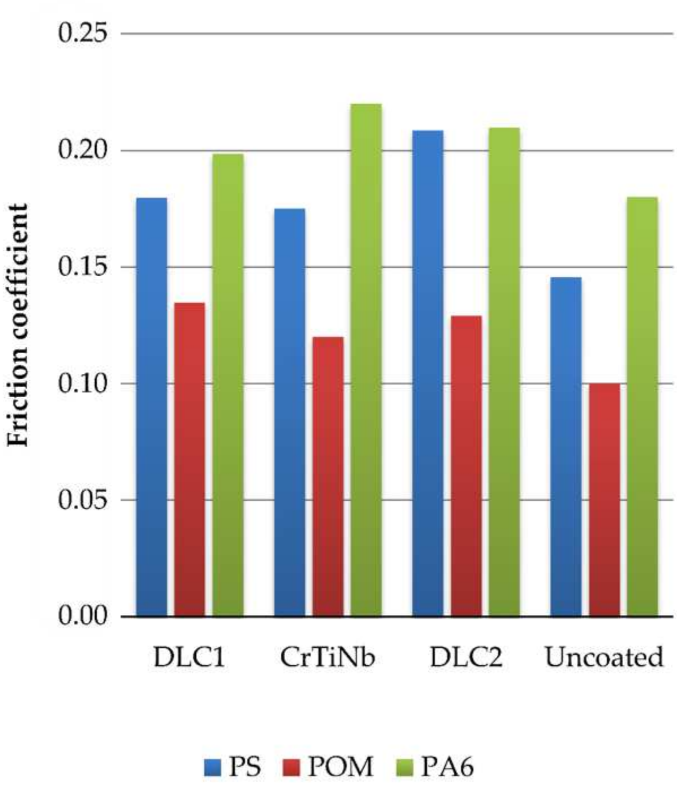

Figure 12.10: Experimental values of the friction coefficient determined for the different polymers and coatings.

The coefficient of friction for each coating was obtained as the linear coefficient of regression (Table 12.4).

Figure 12.10 shows the effects of polymer and coatings selection on the friction coefficient measured using the offline setup. It can be observed that POM, compared to PS and PA66, has the lower friction coefficient with all the considered surface coatings. Moreover, for a fixed polymer selection, the friction coefficient is lower for the uncoated insert for all the polymers.

12.4.2 *Evaluation of offline friction testing*

The results of the injection molding experiments were also compared with those of the offline friction characterization. Specifically, the ejection force peak was correlated to the offline friction coefficient, as shown in Figure 12.11. For each one of the polymers, a good linear correlation ($R^2>0.91$) between the online and the offline friction characterization was identified. This indicates the effectiveness of the proposed ejection friction setup for the evaluation of the tribological properties of different coatings for different materials. Hence, suggesting that offline friction characterization can be used to predict

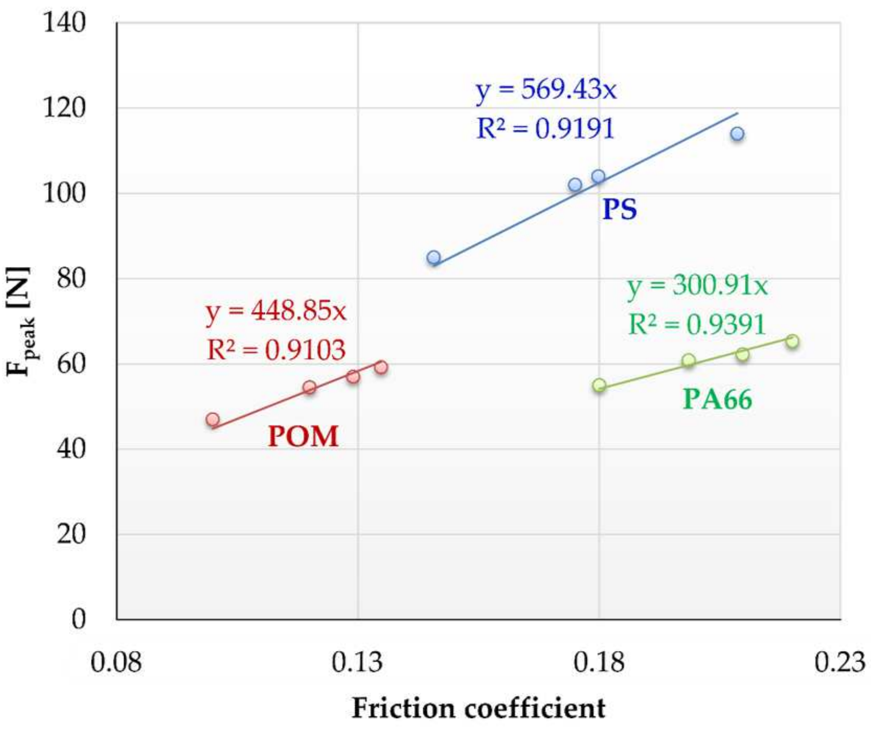

Figure 12.11: Correlation between the ejection force peak and the friction coefficient measured using the offline testing setup.

Polymer	Normal Force [N]	Elastic Modulus [Mpa]
PS	569	3200
POM	449	2450
PA66	301	2970

Table 12.5: Comparison of normal force during ejection and elastic modulus for the three polymers.

the demolding behavior of a specific coating, improving the selection of the mold coating for a specific polymer.

Considering the relation between the friction coefficient and the ejection force, the slope of the curve can be interpreted as the normal load acting on the mold cores during ejection (cf. Amontons law). Table 12.5 reports the value of the normal force obtained as the ratio between the tangential (i.e. friction) force and the friction coefficient. These values are also compared with the mechanical properties (i.e. elastic modulus) of each polymer, showing that PS has the higher normal force because of its higher rigidity.

12.5 DISCUSSION

In this chapter, the characterization of the tribological properties of different mold surface coatings was presented considering their effects on ejection friction. Three different polymers (PS, POM and PA66) and three diversely coated mold inserts (diamond like carbon with two different adhesion layer and chromium titanium niobium nitride) were used for the μIM experiments in which the tribological conditions during demolding were monitored.

The SEM characterization of the coatings showed that, compared to the uncoated surface, the application of the coatings modified their topography. Indeed, while the uncoated cores are characterized by the presence of an inherent surface texture, typical of micro-milled surfaces, and an overall good surface finish, the coated inserts present some agglomerations. These defects are formed during the deposition of the coatings because of the complex geometry and the reduced dimensions of the mold cores. The average value of Sa increases by 30% from the uncoated cores to the coated ones, while Sz increases by 21%, 27% and 32% percent in average from the uncoated insert to the DLC1, DLC2 and CrTiNbN, respectively.

The results of the μIM online acquisitions showed that the demolding force peak is affected by both polymer and coating selection. Indeed, for each one of the selected polymers, the coatings yield different ejection force. In order to provide further understanding of ejection friction, the deformation and the adhesion components were analyzed separately.

Considering the deformation contribution, it was observed that a combination of low viscosity and high surface roughness leads to an increase of the demolding force due to the higher mechanical interlocking at the part/mold interface. In fact, polymer viscosity represents its ability to replicate a certain mold topography, and the higher is surface roughness the more marked is the possible interface stiction.

On the other hand, the adhesion contribution is affected by the chemical affinity of the polymer melt to the coated mold surface. The results of the wettability analysis, which showed different contact angles over the different coatings, were correlated to ejection friction. A good linear regression was observed between the value of the contact angle and the demolding force peak, supporting the hypothesis that two materials showing high interfacial tension are easier to separate. However, considering the ejection force results obtained with the uncoated cores it is clear that the model is strongly affected by surface roughness. Thus further confirming the contribution of deformation to the demolding force, indicating that the adhesion contribution (i.e. wetting) is not capable of describing the whole friction phenomena occurring at the polymer/mold interface.

Ejection friction was also characterized using an offline friction testing setup. The offline coefficient of friction were evaluated for the three polymers over the differently coated surfaces. A good linear correlation was then observed with the ejection force peak, indicating that the offline friction setup could allow the prediction of ejection friction. This could improve the selection of mold coating for a specific polymer, which often is a difficult task for mold designers.

Part V

MODELING

13

MODELING OF THE FILLING PHASE

In micro and thin-wall injection molding processes, the polymer undergoes temperature and pressure increases, significant shear deformation, followed by rapid decay of temperature and pressure in the mold cavity, which leads to solidification, high residual stress, complex molecular orientation, and other part properties that determine the molded part quality.

However, due to those peculiar features of micro and thin-wall injection molding (reduced cavities dimension, high pressure/shear rate, high mold temperature, and fast cooling speed), the flowing behavior and the heat transfer mechanisms of polymer melts is different than it is in conventional injection molding. Therefore, comparing with numerical simulation of conventional injection molding process, there are some new physical aspects associated with the scale-down of forming parts that have to be considered.

13.1 SIMULATION OF MICRO AND THIN-WALL INJECTION MOLDING

In the micro injection molding, due to the irregular geometry in micro-scale and the complex thermo-mechanical history during the cycle, it is generally necessary to resort to numerical simulation methods to properly simulate the molding process and develop the capability of predicting the final configuration of the molded part, which is particularly important in precision injection molding operations.

Software simulation tools are used in polymer micro-manufacturing technology by adapting them from the macro-process, with the following objectives:

- visualization of the flow;
- optimization of the design of the mold before manufacturing;
- simulation of the thermal conditions of the flow during filling and cooling;
- identification of post-processing properties (e.g. residual stresses, shrinkages and warpage);
- supporting the design of experiments in determining influential processing parameters on part quality.

Even though they can provide useful assistance they have the following limitations:

- meshing problem: when dealing with a macro-part with some micro-feature in the same mesh there are elements with dimensions in a wide range (multi-scale problem), this affects the accuracy of modelling;
- the rheological data used in current packages are obtained from macroscopic experiments;
- some phenomena that arises in the micro-scale problem are not implemented within the governing equations;
- pressure and temperature gradients are greater than those found in conventional injection molding and require the use of very small time steps between iterations to ensure convergence of a solution, which also increases solution times.

Therefore, it is considerably important to develop reliable numerical simulation tools which would deal with the issues described which characterize micro injection molding.

13.1.1 *Scaling issues*

When downsizing the part must be completely filled and fully satisfy its designated function requirements, but scaling in quality is difficult to predict. Moldability is directly contingent upon the flow and heat transfer process of the polymer inside the mold cavity, which are influenced by size effects. In fact, when a system is reduced in size of some orders of magnitude, the changes in length, area, and volume alter the relative influence of various physical effects, and that lead to the appearance of unpredicted phenomena. Consequently, some consolidated design and processing strategies might not work as size scales down and so the quality of the micro injection molded part might not be consistent.

The understanding of physical phenomena neglected in conventional injection molding, but significant at the micro-scale due to the increased surface-to-volume ratio, is fundamental. The scaling-related issues that needs to be taken into consideration for micro and thin-wall injection molding are:

- **The filling behavior of polymeric flow in a micro-scale**: due to reduced parts dimensions, it is not unusual to be facing the total incapacity to obtain a complete filling of the micro-cavity or to eject the solid part. Moreover, the wall slip might contribute to determine the filling behavior of the polymer melt in the reduced-size cavity (cf. section 2.4);
- **The differences in dynamics of heat and mass transfer**: pressure and temperature gradients far exceed those found in conventional injection molding (cf. subsection 2.1.3). Therefore

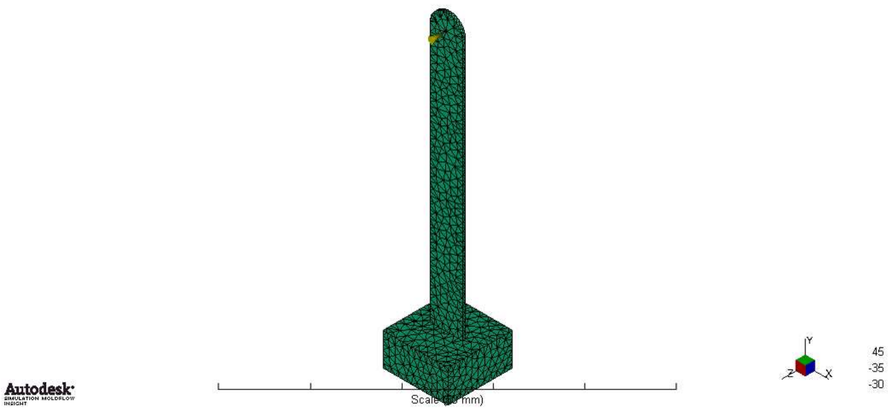

Figure 13.1: Modeling and Dual Domain discretization of the cavity geometry.

the flow in micro-channels cannot be described with a constant heat transfer coefficient, and its standard value appropriate for macro parts differs substantially. Heating of the melt by viscous friction and cooling of the melt due to increased heat loss must be taken into consideration;

13.2 APPROACH TO MODELING

In this chapter, the results of injection molding experimental campaigns were further investigated by using numerical simulation. In order to understand the phenomena that control the melt flow resistance of a polymer melt in thin-wall cavities, a numerical model of the process was calibrated by inverse analysis. Specifically, the effects of mold surface modification on the filling flow resistance were modeled by determination of the Heat Transfer Coefficient (*HTC*). The numerical model was calibrated using the experimental results reported in chapter 11. This allowed the identification of the thermal boundary conditions that characterize each coating in relation to the filling pressure and provided useful information regarding the onset of the wall-slip phenomenon.

13.2.1 *Numerical model*

The non-Newtonian and non-isothermal filling flow of the polymer melt was modelled using the injection molding simulation software Autodesk Moldflow. The geometry of the mold cavity was discretized with a dual domain mesh, as shown in Figure 13.1. The rheological data for the thermoplastic materials were implemented considering the Cross-WLF parameters obtained from the rheological characterization of the polymer (subsection 7.4.1). The flow rate filling con-

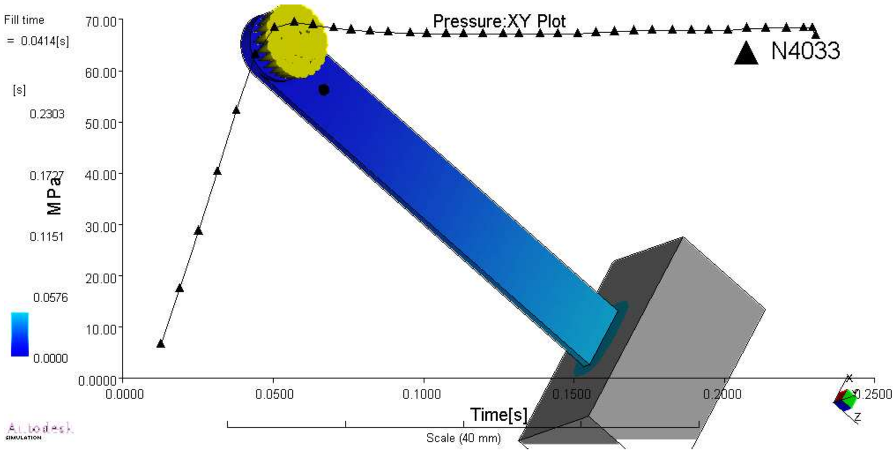
Fill time
= 0.0414[s]
[s]
0.2303
0.1727
0.1151
0.0576
0.0000
MPa
70.00
60.00
50.00
40.00
30.00
20.00
10.00
0.0000
Pressure:XY Plot
N4033
0.0000
0.0500
0.1000
0.1500
0.2000
0.2500
Time[s]
Scale (40 mm)
X
Z
Autodesk
SIMULATION

Figure 13.2: Injection molding simulation in Autodesk Moldflow and plot of cavity pressure in the monitoring position.

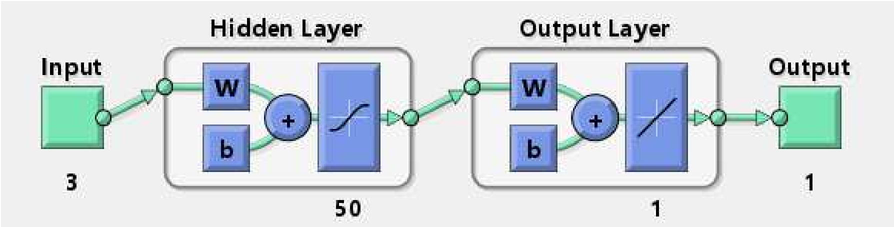
Hidden Layer
Output Layer
Input
Output
W
b
+
W
b
+
3
50
1
1

Figure 13.3: Schematics of the Artificial Neural Network use as meta-model for injection molding simulation.

trol was set accordingly with the experimental values of the injection speed and the diameter of the injection plunger. The numerical value of the cavity pressure was obtained in a mesh node positioned at the same distance from the injection location as the pressure sensors in the experimental setup (cf. *Investigation I* presented in subsection 6.2.1).

The polymer flow during the injection molding process is inherently transient and includes a free surface moving through narrow cavities, thus a good model for the mold-melt heat transfer coefficient (HTC) is essential to describe the non-continuous temperature distribution at the interface and to predict the cavity pressure.

The numerical model was employed in the study to understand how the cavity pressure (cf. Figure 13.2) is influenced by the injection speed and by the HTC value. Preliminary results indicated that the HTC, in agreement with the physics of the process and the results reported in the literature, is the parameter responsible for the shifting of the cavity pressure curves.

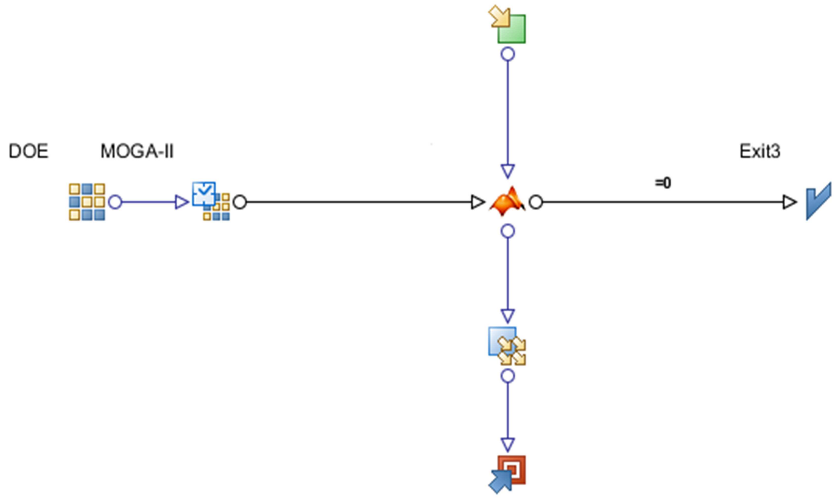

Figure 13.4: ModeFrontier code for the inverse analysis.

13.2.2 *Inverse analysis*

The value of the HTC that forces the numerical results to fit the measured pressure values for each coating was determined using an inverse analysis approach. The differences between numerical and experimental pressure values were minimized using an iterative optimization algorithm. In order to reduce the computational time, artificial neural networks (ANN) were used as a meta-model to locally approximate the simulation results (Figure 13.3). The artificial neural networks were trained to reproduce the results of the simulation [157], for all the experimental process conditions, using the Levenberg-Marquardt back propagation.

The difference between numerical and experimental results was minimized using an optimization procedure implemented in modeFrontier (Figure 13.4), based on a MOGA-II genetic optimization algorithm [158]. MOGA-II was selected for its implicit robustness, as it uses a smart multi-search elitism for robustness and directional crossover for fast convergence. Its efficiency is ruled by its operators and by the use of elitism. Encoding in MOGA-II is done as in classical genetic algorithms and it uses four different operators for reproduction: classical crossover, directional crossover, mutation and selection. At each step of the reproduction process, one of the four operators is chosen (with regard to the predefined operator probabilities) and applied to the current individual [158]. For each iteration and for the corresponding values of the input factors, the neural networks previously trained approximated the numerically calculated pressure values, in order to compare them to the pressure experimentally measured.

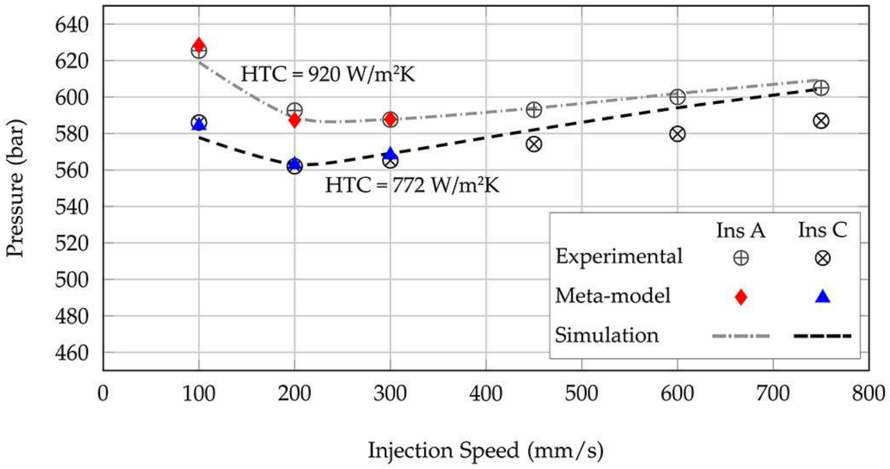

Figure 13.5: Comparison between experimental and numerical results for PET at T_b = 300 °C [138].

		HTC	Thermal Conductivity	Coating Thickness
Insert	Coating	[W/(m^{2}K)]	[W/(mK)]	[μm]
A	-	920	25÷30	-
B	Al2O3	758	1.5÷3	0.02÷0.05
C	DLC	772	5÷10	0.5÷5
D	SiOx	736	1÷2	0.5÷5

Table 13.1: Values of HTC determined for the mold surface coatings with PET.

13.3 HTC CALIBRATION AND WALL-SLIP HYPOTHESIS

The calibration of HTC is presented in this section considering the results of the injection molding experiments discussed in section 11.1 and in section 11.2.

13.3.1 *Modeling of PET filling flow*

As wall slip is likely to occur at high shear rates and the numerical model is based on a non-slip wall-polymer interface, the numerical simulation was calibrated using the experimental results obtained at low values of injection speed. With reference to insert A (uncoated) and C (DLC), Figure 13.5 shows a comparison between experimental and numerical results, the latter varying only the calibrated HTC value. The numerical simulation fits well the pressure results obtained for the uncoated insert even at high injection speed. However, for insert C a constant value of HTC is clearly incapable of reflecting the complex behavior of the polymer at the mold wall, which is likely to be influenced by wall slip.

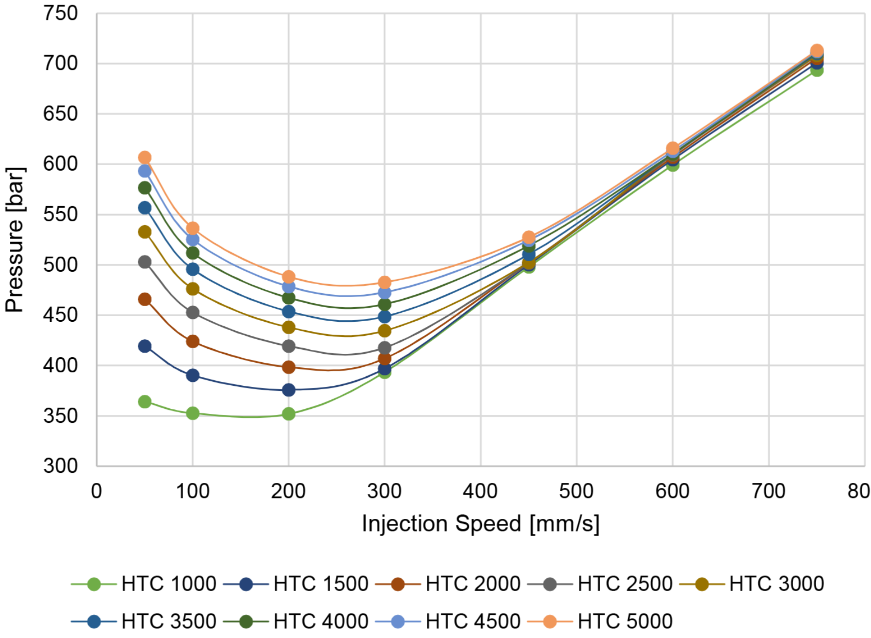

Figure 13.6: Simulated values of cavity pressure as a function of injection speed and HTC.

Table 13.1 reports the values of HTC determined for each coating in relation to their characteristics in terms of thickness and thermal conductivity, as provided by the suppliers. Insert D has the lowest value of HTC, due to the low values of both thermal conductivity and thickness. Even though SiOx and Al_2O_3 have the same thermal conductivity the coating of insert B is thinner, which results in a higher value of HTC. Eventually, insert C has the highest HTC due to its elevated thermal conductivity, which is still an order of magnitude lower than the mold steel.

13.3.2 *Modeling of PS filling flow*

The calibration of the HTC parameter for polystyrene was carried out in the range from 1000 $W/(m^2K)$ to 5000 $W/(m^2K)$, as shown in Figure 13.6. For each one of the coatings, the calibrated HTC value was determined; the results of the calibrations are reported in Table 13.2. The calibration procedure was performed considering only low values of the injection speed (from 100 mm/s to 300 mm/s).

The results of the calibration indicate a marked difference between the values of pressure predicted by the numerical model and those obtained from the injection molding experiments. For instance, Figure 13.7 shows the results of the calibration for the Uncoated insert, indicating a high error in the numerical prediction for high values of the injection speed. Thus confirming the onset of the wall-slip phenomenon during the thin-wall injection molding experiments.

Coating	Calibrated HTC [W/(m^{2}K)]	Error [bar]
Uncoated	3245	22.2
DLC v01	1462	579.3
DLC v02	4061	30.7
CrN	3046	19.0
CrTiNbN	2951	41.1

Table 13.2: Results of HTC calibration for the coated inserts using PS.

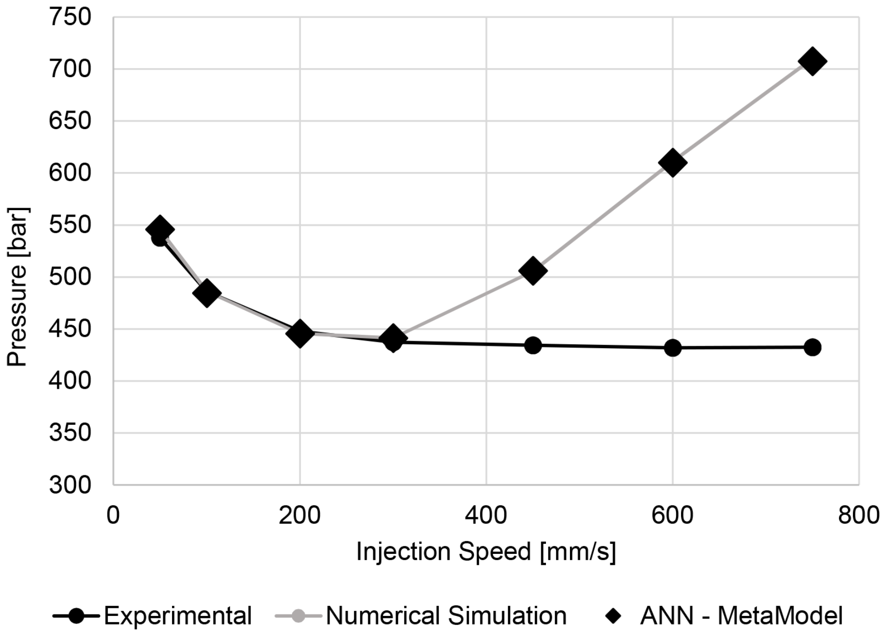

Figure 13.7: Comparison of experimental, simulated and ANN values of pressure as a function of the injection speed for the Uncoated insert.

13.4 DISCUSSION

The calibration strategy proposed in this section allowed to separate the effects of heat conduction from the wall slip related to the low-friction coatings. Indeed, the numerical model considered for the simulation of the filling phase do not account for the wall-slip phenomenon. The effect of the coatings were interpreted as insulating layer that modify the thermal boundary conditions at the interface between the melt polymer and the the mold. The thermal effect of the coatings was implemented in the simulation by modifying the heat transfer coefficient for the simulation.

The calibration of the HTC for the different coatings, which were used for molding experiments with both PET and PS, allowed:

- the evaluation of the thermal effect of mold surface coatings for low values of the injection speed;
- the understanding of the effects of coatings thickness and composition on the melt flow resistance;
- the formulation of the wall-slip hypothesis for higher values of the injection speed, which was verified by means of flow visualization and particle image velocimetry, as discussed in section 11.2.

The calibrated values of HTC not only allowed a better understanding of the filling flow, but they could also be used for calibrated injection molding simulation. For instance, at the mold design stage, they could be useful to evaluate the thickness reduction that could be obtained with each coating.

14

PREDICTION OF EJECTION FORCE IN MICRO INJECTION MOLDING BY CALIBRATION OF A SHRINKAGE MODEL

The results of the injection molding characterization, presented in chapter 10 and in chapter 12, showed the importance of ejection friction. In this sense, the accurate prediction of the demolding force is then fundamental to improve the quality of the micro injection molding process.

In this chapter, a shrinkage model was calibrated following an inverse analysis approach, which is based on the experimental characterization of the shrinkage for a representative micro part. An analytical model was then implemented to evaluate the ejection force and the results were compared to the experimental values of the ejection force previously monitored during the micro injection molding process.

A model for the prediction of the ejection force in μIM was developed and applied to the case study geometry presented in subsection 5.1.2. The calibration of a numerical shrinkage model was performed, following an inverse analysis approach, for three polymer (PS, POM, COC). Experimental shrinkage values obtained from μIM experiments, carried out with a representative geometry (calibration part), were compared to the simulated results in order to optimize the shrinkage parameters in the model. The calibrated model was then applied to the simulation of the contact pressure generated on the surface of deep cores (case study). The values of the shrinkage obtained from the numerical model were then transferred to an analytical model that allowed the calculation of the predicted ejection force.

14.1 EJECTION FORCE MODEL

In injection molding, the ejection force (F_e) for simple mold geometries, as deep cores, can be predicted by using the following equation:

$$F_e = p_c \cdot A_c \cdot \mu = F_N \cdot \mu \tag{14.1}$$

where p_c is the contact pressure, A_c the contact area, μ the friction coefficient and F_N the normal force acting on mold cores during the demolding phase [71].

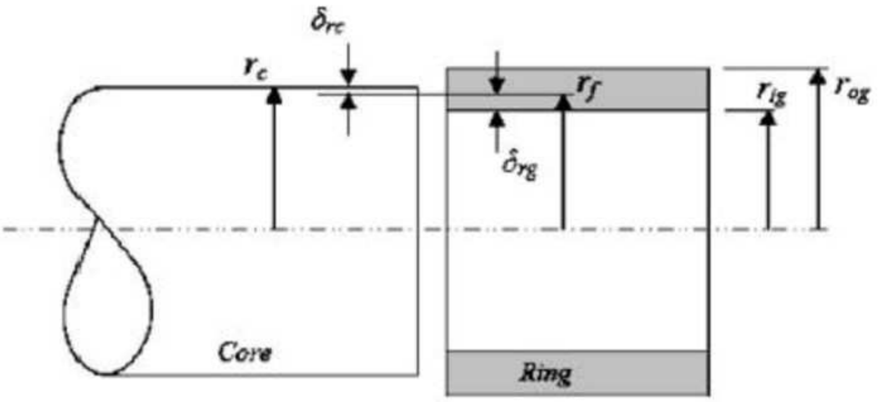

Figure 14.1: Schematics of the model used for the analytical calculation acting on the mold cores [159].

In this work, according to the model proposed by Hamrock et al. [159], F_R was determined using the following:

$$F_N = \frac{\delta_{rg} \cdot E_g}{r_f \cdot \left(\frac{r_{og}^2 + r_f^2}{r_{og}^2 - r_f^2} + \nu_g \right)} \cdot (2 \cdot \pi \cdot r_f \cdot L) \tag{14.2}$$

where δ_{rg} is the radial displacement due to the shrinkage, r_f and L are the dimensions of the ring of polymer shrinking around the core, r_{og} is the external radius of the deformed ring and E_g, ν_g are the mechanical properties of the polymer.

The variables controlling the ejection force prediction are the polymer shrinkage around the cores (i.e. normal force F_R) and the coefficient of friction (μ).

In order to determine the values of the shrinkage, which enters Equation 14.2 as radial displacements, a numerical simulation of the process was performed. The accuracy of the shrinkage prediction, and of the consequent ejection force calculation, was improved by calibrating the numerical shrinkage model adopted for the simulation.

14.2 MATHEMATICAL MODELS FOR SHRINKAGE PREDICTION

Injection molded components usually warp after being demolded, due to the residual stresses developed during the process. High residual stresses are produced due to high pressures, temperature history and relaxation of polymer chains.

For prediction of shrinkage in injection molding three different approaches have been developed [160]:

A. residual strain model;

B. residual stress model;

c. corrected residual in-mold stress (CRIMS) model.

All these models are implemented in Autodesk Moldflow that is the numerical simulation software used in this work for shrinkage calculation.

14.2.1 *Residual strain model*

The residual strain method is based on the following empirical model for shrinkage:

$$\begin{cases} S^{\parallel} = a_1 M_v + a_2 M_c + a_3 M_O^{\parallel} + a_4 M_r + a_5 \\ S^{\perp} = a_6 M_v + a_7 M_c + a_8 M_O^{\perp} + a_9 M_r + a_{10} \end{cases} \tag{14.3}$$

where:

a. $S^{\parallel}$ and $S^{\perp}$ are the predicted values of linear shrinkage parallel and perpendicular to the direction of flow respectively,

b. a_i are constants for a given material,

c. M_v is a measure of the volumetric shrinkage,

d. M_c is a measure of the crystallization,

e. $M_O^{\parallel}$ and $M_O^{\perp}$ are measures of the molecular orientation parallel and perpendicular to the direction of flow, and

f. M_r is a measure of mold restraint.

The various measures of the model (e.g. volumetric shrinkage, molecular orientation,...) are determined by the Fill+Pack analysis. The model is then fitted to the experimental shrinkage values by molding a standard test piece and subsequently determining the a_i material constants. The experimental procedure is the following:

a. a certain number of standard test pieces are molded using different process conditions and part thicknesses,

b. the values of the linear shrinkage parallel and perpendicular to the flow are measured,

c. M_i coefficients are determined via Fill+Pack analysis,

d. equations 14.3 are fitted to the given M_i, $S^{\parallel}$ and $S^{\perp}$,

e. the resulting a_i coefficients are written in a database and used in future analysis.

When a Fill analysis takes place, residual strains are calculated in every node of the meshed part; subsequently, on the basis of the calculated residual strains, a structural analysis determines part shrinkage and warpage.

As far as the M_i coefficients are concerned, the importance of crystallization should be further analyzed. Since PBT is a semi-crystalline material, the degree of crystallization has to be taken into account in order to correctly predict its shrinkage. In fact, *pvT* data alone is not sufficient information, because it refers to equilibrium state, whereas the crystallization-induced shrinkage is a function of both temperature and cooling rate. In injection molded parts, thick regions tend to cool slowly relative to thinner sections and so have higher crystalline content and hence higher volumetric contraction. On the other hand, thin regions cool very quickly and so have lower crystalline content and hence lower volumetric contraction than that predicted from equilibrium *pvT* data.

14.2.2 *Residual stress model*

The residual stress models accounts for the stress developed while the material cools under pressure in the mold. It calculates the thermally and pressure induced residual stress for each element of the meshed part. The stress distribution is then input to the stress analysis program to obtain the deflected shape of the part.

This model is theoretically based on the assumption of linear thermo-viscoelastic behavior, and therefore doesn't need experimental data. However, if this data is available, the results are far more accurate. On the other hand, the residual *strain* model does require experimental data in order to work.

A general form of the anisotropic stress-strain relation for linear thermo-viscoelasticity may be written as:

$$\sigma_{ij} = \int_{-\infty} c_{ijkl}(\xi(t) - \xi(t'))\frac{\partial \varepsilon_{kl}}{\partial t'}\,dt' - \int_{-\infty} \beta_{ij}(\xi(t) - \xi(t'))\frac{\partial T}{\partial t'}\,dt' \qquad (14.4)$$

where:

A. C_{ijkl} is a tensor defining mechanical characteristics of the material,

B. B_{ij} is a tensor defining thermal characteristics of the material,

C. $\xi(t)$ is a pseudo-time scale defined by $\xi(t) = \int_0 \frac{1}{a_T}\,dt'$ where a_T is the time-temperature shift factor characterized by the William Landell Ferry (WLF) equation.

In the absence of experimentally obtained viscoelastic data, assuming non-fiber-filled material, C_{ijkl} is defined by the Poisson's ratio of the material, and B_{ij} is obtained from the *pvT* data for the material.

Since equation 14.4 is not of easy application if the material thermo-rheological behavior is complex (and this is often the case), another assumption is made: there is no stress build up in the material until the material is below the transition temperature. This means that at higher temperature than the glass transition temperature, the material rheological behavior is purely viscous, whereas al lower temperature the material behaves purely elastically.

This assumption is necessary in order to simplify the model, but it causes inaccuracy with regard to the absolute shrinkage values predicted (the part usually shrinks less than the predicted values).

In conclusion, the residual stress model is capable of predicting shrinkage trends, but it can have substantial errors with regard to the absolute values obtained.

The viscous-elastic model is based on the following assumptions:

a. there is no stress build up in the material until the material is below the transition temperature,

b. the shear stress $\sigma_{13} = \sigma_{23} = 0$,

c. the normal stress σ_{33} is constant along the thickness,

d. a constrained quench condition is prescribed in all the cases as long as the material is in the mold,

e. mold elasticity is neglected. (Elasticity of mold cores is taken into account in a core shift analysis),

f. the material behaves as an elastic solid after the part is ejected.

14.2.3 *Corrected residual in-mold stress model (CRIMS)*

This model is the most accurate because it is obtained by fitting the residual stress model to the actual shrinkage values of test specimens.

The main cons of the residual stress model are due to the lack of connection with experimental data (in fact, the model is theoretically based). In particular:

a. transition temperature and pvT data, which greatly influence shrinkage, do not represent the behavior under actual processing conditions,

b. the model does not take into account molecular orientation and therefore anisotropic shrinkage is not predicted,

c. the model does not take into account crystallinity effects.

As one can imagine, these issues come from the fact that the material data is obtained under lab conditions rather than those experienced by the material during actual injection molding. Therefore, the basic concept of the CRIMS model is to compare the shrinkage values obtained from simulations to those actually experienced by test specimens, and to apply a *correction* in order to match them.

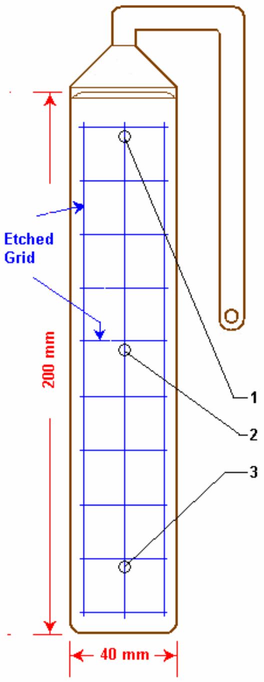

Figure 14.2: Test specimen used for CRIMS coefficients determination by Autodesk.

The CRIMS model is based on the following equations:

$$\begin{cases} \varepsilon_{11}^{(c)} = a_1 \varepsilon_{11}^{(p)} + a_2 \varepsilon^0 + a_3 \\ \varepsilon_{22}^{(c)} = a_4 \varepsilon_{22}^{(p)} + a_5 \varepsilon^0 + a_6 \end{cases} \tag{14.5}$$

where:

A. $\varepsilon_{11}^{(c)}$ and $\varepsilon_{22}^{(c)}$ are the *corrected* principal strains parallel and transversal to the flow, respectively,

B. $\varepsilon_{11}^{(p)}$ and $\varepsilon_{22}^{(p)}$ are the *predicted* principal strains parallel and transversal to the flow, respectively,

C. ε^0 is the strain related to orientation effects,

D. a_i are the *CRIMS coefficients*.

In order to characterize the material, the following procedure is followed:

A. 28 test specimens such as that in figure 14.2 are molded under different process conditions. For each of them the actual principal strains parallel and transversal to the flow are measured

$$\begin{cases} \varepsilon_1^{(m)} = \frac{l_1 - l_1^{(m)}}{l_1} \\ \varepsilon_2^{(m)} = \frac{l_2 - l_2^{(m)}}{l_2} \end{cases} \tag{14.6}$$

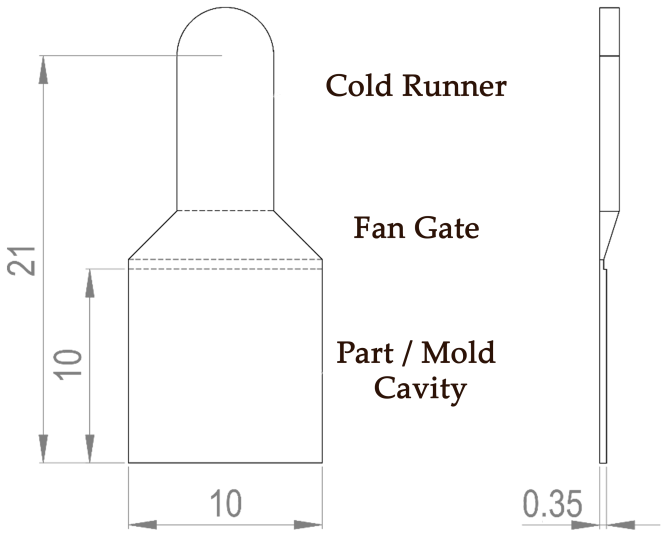

Figure 14.3: Design of the mold cavity and of the part.

where l_i are nominal dimensions and $l_i^{(m)}$ are the measured ones,

B. 28 simulations are run, under the same process conditions as the test specimens where molded, and the predicted principal strains $\varepsilon_{11}^{(p)}$ and $\varepsilon_{22}^{(p)}$ are calculated, along with ε^0, which accounts for molecular orientation,

C. equation 14.5 is fitted to the measured strains 14.6,

D. the resulting b_i CRIMS coefficients are stored in the material database.

14.3 SHRINKAGE CALIBRATION

The intrinsic cause for shrinkage in injection molding is related to the thermodynamic behavior of polymers (i.e. pvt curves). During the process, this causes the generation of residual stresses that affect the contact pressure at the part-tool interface, which ultimately determine the demolding force.

14.3.1 *Part design and manufacturing*

14.3.1.1 *Mold design*

The part considered in this study is a square plaque with a side lenght of 10 mm and a thickness of 350 μm, as shown in Figure 14.3. The design of the part was selected based on conventional injection molding standards [161] and methodologies proposed in the literature for the μIM process [162].

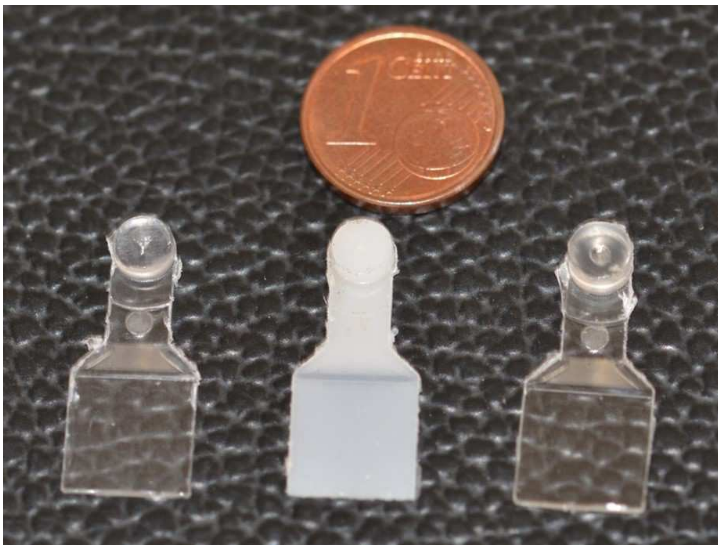

Figure 14.4: Parts molded with three polymers.

Parameter	PS	POM	COC
Mold temperature [°C]	240	235	305
Melt temperature [°C]	60	80	50
Injection speed [mm/s]	200	200	200
Packing pressure [bar]	150	150	150
Packing time [s]	6	6	6
Cooling time [s]	6	6	6

Table 14.1: Process parameters used to mold the parts for shrinkage calibration.

The square cavity was positioned on the mold moving half at the end of a fan gate (thickness: 0.2 mm), which ensured a linear flow front and a balanced filling.

The mold cavity was machined with a 5-axis micro-milling machine (Kugler, Micromaster 5X) and its dimensions were characterized using a multi-sensor coordinate measurement machine (Werth, Video-Check-IP 400). The real dimensions of the cavity were of 9.899 mm in the flow direction and of 9.906 mm in the perpendicular direction.

14.3.1.2 *Injection molding*

The calibration of the shrinkage model was carried out considering the three polymers that were used for the injection molding experiments discussed in section 10.2. Specifically, the CRIMS shrinkage model was calibrated for PS, POM and COC (subsubsection 7.4.2.2). Table 14.1 reports the process parameters that were adopted for the injection molding experiments.

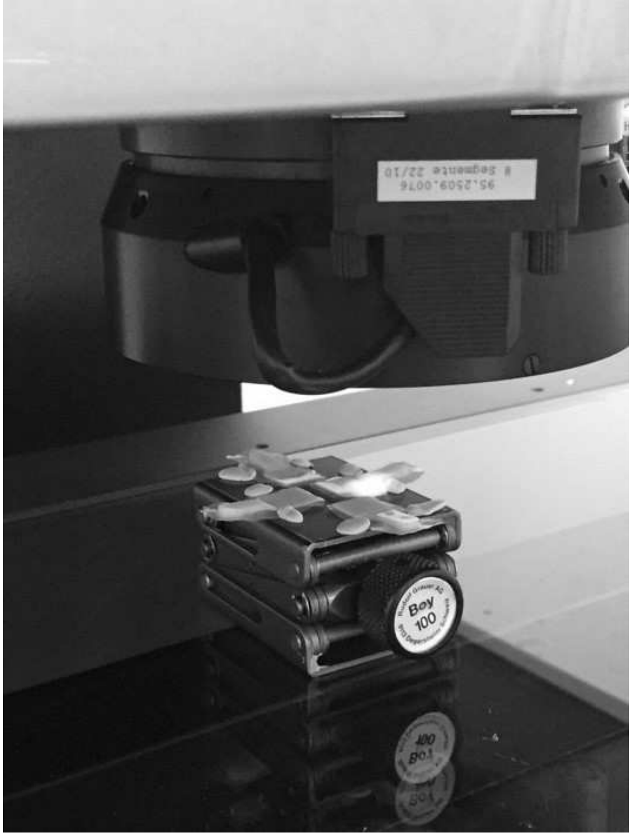

Figure 14.5: Measurements of the molded parts with the CMM machine.

14.3.2 *Shrinkage measurements*

The shrinkage of the molded micro parts was characterized according to Fischer definition as the 'difference between the linear dimension of the mold at room temperature and that of the molded part at room temperature within 48 hours following the ejection' [163].

The dimensional measurements of the parts were evaluated with a multi-sensor coordinate measurement machine (Werth, Video-Check-IP 400) used in optical mode with a direct episcopic illumination (see Figure 14.5).

The following procedure was designed and applied for the measurement of the dimension of the molded part both in the flow direction and in the perpendicular one (see Figure 14.6):

i. acquisition of the coordinates of five equally spaced points for each edge of the square molded parts;

ii. creation of a straight line by interpolating the coordinates of the acquired;

iii. creation of two symmetry lines in the flow and transverse directions;

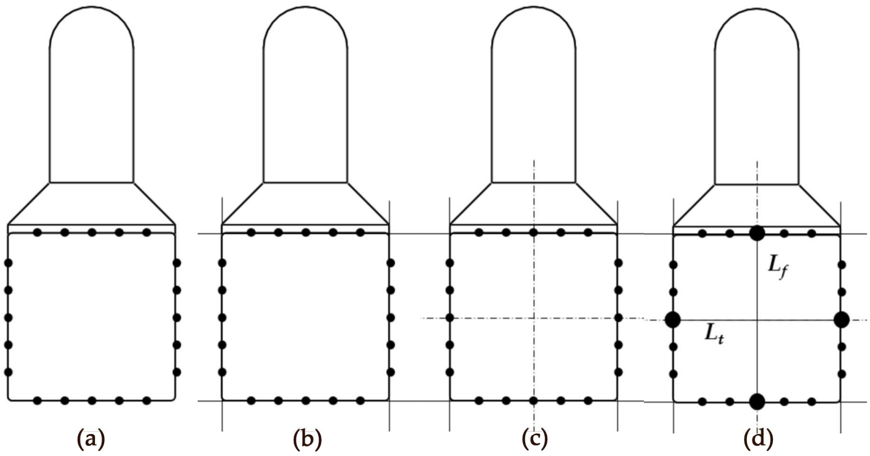

Figure 14.6: Procedure followed for the dimensional measurements of the molded parts.

Polymer	S_f [%]	S_t [%]
PS	0.654	0.954
POM	2.114	2.829
COC	0.404	0.311

Table 14.2: Selected ranges of variations for the CRIMS parameters for each polymer.

iv. intersection of the symmetry lines with the lines representing the edges of the specimen and definition of a midpoint for each edge;

v. evaluation of both in flow and transverse dimensions as the distance between the points on the opposite edges of the parts.

The shrinkage of the molded parts in the flow direction (S_f) and in the perpendicular direction (S_t) were calculated as a percentage reduction from mold dimensions. The following equations were applied:

$$S_f = \frac{L_{f,part} - L_{f,mold}}{L_{f,mold}} \cdot 100 \tag{14.7}$$

$$S_t = \frac{L_{t,part} - L_{t,mold}}{L_{t,mold}} \cdot 100 \tag{14.8}$$

where $L_{f,part}$, $L_{t,part}$ are the dimension of the molded micro part characterized with the CMM in the flow and in the transverse directions respectively, while $L_{f,mold}$, $L_{t,mold}$ are the dimensions of the mold.

Table 14.2 reports the parallel and perpendicular shrinkage values measured for the three materials using the plaque geometry.

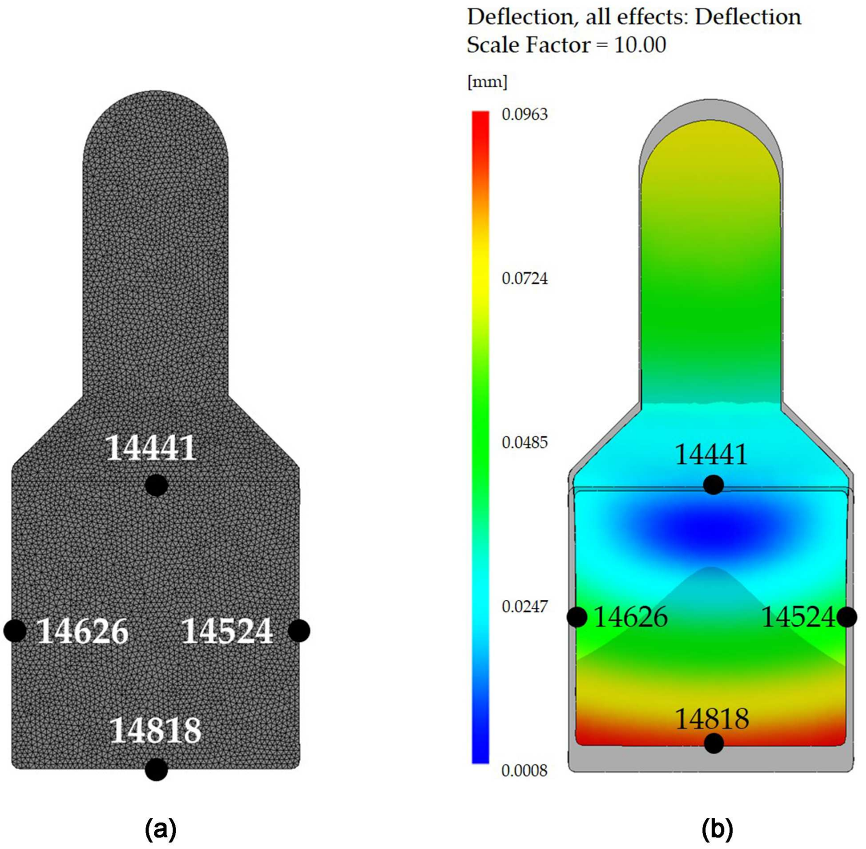
Deflection, all effects: Deflection
Scale Factor = 10.00
[mm]
0.0963
0.0724
0.0485
0.0247
0.0008
14441
14626
14524
14818
(a)
(b)

Figure 14.7: Modeling of parts used for shrinkage calibration - (a) mesh and (b) deflection results of the simulation.

14.3.3 *Inverse analysis*

The value of the CRIMS parameters that forces the numerical results to fit the measured shrinkage values were determined using an inverse analysis approach. The differences between numerical and experimental dimensions of the part were minimized using an iterative optimization algorithm.

14.3.3.1 *Numerical modeling*

The numerical modeling of shrinkage was implemented in Autodesk Moldflow. The geometry of the part was discretized using a *Dual Domain* mesh (see Figure 14.7 (a)). Table 14.3 reports the process parameters that were selected for the injection molding training simulations for the three selected polymers.

From the simulation, the *Deflection* result was considered to evaluate the displacement of 4 nodes selected on the middle of the four opposing sides of the part, as shown in Figure 14.7 (b).

	Polymer		
Parameter	PS	POM	COC
Mold temperature [°C]	60	80	50
Melt temperature [°C]	240	235	305
Flow rate [cm^3/s]	4	4	4
Switch-over pressure [MPa]	18	60	18
Packing pressure [MPa]	15	15	15
Packing time [s]	6	6	6
Cooling time [s]	6	6	6

Table 14.3: Process parameters selection used for the three polymers for the training simulations.

		Polymer	
CRIMS	PS	POM	COC
a1	0.00÷2.49	0.00÷3.38	0.00÷1.52
a2	-0.37÷0.41	-2.09÷1.85	-0.49÷0.32
a3	0.00÷0.01	-0.03÷0.05	0.00÷0.01
a4	0.00÷2.89	0.00÷6.57	0.00÷1.61
a5	-0.56÷0.42	-3.20÷2.74	-0.65÷0.37
a6	0.00÷0.01	-0.0÷0.06	0.00÷0.01

Table 14.4: Selected ranges of variations for the CRIMS parameters for each polymer.

14.3.3.2 *Artifical Neural Network*

In order to reduce the computational time, an artificial neural networks (ANN) was used as a metamodel to locally approximate the simulation results. The artificial neural networks were trained to reproduce the results of the simulation, using the Levenberg–Marquardt back propagation algorithm. The difference between numerical and experimental results was minimized using an optimization procedure implemented in modeFrontier, based on a MOGA-II genetic optimization algorithm.

Considering the values available in the Autodesk Moldflow database for similar polymers, the range of variations for each CRIMS parameters were defined (Table 14.4). Each range was discretized to create 49 combinations of CRIMS parameters (i.e. 49 different material databases) by means of Box-Behnken DoE plan. Three ANN were trained in the selected ranges, one for each polymers by using Autodesk Moldflow to obtain the ouput of the numerical model in the CRIMS range. Figure 14.8 shows the regression plot for the PS, indicating good fit of the ANN to the training simulated values.

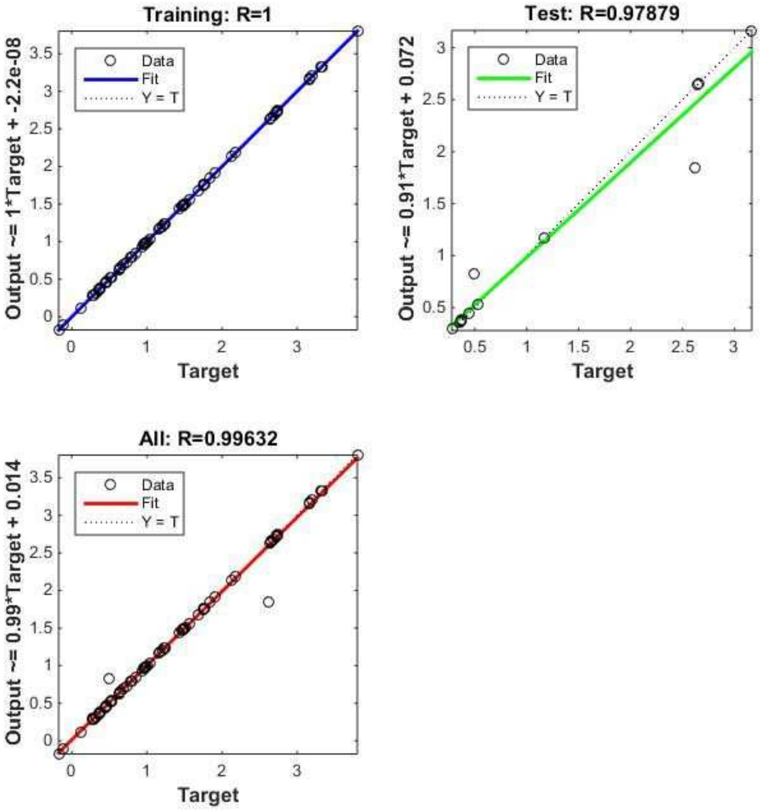

Figure 14.8: Regression plot for the training of the ANN for PS.

CRIMS	PS	POM	COC
a1	1.2275028	1.2384333	0.0610429
a2	−0.0103715	−0.1714228	0.0086159
a3	−0.0016706	−0.0045474	0.0023909
a4	0.0072468	0.0000001	0.0968220
a5	−0.5539396	−0.3147111	−0.4649388
a6	0.0061820	0.0204584	0.0029365

Table 14.5: Optimized CRIMS parameters for the three polymers.

14.4 CALIBRATED SHRINKAGE MODEL

For each polymer and for each iteration (set of CRIMS parameters), the metamodel was used to calculate the shrinkage, which is then compared to the experimental values.Table 14.5 reports the optimized values of CRIMS parameters for each polymer. These values were used to perform injection molding simulation with Autodesk Moldflow. Figure 14.9 displays the comparison between experimental shrinkage values and those obtained with the calibrated simulations. It can be observed that, for all the polymers, the simulation performed with calibrated CRIMS values yield results that are close to the measured shrinkage. Moreover, the comparison with the URSM model show that the calibration could significantly improve the numerical prediction.

14.4.1 *Shrinkage around deep cores*

The calibrated shrinkage model was then used for the prediction of shrinkage around deep cores; the geometry presented in subsection 5.1.2 was considered. Figure 14.10 (a) shows the meshed model (*Dual Domain*) as it was used for the injection molding simulation in Autodesk Moldflow. Simulations were carried out for the three polymers adopting the same selections of process parameters that were used in the experiments (cf. section 10.2).

From the results of the *Fill + Pack + Warp* simulations, the *Isotropic Shrinkage* result was selected to evaluate the shrinkage of the molded part at the mold cores (see Figure 14.10 (b)). Specifically, the shrinkage of triangular elements around the cores was selected. In order to apply the model presented in section 14.1, the shrinkage of a ring of polymer around the core was evaluated by evaluating the shrinkage on two concentric rings of triangular elements. The inner ring had a diameter of 0.4 mm, which is the same of the mold cores; while the outer diameter was fixed at 0.8 mm.

Considering the objective of this section, the results of the simulations are, for each polymer, two values of shrinkage (i.e. one for the

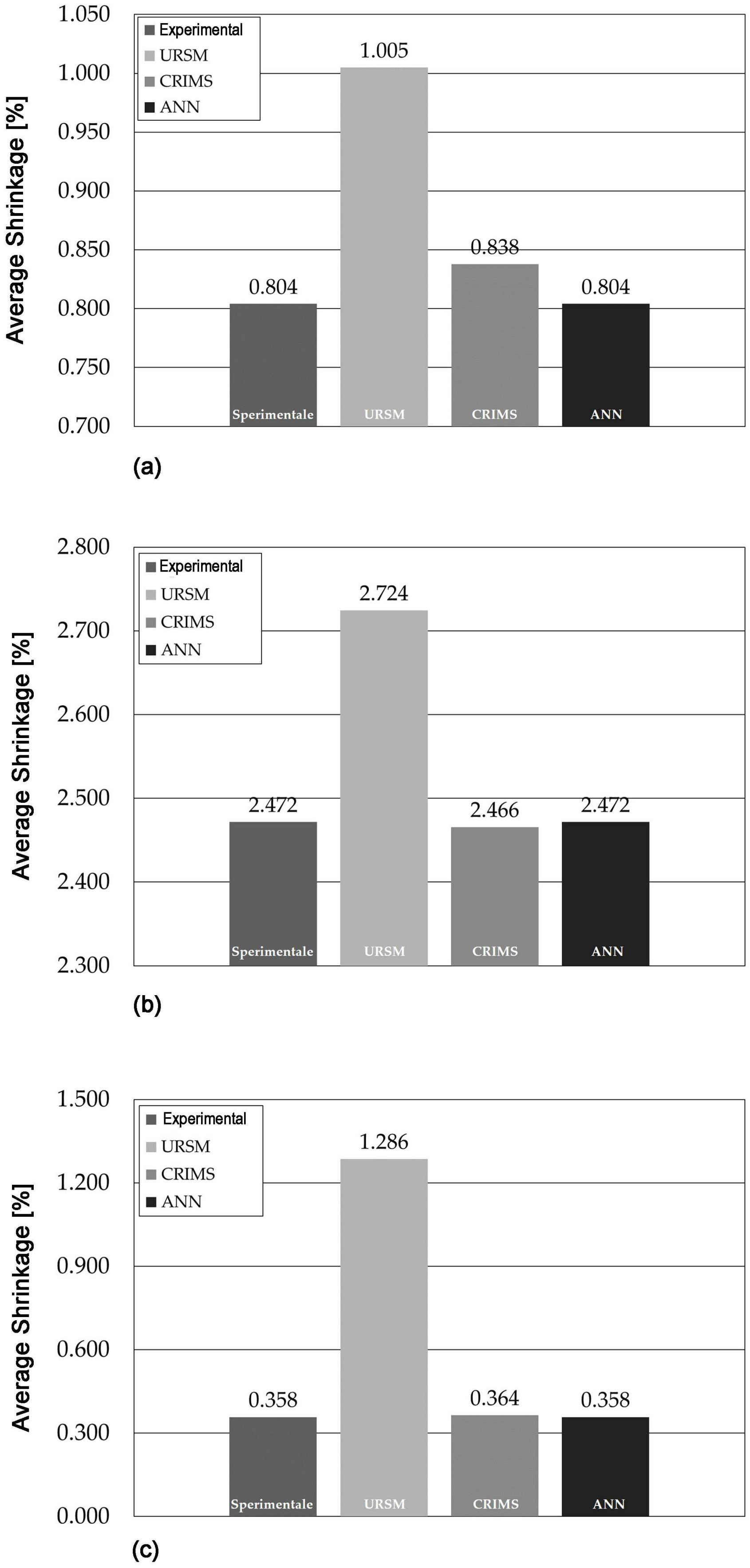

Figure 14.9: Comparison of average shrinkage values for experimental, ANN, CRIMS and URSM - (a) PS, (b) POM and (c) COC.

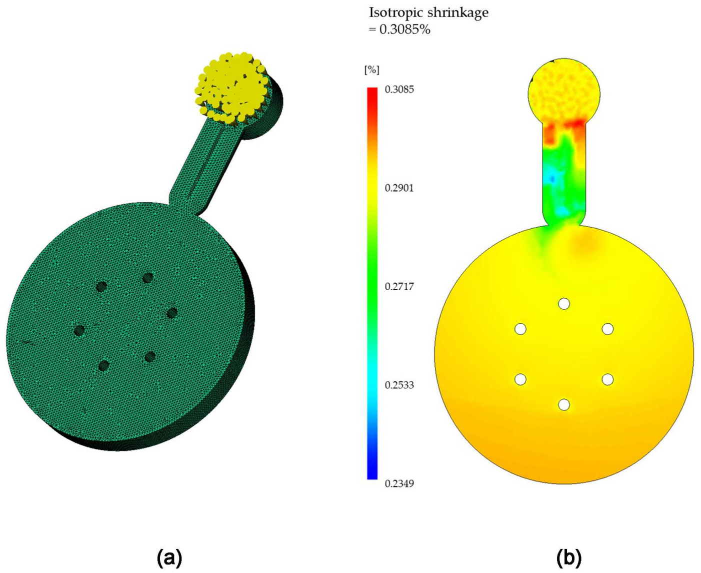

Figure 14.10: Mesh of the case study part (a) and isotropic shrinkage result (b).

	Shrinkage [mm]		
Position	PS	POM	COC
Inner	0.992	2.417	0.291
Outer	1.001	2.436	0.293

Table 14.6: Calibrated predictions for shrinkage around a single mold core for the three polymers.

inner diameter and the other for the outer diameter) of a ring of material around the mold cores. These are the values of the calibrated shrinkage that will be used to predict the demolding force by means of Equation 14.2.

Table 14.6 reports the calibrated predictions for the average shrinkage around a single mold core. Indeed, the shrinkage of the inner and outer diameters was evaluated for all the six through holes and the average values were calculated. It can be observed that POM has the highest shrinkage being a semi-crystalline polymer; while PS has higher shrinkage compared to COC due to its higher rigidity.

14.5 EJECTION FORCE PREDICTION

The prediction of the ejection force was based on the model presented in Equation 14.1, where two variables needed calibration, specifically the normal force acting on the cores (F_N) and the friction coefficient (μ). The normal load acting on mold cores during ejection was predicted using a shrinkage-calibrated numerical simulation. On the other hand, the understanding of ejection friction is more complex.

	Symbol	Value	Unit
Core Geometry			
Lenght	L	2	mm
Radius	r_c	0.2	mm
Centers Interspace	d	3.5	mm
Number	n	6	
Dimensions of a ring molded over a core			
Internal Radius	r_{ig}	0.2	mm
External Radius	r_{og}	0.4	mm
Mold Properties			
Elastic Modulus	E_c	210000	MPa
Poisson Coefficient	ν_c	0.33	

Table 14.7: Geometrical and material parameters used for the ejection force prediction.

Polymer Properties	Symbol	Unit	PS	POM	COC
Elastic Modulus	E_g	MPa	2349	1718	2483
Poisson Coefficient	ν_g	-	0.353	0.420	0.405

Table 14.8: Mechanical properties of the three polymers.

Indeed, as discussed in chapter 10 and in chapter 12, ejection friction is affected by several characteristics of the mold surface and by the injection molding processing.

In this work, the friction coefficient was calculated by means of inverse analysis with the ejection force values obtained from the injection molding experiments. The obtained values of the friction coefficient were then compared to values of the friction coefficient characterized using the offline friction setup presented in chapter 8.

14.5.1 *Friction model calibration*

The model was calibrated by calculation of the values of the friction coefficient that minimize the difference between the predicted ejection force values and those obtained from injection molding experiments. Equation 14.2 was used to predict the normal force. Table 14.7 and Table 14.8 reports the parameters that were used for the model and their designation.

The adoption of an iterative procedure allowed the minimization of the sum of the square differences between experimental and predicted values of the ejection force for different values of surface roughness. Indeed, different experimental ejection force values were considered for different mold roughnes values (cf. section 10.2).

Polymer	Normal Force [N]
PS	172
POM	293
COC	52

Table 14.9: Calibrated values of the normal force around mold cores during ejection.

	Friction Coefficient		
Sa [μm]	PS	POM	COC
1.67	0.66	0.23	5.32
1.01	0.57	0.17	3.58
0.6	0.51	0.15	3.04
0.23	0.38	0.12	2.20

Table 14.10: Calibrated values of the friction coefficients.

The pressure acting on cores during ejection was calculated using Equation 14.2 and the values of shrinkage simulated for the different rings of polymer material. Table 14.9 reports the predicted values for the overall normal force acting on mold cores upon ejection. These values were then used to determine the friction coefficient by means of inverse analysis on the Amonton law of friction (Equation 14.1).

Table 14.10 reports the values of the friction coefficient that fit the ejection force predictive model for the three polymers. It can be observed that the values of the friction coefficient are affected by polymer selection and mold roughness. Indeed, they both contribute to the determination of the stiction at the polymer/mold interface. However, the understanding of the effects of injection molding processing and its interactions with ejection friction is not easy.

Moreover, it should be noted that for COC the friction coefficient are higher than 1, indicating the failure of the Amonton friction model for certain conditions. In particular, when molding a polymer characterized by low viscosity over a mold surface with higher roughness the linearity between the normal load and the tangential friction fails. Hence, ejection friction needs to be further investigated considering different friction models, as will be discussed in the following section 14.7.

14.5.2 *Offline evaluation of friction coefficients*

In order to characterize the friction coefficients between the mold surfaces and the different polymers, an offline characterization was carried out using the setup introduced in chapter 8. The tests were performed using mold surfaces sample reproduced on small steel cylin-

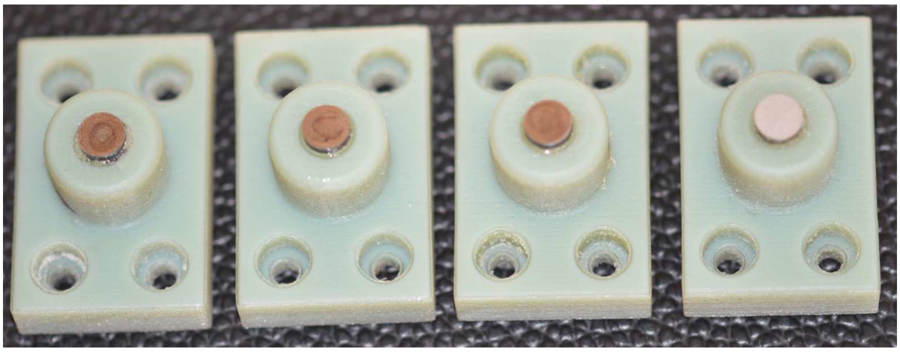

Figure 14.11: Steel surfaces machined by μEDM to reproduce the different topographies of the different mold surfaces.

	Friction Coefficient		
Sa [μm]	PS	POM	COC
1.67	0.25	0.16	0.24
1.01	0.22	0.15	0.21
0.6	0.20	0.13	0.20
0.23	0.15	0.07	0.15

Table 14.11: Values of the friction coefficients obtained from the offline characterization.

ders and mounted on 3D printed holders Figure 14.11. Each steel sample was machined using the same parameters used for the μEDM generation of the different mold surface topographies (cf. subsubsection 6.1.2.2).

The friction tests were conducted for each polymer and each mold surface (i.e. with different roughness) by setting different values of the normal load, i.e. 50, 100, 150 N. The values of the tangential force read by the load cell were then plotted for each roughness value. For each polymer, the experimental data were fitted using a linear regression model that represents the Amontons friction law. The coefficient of friction for each mold surface was obtained as the linear coefficient of regression.

Table 14.11 reports the values of the friction coefficients as determined from the offline characterization for the three polymers. These values are to be compared with those friction coefficients determined from the injection molding experiments (Table 14.10). From the comparison it is clear that the offline characterization gave underestimated values and this is due to the incapability of the offline tester to create the interface interactions between the polymer and the mold topography that are created by the injection molding processing. Indeed, during the filling phase of the injection molding process, the polymer melt replicates the mold topography. Conversely, during the friction test, the same level of replication could not be achieved due to the different temperature and pressure distributions.

The difference between experimental and offline friction values is affected by polymer selection and by mold surface roughness. In fact, the lower is the viscosity of the polymer melt the higher is the interface replication and thus the difference between the two values of friction coefficient. Similarly, surfaces characterized by higher roughness provide more room for the polymer melt during replication, thus accentuating the error of the offline tester.

14.6 DISCUSSION

In this chapter, a model for the prediction of the ejection force was proposed and characterized considering all the involved parameters. At first, particular attention was given to the calibration of a shrinkage model that was used for the calculation of the normal load acting on mold cores upon ejection. The CRIMS parameters were calibrated using a simple geometry for three different polymers and they were then input in the material database used for injection molding simulation.

Using the calibrated values of the normal force and the results of the online monitoring of the demolding force, the friction coefficient was determined for all the tested combinations of polymer selection and mold roughness. The obtained values of friction coefficient indicated a possible failure of the Amonton law of friction. Indeed, ejection friction is greatly affected by the injection molding processing that creates mechanical interlocking at the interface, increasing the deformation contribution of friction.

Finally, the offline characterization of the friction properties of specific combinations of polymer-topography interfaces was carried out. The results showed that the offline tester is able to predict the effects of different surface roughness and polymers. However, if compared to the experimental friction values, these are significantly lower due to the incapability of creating the same interface replication, which was understood to be the main component of the ejection friction.

14.7 UNDERSTANDING EJECTION FRICTION

Friction problems, as the ejection of molded parts, are usually interpreted according to the Amontons' laws, which indicates the constancy of the static friction coefficient $\mu = F/L$ (where F is the tangential force and L the normal load) and its independency to the nominal force. However, as discussed in section 3.2, the friction coefficient is not constant, but dependent on the surface roughness, surface energy, mechanical properties, load and sliding velocity. Moreover, for rough surfaces the mechanisms related to adhesion, deformation, contact, friction and wear are different from those observed for perfectly smooth surfaces. Hence, a more accurate description of the friction force F_e is defined considering the combination of the deformation and adhesion components, as proposed in Equation 3.2.

The friction during the ejection phase of the injection molding process is mainly dominated by the deformation contribution of Equation 3.2, thus being 'deformation-controlled'. In particular, the friction mechanism at the part/mold interface is a combination of ploughing (i.e. plastic deformation of the sub-surface layer caused by hard asperities) and hysteresis (i.e. elastic or viscoelastic recovery of the polymer after indentation by mold surface asperities) acting together during the sliding of the two solid surface.

Considering Equation 3.3, the critical shear stress (S_c) and the applied normal load (F_N) are linearly correlated with the mechanical properties of the polymer, while the real contact area (A) is linearly correlated with both polymer properties and the characteristics of the mold surface. In fact, the real contact area depends on the replication capability of the polymer melt; hence, it is linearly correlated with its viscosity. Moreover, surface roughness provides information about the morphology of mold surface and of the void volumes characterizing it, determining the maximum surface that can be replicated by the molding polymer. In general, the replication capabilities of the injection molding process are determined for a specific combination of mold surface roughness and polymer selection. Hence, the correlation between the real contact area and the ratio between mold roughness and polymer viscosity can be observed:

$$A \propto \frac{R}{\eta} \tag{14.9}$$

where R is a roughness parameter and η is the shear viscosity of the melt polymer.

Considering all the influences of the injection molding process on its variables, Equation 3.3 can be rewritten as:

$$F_e \propto \frac{R \cdot E}{\eta} \tag{14.10}$$

Then, the dependence of ejection friction to polymer properties and mold surface roughness can be analyzed considering the parameters introduced in Equation 14.10.

14.7.1 *Modeling of ejection friction*

The combining effects of polymer selection and mold roughness on the demolding force were modeled considering the combined contribution of adhesion and deformation. Considering Equation 4 the ejection force can be interpreted as a function of E'/η and R, hence a

	POM	COC	PS	
E'/η [10^6/s]	5.6	98.2	39.3	
Sa [μm]	0.23	0.6	1.01	1.67

Table 14.12: General factorial plan designed to model the effects of polymer selection and mold surface roughness on the ejection force.

general full factorial plan was designed to fit the experimental ejection force results obtained without the application of the ultrasound vibration (Table 14.12).

Using the data from the experimental plans introduced in subsection 10.2.2, the following regression equation (R^2 = 98.44) was obtained:

$$F_e = 31.84 + 0.5991 \cdot \frac{E'}{\eta} + 7.28 \cdot Sa + 0.9996 \cdot \frac{E'}{\eta} \cdot Sa \qquad (14.11)$$

The model indicates that the ejection force is linearly correlated with the surface roughness (i.e. R) for a specific polymer selection, confirming observations reported in Figure 10.15. Moreover, the ejection friction is correlated with the ratio between the storage modulus and the shear viscosity of the polymer (E'/η) confirming the importance of the deformation contribution. In fact, the lower the viscosity the higher the interface replication and the higher the mechanical properties the higher the resistance of the replicated interface to deformation during ejection.

14.7.2 *Model verification and discussion*

Considering the heating effect, discussed in subsubsection 10.2.3.5, the effect of the ultrasound vibration was introduced in the model as a reduction of the mechanical properties of the polymer. Thus, Equation 14.11 was used to predict the ejection force peak when the ultrasound vibration is used to promote ejection. From the mechanical characterization (subsubsection 7.4.2.2) the reduced value of the storage modulus (Table 10.16) was used to predict the ejection force peak with the ultrasound vibration.

Figure 14.12 shows the experimental and the predicted values, while Figure 14.12 reports the errors of the model prediction with respect to injection molding experiments performed with the use of the ultrasound-assisted demolding systems, for different polymer selections and different values of mold surface roughness. It can be observed that the model gives good force predictions for COC and POM, where maximum deviation is of about 10%. However, predictions are less accurate for PS (maximum error: 24%), which mechanical properties are more sensitive to the mold surface temperature increase.

	Ejection Force Peak [N]			
	US Off		US On	
	Experimental	Model	Experimental	Model
PS - A	66.0	66.1	63.9	48.7
PS - B	88.3	83.3	75.4	58.2
PS - C	98.7	102.4	80.9	68.6
PS - D	113.5	133.1	86.1	85.5
COC - A	115.3	115.0	115.7	112.8
COC - B	158.9	154.0	151.0	150.9
COC -C	187.1	197.2	175.1	193.1
COC - D	278.4	266.8	259.9	261.0
POM -A	34.6	38.2	34.1	37.4
POM - B	45.3	42.9	44.3	41.9
POM - C	49.7	48.2	48.1	46.8
POM - D	68.2	56.7	58.8	54.7

Table 14.13: Prediction of the ejection force peak for all the experimental combinations and prediction errors.

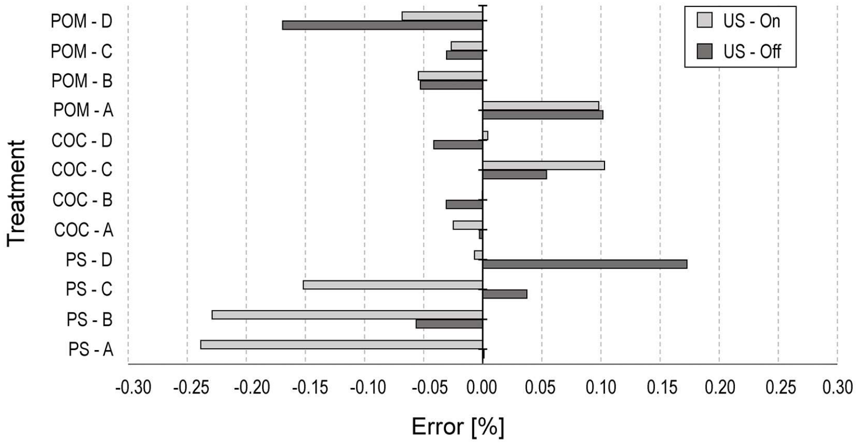

Figure 14.12: Errors of the ejection force model.

The application of the predictive model to ultrasound-assisted ejection proves the importance of the deformation component for the understanding of ejection friction. Specifically, the increase of the part/mold contact area generated during the filling phase has high influence on interface stiction. The model indicates that the higher is the ratio between the mechanical properties and the viscosity the higher is the mechanical interlocking at the interface. Moreover, the effect is more marked for mold surfaces characterized by increasing roughness values. The use of the ultrasound-assisted ejection system proved to be an efficient solution to decrease interface stiction by inducing a heating effect at the mold surface.

Part VI

CONCLUSIONS

15

CONCLUSIONS

In this work, the analysis of the tribological effects of mold surface properties on the injection molding process was carried out, focusing on the characterization of conventional and unconventional treatments. The experimental investigations considered different case studies for both packaging and microfluidic applications. Indeed, due to the reduced dimensions, these applications of the conventional process can be significantly affected by mold design and specifically by the part-tool interface.

The general goals that were fixed approaching the design of mold surface were the reduction of the injection pressure and the reduction of the demolding force. The effects of mold surface on both the filling and ejection phases were investigated following two main strategies, specifically *Surface Generation* and *Surface Modification*. The research was mainly based on experimental injection molding investigations, which were designed aiming at maximizing accuracy in process control. Particular attention has been given to the design of injection molding molds that could allow the characterization of different mold treatments. Two different mold geometries were realized, one for the study of the filling phase and the other to study the ejection phase. Moreover, different monitoring instrumentations were implemented in the injection molding process allowing the accurate control of temperature, pressure and force during the different phases of the process.

FILLING PHASE

The characterization of the effects of mold surface coatings on the filling phase allowed the identification of the phenomena that control the melt flow resistance, i.e. thermal insulation and wall-slip. Different investigations allowed the characterization of this phenomena and the evaluation of their impacts on the injection molding of thin-wall parts. Considering the effect of injection speed, it was observed that at high injection speed the cavity pressure drop reached a plateau, due to the presence of slipping occurring at the cavity walls. The hypothesis of wall slip was further proved by observing periodic oscillations of the pressure signal.

The filling behavior of the polymer melt was then characterized by means of high-speed visualization of the flow. The velocity profile of the injected polymer was characterized for different values of the injection speed, showing a fully developed plug flow with the presence of a significant wall-slip for both coated and uncoated cavities. The measurement of the slip velocities allowed its comparison with the cavity pressure drop for each coating. In particular, it was observed that cavity pressure drop is inversely dependent on the slip velocity, thus indicating the importance of selecting a proper mold surface coating. In order to predict the melt flow resistance characterizing the filling phase in thin-wall injection molding, the interface interactions between the polymer and the coatings can be evaluated considering their wetting behavior.

The understanding of the effects of mold surface properties on the filling phase was then further investigated by characterizing the effects of Laser-Induced Periodic Surface Structures (LIPSS). It was shown that different LIPSS treatments can be exploited to drive the slipping of polymer melts depending on the relative orientation of the ripples. It was reported that LIPSS nanostructures have the capability of reducing the injection pressure up to more than 20% under standard injection molding processing conditions. These results not only showed how LIPSS can be used in injection molding to significantly promote filling, but they indicated that the treatment of the mold can also be used to control the filling flow pattern by selectively design parallel and perpendicular ripples as flow leaders and deflectors, respectively. We anticipate our findings to be the starting point for the design of thinner plastic parts, leading to reduced environmental impact. Through the decrease of material and energy consumptions, significant manufacturing cost saving would be achieved.

EJECTION PHASE

The results of the characterization of surfaces generated by either micro milling or micro electro discharge machining indicated that ejection friction is controlled by the *mechanical interlocking* created at the polymer/mold interface during the filling phase. The latter being strongly related to the replication capability of the polymer. The results of the experimental tests showed the strong interactions between the effect of mold surface topography and the ones of those μIM process parameters that promote the replication, such as mold temperature and holding pressure.

The results of the injection molding experiments indicated that *Ra* is too general to be correlated with the complexity of ejection friction, especially considering the different technologies available for micro molds manufacture. In order to specify and control micro mold surface quality, average parameters need to be complemented by a better description of valleys width.

Moreover, the tribological properties of different mold surface coatings were investigated by characterization of the demolding force signal. The results of the μIM online acquisitions showed that the demolding force peak is affected by both polymer and coating selection. Indeed, for each one of the selected polymers, the coatings yield different ejection force. In order to provide further understanding of ejection friction, the deformation and the adhesion components were analyzed separately. Considering the deformation contribution, it was observed that a combination of low viscosity and high surface roughness leads to an increase of the demolding force due to the higher mechanical interlocking at the part/mold interface. On the other hand, the adhesion contribution is affected by the chemical affinity of the polymer melt to the coated mold surface. The results of the wettability analysis, which showed different contact angles over the different coatings, were correlated to ejection friction.

A novel ultrasound-assisted system was used to vibrated mold cores in order to reduce interface stiction during the ejection phase. The main effect of vibrating the mold cavity before the ejection phase resulted in a reduction of the mean value of the demolding force peak for all the selected polymers. However, the intensity of this reduction is not consistent among the different polymers. In fact, vibrating the mold cores resulted in heating of the mold surface, which results in localized softening of the polymer reducing its mechanical properties.

MODELING

The phenomena occuring during both the filling and ejection phases of thin-wall and micro cavities were modeled. In particular, the physical aspects associated with the scale-down of forming parts were considered.

A calibration strategy was proposed to separate the effects on the filling phase of heat conduction from that of wall slip. The effect of the coatings were interpreted as insulating layers that modify the thermal boundary conditions at the interface between the melt polymer and the the mold. The calibrated thermal boundary conditions not only allowed a better understanding of the filling flow, but they could also be used for calibrated injection molding simulation. In particular, at the mold design stage, they could be useful to evaluate the thickness reduction that could be obtained with a specific mold treatment.

A model for the prediction of the ejection force was proposed based on the calibration of a shrinkage model. The predicted values of ejection friction coefficients indicated the failure of the Amonton law of friction. Indeed, ejection friction is greatly affected by the injection molding processing that creates mechanical interlocking at the interface, increasing the deformation contribution of friction. Thus, the combining effects of polymer selection and mold roughness on the demolding force were modeled considering the combined contribution of adhesion and deformation. The model was then applied to predict the effect of the ultrasound vibration that was introduced as a reduction of the mechanical properties of the polymer. The results showed that the increase of the part/mold contact area generated during the filling phase has high influence on interface stiction. The model indicates that the higher is the ratio between the mechanical properties and the viscosity the higher is the mechanical interlocking at the interface. Moreover, the effect is more marked for mold surfaces characterized by increasing roughness values. The use of the ultrasound-assisted ejection system proved to be an efficient solution to decrease interface stiction by inducing a heating effect at the mold surface.

FINAL REMARKS

In conclusion, this research focused on the characterization of different treatment for injection molding molds. The research provide significant contribution to the scientific literature and innovative solutions and approaches for the industry. The improved understanding of the phenomena that control the injection molding process and the introduction of new technological solutions, would help the development of new solutions and strategies for the design of better injection molded parts.

BIBLIOGRAPHY

[1] PlasticsEurope, Plastics – the Facts 2015, an Analysis of European plastics production, demand and waste data. Tech. rep., Brussels., **2015**.

[2] G. Gourmelon, *New Worldwatch Institute analysis explores trends in global plastic consumption and recycling. Recuperado de http://www. worldwatch. org* **2015**.

[3] C. Yang, X.-H. Yin, G.-M. Cheng, *Journal of Micromechanics and Microengineering* **2013**, *23*, 093001.

[4] D. Yao, B. Kim, *Polymer-plastics technology and engineering* **2002**, *41*, 819–832.

[5] M. C. Song, Z. Liu, M. J. Wang, T. M. Yu, D. Y. Zhao, *Journal of Materials Processing Technology* **2007**, *187*, 668–671.

[6] G. Lucchetta, M. Sorgato, S. Carmignato, E. Savio, *CIRP Annals-Manufacturing Technology* **2014**, *63*, 521–524.

[7] R. Selden, *Journal of Injection Molding Technology* **2000**, *4*, 159.

[8] H. J. Oh, D. J. Lee, C. G. Lee, K. Y. Jo, D. H. Lee, Y. S. Song, J. R. Youn, *Composites Part A: Applied Science and Manufacturing* **2013**, *53*, 34–45.

[9] C. Gornik, *Macromolecular Symposia* **2004**, *217*, 365–374.

[10] U. M. Attia, J. R. Alcock, *Microsystem technologies* **2009**, *15*, 1861.

[11] D. Masato, M. Sorgato, G. Lucchetta, *Microsystem Technologies* **2017**, *23*, 3661–3670.

[12] R. Surace, G. Trotta, V. Bellantone, I. Fassi in *New Technologies-Trends, Innovations and Research*, InTech, **2012**.

[13] Wittmann Battenfeld GmbH, Micro-Moulding: Battenfeld Injection Molding, Kottingbrunn, Austria, **2010**, pp. 1–70.

[14] J. Giboz, T. Copponnex, P. Mélé, *Journal of micromechanics and microengineering* **2007**, *17*, R96.

[15] M. Heckele, W. K. Schomburg, *Journal of Micromechanics and Microengineering* **2003**, *14*, R1.

[16] G. Lucchetta, P. F. Bariani, *CIRP Annals-Manufacturing Technology* **2010**, *59*, 33–36.

[17] A. Thiriez, T. Gutowski in Electronics and the Environment, 2006. Proceedings of the 2006 IEEE International Symposium on, IEEE, **2006**, pp. 195–200.

[18] D. Masato, M. Sorgato, G. Lucchetta, *Materials & Design* **2016**, *95*, 219–224.

[19] M. Sorgato, **2016**.

[20] T. Nguyen-Chung, G. Jüttner, C. Löser, T. Pham, M. Gehde, *Polymer Engineering & Science* **2010**, *50*, 165–173.

[21] H. A. Barnes, J. F. Hutton, F. R. S. K. Walters, *An Introduction to Rheology*, 1a, Elsevier, **1989**, pp. 1–199.

[22] C. W. Macosko, *Rheology: Principles, Measurements And Applications*, 1a, Wiley-VCH, **1994**, pp. 1–514.

[23] B. Xu, K. T. Ooi, T. N. Wong, C. Y. Liu, *Journal of Micromechanics and Microengineering* **1999**, *9*, 377.

[24] E. E. Rosenbaum, S. G. Hatzikiriakos, *AIChE Journal* **1997**, *43*, 598–608.

[25] V. Piotter, K. Mueller, K. Plewa, R. Ruprecht, J. Hausselt, *Microsystem Technologies* **2002**, *8*, 387–390.

[26] L. Yu, L. J. Lee, K. W. Koelling, *Polymer Engineering & Science* **2004**, *44*, 1866–1876.

[27] R. Surace, V. Bellantone, G. Trotta, I. Fassi, *Journal of Manufacturing Processes* **2017**, *28*, 351–361.

[28] F. De Santis, R. Pantani, *Journal of Materials Processing Technology* **2016**, *237*, 1–11.

[29] A. W. McFarland, M. A. Poggi, L. A. Bottomley, J. S. Colton, *Nanotechnology* **2004**, *15*, 1628.

[30] P.-C. Chang, S.-J. Hwang, *International Journal of Heat and Mass Transfer* **2006**, *49*, 3846–3854.

[31] M. Sorgato, D. Masato, G. Lucchetta, *Microsystem Technologies* **2017**, *23*, 2543–2552.

[32] L. Crema, M. Sorgato, G. Lucchetta, *International Journal of Heat and Mass Transfer* **2017**, *109*, 462–469.

[33] D. Masato, J. Rathore, M. Sorgato, S. Carmignato, G. Lucchetta, *Materials & Design* **2017**, *132*, 496–504.

[34] D. Drummer, K. Vetter, *CIRP Journal of Manufacturing Science and Technology* **2011**, *4*, 376–381.

[35] S.-C. Chen, Y. Chang, Y.-P. Chang, Y.-C. Chen, C.-Y. Tseng, *International Communications in Heat and Mass Transfer* **2009**, *36*, 1030–1035.

[36] S. G. Hatzikiriakos, *Progress in Polymer Science* **2012**, *37*, 624–643.

[37] S. G. Hatzikiriakos, K. B. Migler, *Polymer processing instabilities: control and understanding*, CRC Press, **2004**.

[38] F. Brochard, P. G. De Gennes, *Langmuir* **1992**, *8*, 3033–3037.

[39] Y. M. Joshi, A. K. Lele, R. A. Mashelkar, *Journal of non-newtonian fluid mechanics* **2000**, *94*, 135–149.

[40] P. P. Drda, S.-Q. Wang, *Physical review letters* **1995**, *75*, 2698.

[41] E. Chatzigiannakis, M. Ebrahimi, S. G. Hatzikiriakos, *Journal of Rheology* **2017**, *61*, 731–739.

[42] M. Ansari, Y. W. Inn, A. M. Sukhadia, P. J. DesLauriers, S. G. Hatzikiriakos, *Journal of Rheology* **2013**, *57*, 927–948.

[43] D. A. Hill, *Journal of Rheology* **1998**, *42*, 581–601.

[44] S. G. Hatzikiriakos, C. W. Stewart, J. M. Dealy, *International Polymer Processing* **1993**, *8*, 30–35.

[45] V. Mhetar, L. A. Archer, *Macromolecules* **1998**, *31*, 8607–8616.

[46] C. S. Nickerson, J. A. Kornfield, *Journal of Rheology* **2005**, *49*, 865–874.

[47] F. Legrand, J. M. Piau, H. Hervet, *Journal of Rheology* **1998**, *42*, 1389–1402.

[48] P. G. De Gennes, *Comptes rendus hebdomadaires des seances de l'academie des sciences serie B* **1979**, *288*, 219–220.

[49] P. E. Boukany, S.-Q. Wang, *Macromolecules* **2009**, *42*, 2222–2228.

[50] S.-Q. Wang, P. A. Drda, *Rheologica acta* **1997**, *36*, 128–134.

[51] J. Sanchez-Reyes, L. A. Archer, *Langmuir* **2003**, *19*, 3304–3312.

[52] M. Ebrahimi, V. K. Konaganti, S. Moradi, A. K. Doufas, S. G. Hatzikiriakos, *Soft matter* **2016**, *12*, 9759–9768.

[53] H. L. Zhang, N. S. Ong, Y. C. Lam, *Polymer Engineering & Science* **2007**, *47*, 2012–2019.

[54] V. Bellantone, R. Surace, F. Modica, I. Fassi, *The International Journal of Advanced Manufacturing Technology* **2017**, 1–11.

[55] H. J. Larrazabal, A. N. Hrymak, J. Vlachopoulos, *Rheologica acta* **2006**, *45*, 705–715.

[56] J. Israelachvili, **1992**.

[57] J.-L. Barrat, *Faraday discussions* **1999**, *112*, 119–128.

[58] N. Zhang, M. D. Gilchrist, *Polymer testing* **2012**, *31*, 748–758.

[59] A. L. Kelly, T. Gough, B. R. Whiteside, P. D. Coates, *Journal of Applied Polymer Science* **2009**, *114*, 864–873.

[60] T. V. Zhiltsova, M. S. A. Oliveira, J. A. Ferreira, *Journal of Materials Science* **2013**, *48*, 81–94.

[61] A. Gava, G. Lucchetta, *Express Polymer Letters* **2012**, *6*.

[62] R.-D. Chien, W.-R. Jong, S.-C. Chen, *Journal of Micromechanics and Microengineering* **2005**, *15*, 1389.

[63] C.-S. Chen, S.-C. Chen, W.-L. Liaw, R.-D. Chien, *European Polymer Journal* **2008**, *44*, 1891–1898.

[64] L. Yu, C. G. Koh, L. J. Lee, K. W. Koelling, M. J. Madou, *Polymer Engineering & Science* **2002**, *42*, 871–888.

[65] B. J. Araújo, A. S. Pouzada, *O Molde* **2002**, *54*, 36–41.

[66] C. A. Griffiths, S. S. Dimov, E. B. Brousseau, C. Chouquet, J. Gavillet, S. Bigot, *The International Journal of Advanced Manufacturing Technology* **2010**, *47*, 99–110.

[67] S. Marson, U. M. Attia, G. Lucchetta, A. Wilson, J. R. Alcock, D. M. Allen, *Journal of Micromechanics and Microengineering* **2011**, *21*, 115024.

[68] K. D. Delaney, G. Bissacco, D. Kennedy, *International Polymer Processing* **2012**, *27*, 77–90.

[69] D. Masato, M. Sorgato, P. Parenti, M. Annoni, G. Lucchetta, *Journal of Materials Processing Technology* **2017**, *246*, 211–223.

[70] K. Delaney, D. Kennedy, **2010**.

[71] G. Menges, W. Michaeli, P. Mohren, *Hanser Cincinnati*.

[72] C. A. Griffiths, S. S. Dimov, S. G. Scholz, G. Tosello, A. Rees, *Journal of Manufacturing Science and Engineering* **2014**, *136*, 031014.

[73] P. J. Blau, *Tribology International* **2001**, *34*, 585–591.

[74] B. Persson, *Sliding friction: physical principles and applications*, Springer Science & Business Media, **2013**.

[75] D. E. Kim, N. P. Suh, *Wear* **1991**, *149*, 199–208.

[76] N. P. Suh, M. Mosleh, P. S. Howard, *Wear* **1994**, *175*, 151–158.

[77] S. Wu, *Polymer interface and adhesion*, M. Dekker, **1982**.

[78] D. E. Kim, N. P. Suh, *Wear* **1993**, *162*, 873–879.

[79] B. Bhushan, *Handbook of micro/nano tribology*, CRC press, **1998**.

[80] B. Zappone, K. J. Rosenberg, J. Israelachvili, *Tribology Letters* **2007**, *26*, 191.

[81] A. S. Pouzada, E. C. Ferreira, A. J. Pontes, *Polymer Testing* **2006**, *25*, 1017–1023.

[82] P. Parenti, D. Masato, M. Sorgato, G. Lucchetta, M. Annoni, *Journal of Manufacturing Processes* **2017**, *29*, 160–174.

[83] D. Yao, B. Kim, *Transactions of the ASME-B-Journal of Manufacturing Science and Engineering* **2004**, *126*, 733–739.

[84] G. R. Berger, C. Steffel, W. Friesenbichler, *International Journal of Materials and Product Technology* **2016**, *52*, 193–211.

[85] J.-Y. Charmeau, M. Chailly, V. Gilbert, Y. Béreaux, *International Journal of Material Forming* **2008**, *1*, 699–702.

[86] C. Majewski, N. Hopkinson, *International journal of production research* **2003**, *41*, 581–592.

[87] D. Annicchiarico, J. R. Alcock, *Materials and Manufacturing Processes* **2014**, *29*, 662–682.

[88] C. A. Griffiths, G. Tosello, S. S. Dimov, S. G. Scholz, A. Rees, B. Whiteside, *Microsystem Technologies* **2015**, *21*, 1677–1690.

[89] A. J. Pontes, A. S. Pouzada in Materials science forum, *Vol. 514*, Trans Tech Publ, **2006**, pp. 1501–1505.

[90] A. J. Pontes, A. S. Pouzada, *Polymer Engineering & Science* **2004**, *44*, 891–897.

[91] E. C. Ferreira, M. F. Costa, C. R. Laranjeira, M. J. Oliveira, A. S. Pouzada in Materials Science Forum, *Vol. 455*, Trans Tech Publ, **2004**, pp. 467–471.

[92] T. Schaller, M. Heckele, R. Ruprecht, K. Schubert in Proceedings of the ASPE, *Vol. 20*, **1999**, pp. 224–227.

[93] T. Sasaki, N. Koga, K. Shirai, Y. Kobayashi, A. Toyoshima, *Precision engineering* **2000**, *24*, 270–273.

[94] M. S. Correia, A. S. Miranda, M. C. Oliveira, C. A. Capela, A. S. Pouzada, *The International Journal of Advanced Manufacturing Technology* **2012**, *59*, 977–986.

[95] P. A. Dearnley, *Wear* **1999**, *225*, 1109–1113.

[96] J. M. Stormonth-Darling, R. H. Pedersen, C. How, N. Gadegaard, *Journal of Micromechanics and Microengineering* **2014**, *24*, 075019.

[97] B. Saha, W. Q. Toh, E. Liu, S. B. Tor, D. E. Hardt, J. Lee, *Journal of Micromechanics and Microengineering* **2015**, *26*, 013002.

[98] K. Delaney, D. Kennedy, G. Bissacco, **2011**.

[99] W. Michaeli, R. Gärtner, *Journal of polymer engineering* **2006**, *26*, 161–178.

[100] T. Zwicker in Kunststoff-Zentrum in Leipzig GmbH, **2005**.

[101] J. D. Yoon, S. K. Hong, J. H. Kim, S. W. Cha, *Cellular polymers* **2004**, *23*, 39–48.

[102] H. L. Zhang, N. S. Ong, Y. C. Lam, *The International Journal of Advanced Manufacturing Technology* **2008**, *37*, 1105–1112.

[103] T. Masuzawa, *CIRP Annals-Manufacturing Technology* **2000**, *49*, 473–488.

[104] H. Ramasawmy, L. Blunt, *Journal of Materials Processing Technology* **2004**, *148*, 155–164.

[105] D. Huo, *Micro-cutting: fundamentals and applications*, John Wiley & Sons, **2013**.

[106] P. Parenti, L. Pagani, M. Annoni, B. M. Colosimo, Q. Semeraro, *Journal of Manufacturing Science and Engineering* **2017**, *139*, 051002.

[107] G. M. Kim, B. H. Kim, C. N. Chu, *International Journal of Machine Tools and Manufacture* **2003**, *43*, 917–924.

[108] D. Dornfeld, S. Min, Y. Takeuchi, *CIRP Annals-Manufacturing Technology* **2006**, *55*, 745–768.

[109] M. J. B. Fard, E. V. Bordatchev, *The International Journal of Advanced Manufacturing Technology* **2013**, 1–11.

[110] D. Huo, K. Cheng, F. Wardle, *The International Journal of Advanced Manufacturing Technology* **2010**, *47*, 867–877.

[111] E. Uhlmann, S. Piltz, U. Doll, *Journal of Materials Processing Technology* **2005**, *167*, 488–493.

[112] Y. Qin, *Micromanufacturing engineering and technology*, William Andrew, **2010**.

[113] K.-T. Chiang, *The International Journal of Advanced Manufacturing Technology* **2008**, *37*, 523–533.

[114] F. Han, J. Jiang, D. Yu, *International journal of advanced manufacturing technology* **2007**, *34*.

[115] E. Uhlmann, S. Piltz, S. Jerzembeck, *Journal of Materials Processing Technology* **2005**, *160*, 15–23.

[116] Y. S. Liao, J. T. Huang, Y. H. Chen, *Journal of Materials Processing Technology* **2004**, *149*, 165–171.

[117] H. S. Lim, Y. S. Wong, M. Rahman, M. K. E. Lee, *Journal of Materials Processing Technology* **2003**, *140*, 318–325.

[118] S. Kumar, R. Singh, T. P. Singh, B. L. Sethi, *Journal of Materials Processing Technology* **2009**, *209*, 3675–3687.

[119] M. Y. Ali, R. Mehfuz, A. A. Khan, A. F. Ismail in *Micromachining Techniques for Fabrication of Micro and Nano Structures*, InTech, **2012**.

[120] L. Orazi, I. Gnilitskyi, I. Pavlov, A. P. Serro, S. Ilday, F. O. Ilday, *CIRP Annals-Manufacturing Technology* **2015**, *64*, 193–196.

[121] J. Bonse, S. Höhm, S. V. Kirner, A. Rosenfeld, J. Krüger, *IEEE Journal of Selected Topics in Quantum Electronics* **2017**, *23*, 1–15.

[122] A. Y. Vorobyev, C. Guo, *Applied Physics Letters* **2008**, *92*, 041914.

[123] M. Barberoglou, V. Zorba, E. Stratakis, E. Spanakis, P. Tzanetakis, S. H. Anastasiadis, C. Fotakis, *Applied Surface Science* **2009**, *255*, 5425–5429.

[124] V. Zorba, E. Stratakis, M. Barberoglou, E. Spanakis, P. Tzanetakis, C. Fotakis, *Applied Physics A* **2008**, *93*, 819.

[125] A. Cunha, O. F. Zouani, L. Plawinski, A. M. B. Do Rego, A. Almeida, R. Vilar, M.-C. Durrieu, *Nanomedicine* **2015**, *10*, 725–739.

[126] J. J. Yu, Y. F. Lu, *Applied surface science* **1999**, *148*, 248–252.

[127] B. Öktem, I. Pavlov, S. Ilday, H. Kalaycıoğlu, A. Rybak, S. Yavaş, M. Erdoğan, F. Ö. Ilday, *Nature Photonics* **2013**, *7*, 897–901.

[128] D. Bhaduri, A. Batal, S. S. Dimov, Z. Zhang, H. Dong, M. Fallqvist, R. M'Saoubi, *Procedia CIRP* **2017**, *60*, 20–25.

[129] I. Gnilitskyi, F. Rotundo, C. Martini, I. Pavlov, S. Ilday, E. Vovk, F. Ö. Ilday, L. Orazi, *Tribology International* **2016**, *99*, 67–76.

[130] L. De Chiffre, *CIRP Annals-Manufacturing Technology* **1999**, *48*, 74–77.

[131] M. Berins, *Plastics engineering handbook of the society of the plastics industry*, Springer Science & Business Media, **1991**.

[132] N. Dingremont, E. Bergmann, P. Collignon, *Surface and Coatings Technology* **1995**, *72*, 157–162.

[133] C. Mitterer, F. Holler, D. Reitberger, E. Badisch, M. Stoiber, C. Lugmair, R. Nöbauer, T. Müller, R. Kullmer, *Surface and Coatings Technology* **2003**, *163*, 716–722.

[134] M. Heinze, *Surface and Coatings Technology* **1998**, *105*, 38–44.

[135] V. Volpe, R. Pantani, *Journal of Applied Polymer Science*.

[136] M. Kamal, S. Goyal, E Chu, *AIChE journal* **1988**, *34*, 94–106.

[137] J. M. Dealy, *Rheometers for molten plastics: a practical guide to testing and property measurement*, Van Nostrand Reinhold Company, **1982**.

[138] G. Lucchetta, D. Masato, M. Sorgato, L. Crema, E. Savio, *CIRP Annals-Manufacturing Technology* **2016**, *65*, 537–540.

[139] M. Sorgato, D. Masato, G. Lucchetta, *Precision Engineering* **2017**, *50*, 440–448.

[140] R. J. Adrian, J. Westerweel, *Particle image velocimetry*, Cambridge University Press, **2011**.

[141] A. Dhanorker, X. Liu, T. Özel in Proceedings of MSEC-ASME International Conference of Manufacturing Science and Engineering, **2007**.

[142] M. Annoni, L. Rebaioli, Q. Semeraro, *Int J Adv Manuf Technol* **2015**, *79*, 881–895.

[143] *Geometrical Product Specifications (GPS) - Surface texture: Profile method - Terms, definitions and surface texture parameters*, ISO 4287: 1997.

[144] *Geometrical Product Specifications (GPS) - Surface texture: Profile method; Surfaces having stratified functional properties - Part 2: Height characterization using the linear material ratio curve*, ISO 13565-2: 1996.

[145] M. Sorgato, M. Babenko, G. Lucchetta, B. Whiteside, *The International Journal of Advanced Manufacturing Technology* **2017**, *88*, 547–555.

[146] N. Lee, Y.-K. Kim, S. Kang, *Journal of Physics D: Applied Physics* **2004**, *37*, 1624.

[147] N. El Kissi, L. Leger, J.-M. Piau, A. Mezghani, *Journal of non-newtonian fluid mechanics* **1994**, *52*, 249–261.

[148] L. Léger, H. Hervet, G. Massey, E. Durliat, *Journal of Physics: Condensed Matter* **1997**, *9*, 7719.

[149] W. P. Dong, P. J. Sullivan, K. J. Stout, *Wear* **1994**, *178*, 29–43.

[150] P. Bartolo, J. Vasco, B. Silva, C. Galo, *Assembly Automation* **2006**, *26*, 227–234.

[151] G. Lucchetta, F. Marinello, P. F. Bariani, *CIRP Annals-Manufacturing Technology* **2011**, *60*, 559–562.

[152] W. Grzesik, J. Rech, K. Żak, *The International Journal of Advanced Manufacturing Technology* **2015**, *78*, 2049–2056.

[153] R. Rosenholtz, J. Malik, *Vision research* **1997**, *37*, 2283–2293.

[154] H. M. Laun, *Rheologica Acta* **1983**, *22*, 171–185.

[155] H. Münstedt, M. Schmidt, E. Wassner, *Journal of Rheology* **2000**, *44*, 413–427.

[156] J. Vera, E. Contraires, A.-C. Brulez, M. Larochette, S. Valette, S. Benayoun, *Applied Surface Science* **2017**, *410*, 87–98.

[157] B. H. M. Sadeghi, *Journal of materials processing technology* **2000**, *103*, 411–416.

[158] D. Quagliarella, *Genetic algorithms and evolution strategy in engineering and computer science: recent advances and industrial applications*, John Wiley & Son Ltd, **1998**.

[159] F. M. Schmidt, J.-F. Agassant, M. Bellet, *Polymer Engineering & Science* **1998**, *38*, 1399–1412.

[160] D.-S. Choi, Y.-T. Im, *Composite Structures* **1999**, *47*, 655–665.

[161] *Plastics – Injection Moulding of Test Specimens of Thermoplastic Materials - Part 3: Small Plates.* BS EN ISO 294 – 3: 2003.

[162] D. Annicchiarico, U. M. Attia, J. R. Alcock, *Polymer testing* **2013**, *32*, 769–777.

[163] J. Fischer, *Handbook of molded part shrinkage and warpage*, William Andrew, **2012**.

[164] L. Orazi, I. Gnilitskyi, A. P. Serro, *Journal of Micro and Nano-Manufacturing* **2017**, *5*, 021008.

[165] B. J. Hamrock, S. R. Schmid, B. O. Jacobson, *Fundamentals of machine elements*, McGraw-Hill Higher Education, **2005**.